NOAA Project
Report

Tsunami Inundation Maps Development and Continuation of the Meteotsunami Characterization for the GOM

Final Report to the
National Tsunami Hazard Mitigation Program (NTHMP)
in Completion of Project Awards
NA21NWS4670012

Authors

Juan J Horrillo — Texas A&M University at Galveston
Wei Cheng
Alwin Jose
Yuchen Shang

Collaborators:
Jasmine Johnson-Divinity — Earthquake Program Manager, Mississippi Emergency Management Agency

Under the guidance of
NTHMP Mapping and Modeling Subcommittee

National Tsunami Hazard Mitigation Program

National Oceanic and Atmospheric Administration

OCEAN ENGINEERING
TEXAS A&M UNIVERSITY

Ocean Engineering
Texas A&M University at Galveston
Galveston, Texas, 77553

December 2022

Contents

List of Figures

List of Tables

1 Executive Summary

Potential tsunami sources for the GOM are local submarine landslides, which have been examined in the past by the Atlantic and Gulf of Mexico Tsunami Hazard Assessment Group [ten Brink et al., 2009b]. In their findings, they stated that submarine landslides in the GOM are considered a potential tsunami hazard. However, the probability of such an event (tsunamis generated by large landslides) is low. The probability of occurrence is related to ancient (geological) massive landslides which were probably active prior to 7,000 years ago when large quantities of sediments were emptied into the Gulf of Mexico. Nowadays, sediment continues to empty into the Gulf of Mexico mainly from the Mississippi River. This sediment supply contributes to the slope steepening and the increase of fluid pore pressure in sediments, which may lead to further landslide activities and hence, the reason for this study in determining the potential tsunami hazard and its effects in the Gulf of Mexico.

For the triggering mechanism (tsunami generation) we use five geological sources, i.e., the Eastbreaks, Mississippi Canyon, West Florida landslides, and two Yucatán landslides introduced in [Horrillo et al., 2018]. A probabilistic approach was implemented in our previous study, see [Horrillo et al., 2015], to fill gaps along the continental shelf between the geological landslide sources by adding synthetic landslide sources (four in total) to cover the entire northern part of the GOM. Our probabilistic approach confirmed a recurrence period of major landslide events of around 8000 years, consistent with findings by [Geist et al., 2013].

These geological and probabilistic tsunami sources (nine in total) are used as the maximum credible events that could happen in the region according to the local bathymetry, seafloor slope, and sediment information. These credible events are then used to determine the inundation impact on selected communities along the GOM. The extent and magnitude of the tsunami inundation in those selected locations are achieved by using a combination of 3D and 2D coupled-numerical models. For instance, the 3D model, TSUNAMI3D, is used for tsunami generation to determine the initial dynamic wave or initial source and results are passed as an input to the 2D non-hydrostatic model, NEOWAVE, to determine the tsunami wave propagation and the detailed runup and inundation extent in each of the communities. Tsunami flooding inland-extent, maximum inundation water depth, momentum flux and direction, current velocity and vorticity can then be determined within the inundation-prone areas of the selected communities. Also, tsunami inundation and hurricane category flooding can be compared to access tsunami hazard in unmapped locations.

This project focused on the implementation of recent developments in the tsunami science recommended by the National Tsunami Hazard Mitigation Program - Modeling Mapping Subcommittee - Strategic Plan (NTHMP-MMS-SP) into our current Gulf of Mexico (GOM) tsunami mitigation products. Four main developments for tsunami mitigation have been created under this project for communities in the GOM that will provide guidance to state emergency managers for tsunami hazard mitigation and warning purposes.

The first is the development of tsunami inundation maps in Orange Beach, AL and Mexico Beach, FL. Maximum tsunami inundation extent, water height, and momentum flux magnitude and direction are determined from each landslide sources, as well as the maximum of maximum inundation maps from all nine landslide sources. The two new

tsunami inundation map products add to the existing 18 mapped locations, which provide so far good coverage of the most populous coastal areas along the GOM.

The second is a continuing study of the comparison between existing SLOSH hurricane flooding data and our tsunami inundation result, in order to provide temporal-low-order estimate for tsunami hazard areas (community) where inundation studies have not yet been assigned/executed or where little bathymetric and elevation data exists. The adopted approach to define a quick estimate of tsunami vulnerability areas in the GOM has been taken from the existing hurricane storm surge flooding results along coastal areas, in which storm flooding map products are based on hurricane category. The existing storm surge flooding maps cover almost the entire GOM coastal regions and thus they are very well known among GOM regional emergency managers and other parties.

The third is to produce the velocity and vorticity magnitude maps for all the landslide scenarios, for Orange Beach, AL and Mexico Beach, FL. Based on these maritime maps, location of strong currents and their damaging levels are identified. The tsunami hazard maritime products such as tsunami current magnitude, vorticity, safe/hazard zones would be central for future developments of maritime hazard maps, maritime emergency response and as well as infrastructure planning. We hope that the results herein may assist the maritime communities, port managers and other NTHMP's interested parties.

The fourth task is a continuation of the study to obtain an understanding of meteotsunami through the characterization of physical parameters in GOM [Cheng et al., 2021, Horrillo et al., 2020, 2021]. In this project, we expanded the previous parameter study from 1260 runs (on 1 arcminute resolution grid) to 17280 runs (15 arcsecond grid) for each subregion (northeastern & northwestern GOM), thanks to the huge performance increase using CUDA on our newly built multi-GPU workstation. The GPU workstation has three Nvidia RTX 3090 GPUs, and is able to run our meteotsunami Fortran code 50 – 100 times faster than it CPU versoin, depending on the grid. The result is a significantly improved resolution of different incident wave direction, forward speed and trajectory position, and their effect on maximum gauge water elevation across the whole GOM.

Although the recurrence of destructive tsunami events have been verified to be quite low in the GOM, our work has confirmed that submarine landslide events with similar characteristics to those used here, have indeed the potential to cause severe damage to GOM coastal communities. Therefore, this work is intended to provide guidance to local emergency managers to help managing urban growth, evacuation planning, and public education with final objective to mitigate potential tsunami hazards in the GOM.

2 Introduction

2.1 Background

The U.S. Tsunami Warning System has included Gulf of Mexico (GOM) coasts since 2005 in order to enable local emergency management to act in response to tsunami warnings. To plan for the warning response, emergency managers must understand what specific areas within their jurisdictions are threatened by tsunamis. Coastal hazard areas susceptible to

tsunami inundation can be determined by historical events, by modeling potential tsunami events (worst-case scenarios), or by using a probabilistic approach to determine the rate of recurrence or likelihood of exceeding a certain threshold. As the GOM coastal regions have no significant recent historical tsunami records, numerical modeling and probabilistic methodologies for source identification must be used to determine coastal hazard zones.

Potential tsunami sources for the GOM are local submarine landslides [ten Brink et al., 2009b]; sources outside the GOM are considered a very low threat and may not significantly impact GOM coastal communities or infrastructure [Knight, 2006]. Although a massive tsunamigenic underwater landslide in the GOM is considered a potential hazard, the frequency of such events (though not well-constrained) is probably quite low based on historical evidence [Dunbar and Weaver, 2008] and available data on ages of failures which suggest they were probably active prior to 7,000 years ago when large quantities of sediments were emptied into the GOM [ten Brink et al., 2009b]. However, sediments continue to empty into the GOM, mainly from the Mississippi River, contributing to slope steepening and the increase of fluid pore pressure in sediments which may lead to unstable slopes that can be subsequently triggered to failure by seismic loading [Masson et al., 2006, ten Brink et al., 2009a, Dugan and Stigall, 2010, Harbitz et al., 2014]. In addition, the unique geometry of the GOM basin makes even unlikely tsunami events potentially hazardous to the entire Gulf Coast. Waves tend to refract along continental slopes; thus, given the curved geomorphology of the GOM shelf and the concave shape of the coastline, any outgoing tsunami wave could potentially affect the opposite coast in addition to the coast close to the landslide source.

Five large-scale geological submarine landslides with tsunamigenic potential have been identified within the GOM [ten Brink et al., 2009b, Chaytor et al., 2016], representing possible worst-case tsunami scenarios affecting GOM coasts in the past. In order to generate a more complete picture of landslide tsunami potential in the GOM, a probabilistic approach has been implemented to develop four additional synthetic landslide sources which fill gaps along the continental shelf between the geological landslide sources [Pampell-Manis et al., 2016]. These probabilistic tsunami sources are considered to be the maximum credible events that could happen in a particular region of the GOM according to the local bathymetry, seafloor slope, sediment information, and seismic loading. The probabilistic maximum credible events together with the geological sources form a suite of tsunami sources that have been used within coupled 3D and 2D numerical models to model tsunami generation and propagation throughout the GOM and to develop high-resolution inundation maps for the inundation-prone areas of two new communities along the Gulf Coast: Orange Beach, AL and Mexico Beach, FL. These inundation studies showed that tsunamis triggered by massive submarine landslides have the potential to cause widespread and significant inundation of coastal cities. All of the 20 communities from both previous and current work and nine landslide sources are shown in Fig. 1.

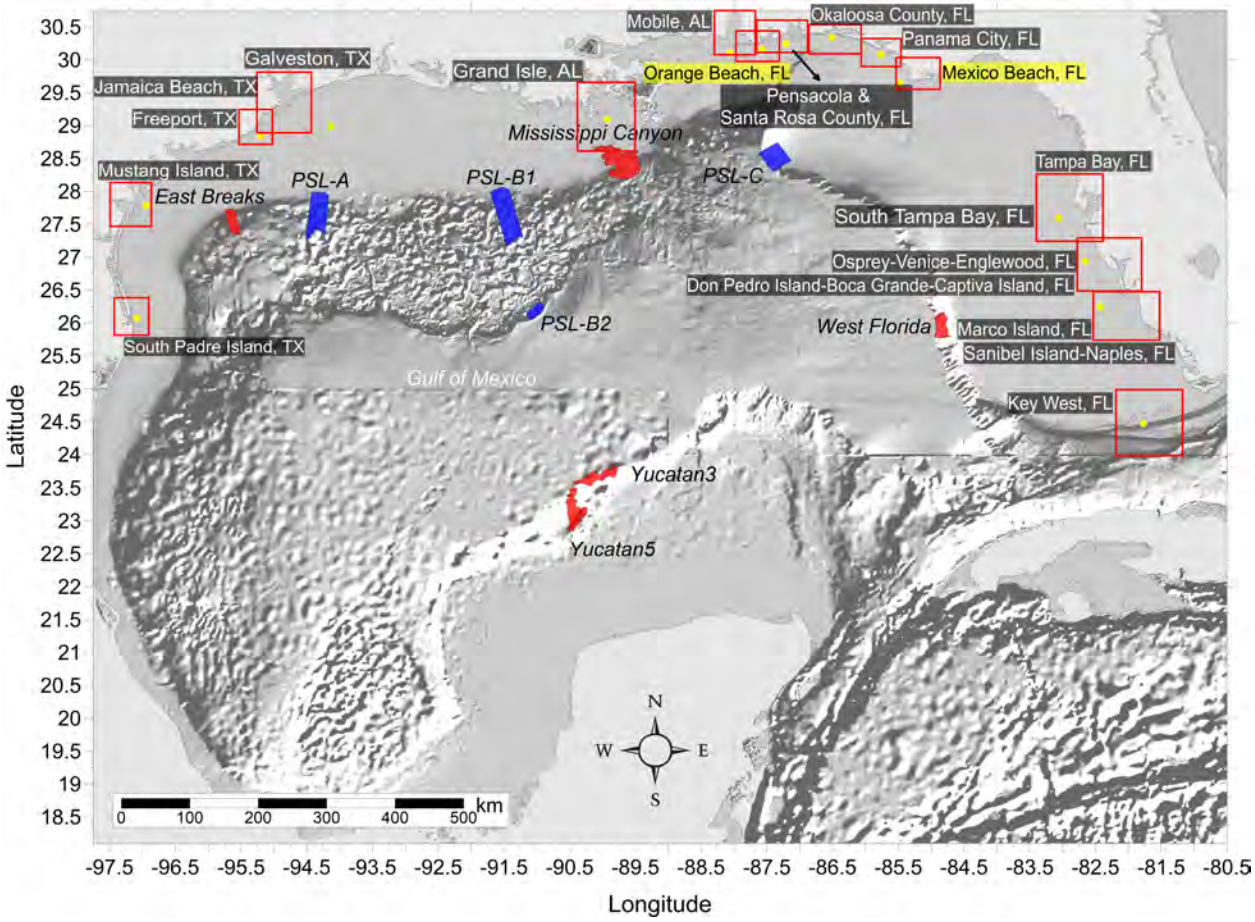

Figure 1: Selected communities or geography regions along the US GOM coastline where tsunami maps have been developed. Red rectangles denote 3 arcsecond (∼90m) domains of coastal communities where tsunami inundation has been modeled (highlighted Orange Beach, AL and Mexico Beach, FL are developed in the current project); red hatched areas are geological landslide sources; blue hatched areas are Probabilistic Submarine Landslide (PSL) sources; yellow dots are locations of numerical wave gauges. The zero-meter elevation contour is drawn to show the GOM coastline.

While high-resolution tsunami inundation studies have been completed for these 20 communities and are planned for additional locations, vulnerability assessments are still essential for coastal locations where inundation studies have not yet been performed or planned, or where there is a lack of high-resolution bathymetric and/or elevation data. Therefore, we aim to extend the results of the completed mapping studies in order to provide estimates of tsunami inundation zones for hazard mitigation efforts in unmapped locations. Inundation maps with even low resolution are useful to emergency managers to create first-order evacuation maps, and some methods currently exist to provide low-resolution estimates of hazard zones for regions which do not currently have or warrant high-resolution maps. For example, guidance given by the National Tsunami Hazard Mitigation Program (NTHMP) Mapping and Modeling Subcommittee in "Guidelines and Best Practices to Establish Areas of Tsunami Inundation for Non-modeled or Low-hazard Regions" (available from `https://nws.weather.gov/nthmp/documents/3nonmodeledregionguidelines.pdf`) recommends that coastal areas and areas along ocean-connected waterways that are below 10 m (33 ft) elevation are at risk for most tsunamis, and rare and large tsunamis may inundate above this elevation. However, in low-lying coastal regions such as along the Gulf Coast, the 10 m (33 ft) elevation contour is too far inland to be reasonably applicable for estimating potential tsunami inundation zones. The guidance additionally suggests that low-lying areas are prone to inundation within 3 km (1.9 mi) inland for locally-generated tsunamis and within 2 km (1.3 mi) inland for distant sources. While these distances may be reasonable for some regions of the Gulf Coast, prevalent bathymetric and topographic features such as barrier islands/peninsulas complicate the method of delineating inundation-prone areas based on distance from the shoreline. As a result, the purpose of the current work is to improve the methodology which compares modeled tsunami inundation to modeled/predicted hurricane storm surge. Specifically, we aim to identify the hurricane category which produces modeled maximum storm surge that best approximates the maximum tsunami inundation in the two new locations modeled in this project. Even though many physical aspects of storm surge inundation are completely different from those of tsunamis (time scale, triggering mechanism, inundation process, etc.), good agreement or clear trends between tsunami and storm surge flooding on a regional scale can be used to provide first-order estimates of potential tsunami inundation in communities where detailed inundation maps have not yet been developed or are not possible due to unavailability of high-resolution bathymetry/elevation data. Additionally, since tsunamis are not well-understood as a threat along the Gulf Coast, while hurricane hazards are well-known, this method of predicting tsunami inundation from storm surge provides a way for GOM emergency managers to better prepare for potential tsunami events based on more understandable and accessible information. This hurricane-tsunami comparison was first carried out in Horrillo et al. [2016] (award number NA14NWS4670049) where five previously mapped locations were studied, namely South Padre Island, TX, Galveston, TX, Mobile, AL, Panama City, FL, and Tampa, FL; then as a regular procedure for all the newly mapped locations during the following mapping projects.

Past tsunamis have shown that the maritime community requires additional information and guidance about tsunami hazards and post-tsunami recovery [Wilson et al., 2012, 2013]. To accomplish mapping and modeling activities to meet NTHMP's planning/response purposes for the maritime community and port emergency management and other customer

requirements, it is necessary to continue the process to include maritime products in our current inundation map development. These activities will include tsunami hazard maritime products generated by GOM's tsunami sources (submarine landslides) that may impact specifically ship channels, bay inlets, harbors, marinas, and oil infrastructures (e.g., designated lightering and oil tanker waiting zones), which has already been applied in other tsunami risk regions, e.g., California, Oregon and Washington. It is worth noting that Galveston was the first city where we implemented the maritime products [Horrillo et al., 2016]. South Padre Island, TX, Mobile, AL, Panama City, FL, and Tampa, FL, Pensacola, FL, Key West, FL, Okaloosa County, FL, Santa Rosa County, FL and Mustang Island, TX, were implemented in project NA15NWS4670031 and NA16NWS4670039 [Horrillo et al., 2017], and then as a regular procedure for all the newly mapped locations during the following mapping projects.

An additional task is a study where we conducted numerical experiments to investigate the generation and propagation of meteotsunami waves and assessed hazards on a broad scale in the whole GOM [Cheng et al., 2021]. In previous two projects, we assessed the tsunami hazards in both northeastern [Horrillo et al., 2020] and northwestern GOM [Horrillo et al., 2021], each with 1260 meteotsunami simulations (12 incident wave directions $\times$ 15 trajectories $\times$ 7 velocities) on a 1 arcminute resolution grid. With the help of a newly built multi-GPU workstation which has three Nvidia RTX 3090 GPUs and is capable of running our meteotsunami Fortran code in CUDA 50 – 100 times faster than the CPU version, depending on the grid, we expanded the previous parameter study to 17280 runs (i.e., 36 incident wave directions $\times$ 30 trajectories $\times$ 16 velocities) on a more accurate 15 arcseconds resolution grid for each subregion. The result is a significantly improved resolution of different incident wave direction, forward speed and trajectory position, and their effect on maximum gauge water elevation across the whole GOM.

The previous MT rose charts were modified to a finer resolution (adding more directions and including other variables or parameters, example: forward speed of the AD, etc.), at 98 numerical gauges or locations along the GOM coastline. However, the sealevel increase of most of the MT cases represented in the MT hazard rose chart is small. In order to better represent the MTs posed with extreme hazards, a new visualization hazard rose chart was developed, named the severe meteotsunami rose chart. This visualization chart facilitates identification of severe case scenarios. Severe MT rose charts were then used to characterize the MT hazard for the102 locations along the GOM; eight of these locations are shown in this report and are discussed in greater detail in the following sections.

Last, to provide a broader and faster way to predict the hazards on a broad scale, an optimal artificial neural network (ANN) was trained using data from a large number of MT simulations in the northeastern GOM. The trained BP neural network is then used to generate a more comprehensive data set in order to investigate the effect of three new parameters, which are storm surge, yaw angle, and pressure slope.

2.2 Regional and Historical Context

Orange Beach, AL

Orange Beach, AL is the easternmost community on Alabama's Gulf Coast. In this study, the finest grid (1/3 arcsecond) also includes Gulf Shores, AL to the west and Ono Island, AL and Perdido Key, FL to the east. This study area was selected for this project to fill in the gap between Daulphin Island & west of Gulf Shores, AL and Pensacola Beach, FL mapping areas investigated in Horrillo et al. [2015, 2016], respectively. The Alabama portion of the study area belongs to Baldwin County, and the Florida portion belongs to Escambia County. Gulf Shores had a population of 15,014 in 2020, up from 9,741 in 2010. Orange Beach population rosed 48.8% from 5,441 in 2010 to 8,095 in 2020. In case of emergency, the mainland can be accessed from Gulf shores via State Highway 180, State Highway 59, Alabama's Coastal Connection, and County Road 2, while Orange Beach via Orange Beach Blvd, Ono Ts Bridge, River Rd, and Perdido Key Dr.

Mexico Beach, FL

The Mexico Beach, FL 1/3 arcsecond computational domain encompasses the whole populated communities surrounding the St. Joseph Bay, which includes Mexico Beach, Port St. Joe, the St. Joseph Pennisula, Cape San Blas, and Indian Pass. Panama City is the closest coastal community previously mapped for tsunami inundation to the west [Horrillo et al., 2016], and there are no residents on the barrier islands between Panama City and Mexico Beach. Mexico Beach, which belongs to Bay County, FL, has largely kept a steady population since 1990s with its 2020 population at 1,060, while Port St. Joe, located in Gulf County, has been in decline since 1970's 4000 plus to 2020's 3,357. In case of emergency, the mainland can be reached from the Mexico Beach study area via Highway 98, County Road 386 S, Old Parkwood Tramroad, State Highway 382, State Road 71, and Old Niles Tramroad.

Recent Hurricane History

The 2004 Hurricane Ivan weakened from Category 5 in its peak to Category 3 when it made landfall in Gulf Shores, AL, on September 16. Major damage was observed along the Florida Panhandle from Baldwin County (Perdido Key), AL to Santa Rosa County, FL. A few roads in Perdido wasn't open until a year after the hit. In total, Hurricane Ivan caused over 20 billion $ of damage in the US.

Merely 10 months later, in September 2005, Hurricane Dennis made landfall approximately 30 miles east of Ivan's landfall location. Because of its compact size and previous impact from Ivan, Dennis did not cause much damage but had left many without power in four southern states and caused 15 deaths.

Hurricane Michael of 2018 was the first Category 5 since 1992 Andrew in the US, causing 49 death in the US and more than 25 billion $ of damage. Micheal made landfall near Mexico Beach, which together with Panama City suffered the worst of Michael, with catastrophic damage reported due to the extreme winds and storm surge. The only road connecting

St. Joseph State Park on the pennisula to the mainland was washed away and the beach breached. Tyndall Air Force Base, located just southeast of Panama City, suffered great damage to all the structures and many aircrafts due to the strong winds brought by Hurricane Michael.

2.3 Summary

Although the probability of a large-scale tsunami event in the GOM is low, this and previous studies have indicated that tsunami events with characteristics similar to those detailed in Horrillo et al. [2015] have the potential to cause severe flooding and damage to GOM coastal communities that is similar to or even greater than that seen from major hurricanes, particularly in open beach and barrier island regions. Tsunami hazard maritime products such as tsunami current magnitude, vorticity, safe/hazard zones would be central for future developments of maritime hazard maps, maritime emergency response as well as infrastructure planning. The results of this work are intended to provide guidance to local emergency managers to help with managing urban growth, evacuation planning, and public education with the vision to mitigate potential GOM tsunami hazards.

This report is organized as follows. Section 3 briefly describes all 9 landslide sources used for tsunami modeling (3.1) and the numerical models used for simulations (3.2). Section 4 covers the inundation and momentum flux maps for Orange Beach, AL and Mexico Beach, FL. The comparison between tsunami inundation and hurricane storm surge inundation (tsunami inundation in terms of hurricane category) is given in Section 5 for the two new Gulf Coast communities. Current velocity and vorticity maps are described in Section 6 for the two new communities. Section 7 presents a new CUDA meteotsunami model and the refined numerical results for a parameter study of GOM, with identification of coastal communities vulnerable to meteotsunami inundation. Section 8 is the characterization of meteotsunamis in northern GOM using meteotsunami rose charts. Section 9 is the application of ANN in meteotsunami water elevation prediction. Concluding remarks on general trends seen among the communities and practical applications for other regions are given in Section 10.

3 Tsunami Inundation Modeling

3.1 Landslide Tsunami Sources

Nine large-scale landslide configurations were created assuming an unstable (gravity-driven) sediment deposit condition. Five of these landslide configurations are geological events identified by ten Brink et al. [2009b]: the Eastbreaks, Mississippi Canyon, and West Florida submarine landslides; and Chaytor et al. [2016]: the Yucatán #3 and Yucatán #5 landslides, which are shown as red hatched regions in Fig. 1. The Yucatán Shelf/Campeche Escarpment was the last remaining area of the GOM that had not been evaluated for landslide tsunami hazards, until high-resolution mapping data collected in 2013 [Paull et al., 2014] shows that the Yucatán Shelf/Campeche Escarpment margin has been subjected to intense modifications by Cenozoic mass wasting processes. Although no known tsunami events have been linked to these Yucatán sources, numerical modeling result shows that they are capable of generating tsunamis that could propagate throughout the GOM Basin [Chaytor et al., 2016]. The other four were obtained using a probabilistic methodology based on work by Maretzki et al. [2007] and Grilli et al. [2009] and extended for the GOM by Pampell-Manis et al. [2016]. The probabilistic landslide configurations were determined based on distributions of previous GOM submarine landslide dimensions through a Monte Carlo Simulation (MCS) approach. The MCS methodology incorporates a statistical correlation method for capturing trends seen in observational data for landslide size parameters while still allowing for randomness in the generated landslide dimensions. Slope stability analyses are performed for the MCS-generated trial landslide configurations using landslide and sediment properties and regional seismic loading (Peak Horizontal ground Acceleration, PHA) to determine landslide configurations which fail and produce a tsunami. The probability of each tsunamigenic failure is calculated based on the joint probability of the earthquake PHA and the probability that the trial landslide fails and produces a tsunami wave above a certain threshold. Those failures which produce the largest tsunami amplitude and have the highest probability of occurrence are deemed the most extreme probabilistic events, and the dimensions of these events are averaged to determine maximum credible probabilistic sources. The four maximum credible Probabilistic Submarine Landslides (PSLs) used as tsunami sources for this study are termed PSL-A, PSL-B1, PSL-B2, and PSL-C and are shown as blue hatched regions in Fig. 1. For a more complete discussion of GOM submarine landslide sources, the reader can consult Horrillo et al. [2015, 2018], Pampell-Manis et al. [2016].

Table 1: Submarine Landslide general information.

Submarine Landslide	Location (Lon, Lat)	Age/Recurrence (Years)	Area (km^2)	Volume (km^3)	Excavation Depth (m)	Modeled Volume (km^3)
East Breaks	-95.68, 27.70	$\sim 10000 - 25000$	~ 519.52	~ 21.95	~ 160	26.7
Mississippi	-90.00, 28.60	$\sim 7500 - 11000$	~ 3687.26	~ 425.54	~ 300	425
West Florida	-84.75, 25.95	> 10000	~ 647.57	~ 16.2	~ 150	18.4
Yucatán #3	-90.07, 23.00	–	~ 578	~ 38	~ 278	39.3
Yucatán #5	-89.80, 23.54	–	~ 1094	~ 70.2	~ 385	69.5
PSL-A	-94.30, 27.98	$\sim 7700 - 7800$	~ 1686	~ 57	~ 67	58
PSL-B1	-91.56, 28.05	$\sim 5400 - 5500$	~ 3118	~ 69	~ 44	57.3
PSL-B2	-91.01, 26.17	$\sim 4700 - 4800$	~ 282	~ 45	~ 323	68
PSL-C	-87.20, 28.62	$\sim 550 - 650$	~ 1529	~ 315	~ 404	357

3.2 Numerical Models

For the nine landslide tsunami sources considered here, tsunami wave development and subsequent propagation and inundation of coastal communities was modeled using coupled 3D and 2D numerical models [Horrillo et al., 2015]. The tsunami generation phase was modeled using the 3D model TSUNAMI3D [Horrillo, 2006, Horrillo et al., 2013], which solves the finite difference approximation of the full Navier-Stokes equations and the incompressibility (continuity) equation. Water and landslide material are represented as Newtonian fluids with different densities, and the landslide-water and water-air interfaces are tracked using the Volume of Fluid (VOF) method of Hirt and Nichols [1981], which is simplified to account for the large horizontal/vertical aspect ratio of the tsunami wave and the selected computational cell size required to construct an efficient 3D grid. The pressure term is split into hydrostatic and non-hydrostatic components. Although TSUNAMI3D has the capability of variable grids, the nesting capability necessary for modeling detailed inundation of coastal regions is too computationally intensive within the fully 3D model; thus, detailed inundation modeling is achieved by coupling the 3D model to a 2D model. Once the tsunami wave generated by the 3D model is fully developed, the wave is passed as an initial condition to the 2D model for modeling wave propagation and coastal inundation. The generated wave is considered fully developed when the total wave energy (potential plus kinetic) reaches a maximum and before the wave leaves the computational domain, as discussed in López-Venegas et al. [2015]. The 2D model used here is NEOWAVE [Yamazaki et al., 2008], a depth-integrated and non-hydrostatic model built on the nonlinear shallow water equations which includes a momentum-conserved advection scheme to model wave breaking and two-way nested grids for modeling higher-resolution wave runup and inundation. Propagation and inundation are calculated via a series of nested grids of increasing resolution, from 15 arcsecond (450 m) resolution for a domain encompassing the entire northern GOM (Fig. 1), to finer resolutions of 3 arcseconds (90 m, from NOAA NCEI Coastal Relief Models), 1 arcsecond (30 m), and 1/3 arcsecond (10 m, from NOAA NCEI Tsunami Inundation Digital Elevation Models [DEMs]) to model detailed inundation of the most populated/ inundation-prone areas of each coastal community. The 3 arcsecond (90 m) subdomains encompassing each coastal community studied here are shown by red rectangles in Fig. 1.

4 Tsunami Maps

Tsunami inundation depth and extent has been modeled for two selected coastal communities: Orange Beach, AL and Mexico Beach, FL. Inundation (flooding) is determined by subtracting land elevation from water elevation, and elevations used are in reference to the Mean High Water (MHW) tidal datum. For this study, the tsunami inundation depth/extent modeled for each community is the maximum-of-maximums (MOM) inundation, which is calculated as the maximum inundation depth from an ensemble of inundation depths produced by each of the nine tsunami sources considered. That is, once inundation in a community has been modeled for each of the nine sources, the overall maximum inundation depth in each computational grid cell is taken as the MOM tsunami inundation in that cell. This approach gives a worst-case scenario of estimated tsunami inundation for each coastal community.

In this section, the numerical results (inundation and momentum flux maps) for each landslide source are presented for Orange Beach, AL and Mexico Beach, FL. The MOM inundation map from all sources and the maximum inundation map by source are also shown. A summary table of each location's numerical gauge (at an approximate water depth of 20 m) shows maximum wave amplitude and arrival time after each landslide failure.

It is worth noting, however, that for both communities, the MOM tsunami inundation is produced solely by the Mississippi Canyon submarine landslide failure. That geological failure is the largest in both area and volume of material removed, and therefore produces the highest amplitude wave of all sources simulated.

4.1 Orange Beach, AL

Table 2: Maximum tsunami wave amplitude and corresponding arrival time after landslide failure at Orange Beach, AL numerical wave gauge: 30°14'45.00"N, 87°12'30.00"W (Fig. 1), approximate water depth 21 m.

Tsunami Source	Maximum Wave Amplitude (m)	Arrival Time After Landslide Failure (hr)
East Breaks	0.26	2.7
PSL-A	0.36	2.3
PSL-B1	0.38	1.5
PSL-B2	0.36	1.7
Mississippi Canyon	4.13	1.0
PSL-C	1.58	0.9
West Florida	0.40	1.7
Yucatán #3	0.58	1.9
Yucatán #5	0.33	2.0

Orange Beach, AL
East Breaks submarine landslide
Maximum Momentum Flux

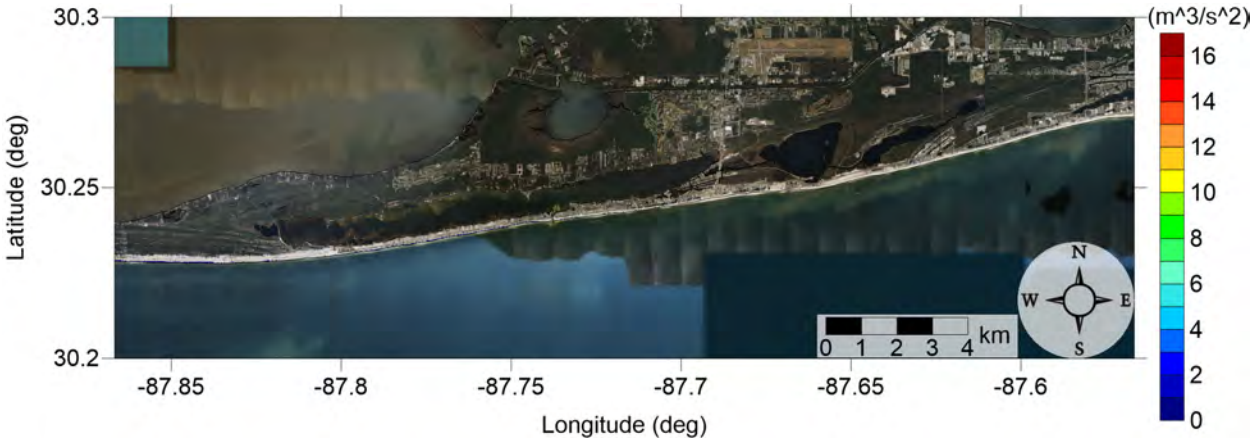

Figure 2: Maximum momentum flux (m^3/s^2) caused by the East Breaks submarine landslide in Gulf Shores, AL. Arrows represent direction of maximum momentum flux. Contour drawn is the zero-meter contour for land elevation.

Orange Beach, AL
East Breaks submarine landslide
Maximum Momentum Flux

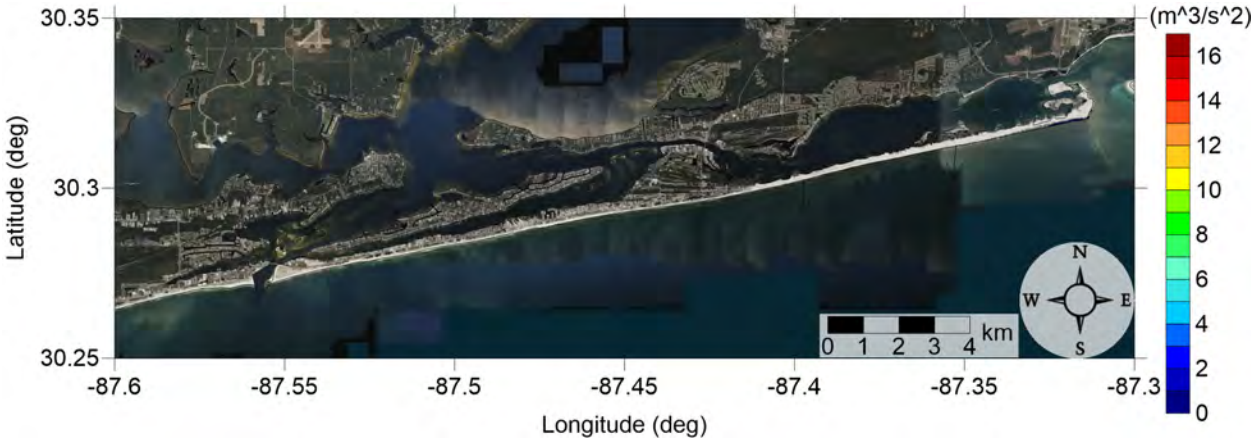

Figure 3: Maximum momentum flux (m^3/s^2) caused by the East Breaks submarine landslide in Orange Beach, AL. Arrows represent direction of maximum momentum flux. Contour drawn is the zero-meter contour for land elevation.

Orange Beach, AL
East Breaks submarine landslide
Maximum Inundation Depth

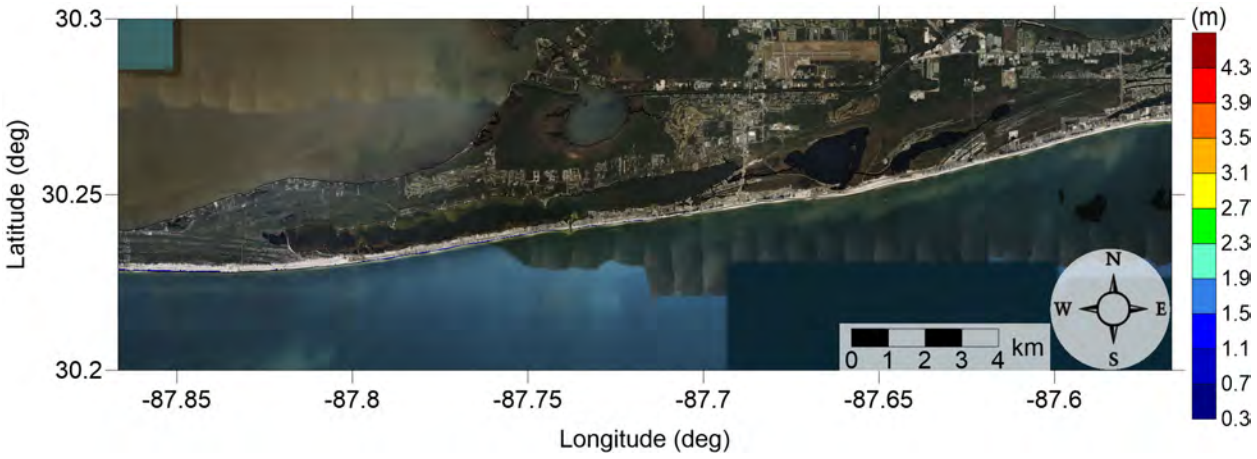

Figure 4: Maximum inundation depth (m) caused by the East Breaks submarine landslide in Gulf Shores, AL. Contour drawn is the zero-meter contour for land elevation.

Orange Beach, AL
East Breaks submarine landslide
Maximum Inundation Depth

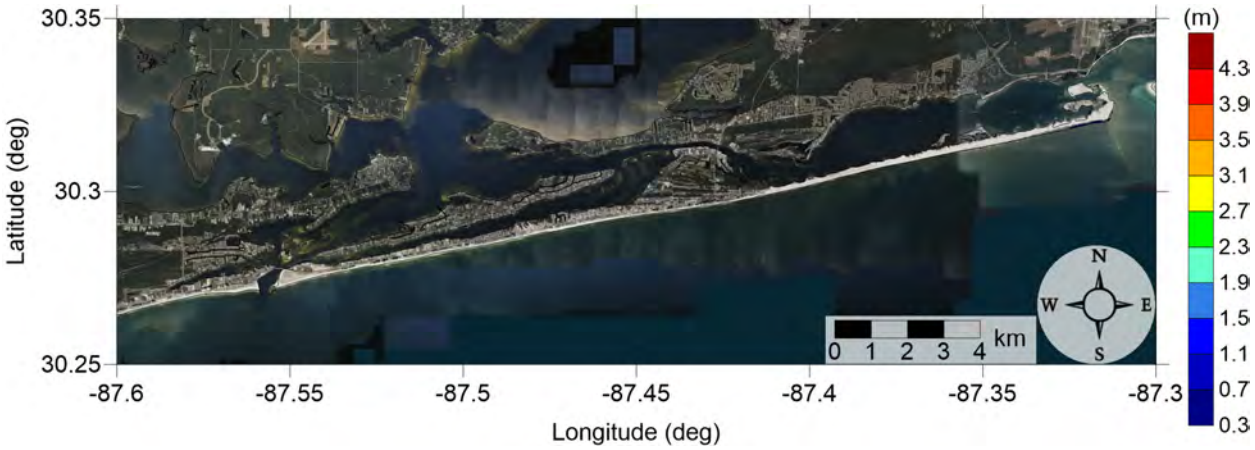

Figure 5: Maximum inundation depth (m) caused by the East Breaks submarine landslide in Orange Beach, AL. Contour drawn is the zero-meter contour for land elevation.

Orange Beach, AL
Probabilistic Submarine Landslide A
Maximum Momentum Flux

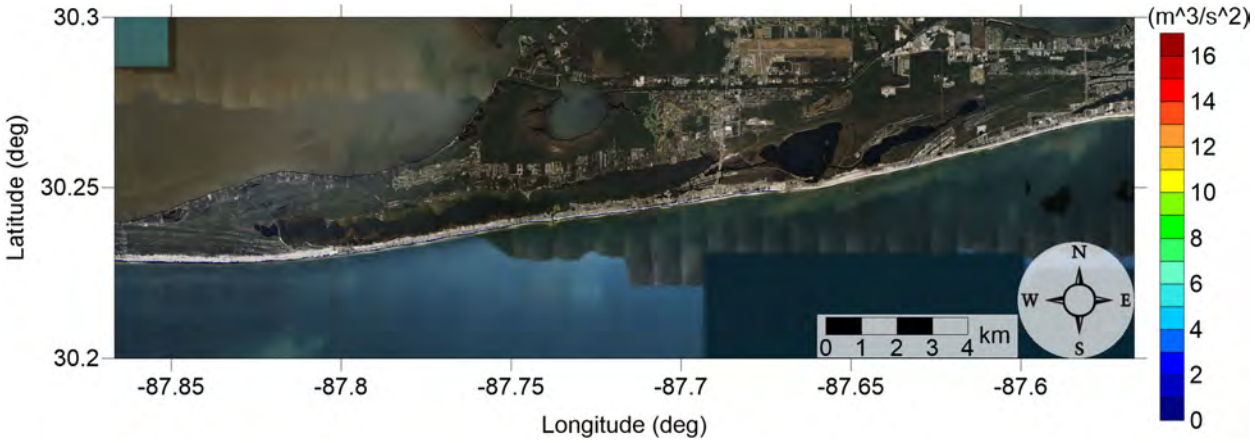

Figure 6: Maximum momentum flux (m^3/s^2) caused by the Probabilistic Submarine Landslide A in Gulf Shores, AL. Arrows represent direction of maximum momentum flux. Contour drawn is the zero-meter contour for land elevation.

Orange Beach, AL
Probabilistic Submarine Landslide A
Maximum Momentum Flux

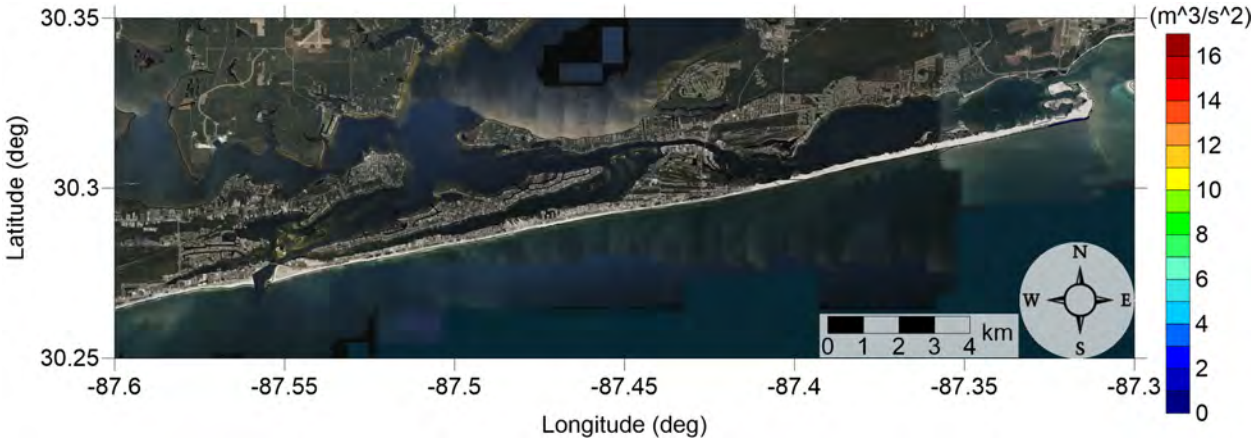

Figure 7: Maximum momentum flux (m^3/s^2) caused by the Probabilistic Submarine Landslide A in Orange Beach, AL. Arrows represent direction of maximum momentum flux. Contour drawn is the zero-meter contour for land elevation.

Orange Beach, AL
Probabilistic Submarine Landslide A
Maximum Inundation Depth

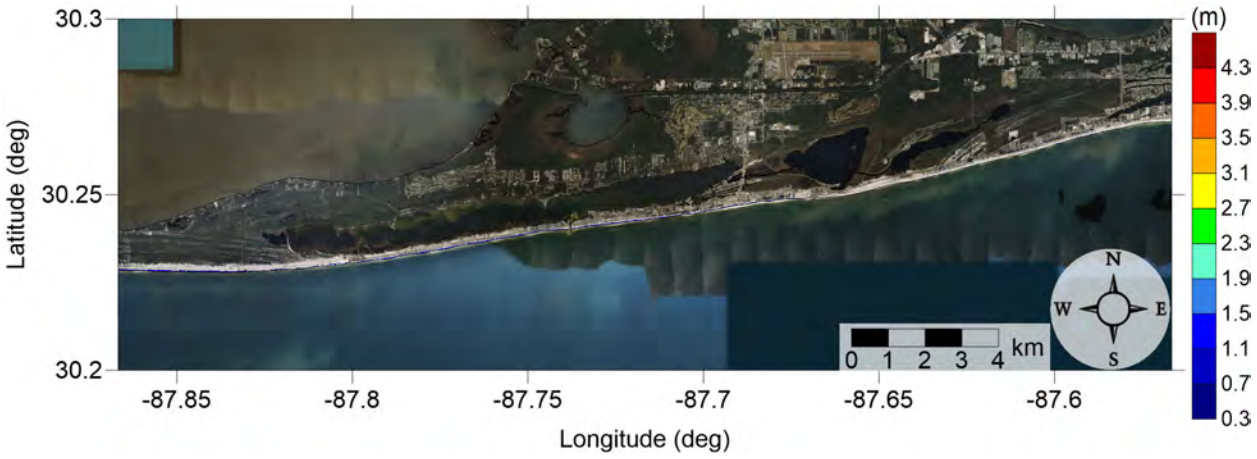

Figure 8: Maximum inundation depth (m) caused by the Probabilistic Submarine Landslide A in Gulf Shores, AL. Contour drawn is the zero-meter contour for land elevation.

Orange Beach, AL
Probabilistic Submarine Landslide A
Maximum Inundation Depth

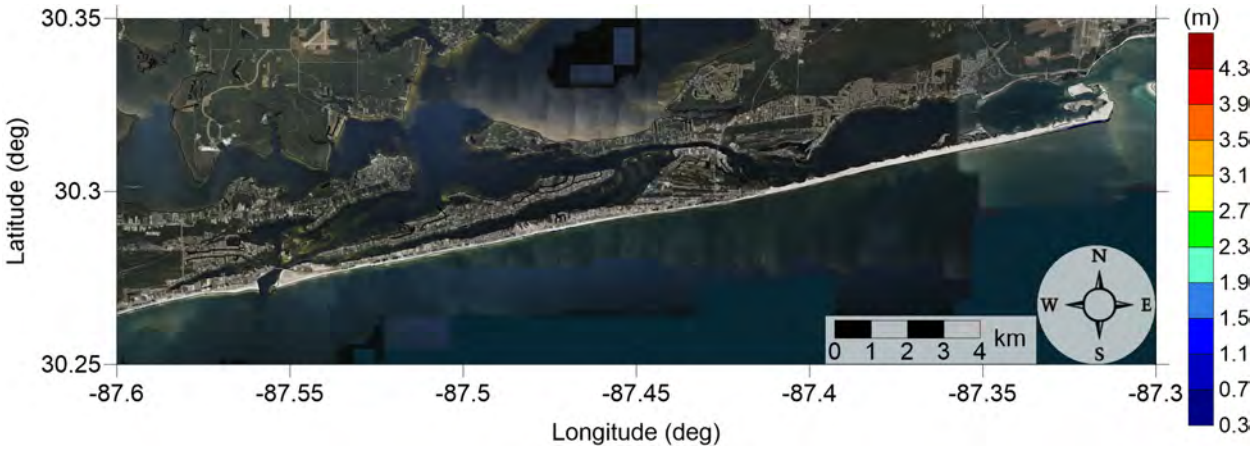

Figure 9: Maximum inundation depth (m) caused by the Probabilistic Submarine Landslide A in Orange Beach, AL. Contour drawn is the zero-meter contour for land elevation.

Orange Beach, AL
Probabilistic Submarine Landslide B1
Maximum Momentum Flux

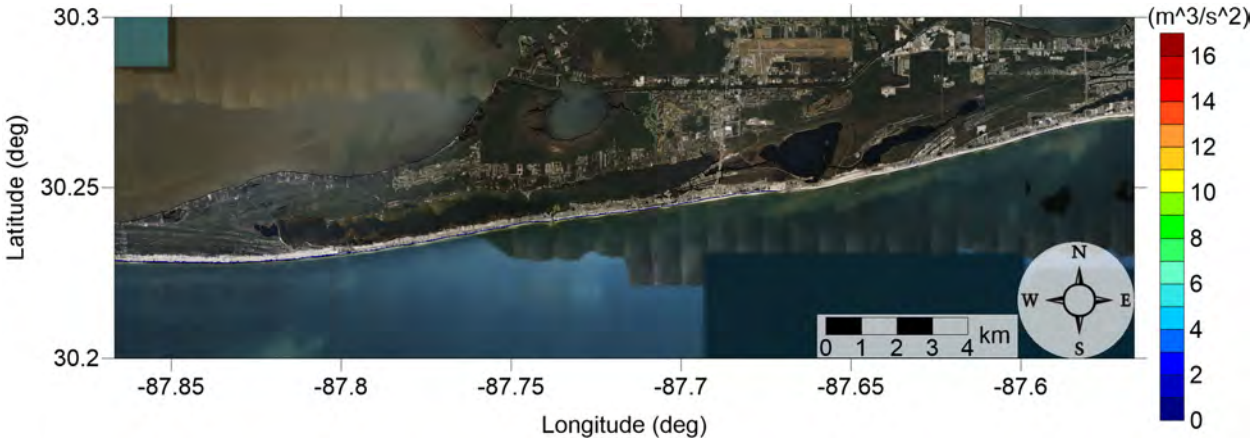

Figure 10: Maximum momentum flux (m^3/s^2) caused by the Probabilistic Submarine Landslide B1 in Gulf Shores, AL. Arrows represent direction of maximum momentum flux. Contour drawn is the zero-meter contour for land elevation.

Orange Beach, AL
Probabilistic Submarine Landslide B1
Maximum Momentum Flux

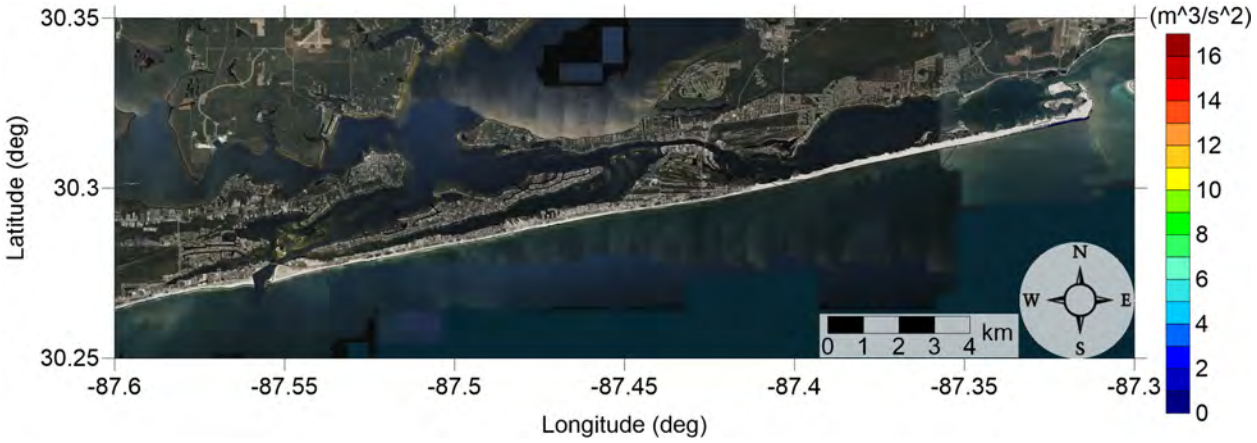

Figure 11: Maximum momentum flux (m^3/s^2) caused by the Probabilistic Submarine Landslide B1 in Orange Beach, AL. Arrows represent direction of maximum momentum flux. Contour drawn is the zero-meter contour for land elevation.

Orange Beach, AL
Probabilistic Submarine Landslide B1
Maximum Inundation Depth

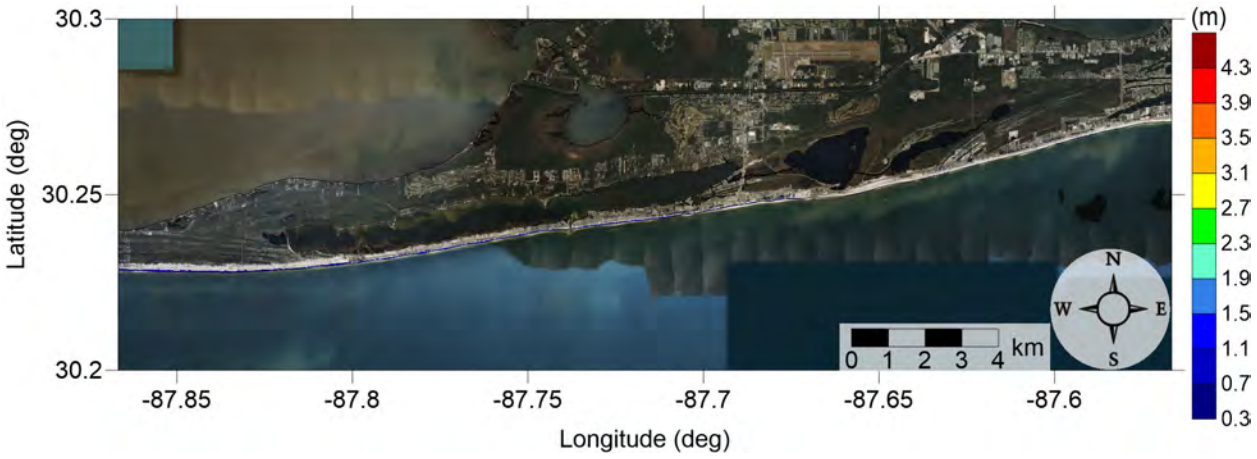

Figure 12: Maximum inundation depth (m) caused by the Probabilistic Submarine Landslide B1 in Gulf Shores, AL. Contour drawn is the zero-meter contour for land elevation.

Orange Beach, AL
Probabilistic Submarine Landslide B1
Maximum Inundation Depth

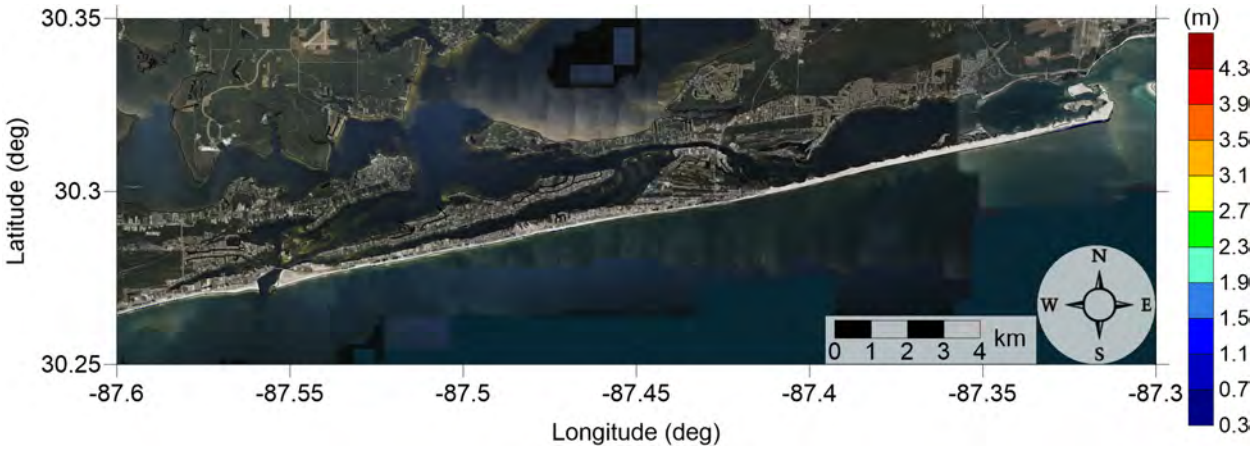

Figure 13: Maximum inundation depth (m) caused by the Probabilistic Submarine Landslide B1 in Orange Beach, AL. Contour drawn is the zero-meter contour for land elevation.

Orange Beach, AL
Probabilistic Submarine Landslide B2
Maximum Momentum Flux

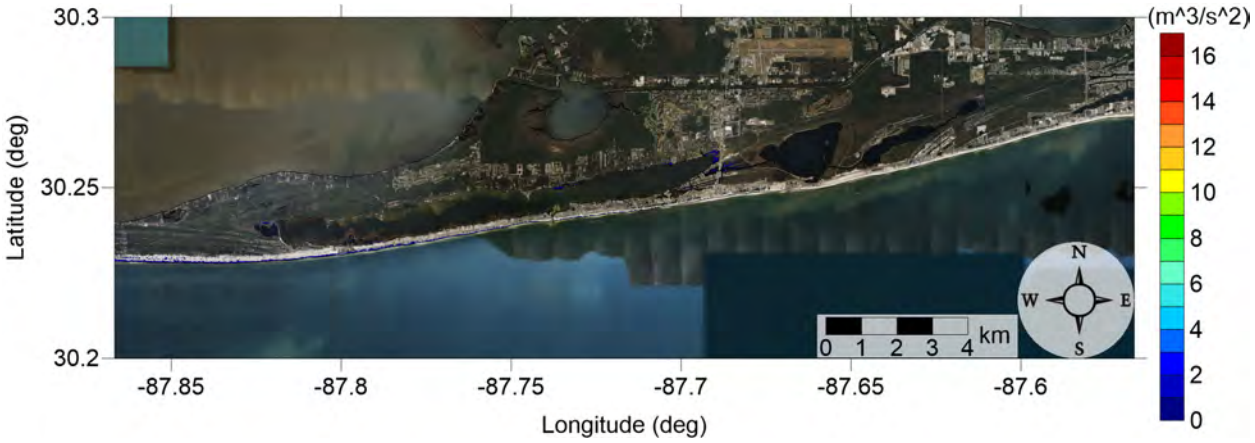

Figure 14: Maximum momentum flux (m^3/s^2) caused by the Probabilistic Submarine Landslide B2 in Gulf Shores, AL. Arrows represent direction of maximum momentum flux. Contour drawn is the zero-meter contour for land elevation.

Orange Beach, AL
Probabilistic Submarine Landslide B2
Maximum Momentum Flux

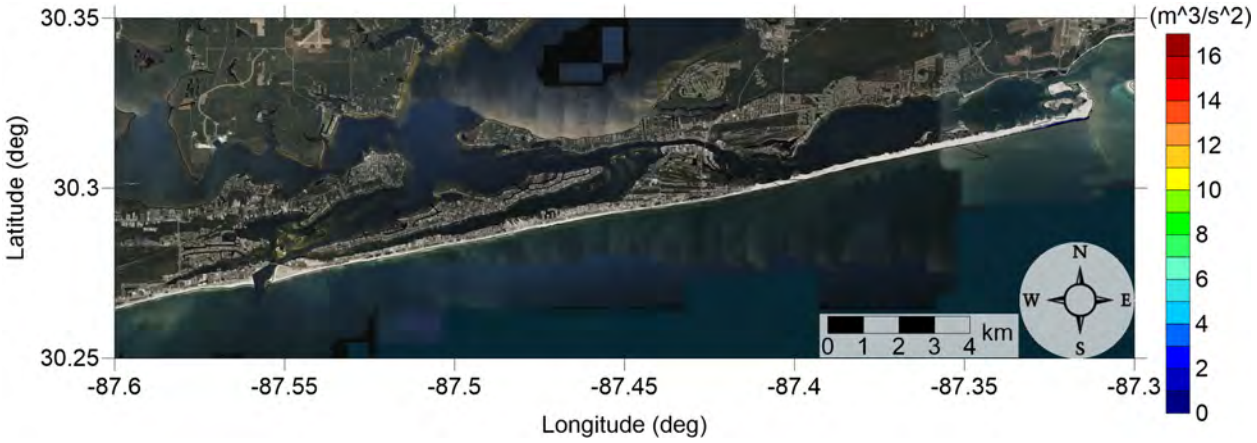

Figure 15: Maximum momentum flux (m^3/s^2) caused by the Probabilistic Submarine Landslide B2 in Orange Beach, AL. Arrows represent direction of maximum momentum flux. Contour drawn is the zero-meter contour for land elevation.

Orange Beach, AL
Probabilistic Submarine Landslide B2
Maximum Inundation Depth

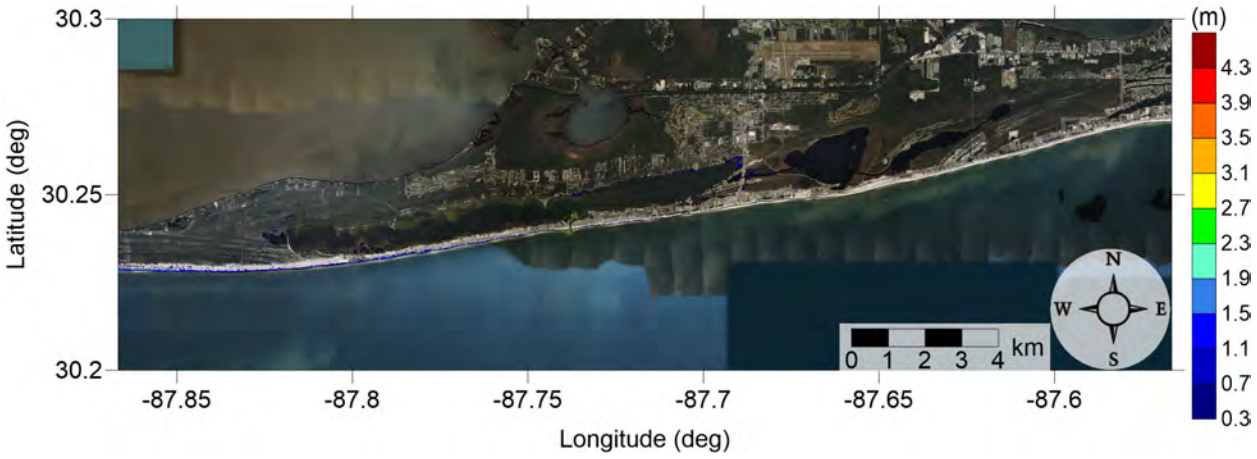

Figure 16: Maximum inundation depth (m) caused by the Probabilistic Submarine Landslide B2 in Gulf Shores, AL. Contour drawn is the zero-meter contour for land elevation.

Orange Beach, AL
Probabilistic Submarine Landslide B2
Maximum Inundation Depth

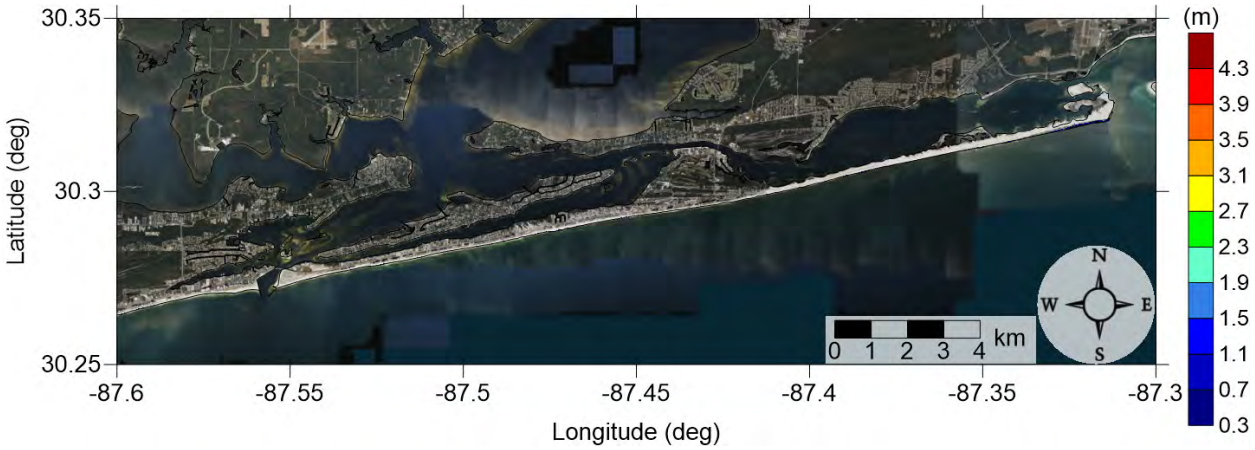

Figure 17: Maximum inundation depth (m) caused by the Probabilistic Submarine Landslide B2 in Orange Beach, AL. Contour drawn is the zero-meter contour for land elevation.

Orange Beach, AL
Mississippi Canyon submarine landslide
Maximum Momentum Flux

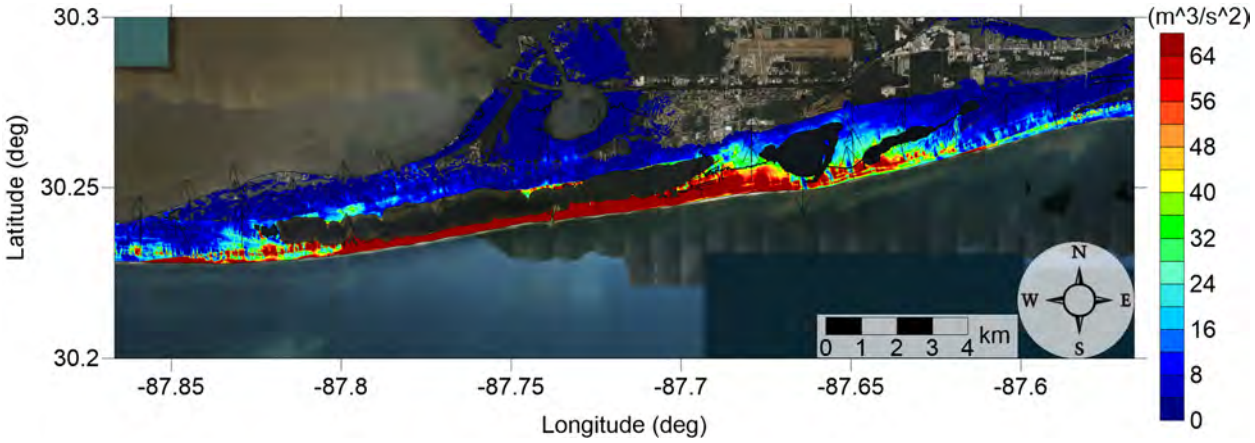

Figure 18: Maximum momentum flux (m^3/s^2) caused by the Mississippi Canyon submarine landslide in Gulf Shores, AL. Arrows represent direction of maximum momentum flux. Contour drawn is the zero-meter contour for land elevation.

Orange Beach, AL
Mississippi Canyon submarine landslide
Maximum Momentum Flux

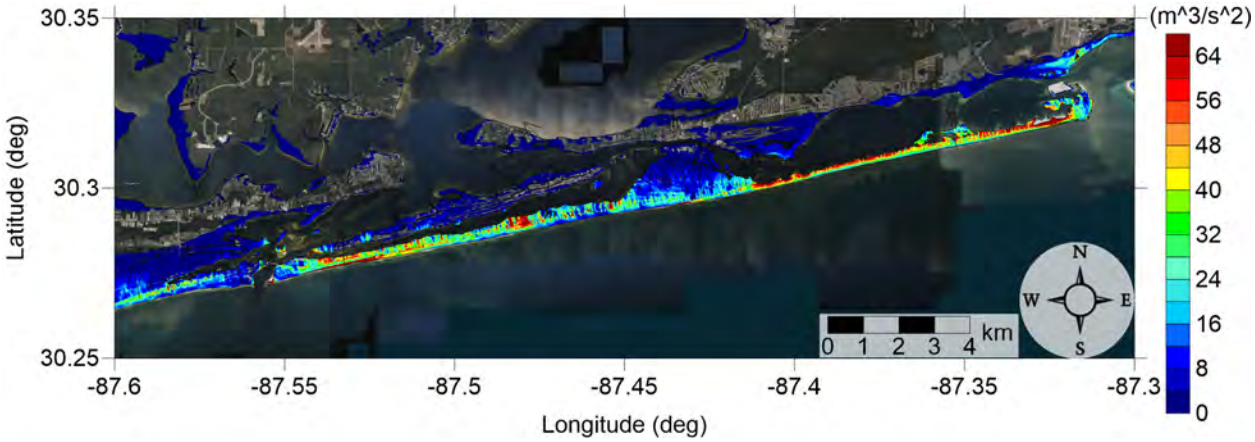

Figure 19: Maximum momentum flux (m^3/s^2) caused by the Mississippi Canyon submarine landslide in Orange Beach, AL. Arrows represent direction of maximum momentum flux. Contour drawn is the zero-meter contour for land elevation.

Orange Beach, AL
Mississippi Canyon submarine landslide
Maximum Inundation Depth

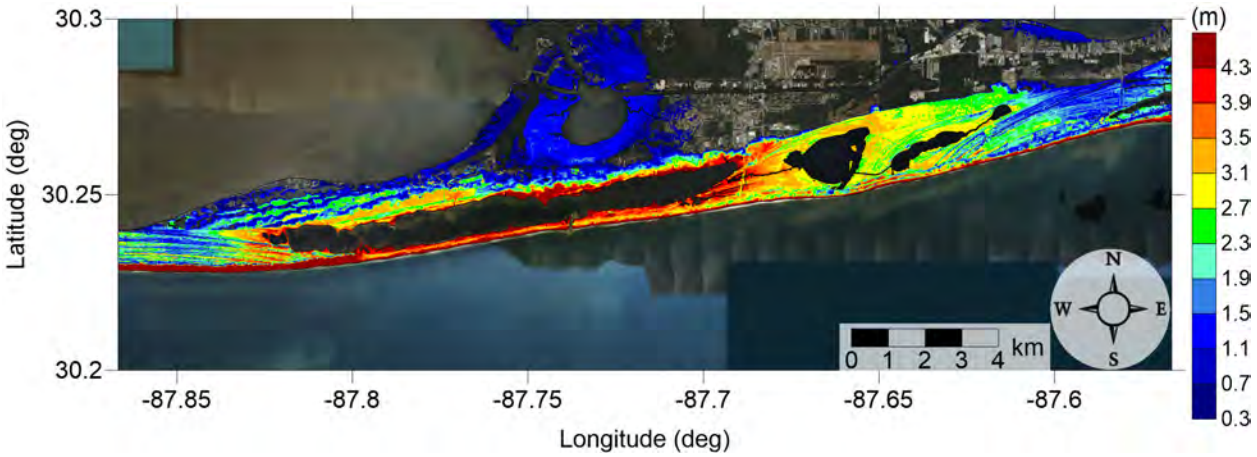

Figure 20: Maximum inundation depth (m) caused by the Mississippi Canyon submarine landslide in Gulf Shores, AL. Contour drawn is the zero-meter contour for land elevation.

Orange Beach, AL
Mississippi Canyon submarine landslide
Maximum Inundation Depth

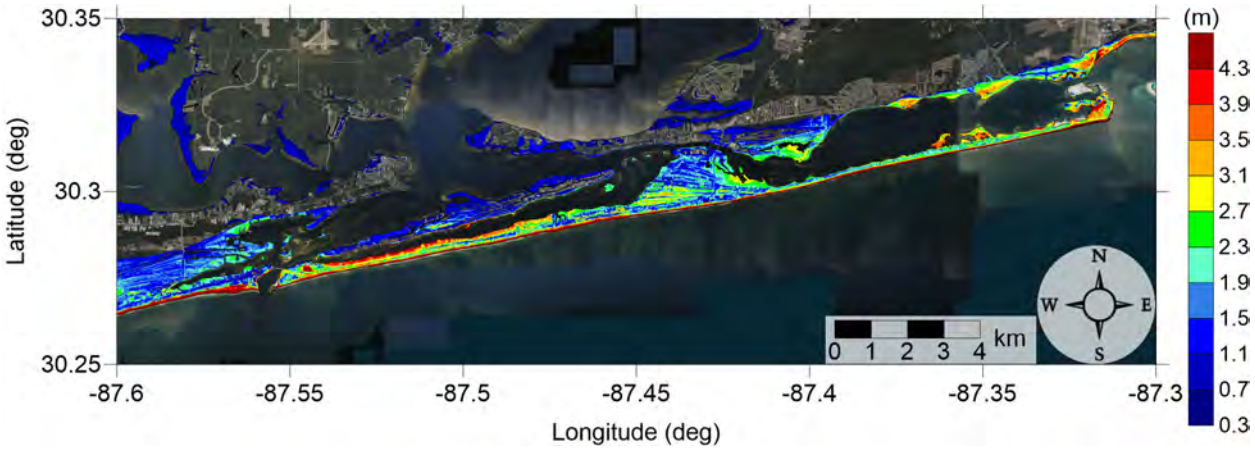

Figure 21: Maximum inundation depth (m) caused by the Mississippi Canyon submarine landslide in Orange Beach, AL. Contour drawn is the zero-meter contour for land elevation.

Orange Beach, AL
Probabilistic Submarine Landslide C
Maximum Momentum Flux

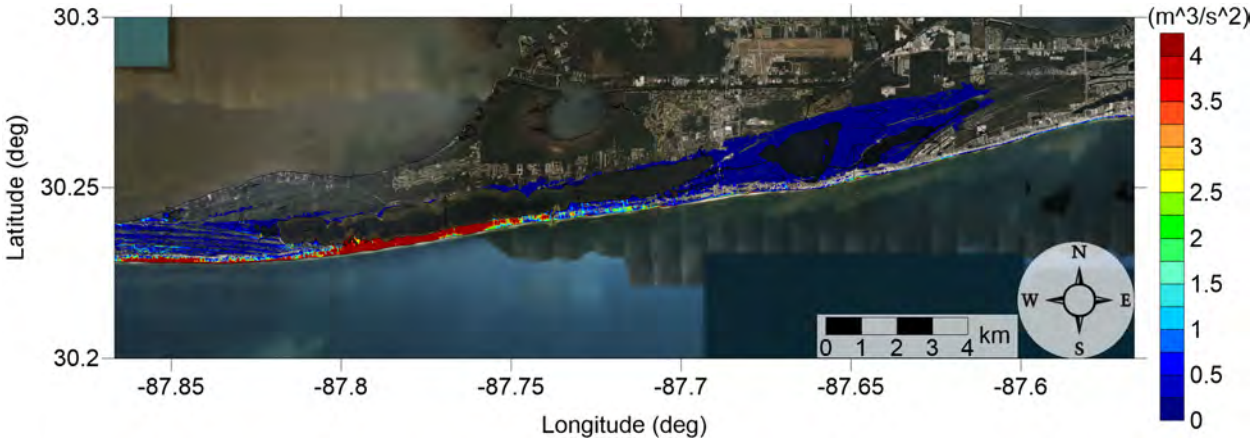

Figure 22: Maximum momentum flux (m^3/s^2) caused by the Probabilistic Submarine Landslide C in Gulf Shores, AL. Arrows represent direction of maximum momentum flux. Contour drawn is the zero-meter contour for land elevation.

Orange Beach, AL
Probabilistic Submarine Landslide C
Maximum Momentum Flux

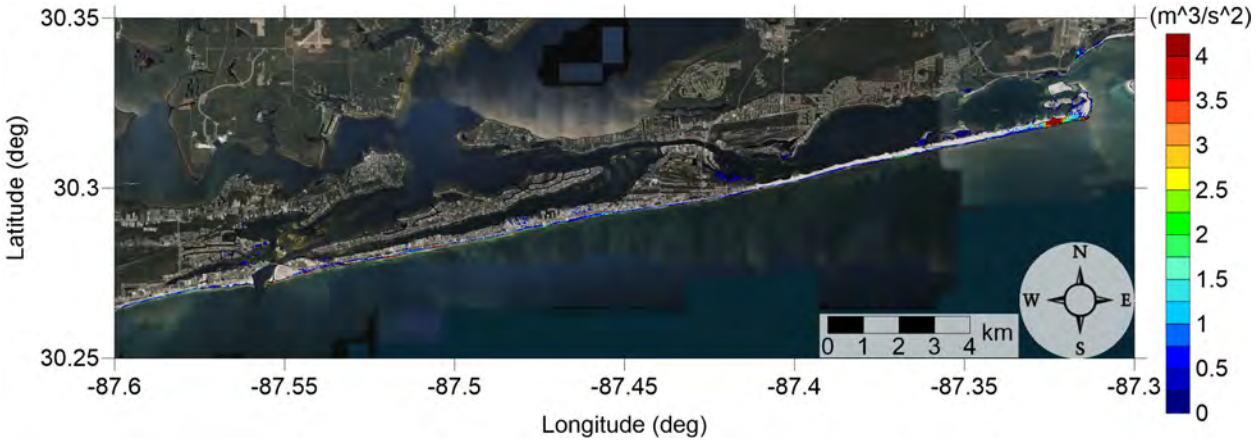

Figure 23: Maximum momentum flux (m^3/s^2) caused by the Probabilistic Submarine Landslide C in Orange Beach, AL. Arrows represent direction of maximum momentum flux. Contour drawn is the zero-meter contour for land elevation.

Orange Beach, AL
Probabilistic Submarine Landslide C
Maximum Inundation Depth

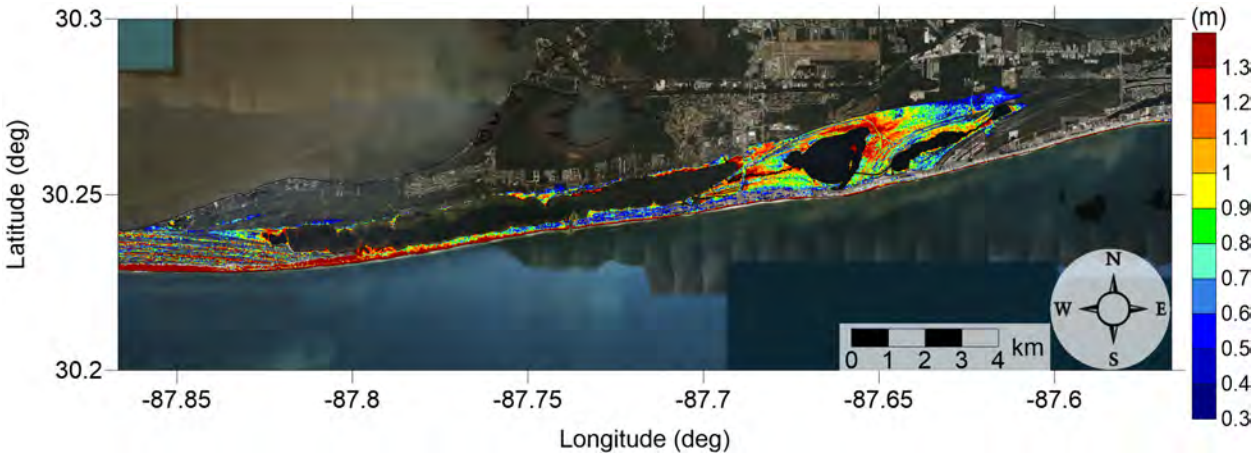

Figure 24: Maximum inundation depth (m) caused by the Probabilistic Submarine Landslide C in Gulf Shores, AL. Contour drawn is the zero-meter contour for land elevation.

Orange Beach, AL
Probabilistic Submarine Landslide C
Maximum Inundation Depth

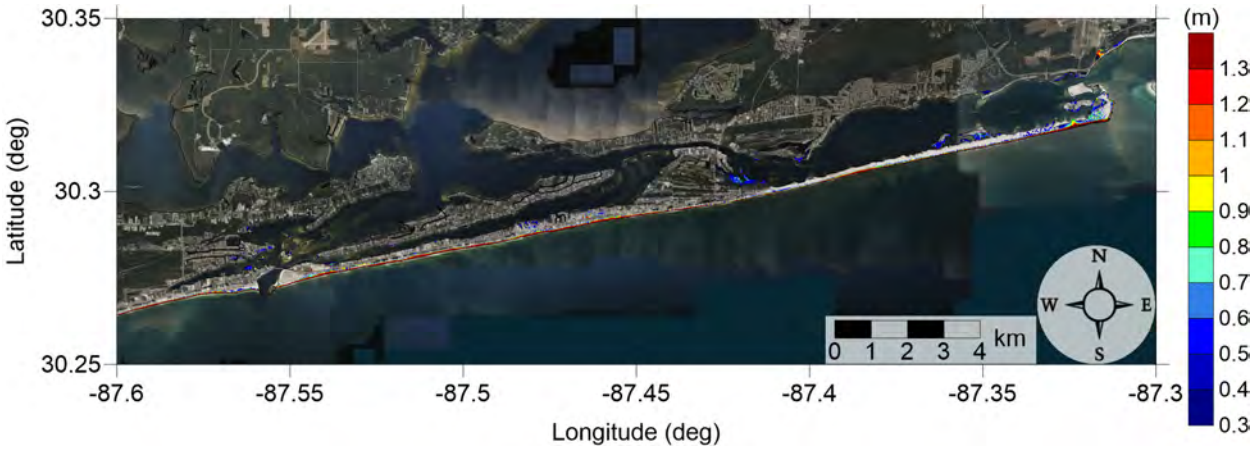

Figure 25: Maximum inundation depth (m) caused by the Probabilistic Submarine Landslide C in Orange Beach, AL. Contour drawn is the zero-meter contour for land elevation.

Orange Beach, AL
West Florida submarine landslide
Maximum Momentum Flux

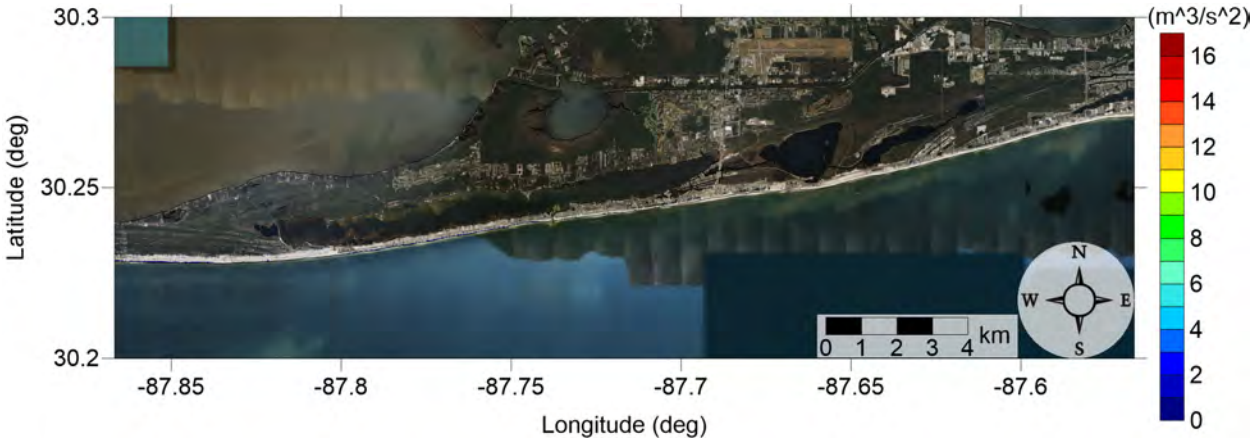

Figure 26: Maximum momentum flux (m^3/s^2) caused by the West Florida submarine landslide in Gulf Shores, AL. Arrows represent direction of maximum momentum flux. Contour drawn is the zero-meter contour for land elevation.

Orange Beach, AL
West Florida submarine landslide
Maximum Momentum Flux

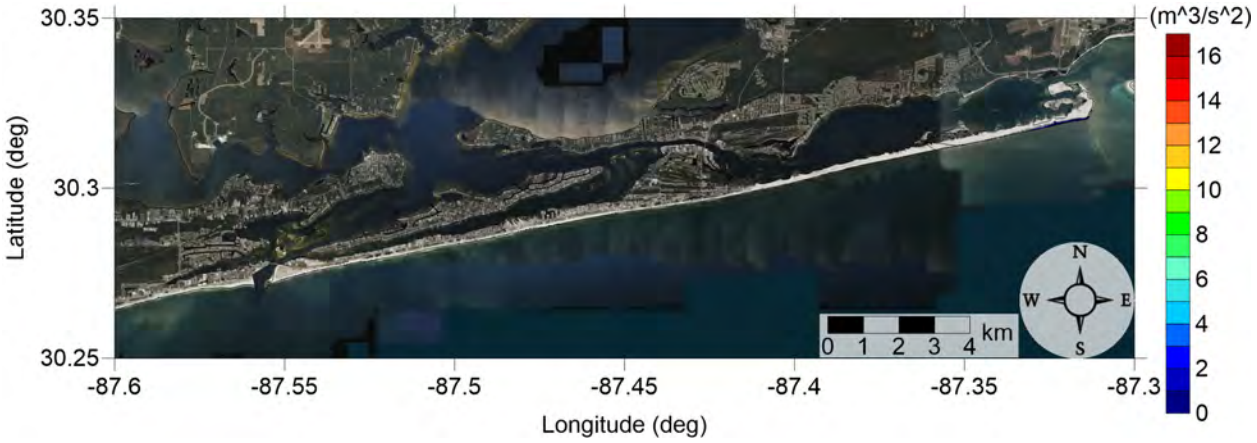

Figure 27: Maximum momentum flux (m^3/s^2) caused by the West Florida submarine landslide in Orange Beach, AL. Arrows represent direction of maximum momentum flux. Contour drawn is the zero-meter contour for land elevation.

Orange Beach, AL
West Florida submarine landslide
Maximum Inundation Depth

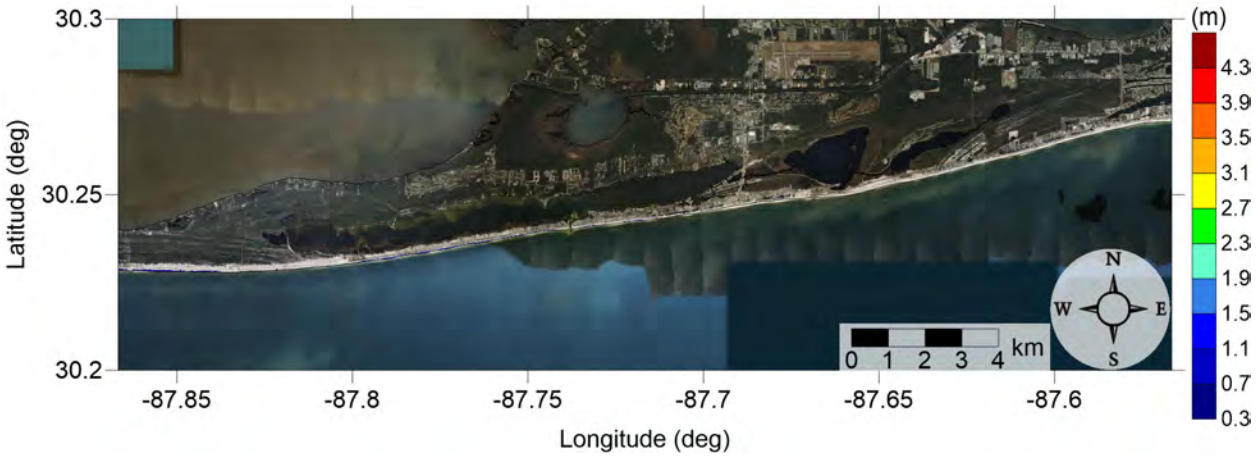

Figure 28: Maximum inundation depth (m) caused by the West Florida submarine landslide in Gulf Shores, AL. Contour drawn is the zero-meter contour for land elevation.

Orange Beach, AL
West Florida submarine landslide
Maximum Inundation Depth

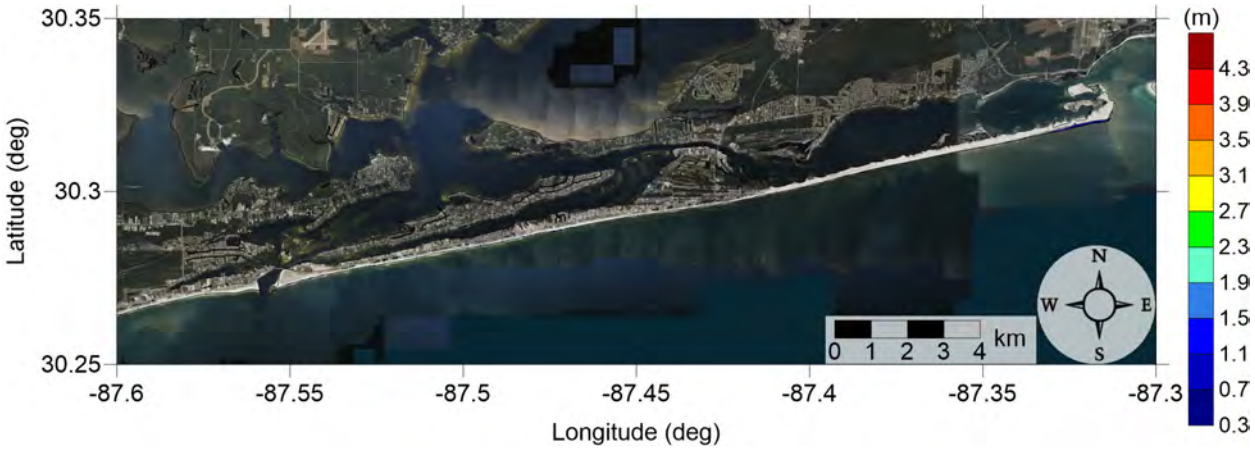

Figure 29: Maximum inundation depth (m) caused by the West Florida submarine landslide in Orange Beach, AL. Contour drawn is the zero-meter contour for land elevation.

Orange Beach, AL
Yucatán 3 submarine landslide
Maximum Momentum Flux

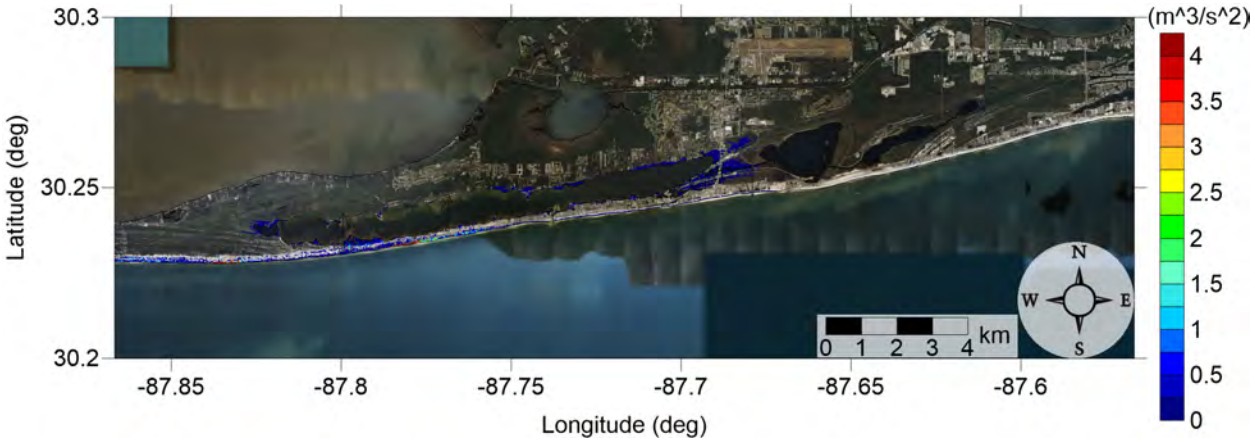

Figure 30: Maximum momentum flux (m^3/s^2) caused by the Yucatán 3 submarine landslide in Gulf Shores, AL. Arrows represent direction of maximum momentum flux. Contour drawn is the zero-meter contour for land elevation.

Orange Beach, AL
Yucatán 3 submarine landslide
Maximum Momentum Flux

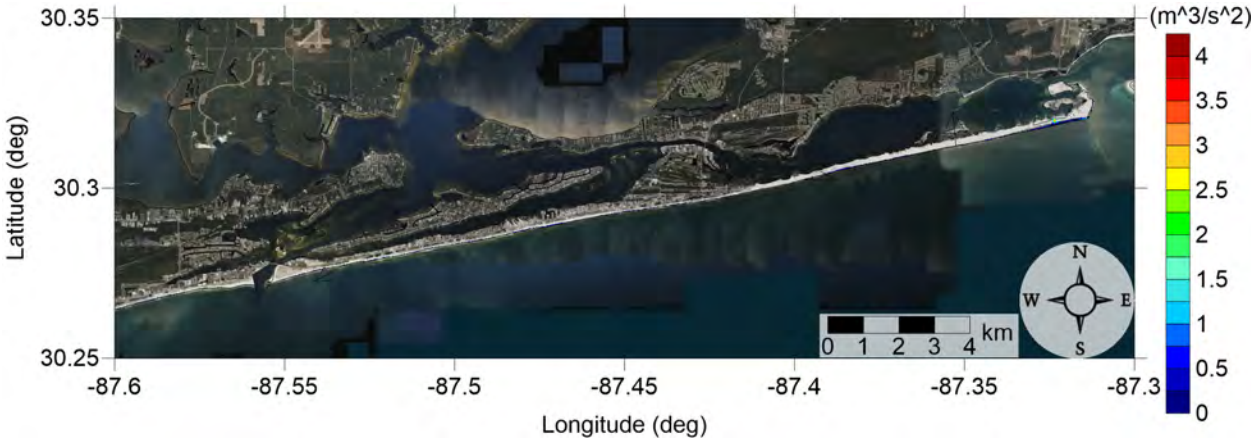

Figure 31: Maximum momentum flux (m^3/s^2) caused by the Yucatán 3 submarine landslide in Orange Beach, AL. Arrows represent direction of maximum momentum flux. Contour drawn is the zero-meter contour for land elevation.

Orange Beach, AL
Yucatán 3 submarine landslide
Maximum Inundation Depth

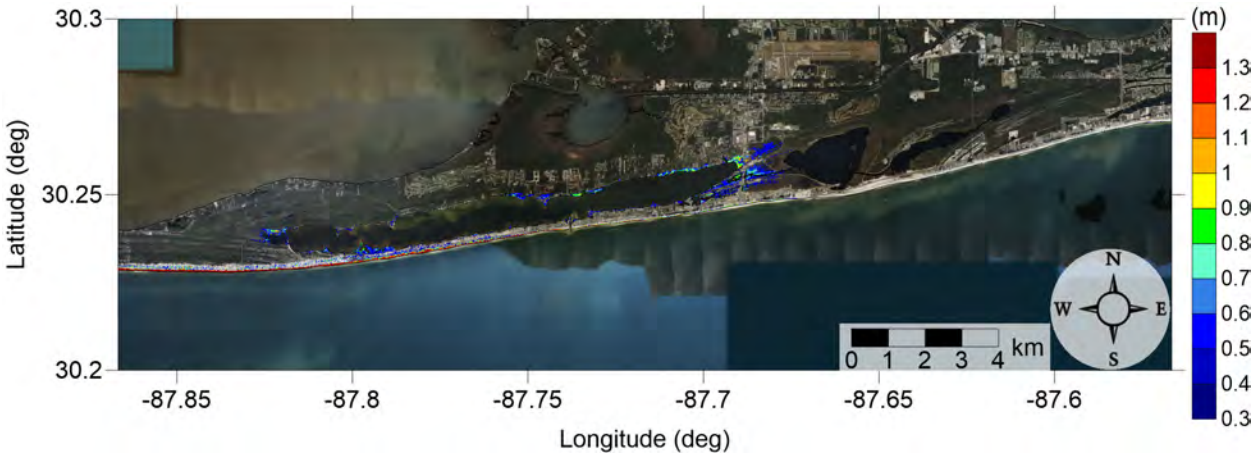

Figure 32: Maximum inundation depth (m) caused by the Yucatán 3 submarine landslide in Gulf Shores, AL. Contour drawn is the zero-meter contour for land elevation.

Orange Beach, AL
Yucatán 3 submarine landslide
Maximum Inundation Depth

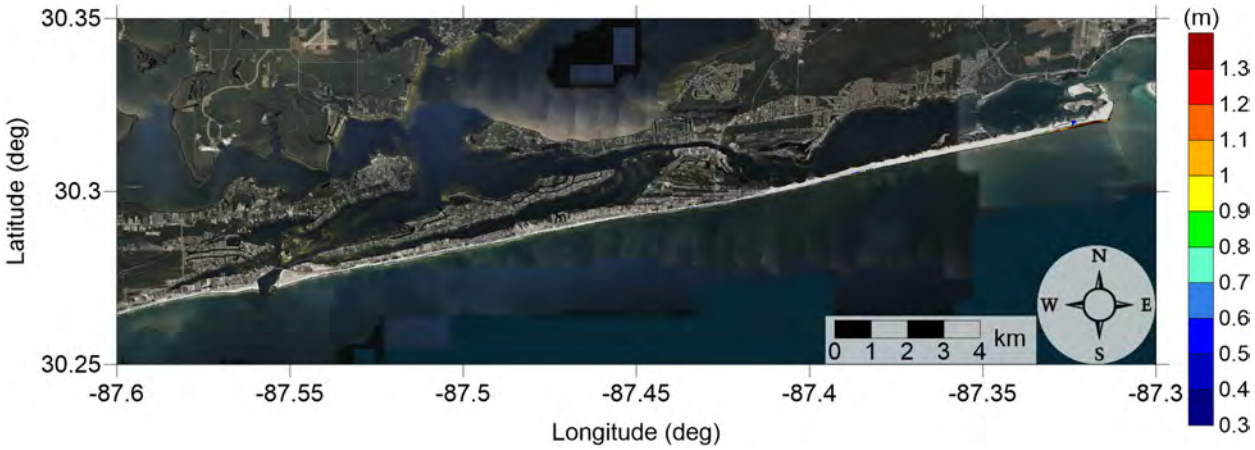

Figure 33: Maximum inundation depth (m) caused by the Yucatán 3 submarine landslide in Orange Beach, AL. Contour drawn is the zero-meter contour for land elevation.

Orange Beach, AL
Yucatán 5 submarine landslide
Maximum Momentum Flux

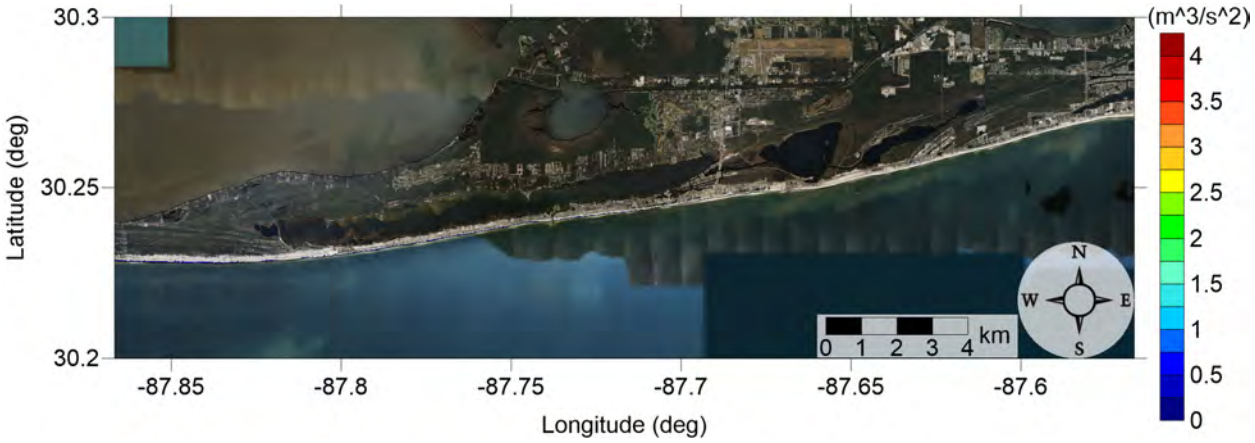

Figure 34: Maximum momentum flux (m^3/s^2) caused by the Yucatán 5 submarine landslide in Gulf Shores, AL. Arrows represent direction of maximum momentum flux. Contour drawn is the zero-meter contour for land elevation.

Orange Beach, AL
Yucatán 5 submarine landslide
Maximum Momentum Flux

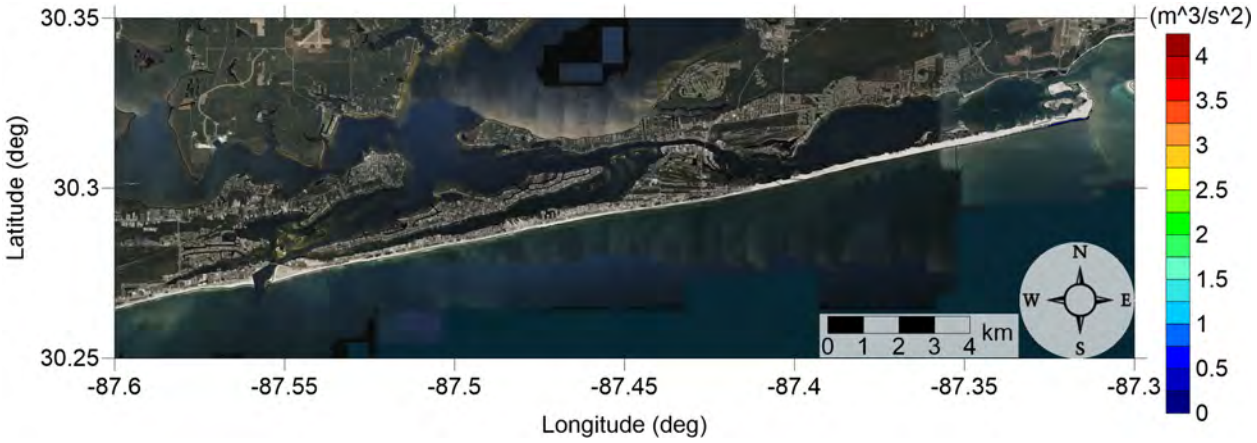

Figure 35: Maximum momentum flux (m^3/s^2) caused by the Yucatán 5 submarine landslide in Orange Beach, AL. Arrows represent direction of maximum momentum flux. Contour drawn is the zero-meter contour for land elevation.

Orange Beach, AL
Yucatán 5 submarine landslide
Maximum Inundation Depth

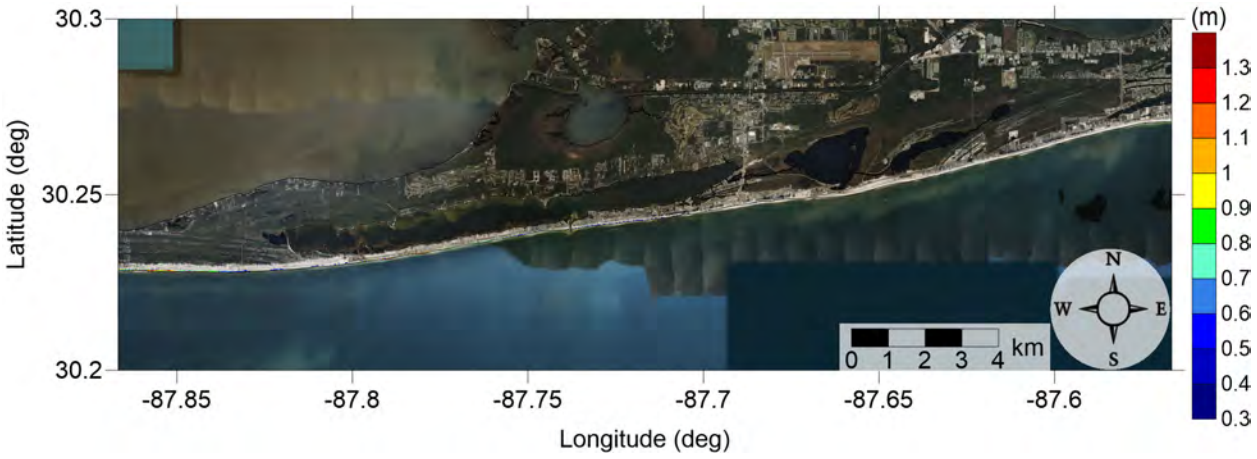

Figure 36: Maximum inundation depth (m) caused by the Yucatán 5 submarine landslide in Gulf Shores, AL. Contour drawn is the zero-meter contour for land elevation.

Orange Beach, AL
Yucatán 5 submarine landslide
Maximum Inundation Depth

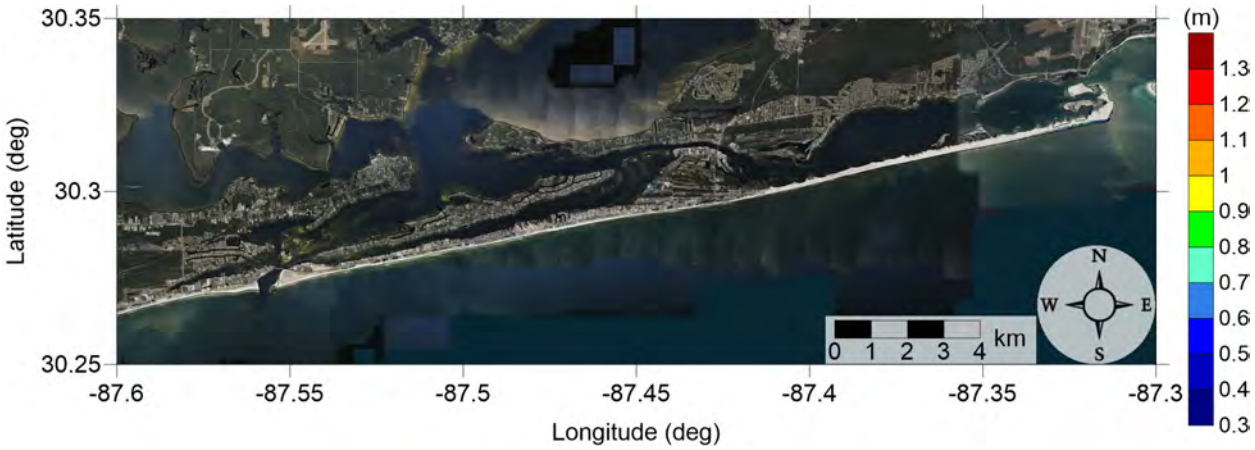

Figure 37: Maximum inundation depth (m) caused by the Yucatán 5 submarine landslide in Orange Beach, AL. Contour drawn is the zero-meter contour for land elevation.

Orange Beach, AL
All Sources
Maximum of Maximum Inundation Depth

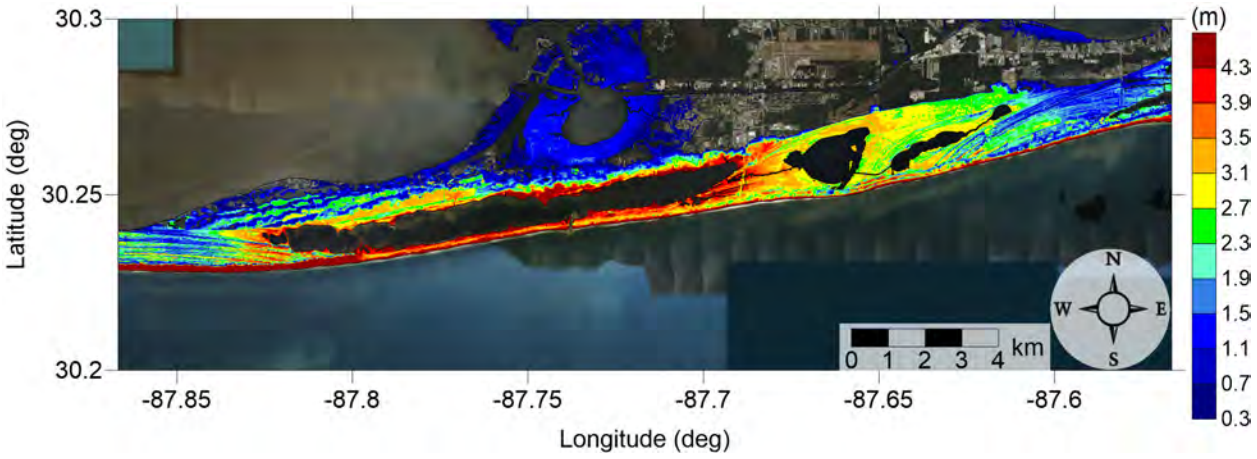

Figure 38: Maximum of maximums inundation depth (m) in Gulf Shores, AL, calculated as the maximum inundation depth in each grid cell from an ensemble of all tsunami sources considered. Contour drawn is the zero-meter contour for land elevation.

Orange Beach, AL
All Sources
Maximum of Maximum Inundation Depth

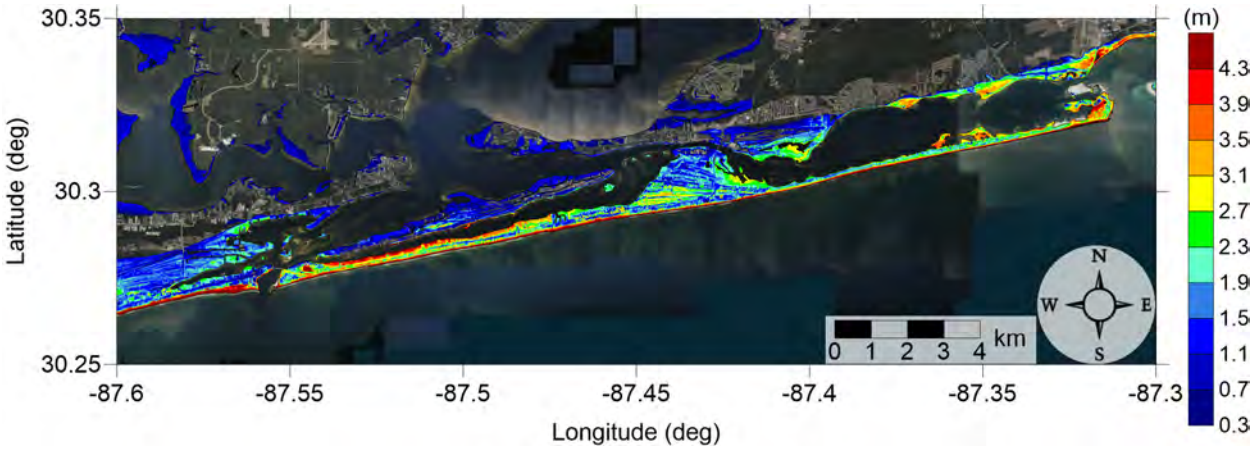

Figure 39: Maximum of maximums inundation depth (m) in Orange Beach, AL, calculated as the maximum inundation depth in each grid cell from an ensemble of all tsunami sources considered. Contour drawn is the zero-meter contour for land elevation.

Orange Beach, AL
All Sources
Maximum Inundation Depth by Source

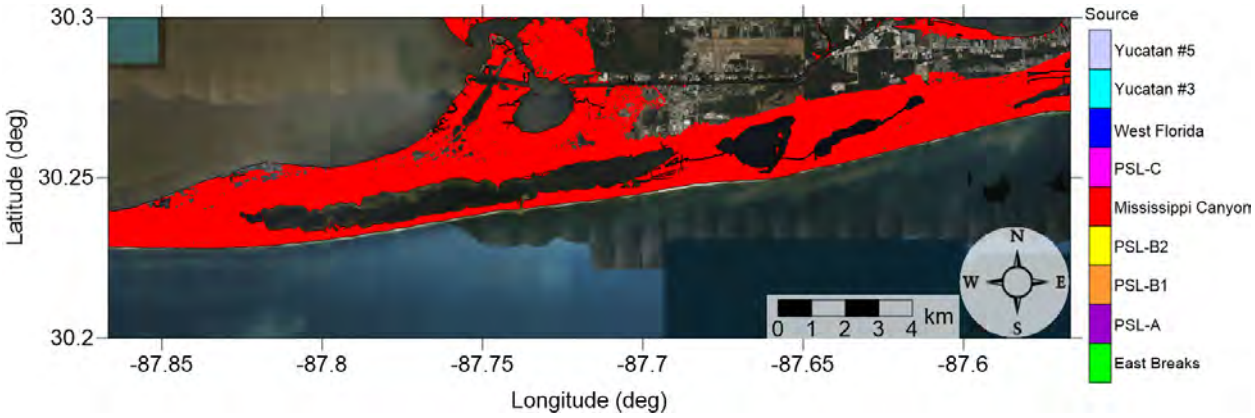

Figure 40: Indication of the tsunami source which causes the maximum of maximums inundation depth (m) in each grid cell from an ensemble of all tsunami sources in Gulf Shores, AL. Contour drawn is the zero-meter contour for land elevation.

Orange Beach, AL
All Sources
Maximum Inundation Depth by Source

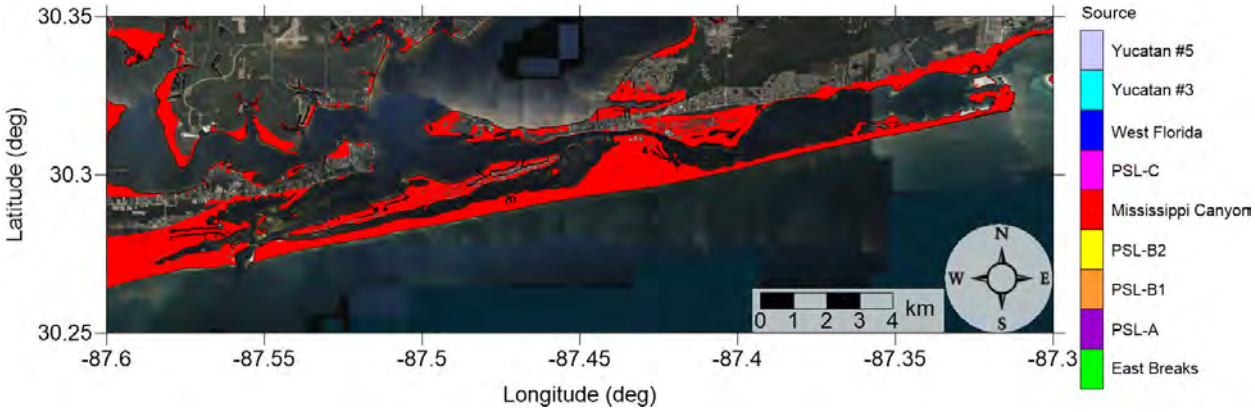

Figure 41: Indication of the tsunami source which causes the maximum of maximums inundation depth (m) in each grid cell from an ensemble of all tsunami sources in Orange Beach, AL. Contour drawn is the zero-meter contour for land elevation.

4.2 Mexico Beach, FL

Table 3: Maximum tsunami wave amplitude and corresponding arrival time after landslide failure at Mexico Beach, FL numerical wave gauge: 30°4'45.0012"N, 85°46'14.9982"W, approximate water depth 20 m.

Tsunami Source	Maximum Wave Amplitude (m)	Arrival Time After Landslide Failure (hr)
East Breaks	0.44	3.2
PSL-A	0.60	2.8
PSL-B1	0.61	2.0
PSL-B2	0.59	2.2
Mississippi Canyon	4.79	1.5
PSL-C	2.40	1.4
West Florida	1.08	2.1
Yucatán #3	1.42	2.4
Yucatán #5	0.91	2.5

Mexico Beach, FL
East Breaks submarine landslide
Maximum Momentum Flux

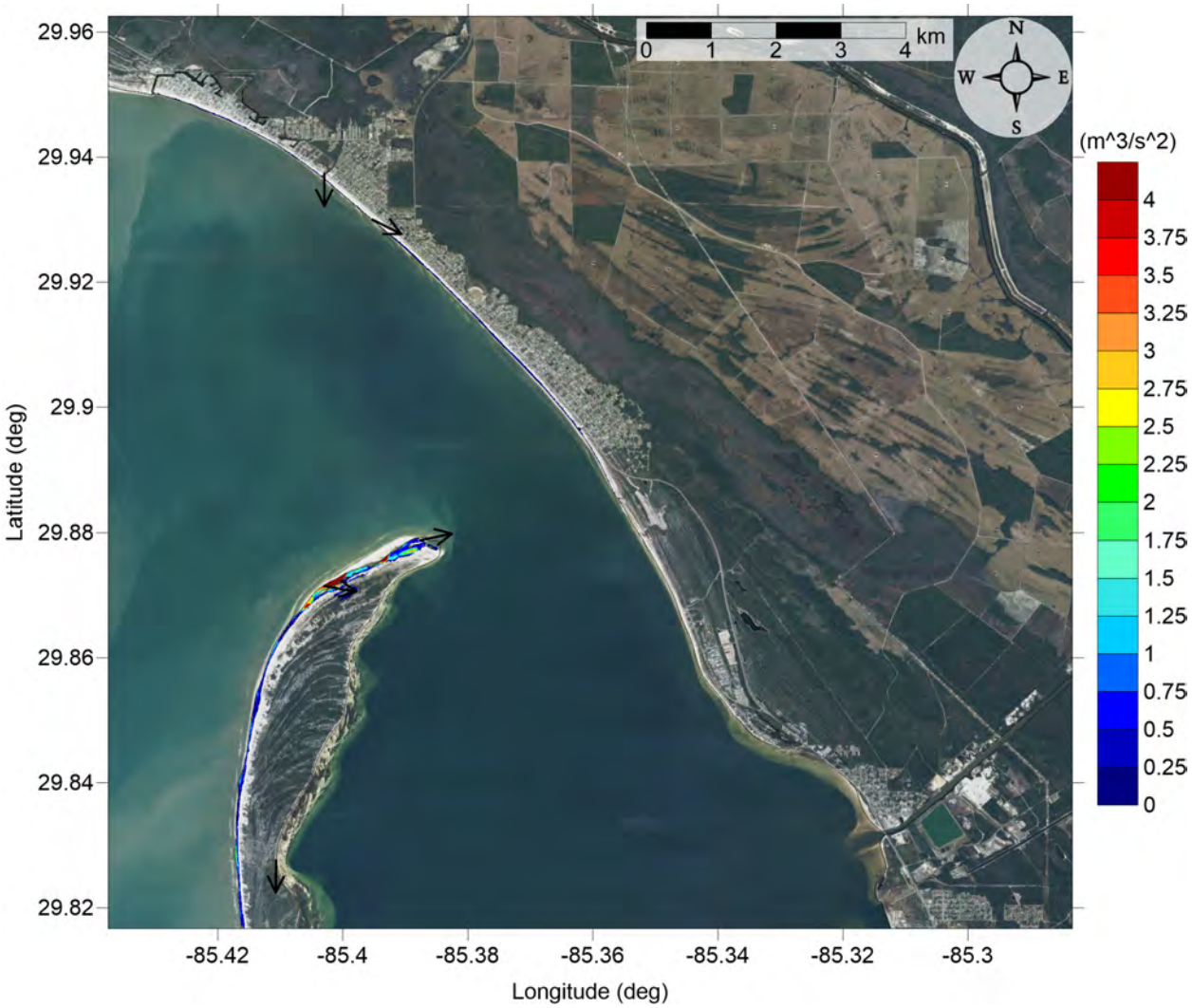

Figure 42: Maximum momentum flux (m^3/s^2) caused by the East Breaks submarine landslide in Mexico Beach, FL. Arrows represent direction of maximum momentum flux. Contour drawn is the zero-meter contour for land elevation.

Mexico Beach, FL
East Breaks submarine landslide
Maximum Momentum Flux

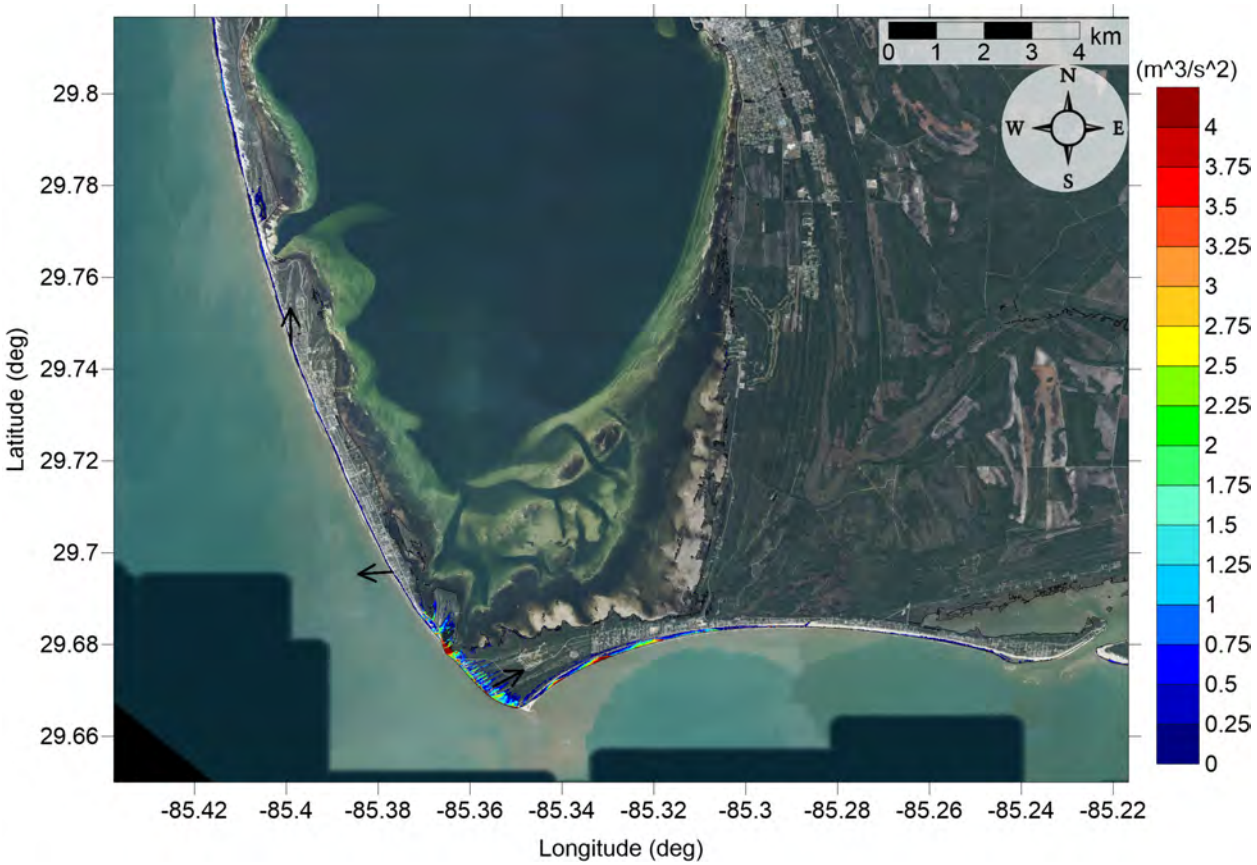

Figure 43: Maximum momentum flux (m^3/s^2) caused by the East Breaks submarine landslide in Port St. Joe, FL. Arrows represent direction of maximum momentum flux. Contour drawn is the zero-meter contour for land elevation.

Mexico Beach, FL
East Breaks submarine landslide
Maximum Inundation Depth

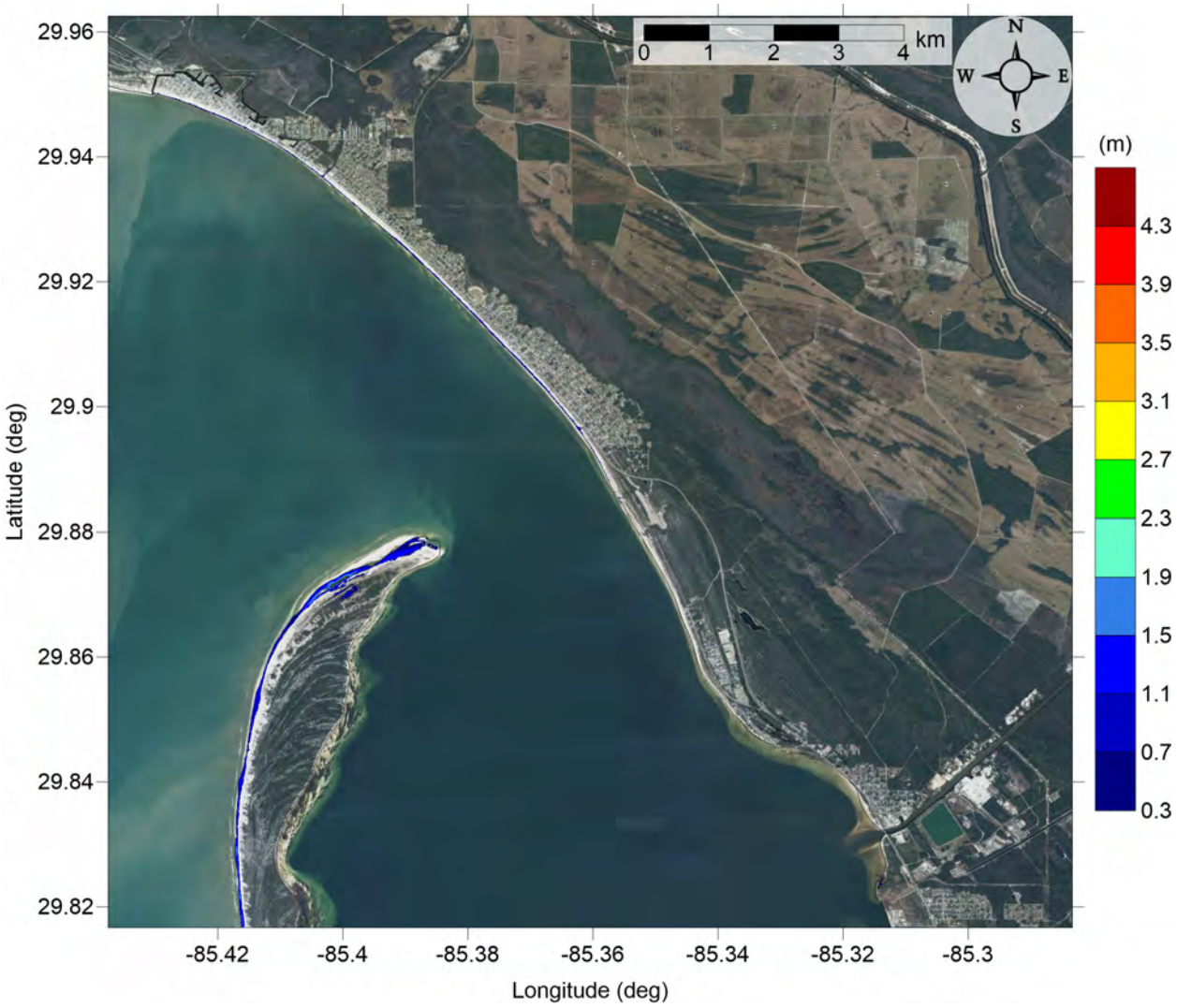

Figure 44: Maximum inundation depth (m) caused by the East Breaks submarine landslide in Mexico Beach, FL. Contour drawn is the zero-meter contour for land elevation.

Mexico Beach, FL
East Breaks submarine landslide
Maximum Inundation Depth

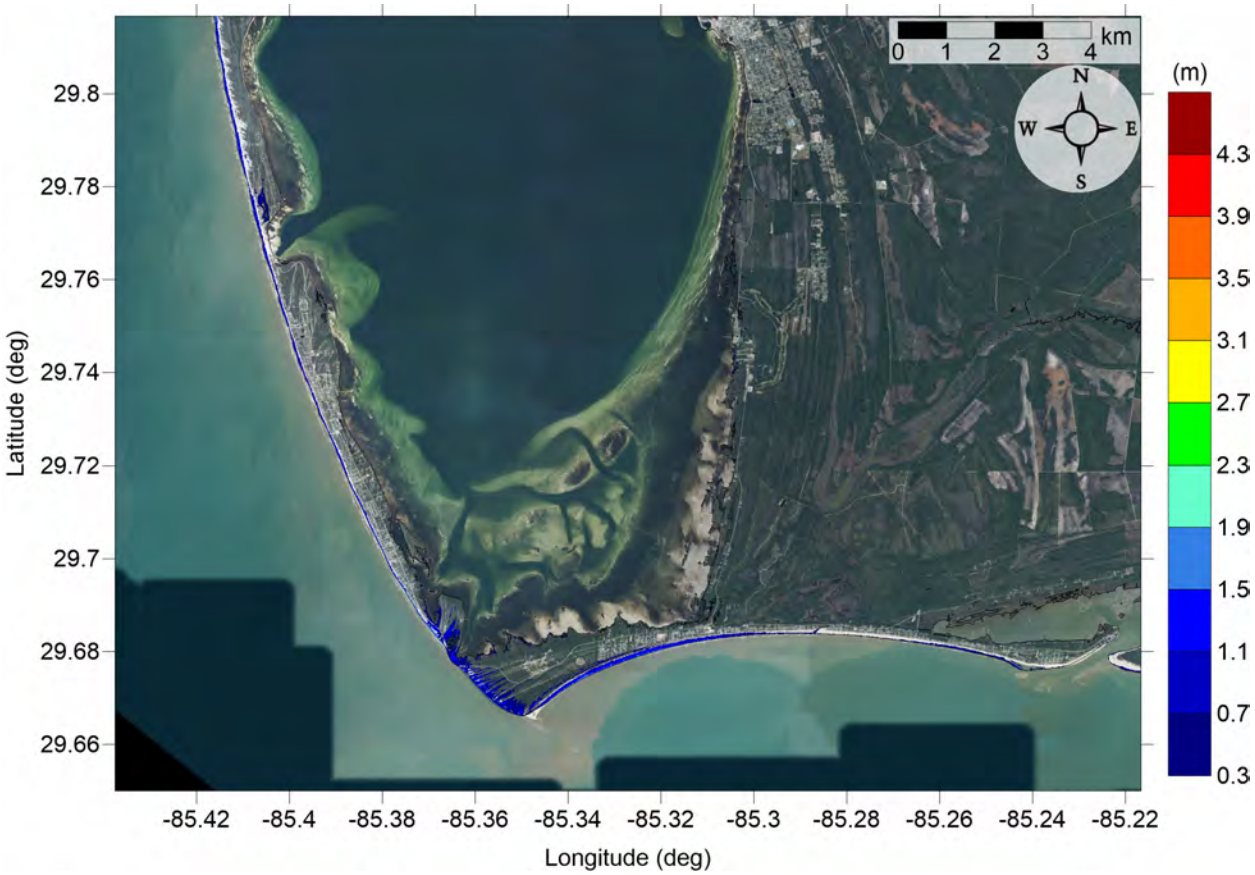

Figure 45: Maximum inundation depth (m) caused by the East Breaks submarine landslide in Port St. Joe, FL. Contour drawn is the zero-meter contour for land elevation.

Mexico Beach, FL
Probabilistic Submarine Landslide A
Maximum Momentum Flux

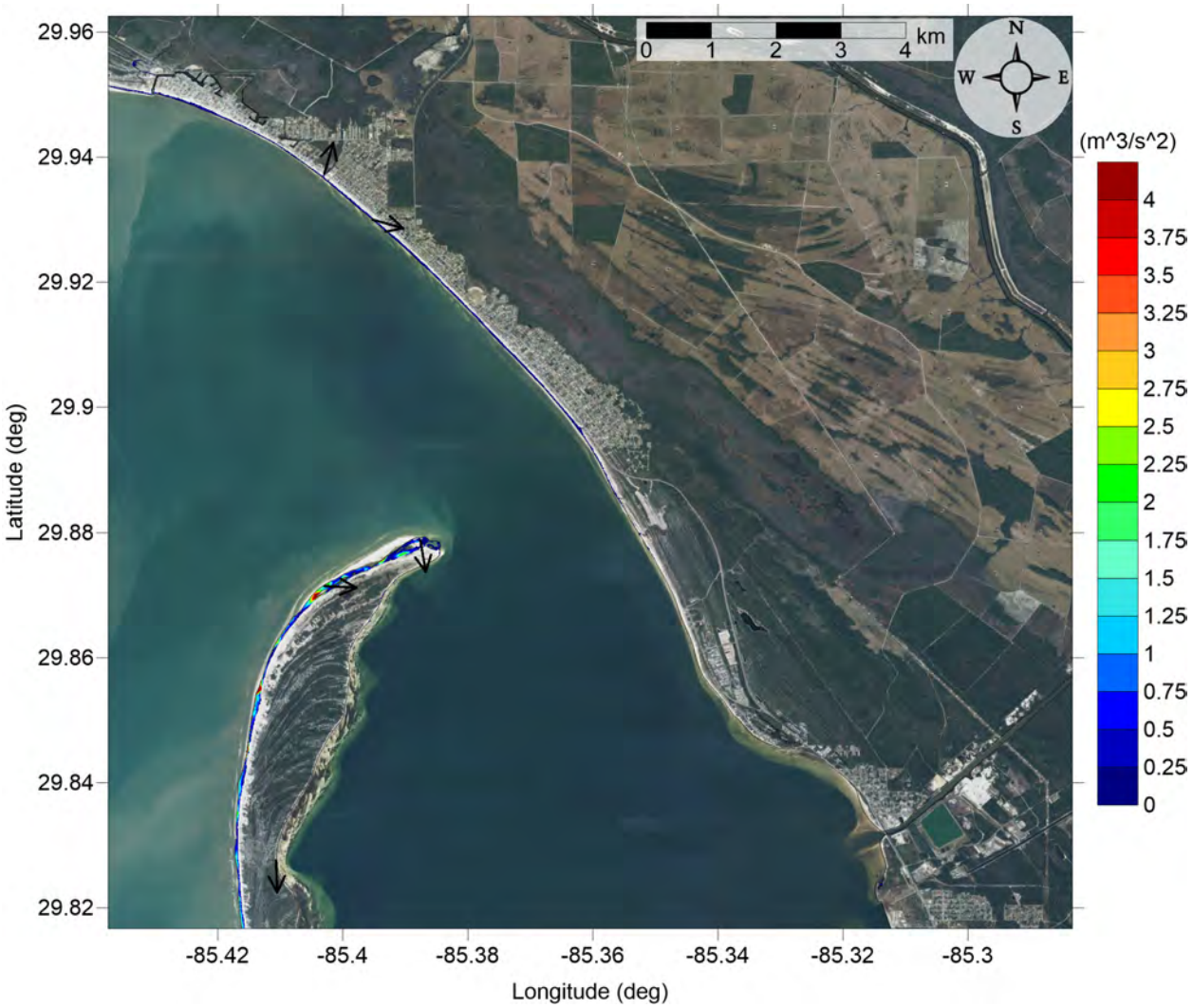

Figure 46: Maximum momentum flux (m^3/s^2) caused by the Probabilistic Submarine Landslide A in Mexico Beach, FL. Arrows represent direction of maximum momentum flux. Contour drawn is the zero-meter contour for land elevation.

Mexico Beach, FL
Probabilistic Submarine Landslide A
Maximum Momentum Flux

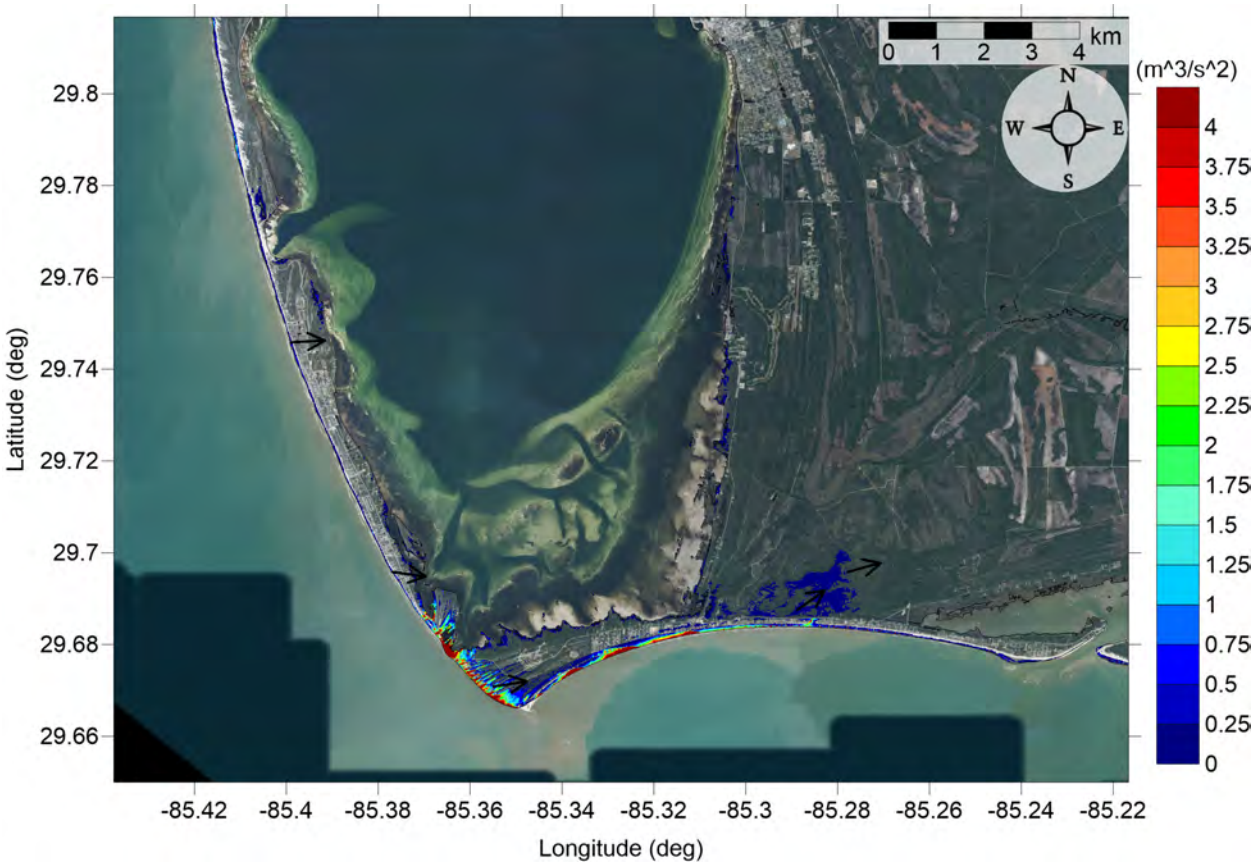

Figure 47: Maximum momentum flux (m^3/s^2) caused by the Probabilistic Submarine Landslide A in Port St. Joe, FL. Arrows represent direction of maximum momentum flux. Contour drawn is the zero-meter contour for land elevation.

Mexico Beach, FL
Probabilistic Submarine Landslide A
Maximum Inundation Depth

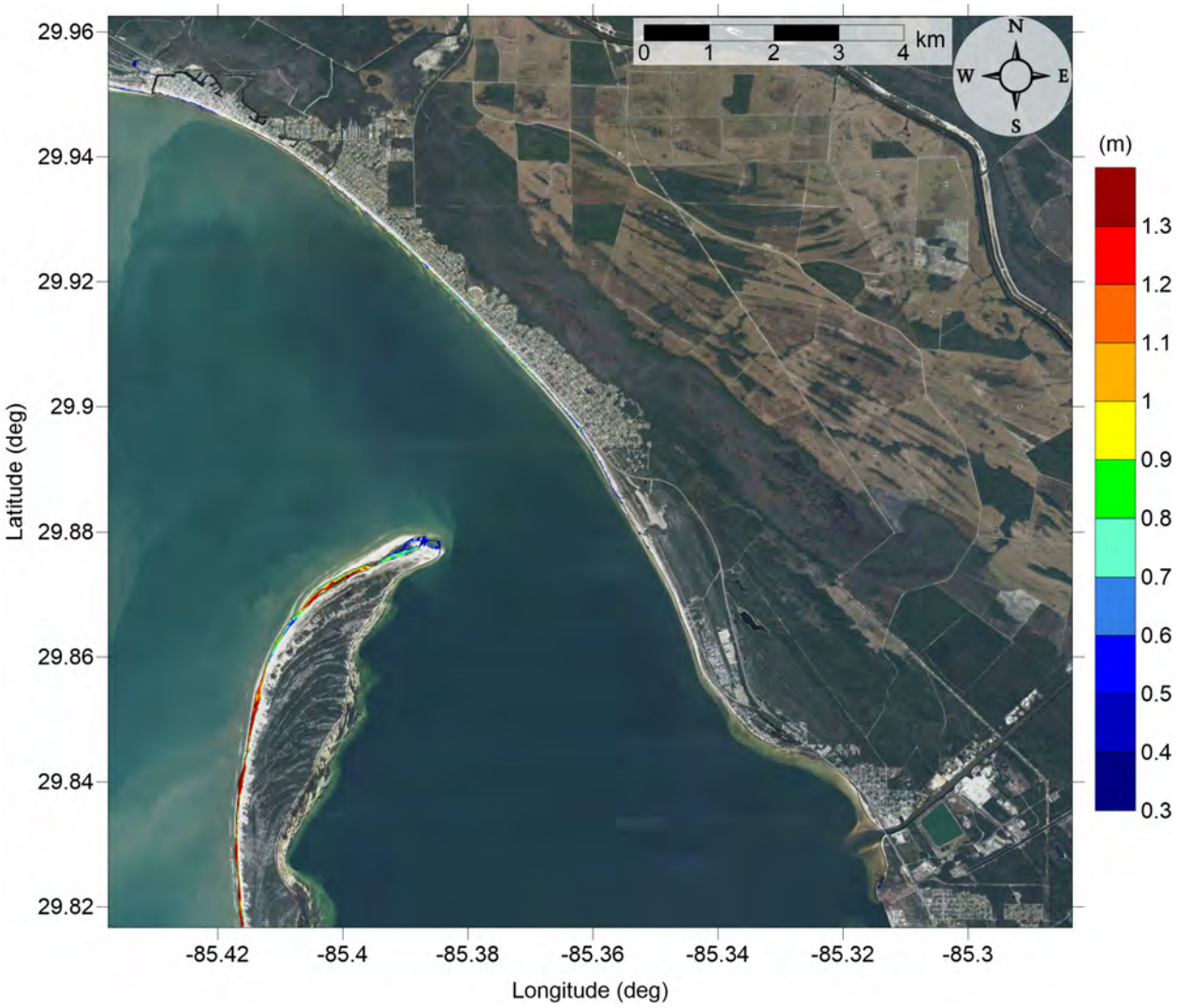

Figure 48: Maximum inundation depth (m) caused by the Probabilistic Submarine Landslide A in Mexico Beach, FL. Contour drawn is the zero-meter contour for land elevation.

Mexico Beach, FL
Probabilistic Submarine Landslide A
Maximum Inundation Depth

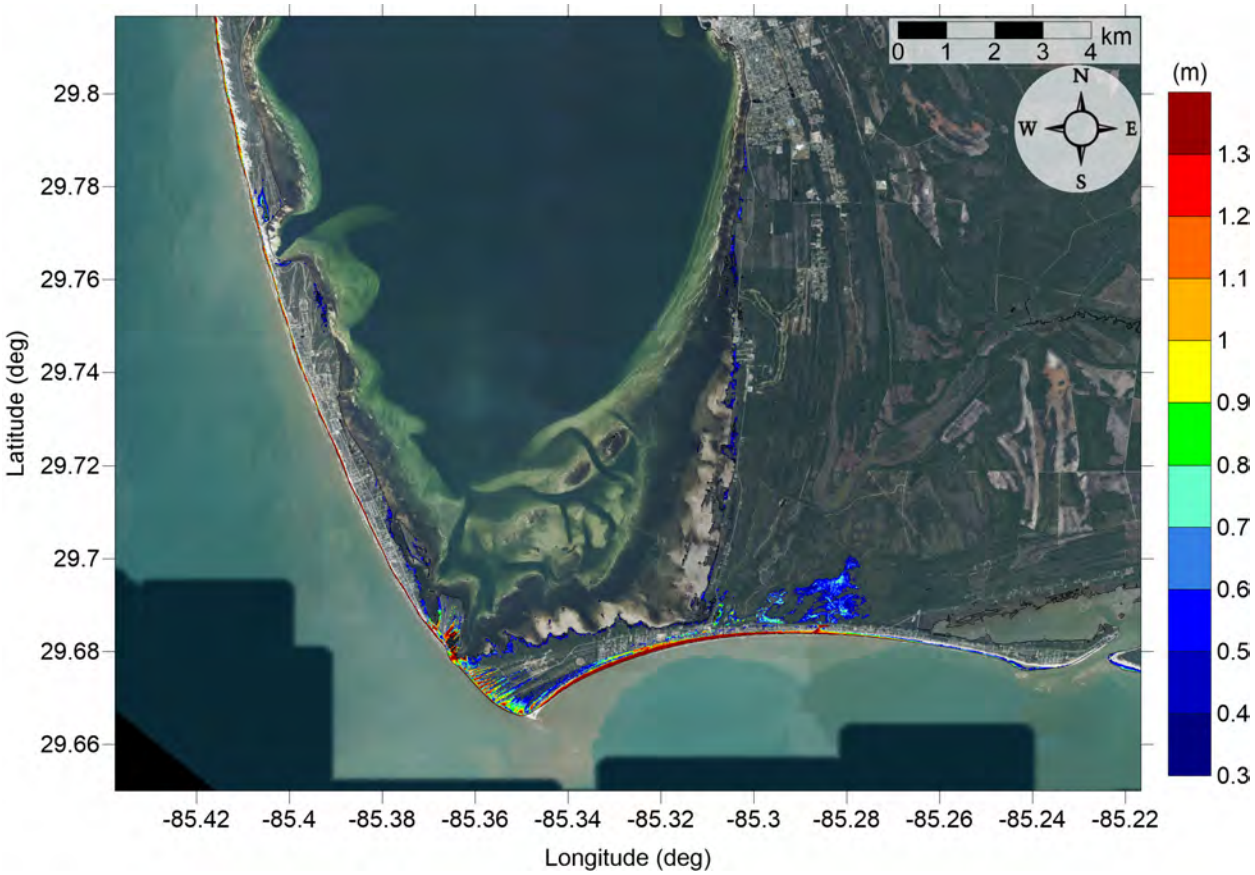

Figure 49: Maximum inundation depth (m) caused by the Probabilistic Submarine Landslide A in Port St. Joe, FL. Contour drawn is the zero-meter contour for land elevation.

Mexico Beach, FL
Probabilistic Submarine Landslide B1
Maximum Momentum Flux

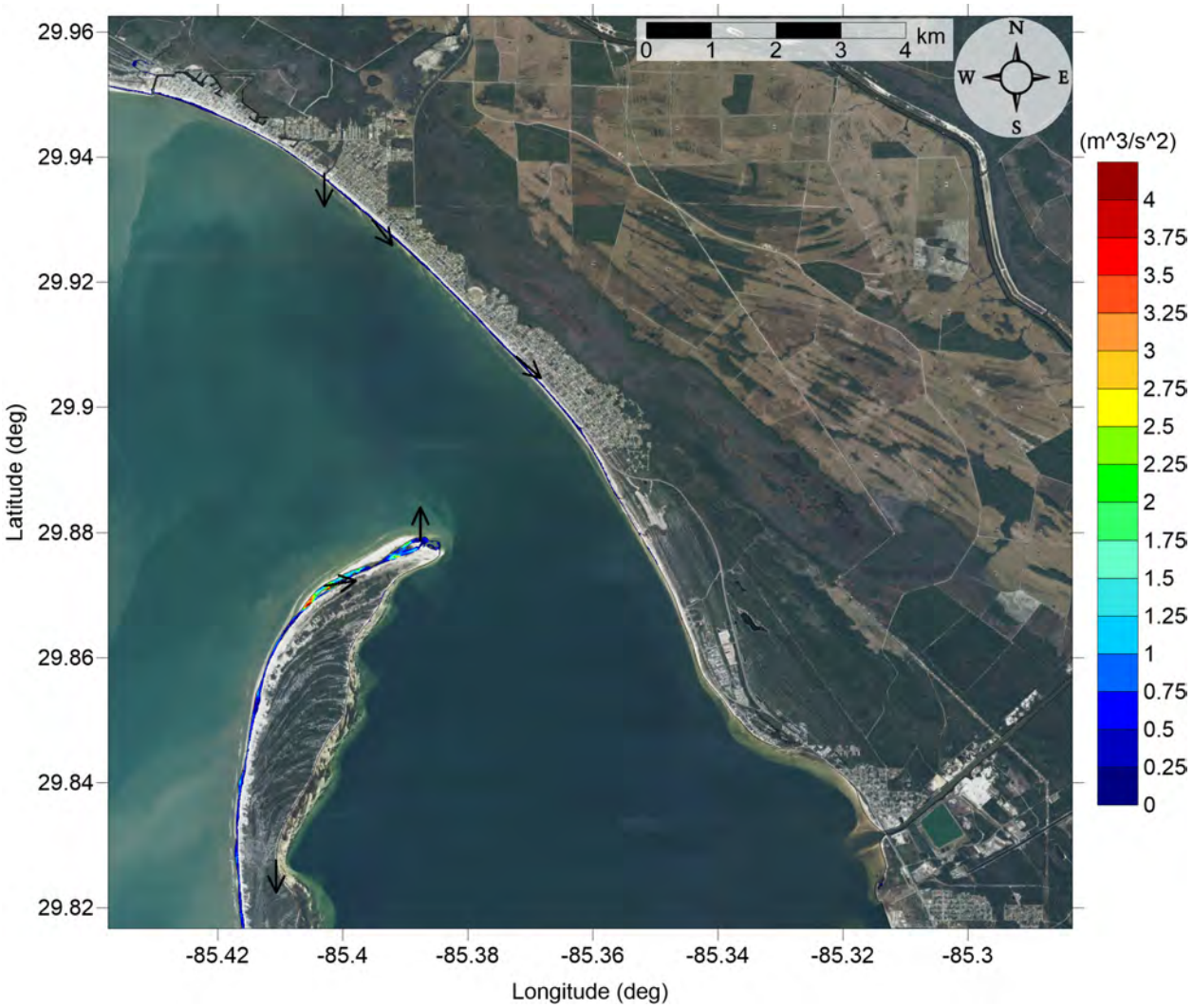

Figure 50: Maximum momentum flux (m^3/s^2) caused by the Probabilistic Submarine Landslide B1 in Mexico Beach, FL. Arrows represent direction of maximum momentum flux. Contour drawn is the zero-meter contour for land elevation.

Mexico Beach, FL
Probabilistic Submarine Landslide B1
Maximum Momentum Flux

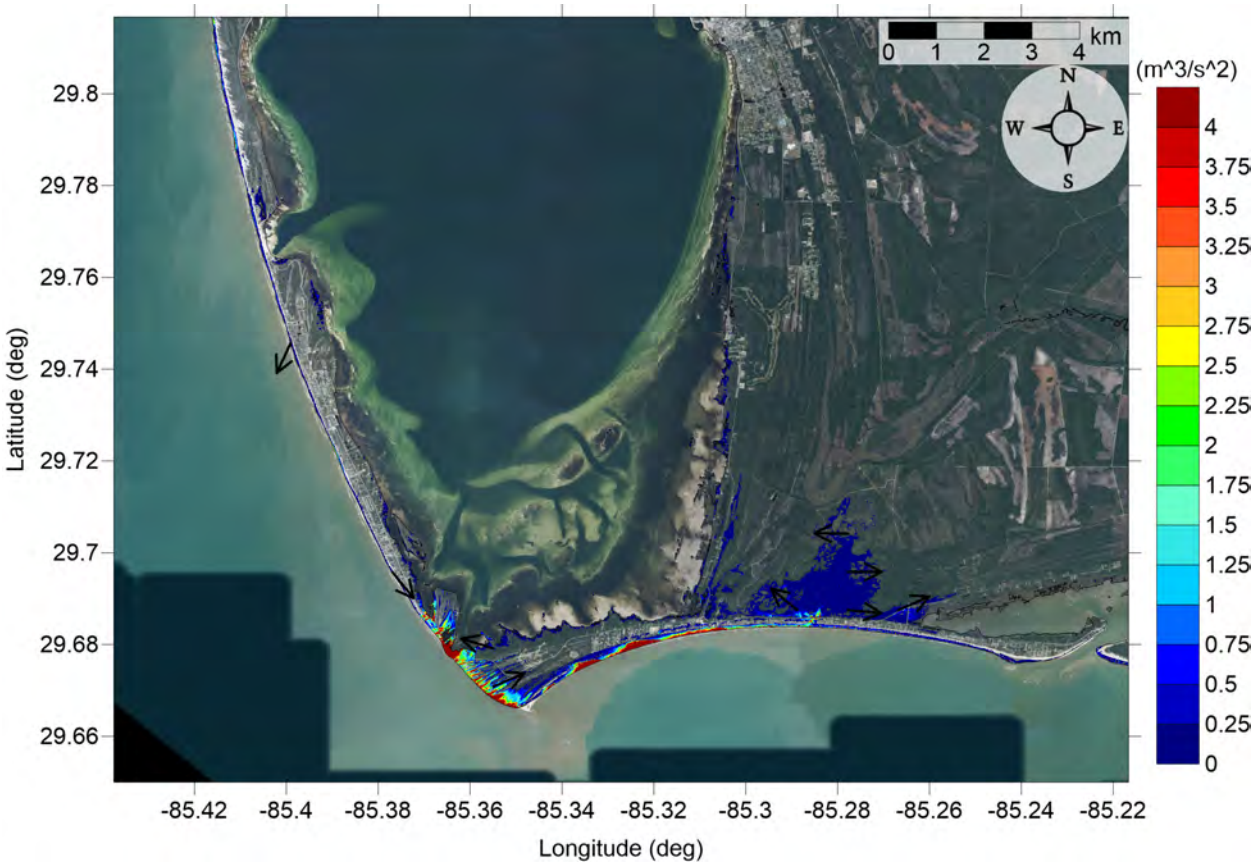

Figure 51: Maximum momentum flux (m^3/s^2) caused by the Probabilistic Submarine Landslide B1 in Port St. Joe, FL. Arrows represent direction of maximum momentum flux. Contour drawn is the zero-meter contour for land elevation.

Mexico Beach, FL
Probabilistic Submarine Landslide B1
Maximum Inundation Depth

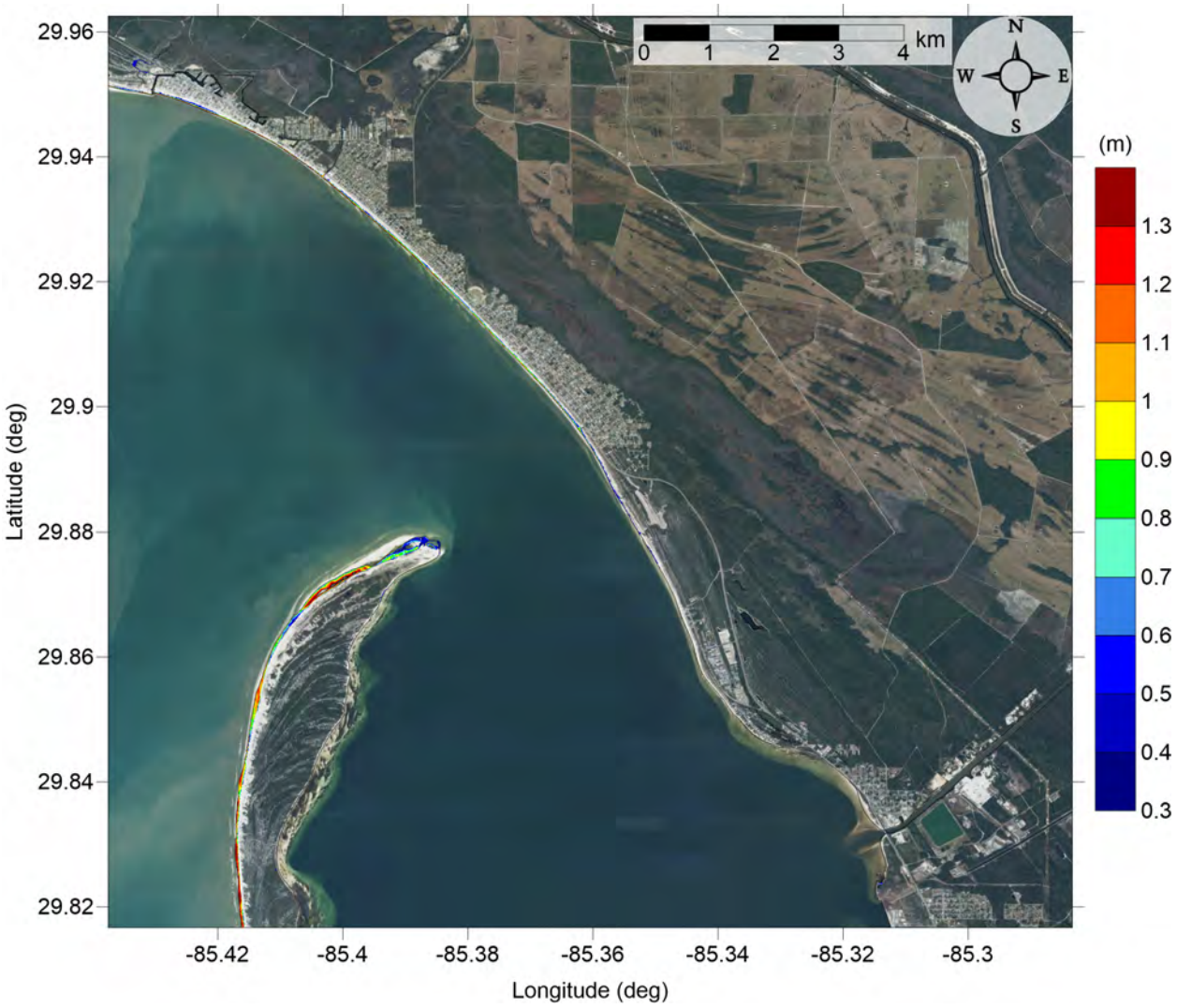

Figure 52: Maximum inundation depth (m) caused by the Probabilistic Submarine Landslide B1 in Mexico Beach, FL. Contour drawn is the zero-meter contour for land elevation.

Mexico Beach, FL
Probabilistic Submarine Landslide B1
Maximum Inundation Depth

Figure 53: Maximum inundation depth (m) caused by the Probabilistic Submarine Landslide B1 in Port St. Joe, FL. Contour drawn is the zero-meter contour for land elevation.

Mexico Beach, FL
Probabilistic Submarine Landslide B2
Maximum Momentum Flux

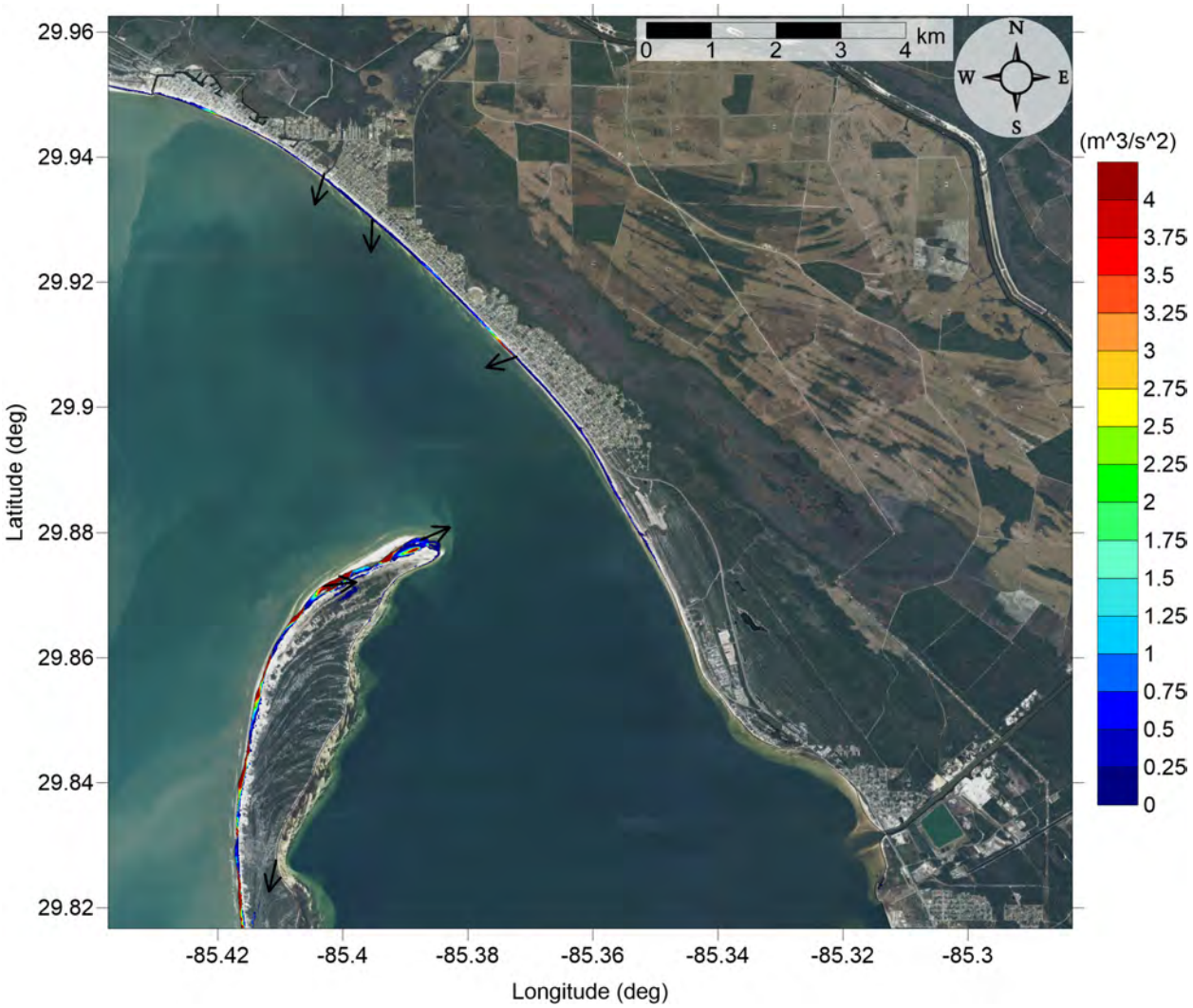

Figure 54: Maximum momentum flux (m^3/s^2) caused by the Probabilistic Submarine Landslide B2 in Mexico Beach, FL. Arrows represent direction of maximum momentum flux. Contour drawn is the zero-meter contour for land elevation.

Mexico Beach, FL
Probabilistic Submarine Landslide B2
Maximum Momentum Flux

Figure 55: Maximum momentum flux (m^3/s^2) caused by the Probabilistic Submarine Landslide B2 in Port St. Joe, FL. Arrows represent direction of maximum momentum flux. Contour drawn is the zero-meter contour for land elevation.

Mexico Beach, FL
Probabilistic Submarine Landslide B2
Maximum Inundation Depth

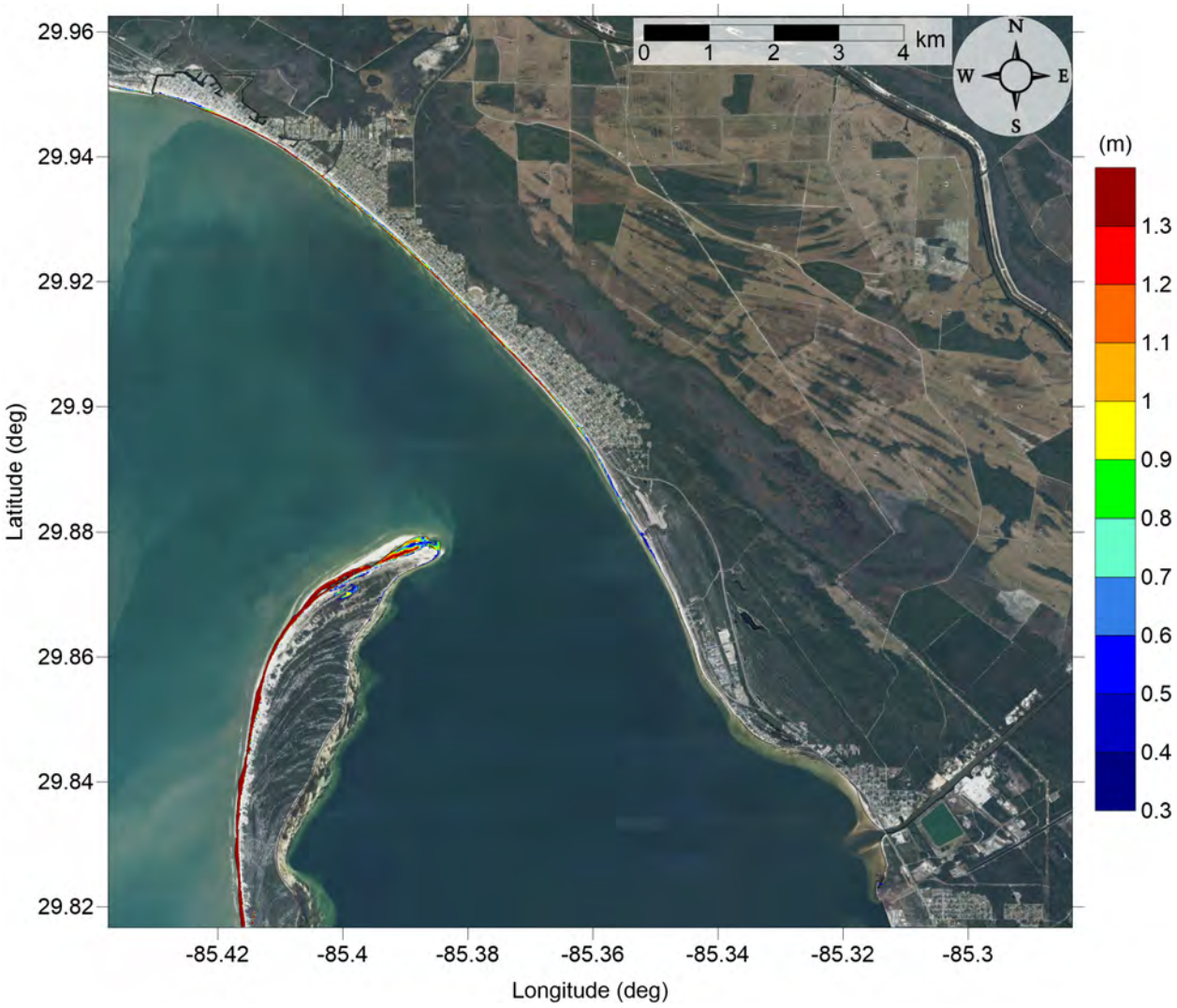

Figure 56: Maximum inundation depth (m) caused by the Probabilistic Submarine Landslide B2 in Mexico Beach, FL. Contour drawn is the zero-meter contour for land elevation.

Mexico Beach, FL
Probabilistic Submarine Landslide B2
Maximum Inundation Depth

Figure 57: Maximum inundation depth (m) caused by the Probabilistic Submarine Landslide B2 in Port St. Joe, FL. Contour drawn is the zero-meter contour for land elevation.

Mexico Beach, FL
Mississippi Canyon submarine landslide
Maximum Momentum Flux

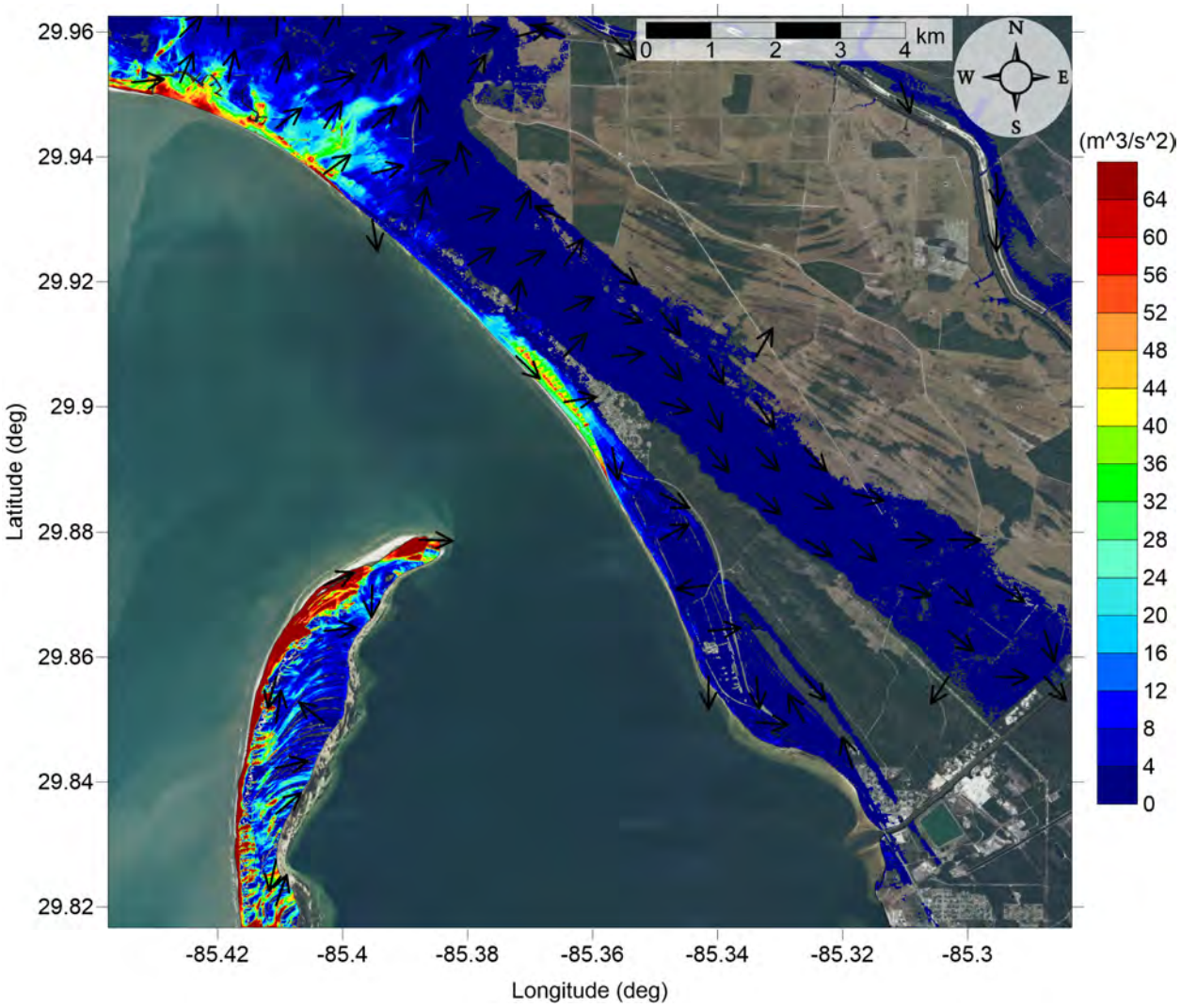

Figure 58: Maximum momentum flux (m^3/s^2) caused by the Mississippi Canyon submarine landslide in Mexico Beach, FL. Arrows represent direction of maximum momentum flux. Contour drawn is the zero-meter contour for land elevation.

Mexico Beach, FL
Mississippi Canyon submarine landslide
Maximum Momentum Flux

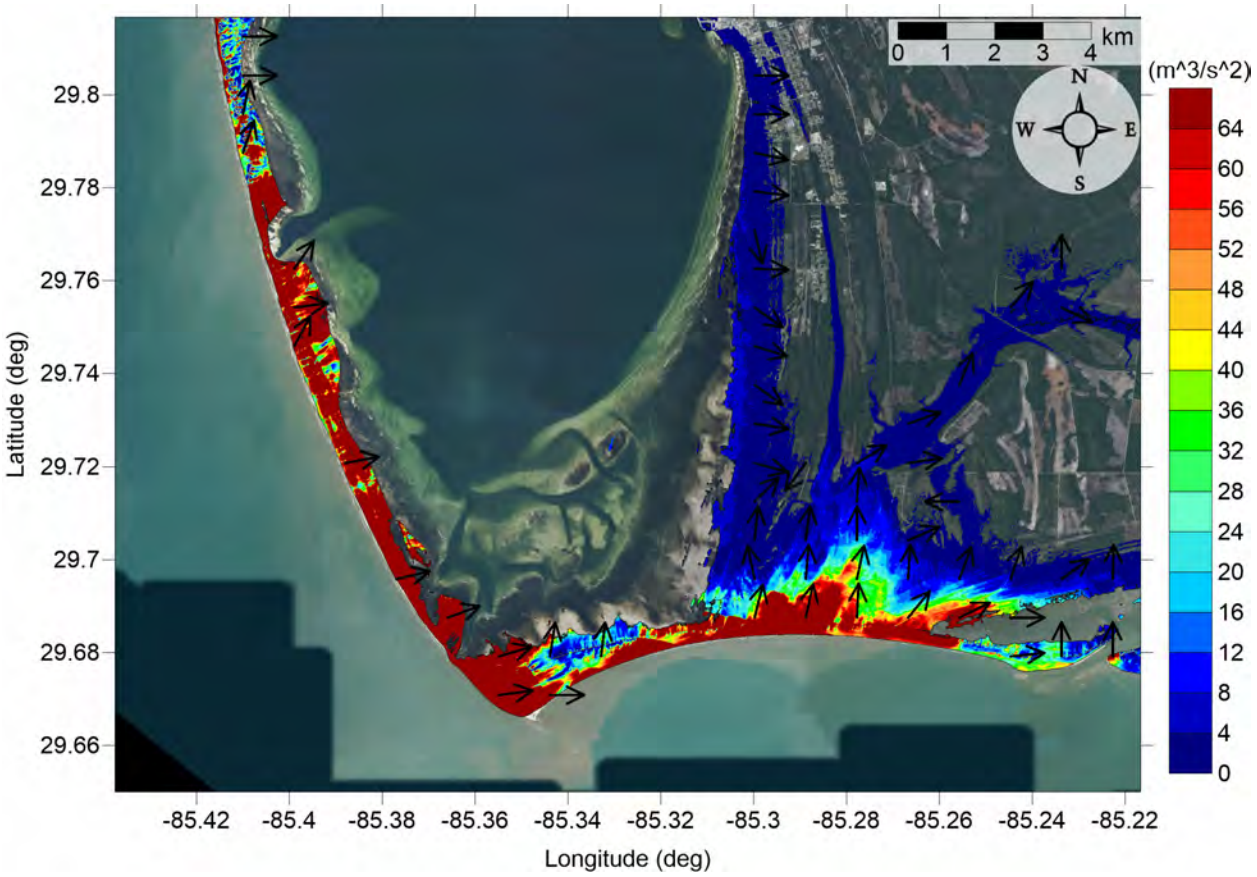

Figure 59: Maximum momentum flux (m^3/s^2) caused by the Mississippi Canyon submarine landslide in Port St. Joe, FL. Arrows represent direction of maximum momentum flux. Contour drawn is the zero-meter contour for land elevation.

Mexico Beach, FL
Mississippi Canyon submarine landslide
Maximum Inundation Depth

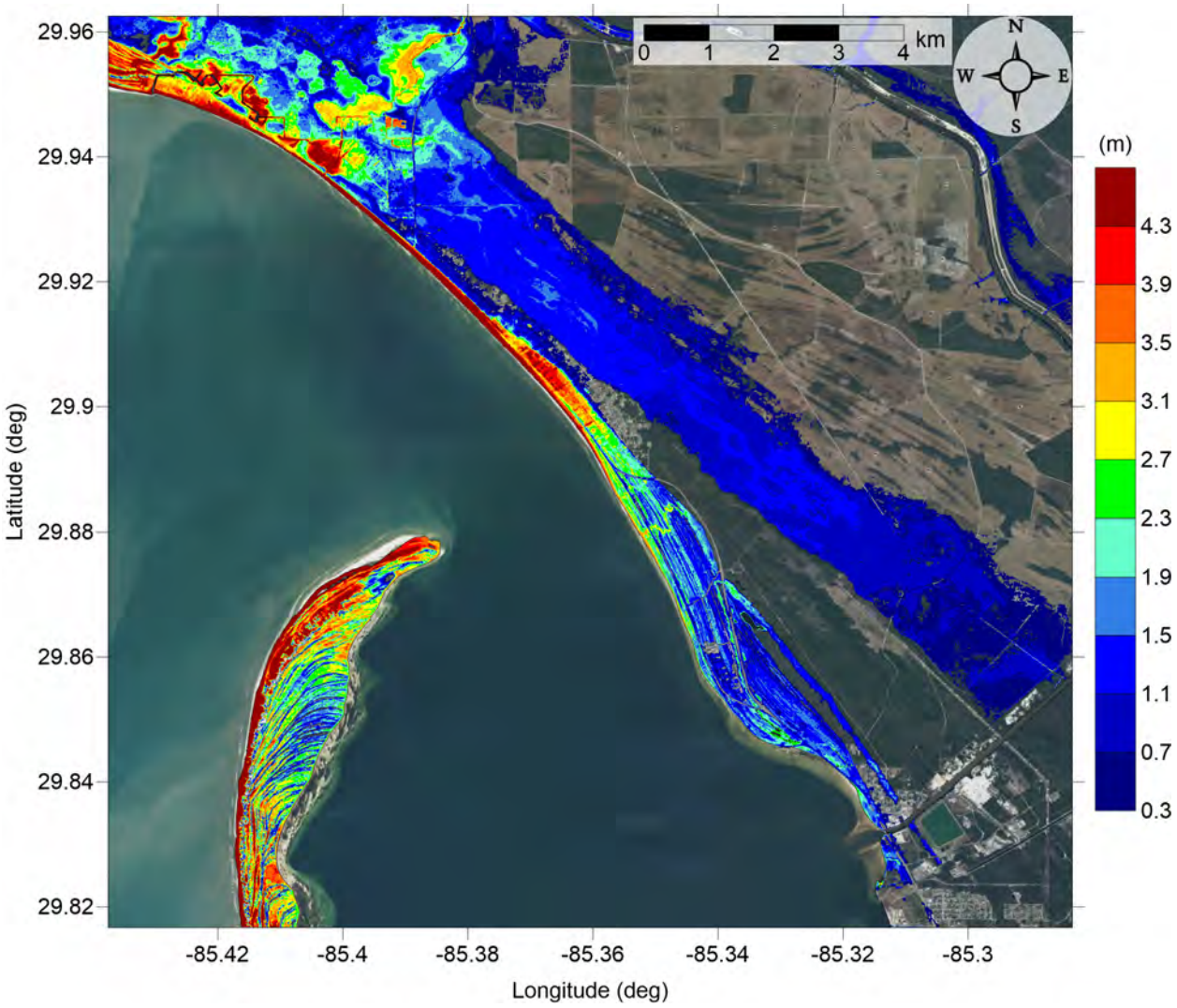

Figure 60: Maximum inundation depth (m) caused by the Mississippi Canyon submarine landslide in Mexico Beach, FL. Contour drawn is the zero-meter contour for land elevation.

Mexico Beach, FL
Mississippi Canyon submarine landslide
Maximum Inundation Depth

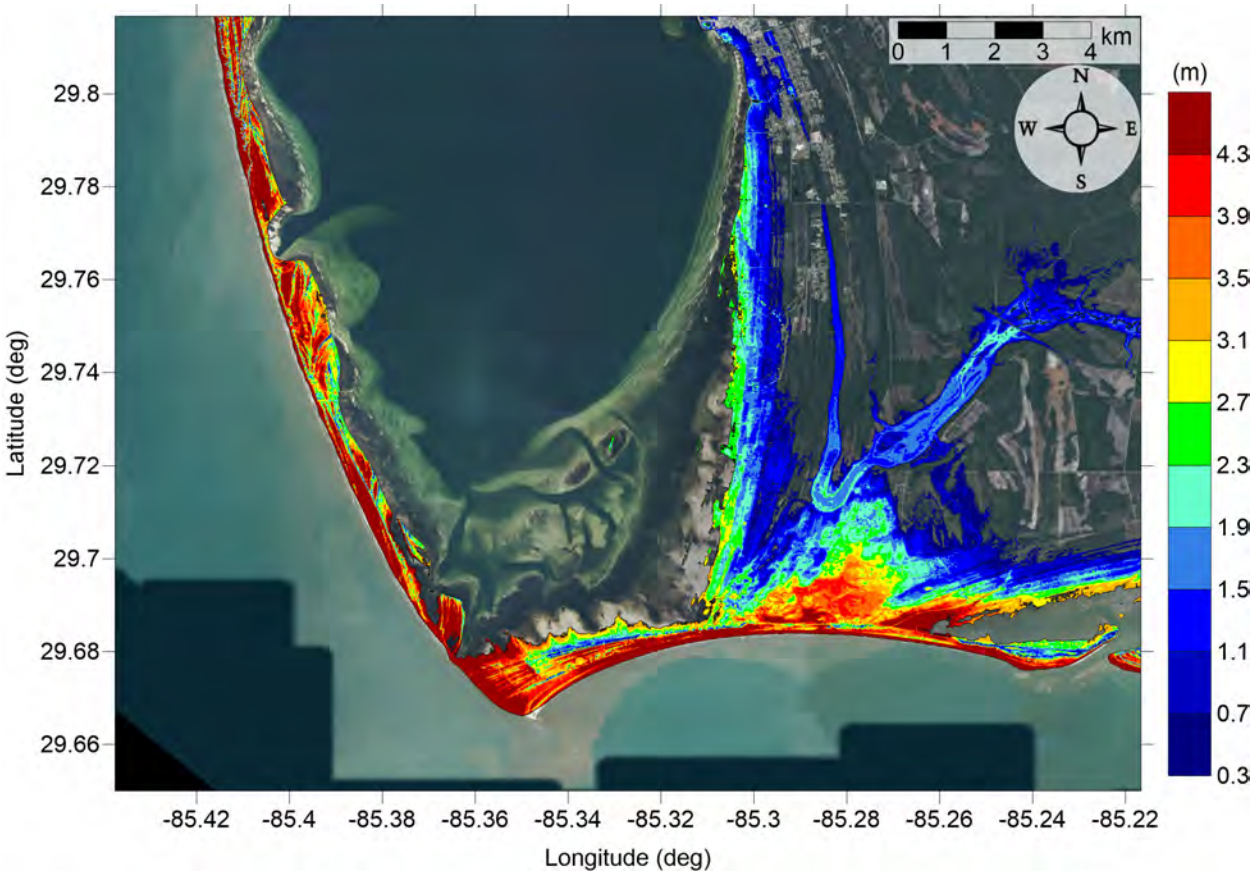

Figure 61: Maximum inundation depth (m) caused by the Mississippi Canyon submarine landslide in Port St. Joe, FL. Contour drawn is the zero-meter contour for land elevation.

Mexico Beach, FL
Probabilistic Submarine Landslide C
Maximum Momentum Flux

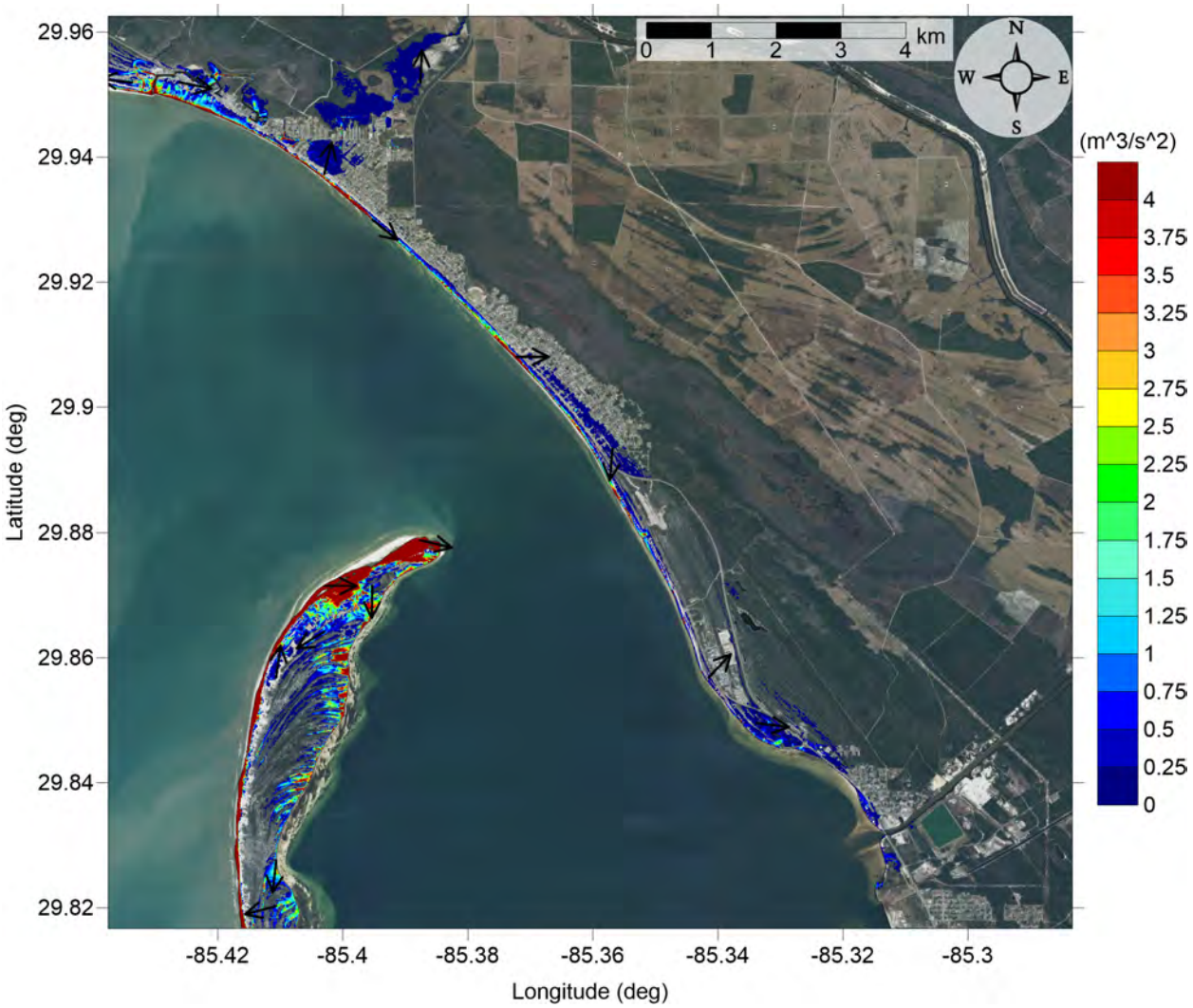

Figure 62: Maximum momentum flux (m^3/s^2) caused by the Probabilistic Submarine Landslide C in Mexico Beach, FL. Arrows represent direction of maximum momentum flux. Contour drawn is the zero-meter contour for land elevation.

Mexico Beach, FL
Probabilistic Submarine Landslide C
Maximum Momentum Flux

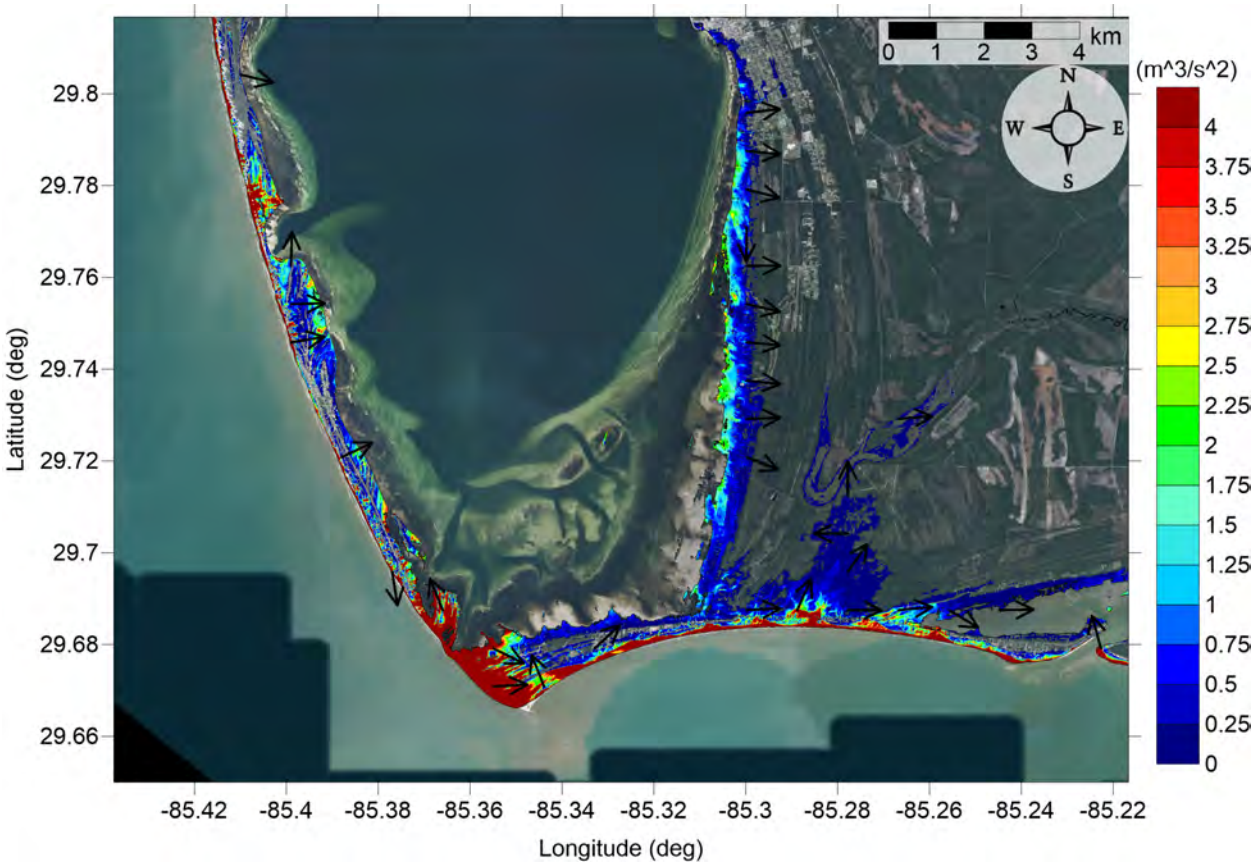

Figure 63: Maximum momentum flux (m^3/s^2) caused by the Probabilistic Submarine Landslide C in Port St. Joe, FL. Arrows represent direction of maximum momentum flux. Contour drawn is the zero-meter contour for land elevation.

Mexico Beach, FL
Probabilistic Submarine Landslide C
Maximum Inundation Depth

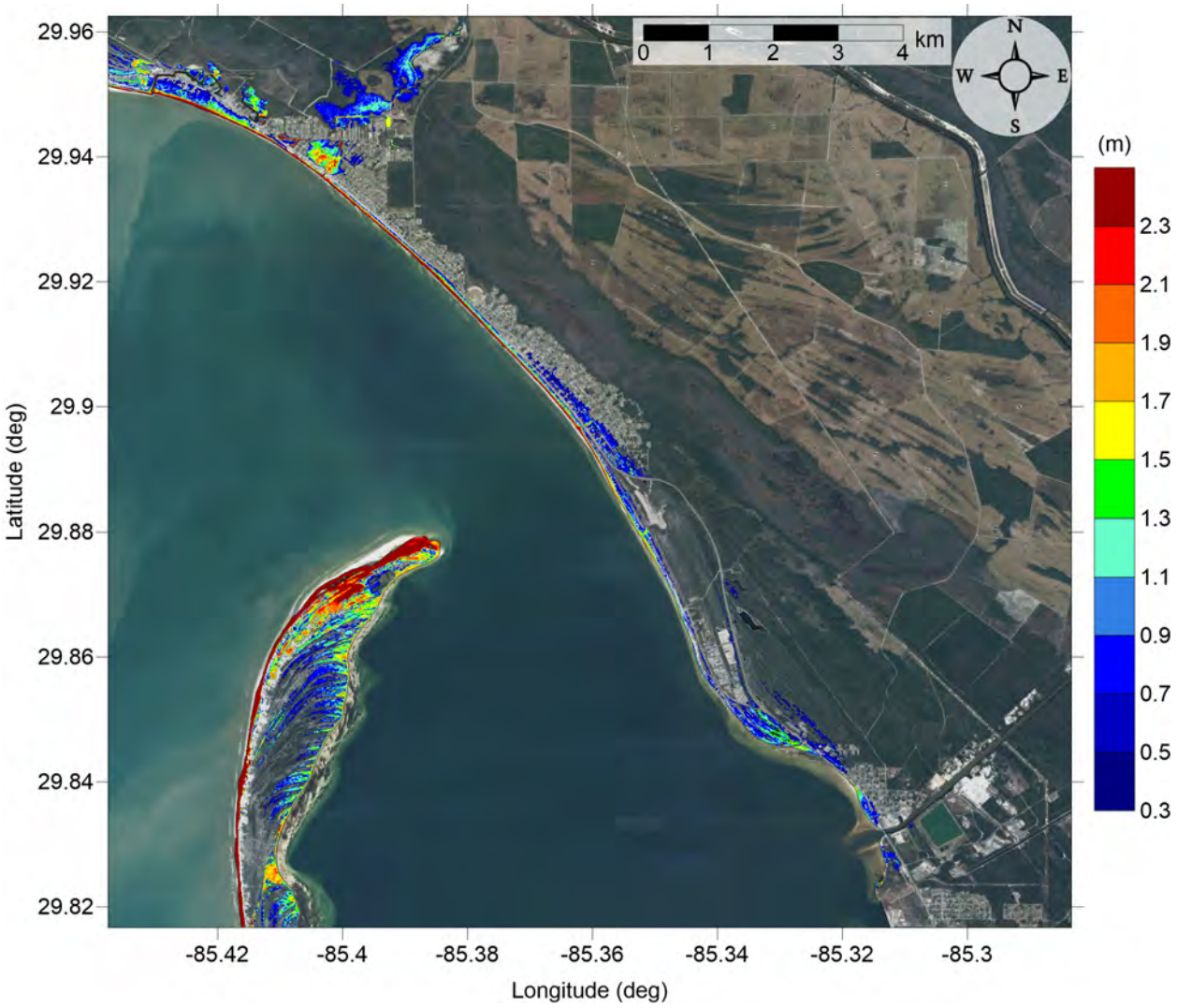

Figure 64: Maximum inundation depth (m) caused by the Probabilistic Submarine Landslide C in Mexico Beach, FL. Contour drawn is the zero-meter contour for land elevation.

Mexico Beach, FL
Probabilistic Submarine Landslide C
Maximum Inundation Depth

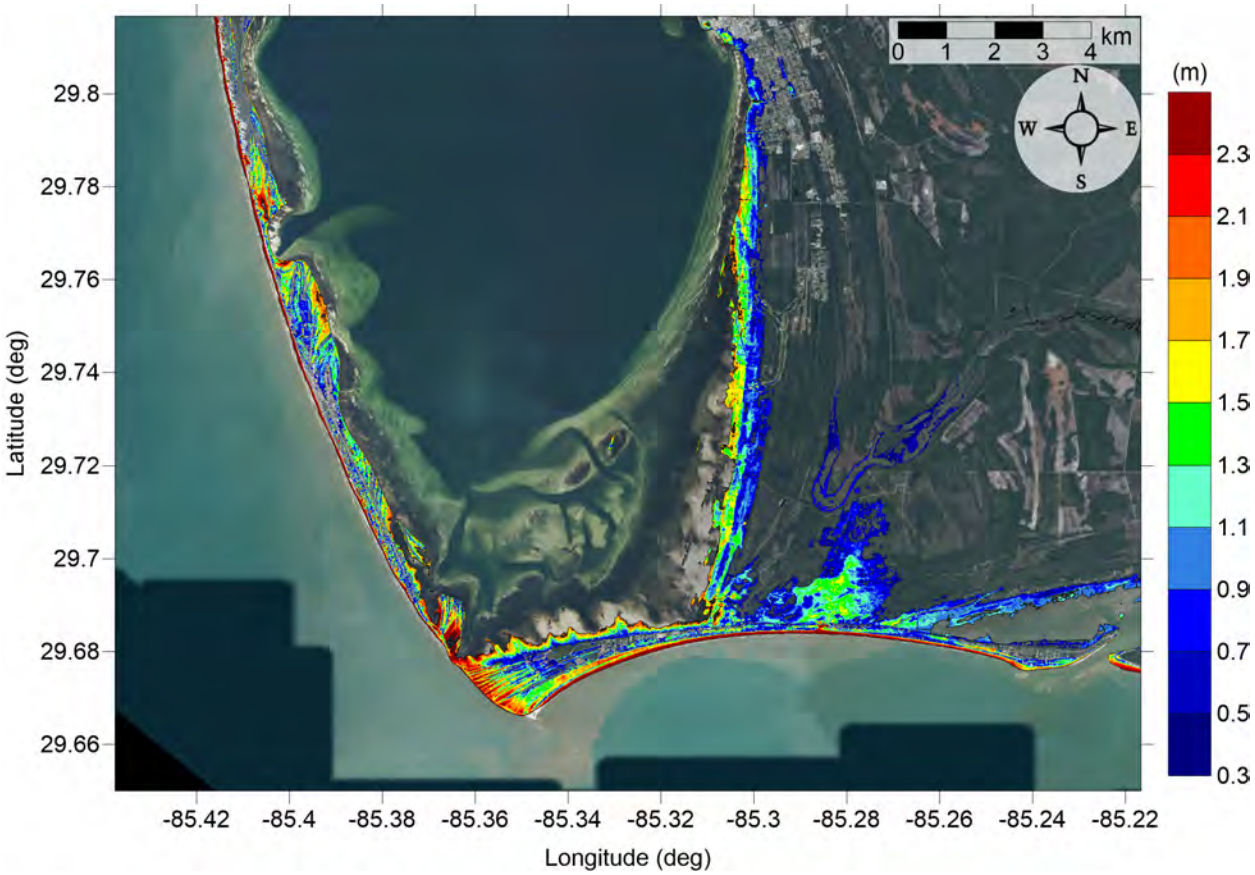

Figure 65: Maximum inundation depth (m) caused by the Probabilistic Submarine Landslide C in Port St. Joe, FL. Contour drawn is the zero-meter contour for land elevation.

Mexico Beach, FL
West Florida submarine landslide
Maximum Momentum Flux

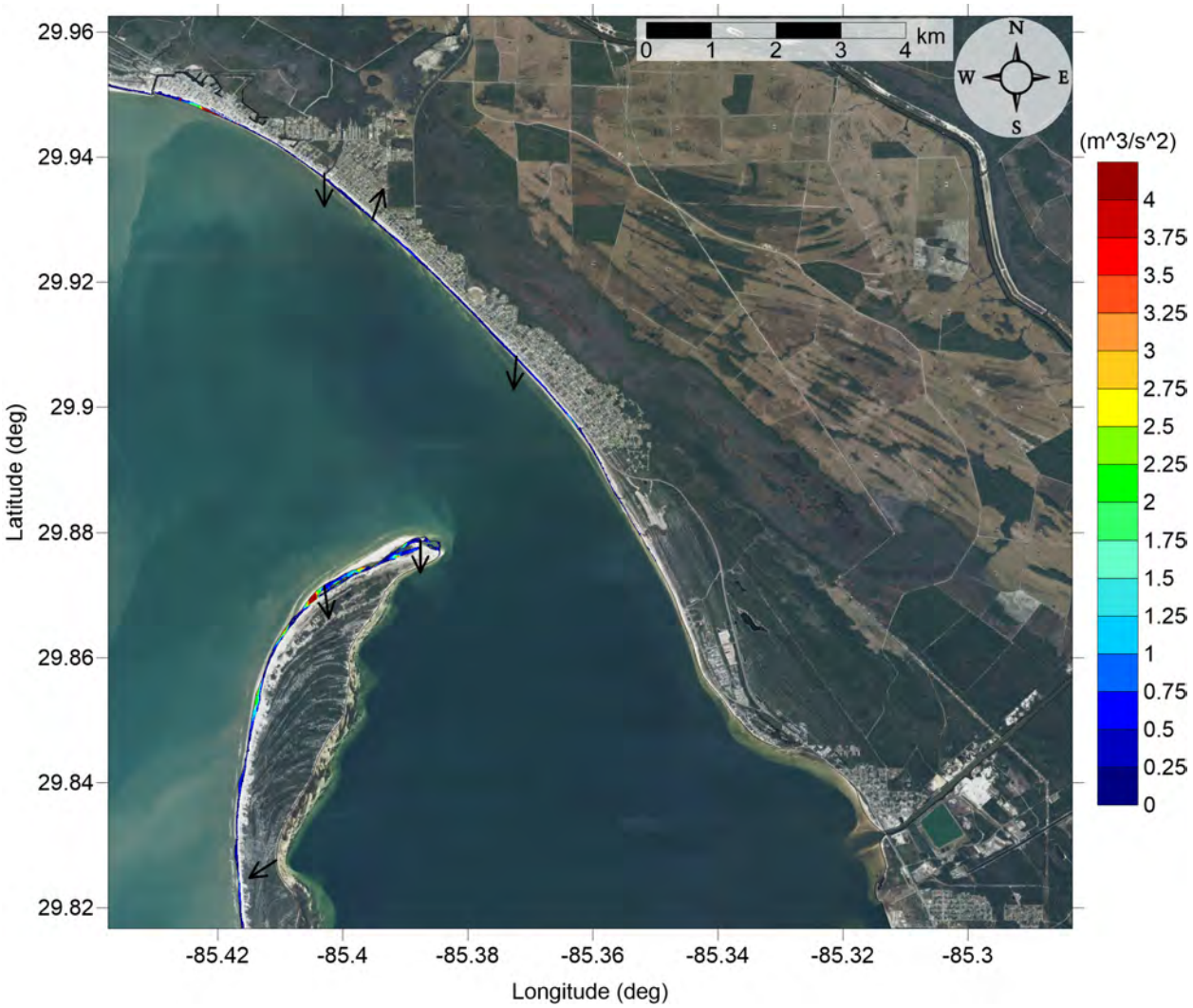

Figure 66: Maximum momentum flux (m^3/s^2) caused by the West Florida submarine landslide in Mexico Beach, FL. Arrows represent direction of maximum momentum flux. Contour drawn is the zero-meter contour for land elevation.

Mexico Beach, FL
West Florida submarine landslide
Maximum Momentum Flux

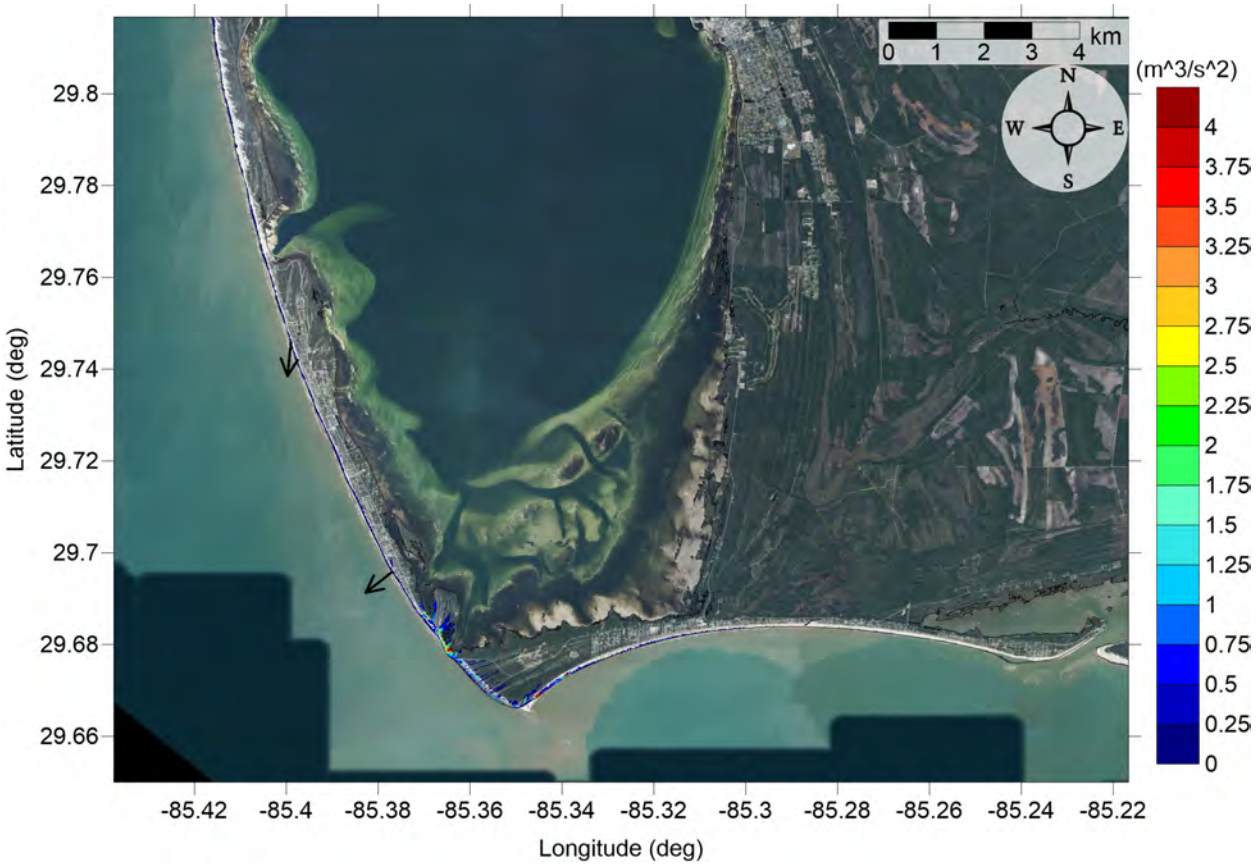

Figure 67: Maximum momentum flux (m^3/s^2) caused by the West Florida submarine landslide in Port St. Joe, FL. Arrows represent direction of maximum momentum flux. Contour drawn is the zero-meter contour for land elevation.

Mexico Beach, FL
West Florida submarine landslide
Maximum Inundation Depth

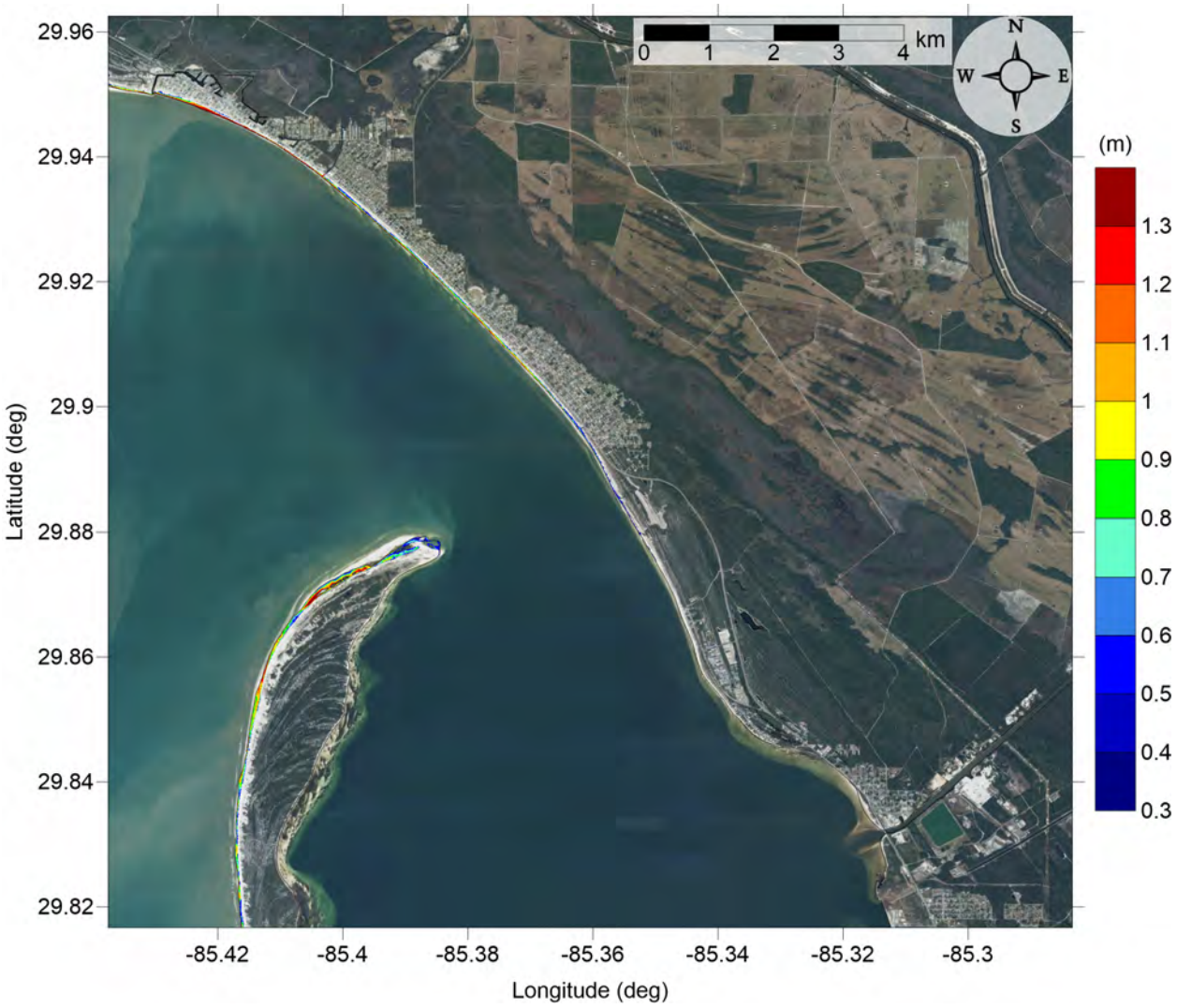

Figure 68: Maximum inundation depth (m) caused by the West Florida submarine landslide in Mexico Beach, FL. Contour drawn is the zero-meter contour for land elevation.

Mexico Beach, FL
West Florida submarine landslide
Maximum Inundation Depth

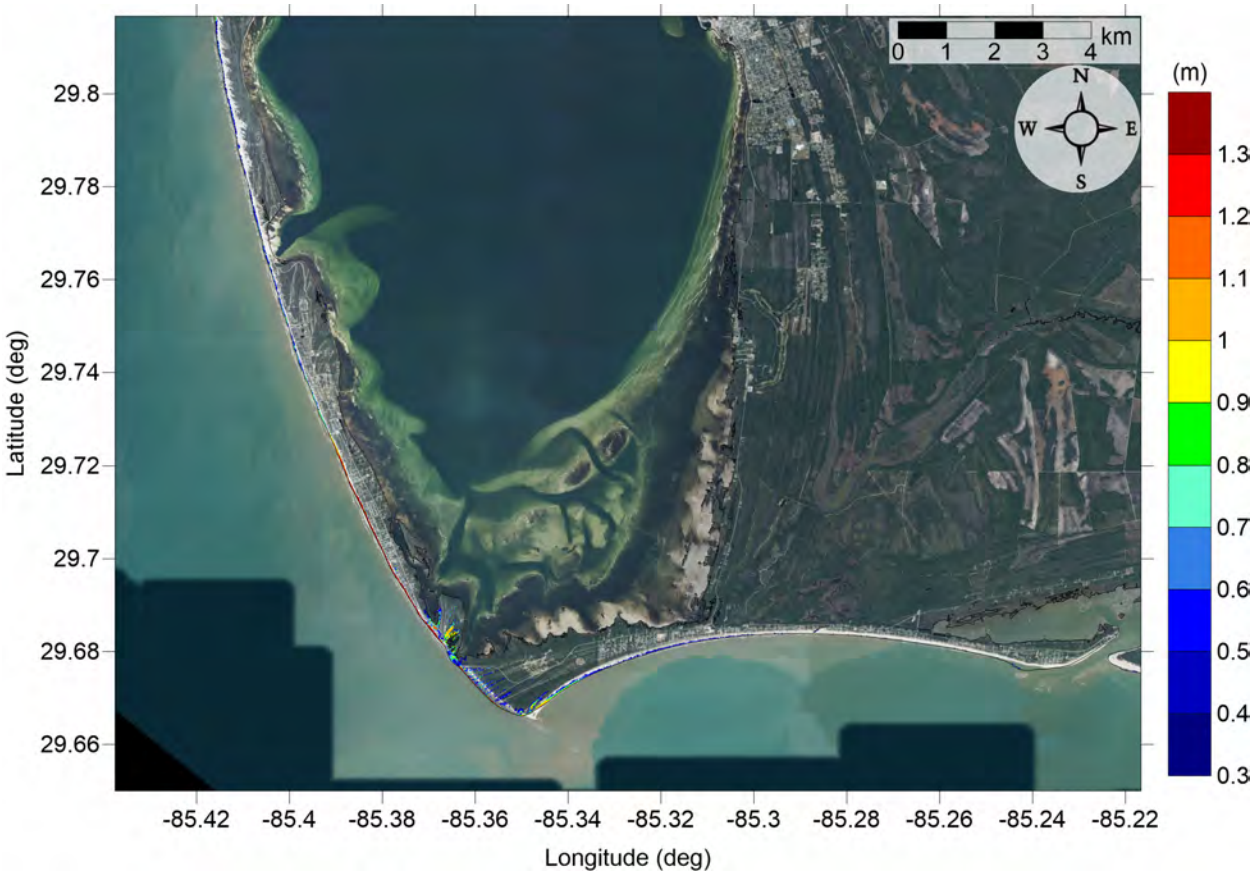

Figure 69: Maximum inundation depth (m) caused by the West Florida submarine landslide in Port St. Joe, FL. Contour drawn is the zero-meter contour for land elevation.

Mexico Beach, FL
Yucatán 3 submarine landslide
Maximum Momentum Flux

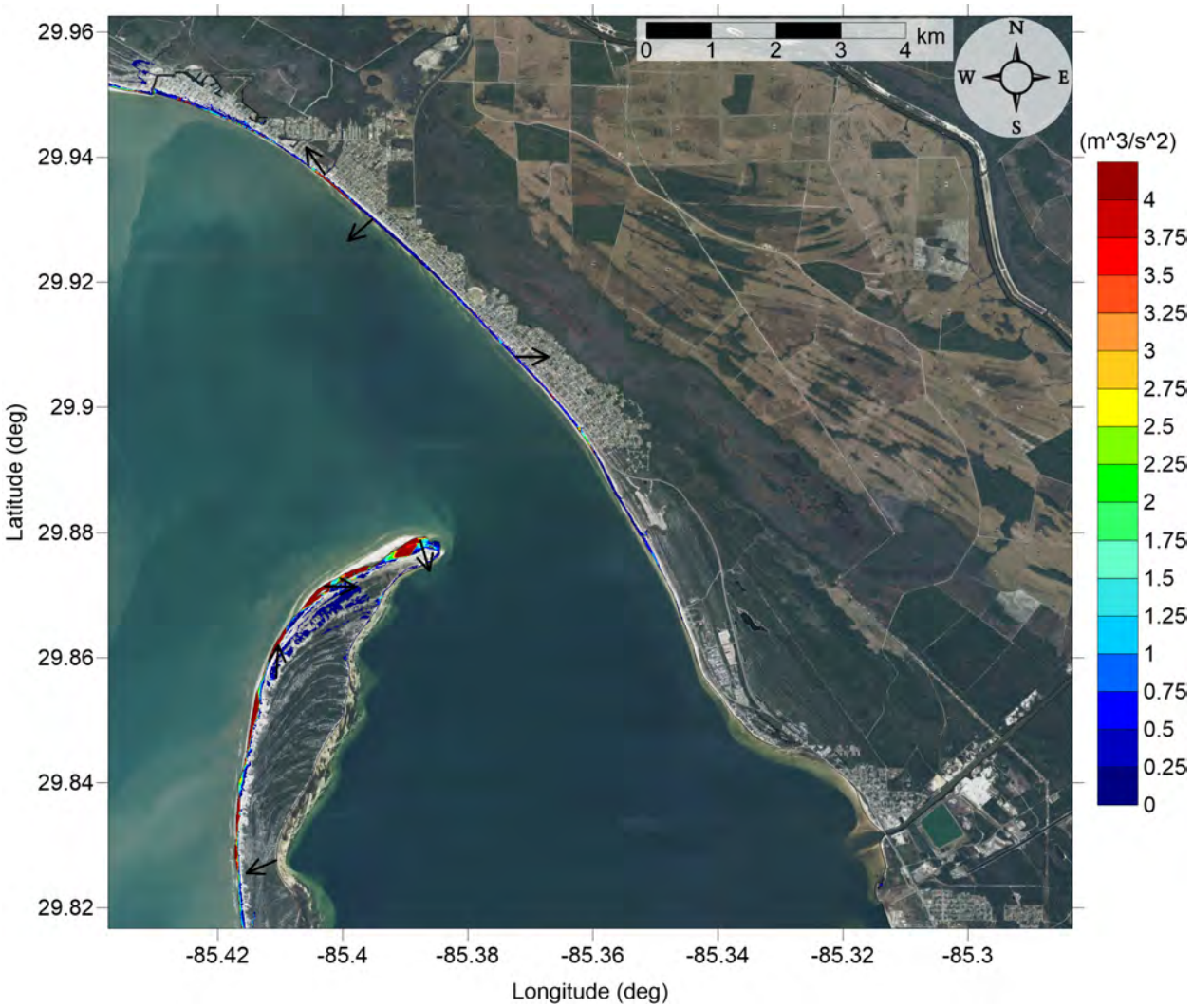

Figure 70: Maximum momentum flux (m^3/s^2) caused by the Yucatán 3 submarine landslide in Mexico Beach, FL. Arrows represent direction of maximum momentum flux. Contour drawn is the zero-meter contour for land elevation.

Mexico Beach, FL
Yucatán 3 submarine landslide
Maximum Momentum Flux

Figure 71: Maximum momentum flux (m^3/s^2) caused by the Yucatán 3 submarine landslide in Port St. Joe, FL. Arrows represent direction of maximum momentum flux. Contour drawn is the zero-meter contour for land elevation.

Mexico Beach, FL
Yucatán 3 submarine landslide
Maximum Inundation Depth

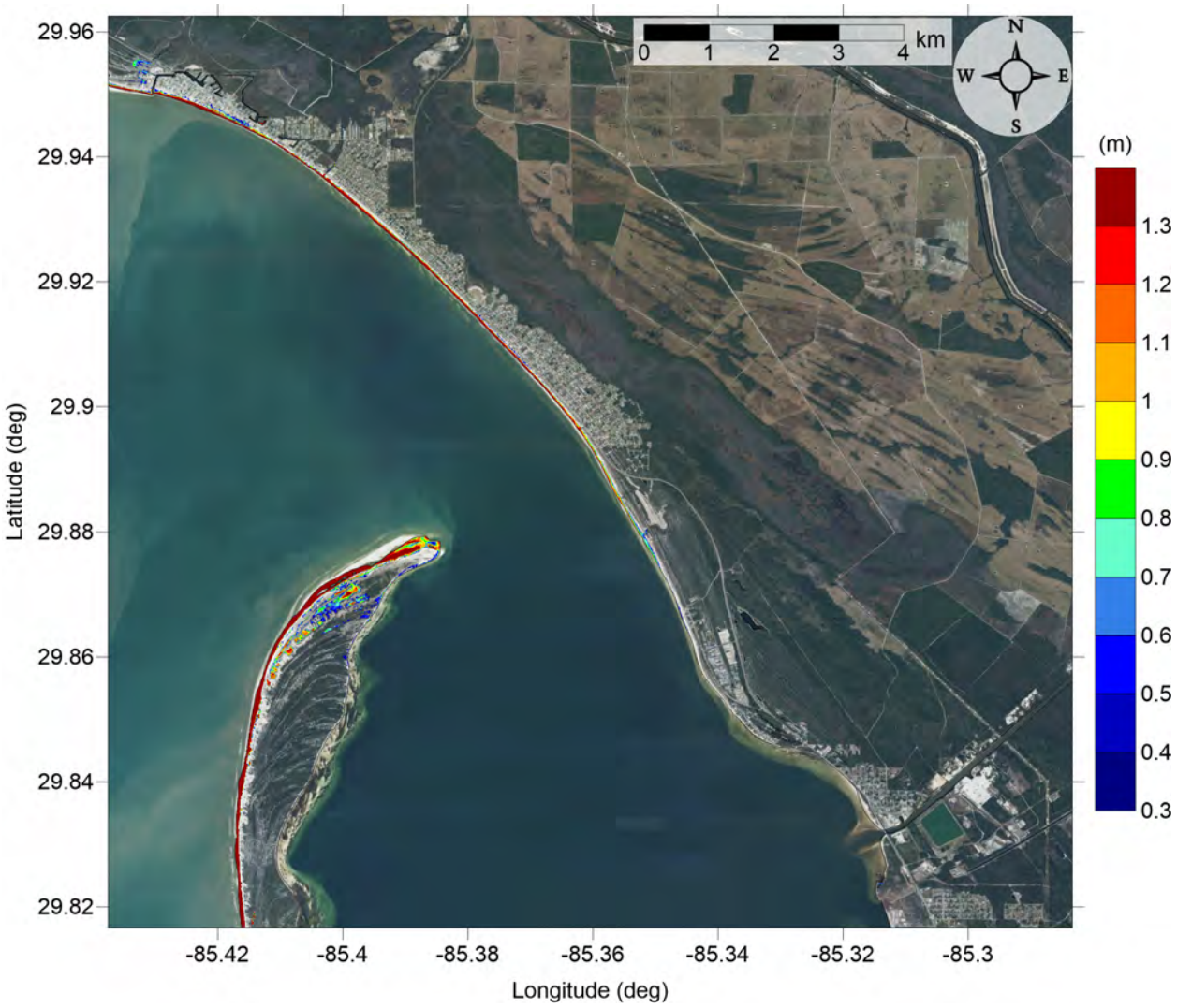

Figure 72: Maximum inundation depth (m) caused by the Yucatán 3 submarine landslide in Mexico Beach, FL. Contour drawn is the zero-meter contour for land elevation.

Mexico Beach, FL
Yucatán 3 submarine landslide
Maximum Inundation Depth

Figure 73: Maximum inundation depth (m) caused by the Yucatán 3 submarine landslide in Port St. Joe, FL. Contour drawn is the zero-meter contour for land elevation.

Mexico Beach, FL
Yucatán 5 submarine landslide
Maximum Momentum Flux

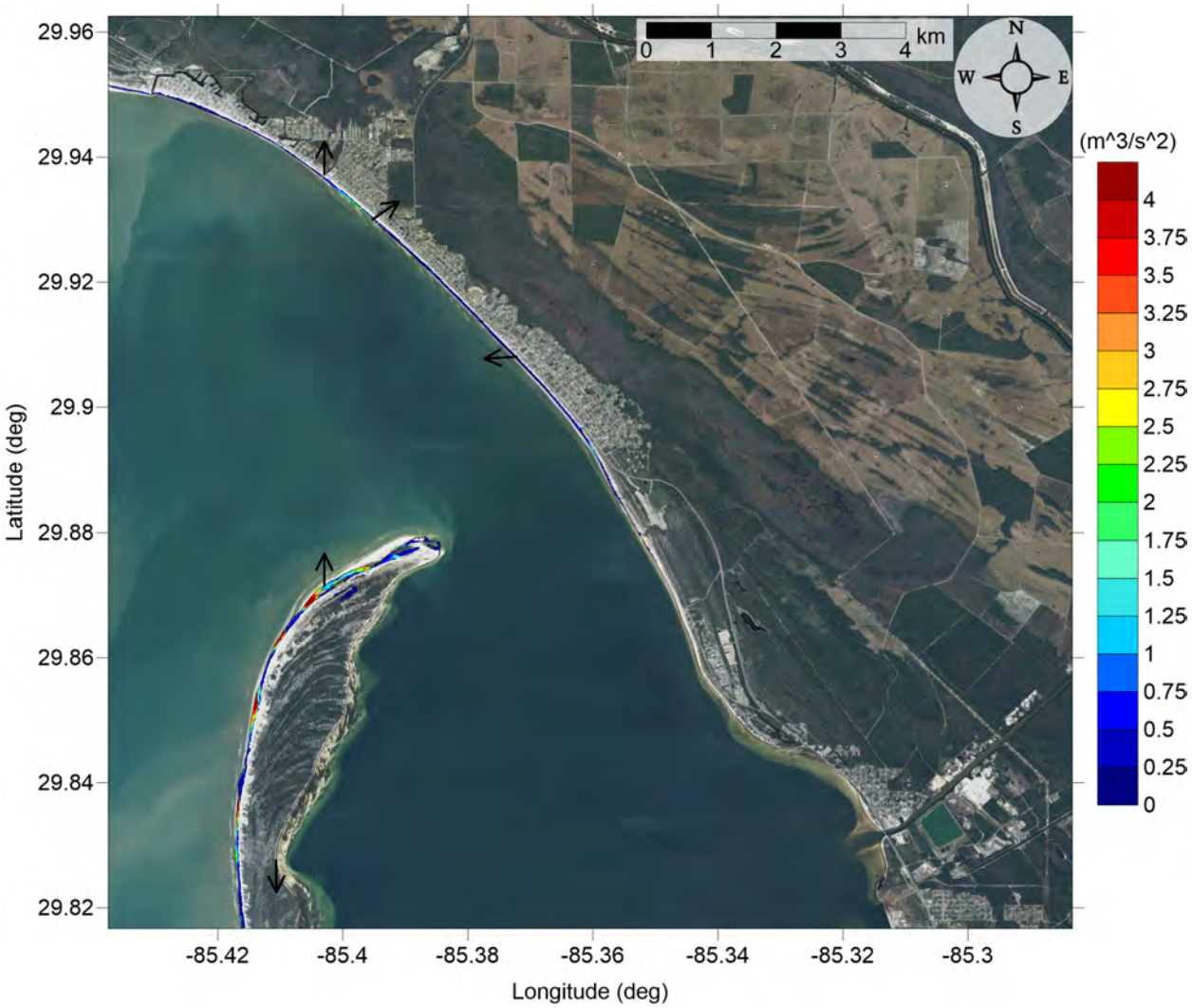

Figure 74: Maximum momentum flux (m^3/s^2) caused by the Yucatán 5 submarine landslide in Mexico Beach, FL. Arrows represent direction of maximum momentum flux. Contour drawn is the zero-meter contour for land elevation.

Mexico Beach, FL
Yucatán 5 submarine landslide
Maximum Momentum Flux

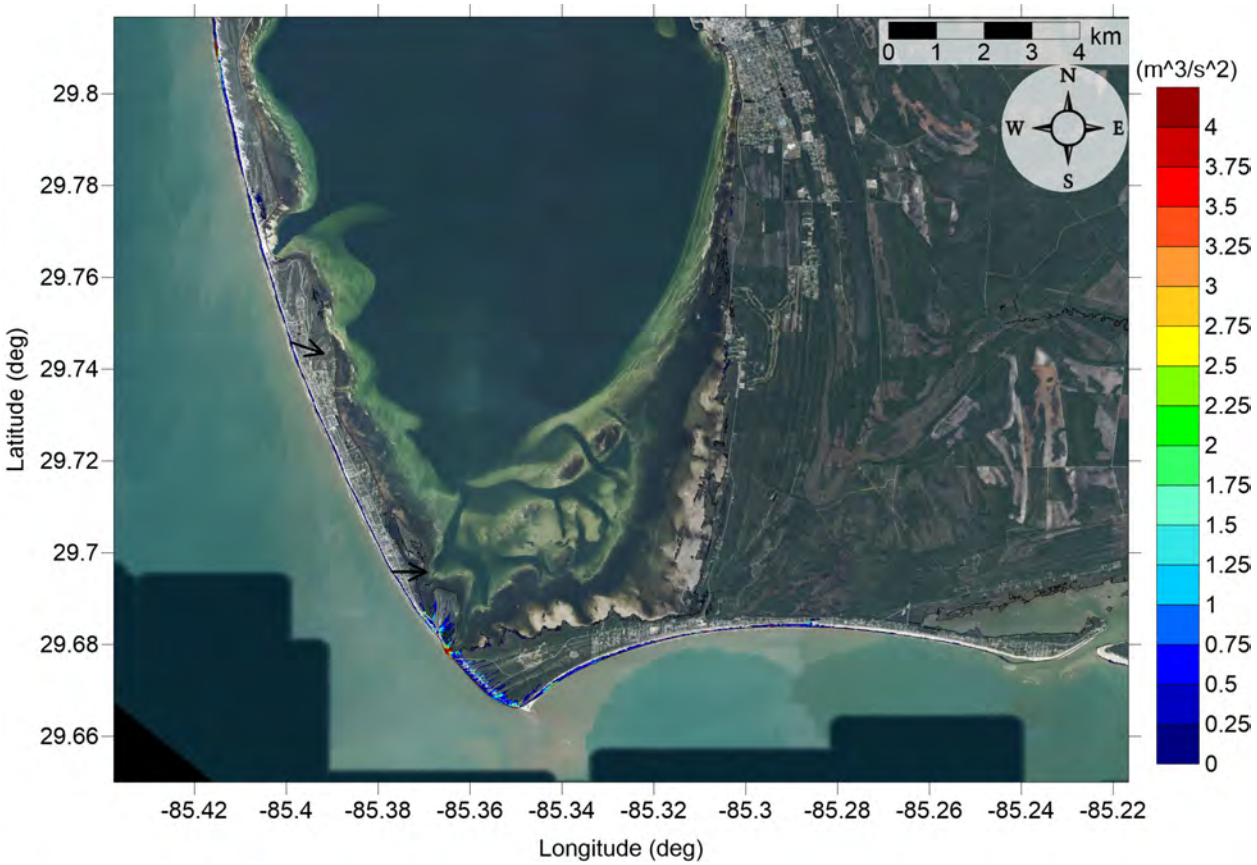

Figure 75: Maximum momentum flux (m^3/s^2) caused by the Yucatán 5 submarine landslide in Port St. Joe, FL. Arrows represent direction of maximum momentum flux. Contour drawn is the zero-meter contour for land elevation.

Mexico Beach, FL
Yucatán 5 submarine landslide
Maximum Inundation Depth

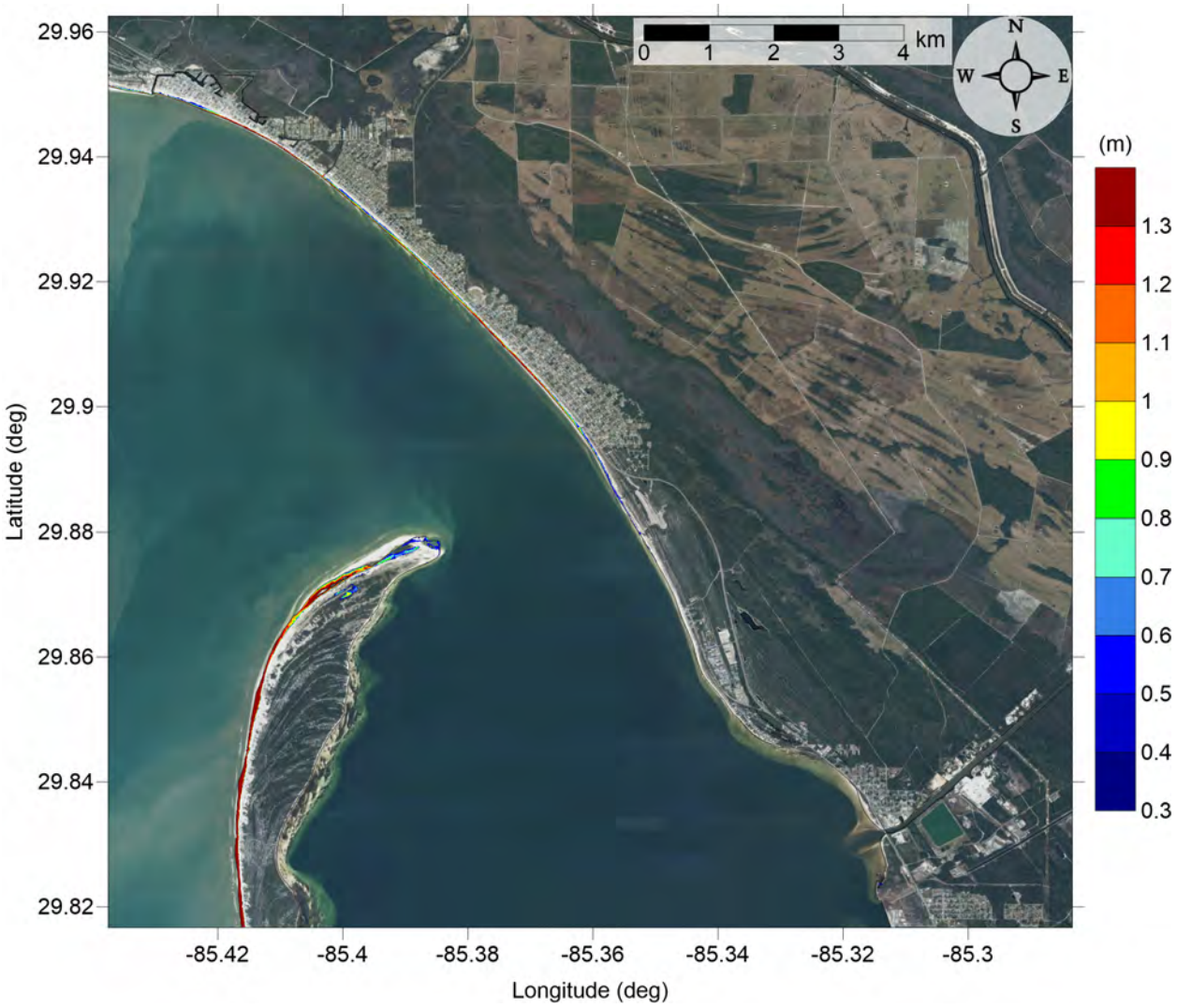

Figure 76: Maximum inundation depth (m) caused by the Yucatán 5 submarine landslide in Mexico Beach, FL. Contour drawn is the zero-meter contour for land elevation.

Mexico Beach, FL
Yucatán 5 submarine landslide
Maximum Inundation Depth

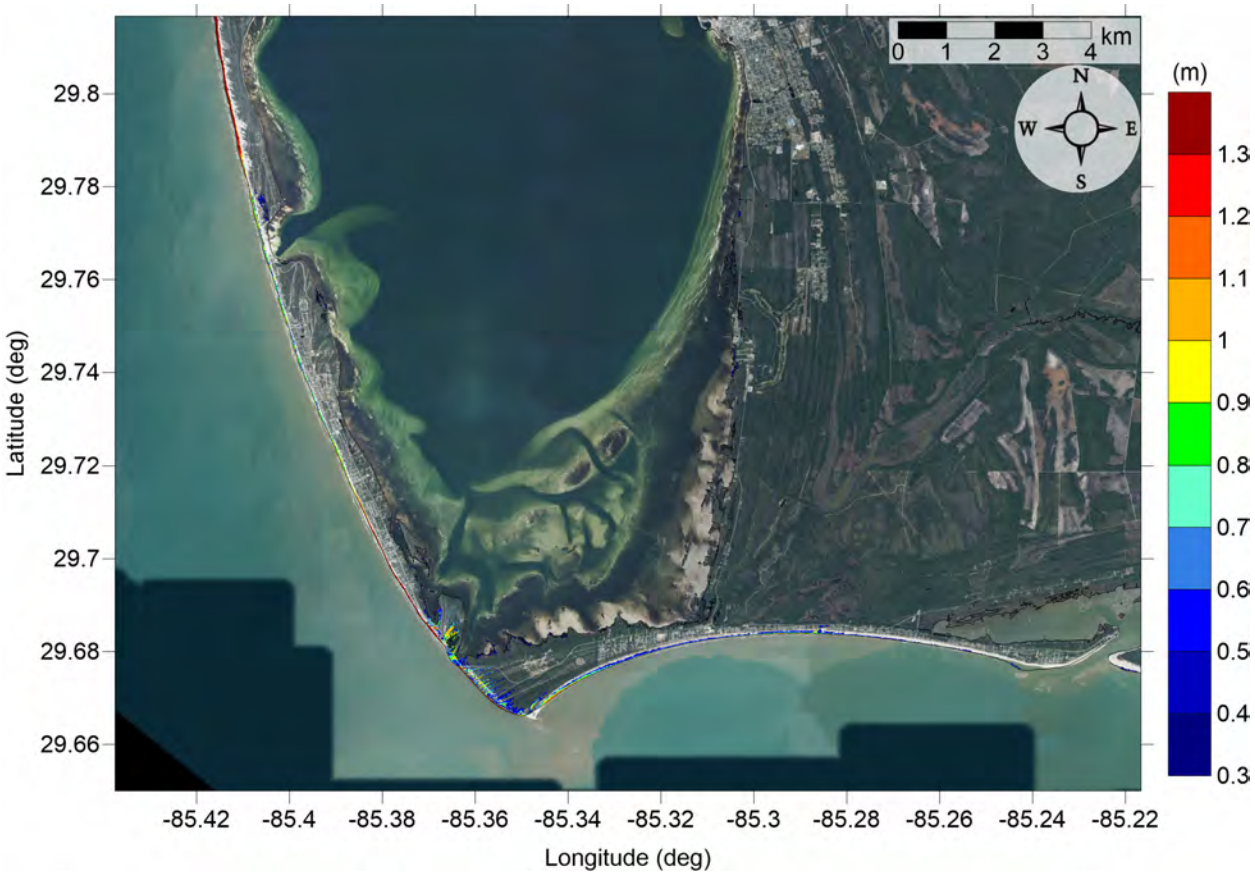

Figure 77: Maximum inundation depth (m) caused by the Yucatán 5 submarine landslide in Port St. Joe, FL. Contour drawn is the zero-meter contour for land elevation.

Mexico Beach, FL
All Sources
Maximum of Maximum Inundation Depth

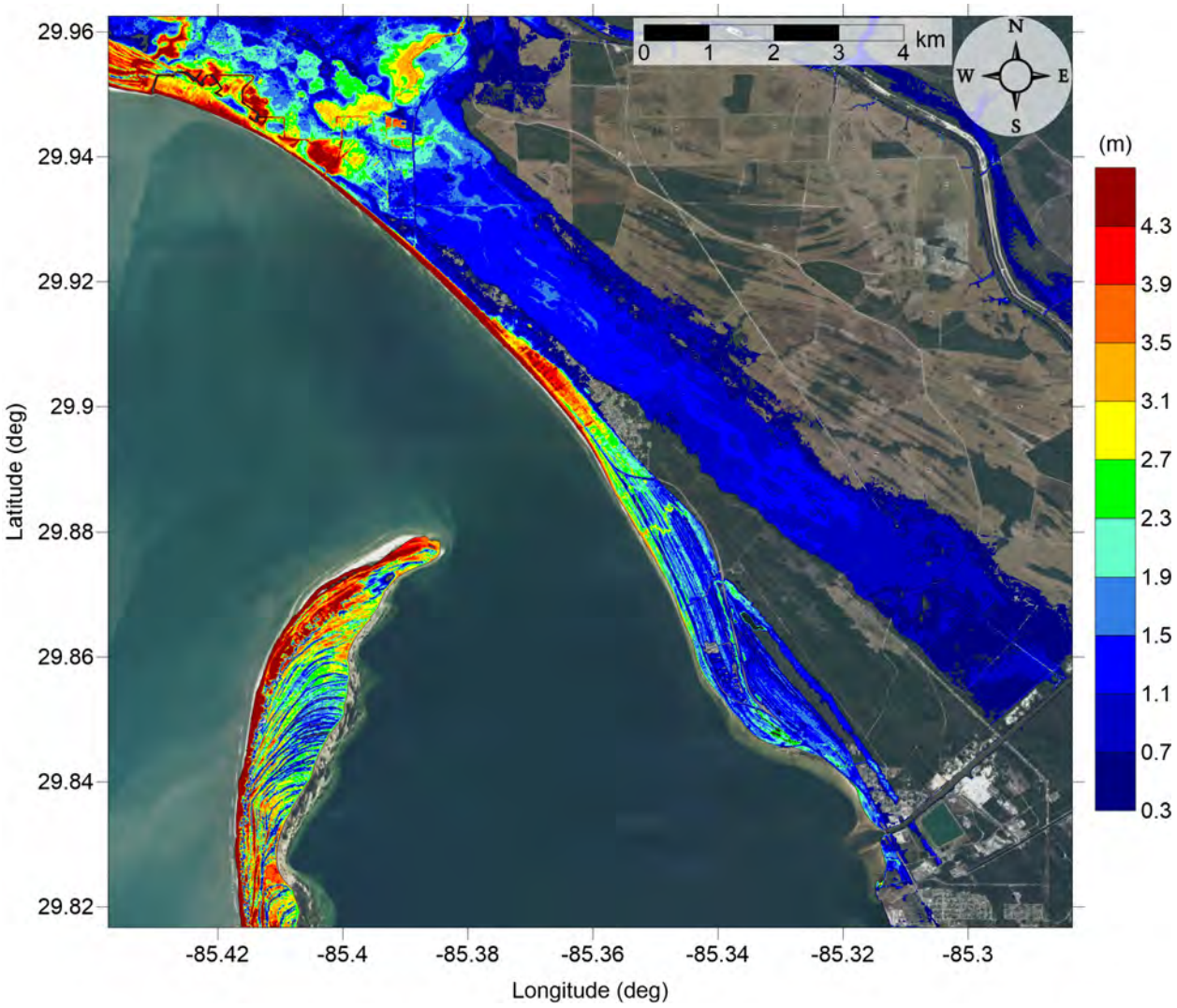

Figure 78: Maximum of maximums inundation depth (m) in Mexico Beach, FL, calculated as the maximum inundation depth in each grid cell from an ensemble of all tsunami sources considered. Contour drawn is the zero-meter contour for land elevation.

Mexico Beach, FL
All Sources
Maximum of Maximum Inundation Depth

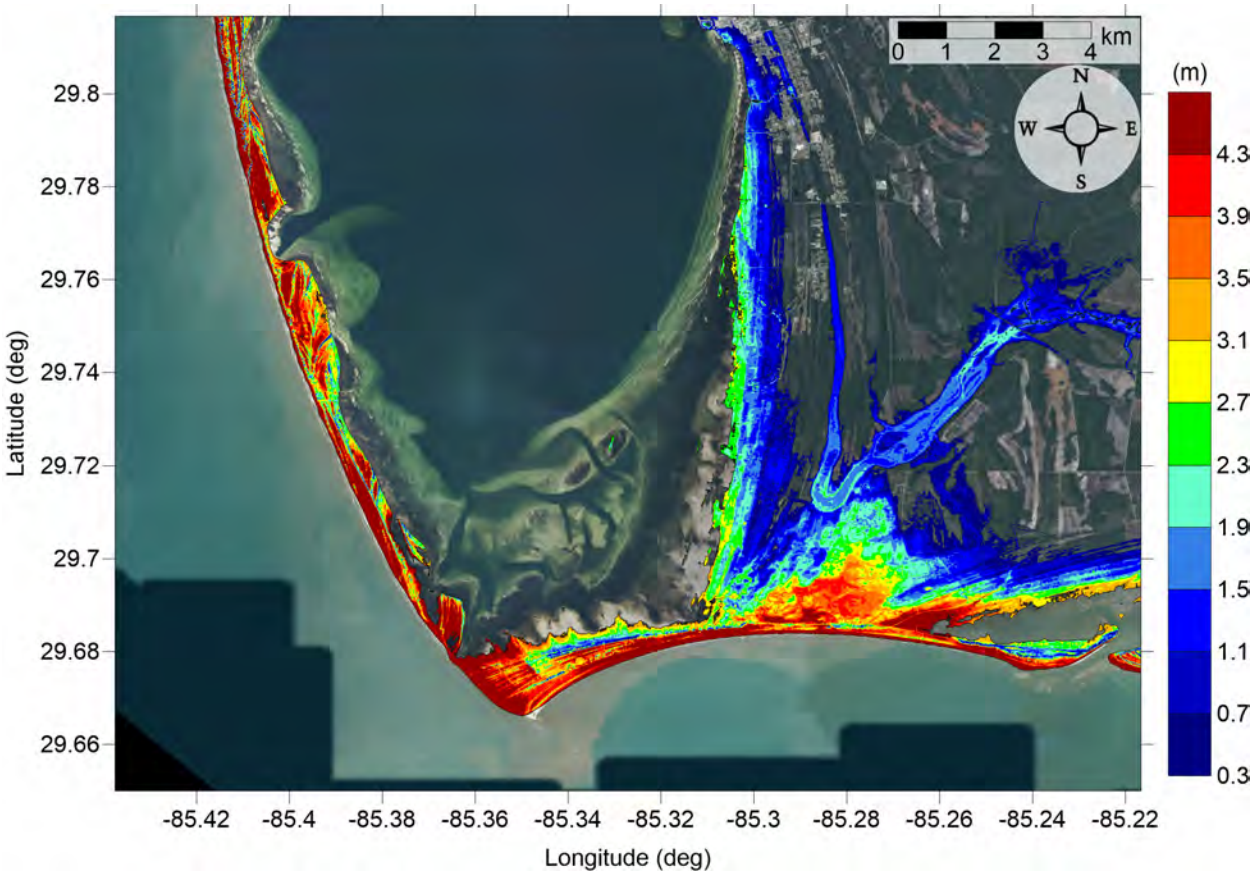

Figure 79: Maximum of maximums inundation depth (m) in Port St. Joe, FL, calculated as the maximum inundation depth in each grid cell from an ensemble of all tsunami sources considered. Contour drawn is the zero-meter contour for land elevation.

Mexico Beach, FL
All Sources
Maximum Inundation Depth by Source

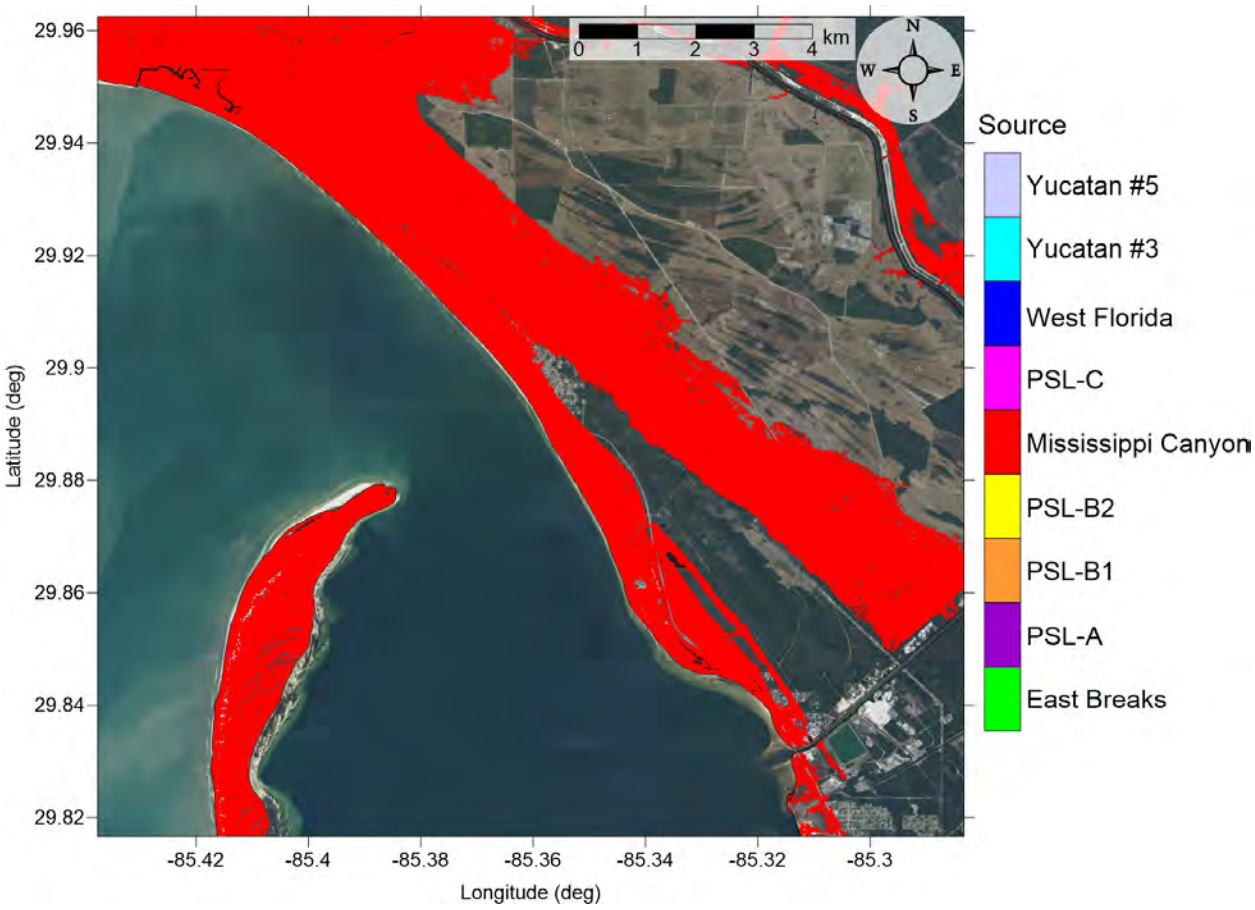

Figure 80: Indication of the tsunami source which causes the maximum of maximums inundation depth (m) in each grid cell from an ensemble of all tsunami sources in Mexico Beach, FL. Contour drawn is the zero-meter contour for land elevation.

Mexico Beach, FL
All Sources
Maximum Inundation Depth by Source

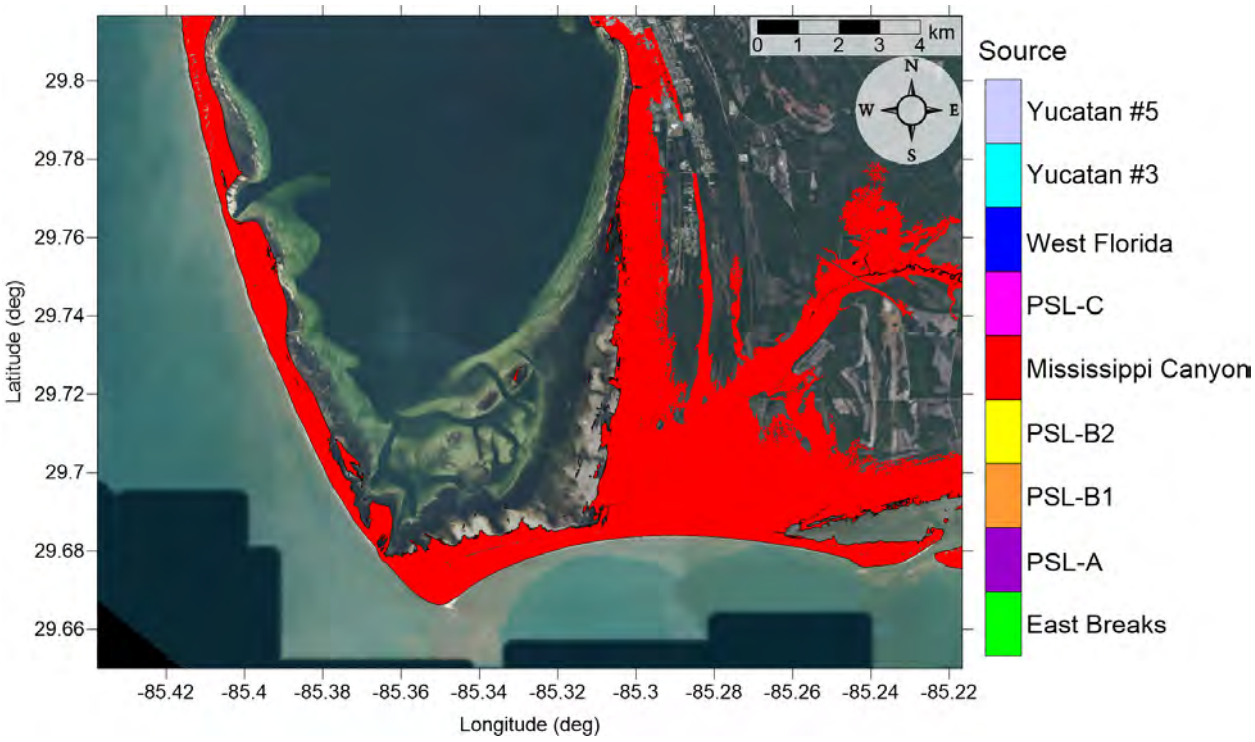

Figure 81: Indication of the tsunami source which causes the maximum of maximums inundation depth (m) in each grid cell from an ensemble of all tsunami sources in Port St. Joe, FL. Contour drawn is the zero-meter contour for land elevation.

5 Tsunami and Hurricane Storm Surge Inundation

Due to the limitations on availability of high-resolution (1/3 arcsecond) DEMs, detailed inundation maps for all communities along the Gulf Coast are not yet possible. In an effort to develop a first-order estimate of potential tsunami inundation for those locations where detailed inundation maps have not yet been developed, we compare tsunami inundation modeled for the communities mentioned above to hurricane storm surge modeled data. The motivation for and implications of this approach are twofold. It provides a way to assess tsunami inundation in unmapped communities based on existing storm surge flood data and also relates the level of tsunami hazard to that of another hazard that is better defined in this region. Tsunamis are not well-understood as a threat along the Gulf Coast, making tsunami hazard mitigation efforts somewhat difficult. However, hurricane is a relatively well-understood threat in this region, and hurricane preparedness approaches are well-developed. As a result, comparisons of tsunami and hurricane storm surge inundation levels provide a more understandable and accessible idea of the level of hazard presented by potential tsunami events and can serve as a basis for tsunami preparedness efforts.

The hurricane storm surge data used here is available from the Sea, Lake, and Overland Surges from Hurricanes (SLOSH) model (http://www.nhc.noaa.gov/surge/slosh.php). The SLOSH model was developed by the National Weather Service (NWS) to provide estimates of storm surge heights caused by historical, predicted, or hypothetical hurricanes based on different values for atmospheric pressure, hurricane size, forward speed, and track. It uses a polar, elliptical, or hyperbolic grid for computations, leading to higher resolutions near coastal areas of interest. Some limitations of the SLOSH model should be acknowledged. Resolution of the model varies from tens of meters to a kilometer or more. Near the coastal communities of interest here, resolution is on the order of 1 km. Sub-grid scale water and topographic features such as channels, rivers, levees, and roads, are parameterized instead of being explicitly modeled. Despite these limitations, the hurricane storm surge data from the SLOSH model is currently the best data publicly available for our purposes, and efforts have been made to ensure the validity of the SLOSH data in performing comparisons with tsunami inundation.

The SLOSH MOM results provide the worst-case storm surge for a given hurricane category and initial tide level based on a set of model runs with various combinations of parameters such as forward speed, trajectory, and landfall location. To perform the storm surge and tsunami comparisons, SLOSH storm surge elevation data was first converted to meters and adjusted from the NAVD88 to the MHW vertical datum using NOAA's VDatum tool (http://vdatum.noaa.gov/). Due to the relatively low resolution of the SLOSH data as compared to the DEMs used for tsunami modeling, the SLOSH data was interpolated to 1/3 arcsecond (10 m) resolution using a kriging method. Inundation was then determined by subtracting land elevation from the storm surge elevation.

Here, an initial high tide level is used for the SLOSH MOM results in order to compare the worst-case tsunami inundation with a worst-case storm surge scenario. The high tide SLOSH MOM data includes effects of the highest predicted tide level at each location. In comparison, water elevations in the tsunami modeling are based on the MHW datum, which averages the high water levels over the National Tidal Datum Epoch (NTDE). Within the

GOM, tidal ranges are relatively small, with diurnal ranges on the order of 1.5 ft (0.5 m) for most of the communities studied here, and slightly higher at around 2.5 ft (0.8 m) for the west coast of Florida. Thus, differences between highest tide levels and the mean of the highest tide levels are expected to be relatively small, though local bathymetric effects combined with tidal effects can still be significant.

It should be noted that the updated Saffir-Simpson Hurricane Wind Scale which delineates hurricane categories 1-5 does not include storm surge as a component of the measure of hurricane intensity and that other methods may capture the physics of hurricane severity and damage in a more appropriate manner (e.g. Kantha [2006], Basco and Klentzman [2006], Irish and Resio [2010]). However, the SLOSH MOM results take into account thousands of scenarios for a given hurricane category, resulting in a composite worst-case storm surge scenario for each Saffir-Simpson hurricane category. Thus, since hurricane preparedness, storm surge evacuation zones, and hazard mitigation efforts are based on hurricane category assignment, we aim to determine the hurricane category which produces MOM storm surge inundation ζ_h that is a best match to the tsunami MOM inundation ζ_t. That is, we determine the hurricane category which satisfies

$$min_c(|\zeta_{h_c} - \zeta_t|), \qquad c = \text{Cat1,..,Cat5} \tag{1}$$

for each grid cell. The inundation level for the best-match category is denoted $\zeta_{h_{min}}$. The actual difference between hurricane and tsunami inundation levels $\Delta\zeta = \zeta_{h_{min}} - \zeta_t$ then indicates how close of a match the best-match category actually is. Thus, positive values of $\Delta\zeta$ indicate where hurricane storm surge inundation is higher than tsunami inundation, and negative values indicate where tsunami inundation is higher. A common local practice in tsunami modeling is to only consider inundation above a threshold of 0.3 m (1 ft) [Horrillo et al., 2011, 2015]. This is due to the extensive flat and low-lying elevation found along the Gulf Coast. All depths are calculated for tsunami inundation modeling, but inundation less than 0.3 m (1 ft) is considered negligible here for inundation mapping purposes. Thus, comparisons are only made where either the tsunami or hurricane MOM inundation is at least 0.3 m (1 ft). Results for the two selected Gulf Coast communities are given in the following subsections. It is possible that tsunami inundation zone has no hurricane flooding, therefore matching with hurricane category cannot be made.

5.1 Orange Beach, AL

Gulf Shores, AL

Fig. 38 shows the MOM tsunami inundation affecting Gulf Shores, AL. Under the worst case scenario, tsunami waves would inundate all of the barrier islands south of the Fort Morgan Road (west of Alabama's Coastal Connection or State Highway 135) and south of the Gulf Oak Ridge Trail and the Rattlesnake Ridge Trail. The highest inundation (> 4 m) occurs at the immediate ocean front and around the Little Lagoon, and the other potentially at-risk areas would expect less than 3 meters of inundation. The area around the Oyster Bay is also inundated, albeit this area is not populated and the water height is mostly under 1.5 m. The Mississippi Canyon landslide is responsible for the MOM inundation (see Fig. 40).

The hurricane category which best matches the tsunami inundation in Gulf Shores, AL is shown in Fig. 82, and Fig. 83 shows $\Delta\zeta$ for the best-matching hurricane category satisfying Eq. 1. The hurricane category that best matches tsunami inundation closely follows the MOM tsunami inundation trend, where Category 5 appears near the beach and around the Little Lagoon. Going away from Category 5 are Category 4 and 3 for the barrier island and Category 2 and 1 appear around the Oyster Bay. The difference between hurricane flooding and tsunami inundation is mostly within ± 1 m.

Orange Beach, AL

Fig. 39 shows the MOM tsunami inundation affecting Orange Beach, AL (also including Ono Island, AL and Perdido Key, FL). Under the worst case scenario, tsunami would inundate all of the barrier islands. Overall water depth exhibits decreasing trend from oceanfront toward the bay, with maximum over 4 m. The MOM tsunami inundation at Orange Beach and western section of Perdido Key, FL are generally higher than eastern Perdido Key. On Ono Island, AL, $>$ 4 m inundation only occurs at the south ocean front, while 2 - 3 m inundation occurs around the intersection between River Rd and Ono Blvd. On mainland Florida, the areas south of the Gulf Beach Hwy and S Blue Angel Pkwy can be flooded. Tsunami inundation area higher than 4 m is larger south of S Blue Angel Pkwy than south of Gulf Beach Hwy due to its proximity to the inlet (between Fort Pickens and Fort McRee). The Mississippi Canyon landslide is responsible for the MOM inundation (see Fig. 41).

The hurricane category which best matches the tsunami inundation in Orange Beach, AL is shown in Fig. 84, and Fig. 85 shows $\Delta\zeta$ for the best-matching hurricane category satisfying Eq. 1. The hurricane category that best matches tsunami inundation closely follows the MOM tsunami inundation trend. On Perdido Key, Category 5 to 3 appears from the beach to the bay, and similar to the inundation pattern, there are larger areas of Category 4 and 5 at western Perdido Key than the eastern. On mainland Florida, Category 3 and 4 appear in the areas south of the Gulf Beach Hwy and Category 4 and 5 south of S Blue Angel Pkwy. The difference between hurricane flooding and tsunami inundation is mostly within ± 1 m.

Orange Beach, FL
All Sources
SLOSH Storm Surge and MOM Tsunami Inundation Comparison

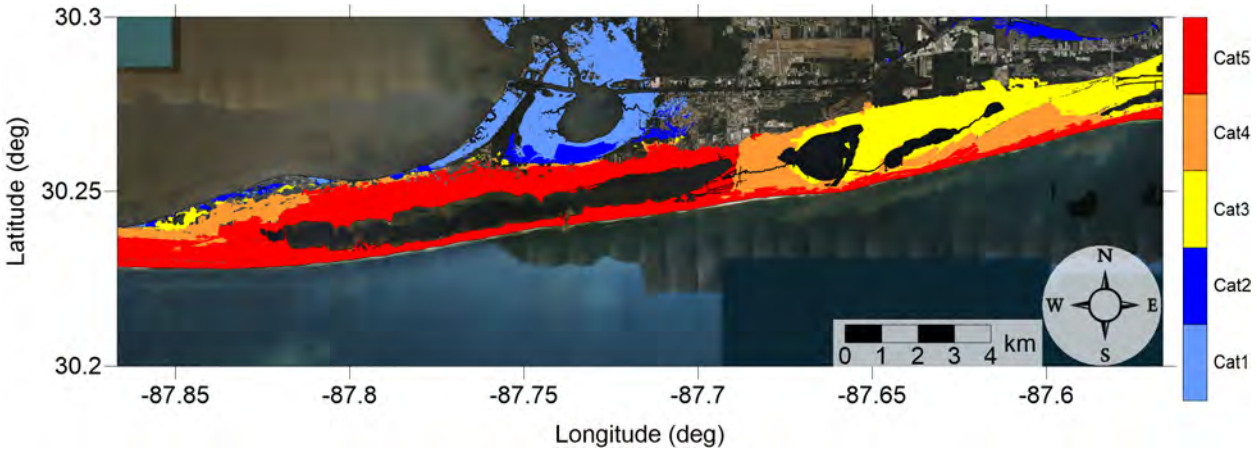

Figure 82: Hurricane category which produces inundation at high tide that best matches the MOM tsunami inundation shown in Figure 83 for Gulf Shores, AL. The contours drawn and labeled are at -5 m, -10 m, and -15 m levels.

Orange Beach, FL
All Sources
SLOSH Storm Surge and MOM Tsunami Inundation Comparison

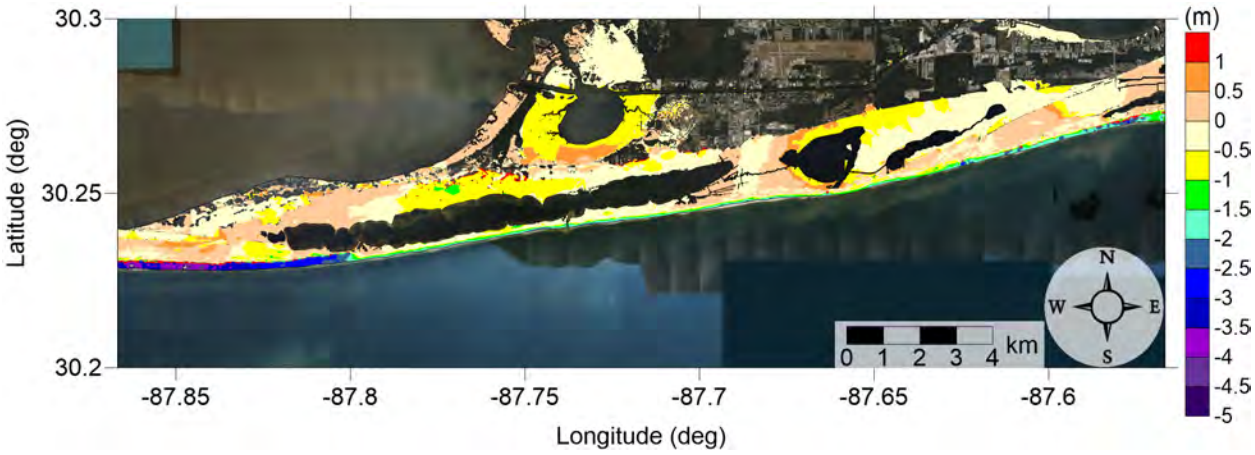

Figure 83: Actual difference $\Delta\zeta$ (in meters) between SLOSH MOM storm surge inundation and MOM tsunami inundation for the best-match hurricane category shown in Figure 82 for Gulf Shores, AL. Note that negative values indicate where tsunami inundation is higher than hurricane inundation, and pale colors indicate relatively good agreement between tsunami and storm surge inundation, i.e. $|\Delta\zeta| \leq 0.5$ m. The contours drawn and labeled are at -5 m, -10 m, and -15 m levels.

Orange Beach, FL
All Sources
SLOSH Storm Surge and MOM Tsunami Inundation Comparison

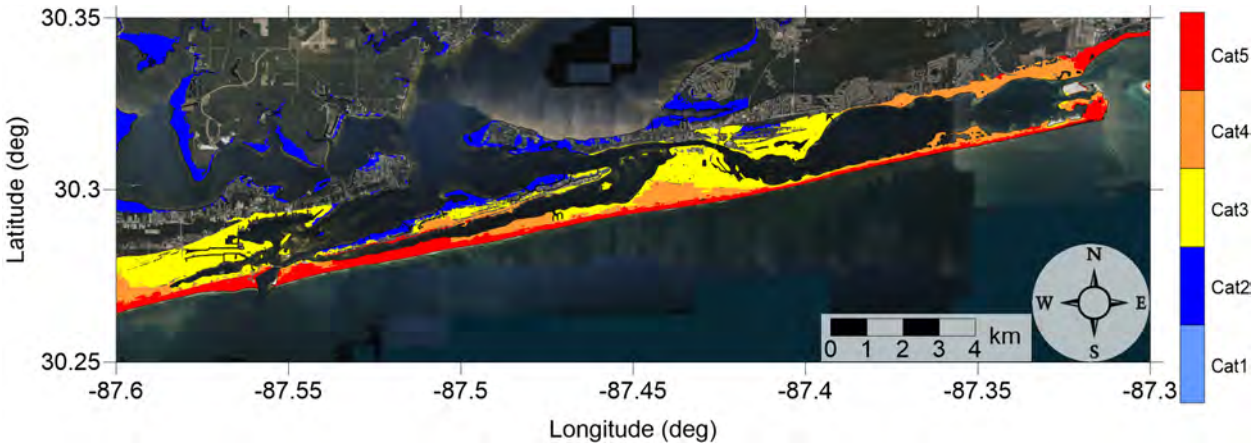

Figure 84: Hurricane category which produces inundation at high tide that best matches the MOM tsunami inundation shown in Figure 85 for Orange Beach, FL. The contours drawn and labeled are at -5 m, -10 m, and -15 m levels.

Orange Beach, FL
All Sources
SLOSH Storm Surge and MOM Tsunami Inundation Comparison

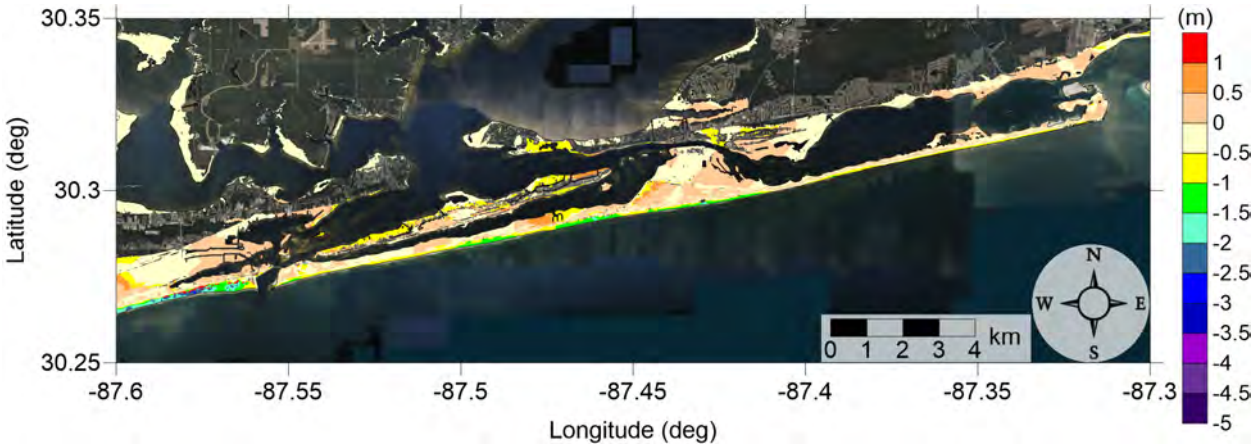

Figure 85: Actual difference $\Delta\zeta$ (in meters) between SLOSH MOM storm surge inundation and MOM tsunami inundation for the best-match hurricane category shown in Figure 84 for Orange Beach, FL. Note that negative values indicate where tsunami inundation is higher than hurricane inundation, and pale colors indicate relatively good agreement between tsunami and storm surge inundation, i.e. $|\Delta\zeta| \leq 0.5$ m. The contours drawn and labeled are at -5 m, -10 m, and -15 m levels.

5.2 Mexico Beach, FL

Fig. 78 and 79 shows the MOM tsunami inundation affecting Mexico Beach and Port St Joe mapping area. Overall, the St Joseph Pennisula/barrier island could be completely inundated under the worst case scenario (MOM). The pennisula provides ample protection for Port St Joe, but not so much for the exposed Mexico Beach. While inundation depth at the St Joseph Pennisula ranges from 2 to over 4 m from the GOM side to the bay, the residential areas are mostly located in the $>$ 4 m zone since they are closer to the GOM. Similarly on the south barrier island of Port St Joe, high inundation water depth can be expected south of the line connecting Cape San Blas Rd, Florida County Rd 30A, and Indian Pass Rd, where the residential areas are located. On the mainland, Mexico Beach's worst case scenario (MOM) inundation is much higher than Port St Joe due to its lack of protection from St Joseph Pennisula. Southwest of Highway 98 in Mexico Beach, inundation is larger than 3 - 4 m. Northeast of Highway 98, high ($>$ 3 - 4 m) inundation occurs mostly around the water channels/marinas, while it decreases from 3 to 1 m outwards from the channels. Moving south toward Port St Joe, inundation is mostly contained southwest of Highway 98, however, high ($>$ 3 - 4 m) water depth starts to occurs south of the line formed by Lightkeepers Dr, Sea Pines Ln, Cristins Curve Rd, Ocean Ridge Ln, and Alabama Ave. Further south passing the north tip of St Josepth Pennisula, maximum inundation in Port St Joe adjacent to St Joseph Bay falls below 3 m. South of Gulf County Canal, the worst case scenario (MOM) inundation in Port St Joe occurs mostly south of Marine Dr (First St) and west of Woodward Ave based on Fig. 79). The Mississippi Canyon landslide is responsible for the MOM inundation (see Fig. 80). The large tsunami inundation depth observed in our inundation maps could be caused by the wave enhancement by the DeSoto Canyon acting as a wave guide.

The hurricane category which best matches the tsunami inundation in this area is shown in Fig. 86 and 88. $\Delta\zeta$ for the best-match hurricane category satisfying Eq. 1 is shown in Fig. 87 and 89, respectively. The matching hurricane category distribution closely reflects that of tsunami inundation. Category 5 is dominant on St Joseph Pennisula and on the south barrier island. On Mexico Beach, similarly, there are mostly Category 5. Following south along Highway 98 (where there are residents), hurricane category reduces from 5 to 4, and eventually to 3 when entering St Joseph Bay. South of Gulf County Canal, Category 3 becomes dominant until it reaches south of W Rutherford St where it is close to the south barrier island and is covered by Category 5 (mostly) and 4 again. The difference between hurricane flooding and tsunami inundation $\Delta\zeta$ is generally within $\pm$ 0.5 m, except for Mexico Beach and GOM side of the St Joseph Pennisula and most of the Port St Joe barrier island. This negative difference means storm surge inundation depth is shallower than tsunami inundation.

Mexico Beach, FL
All Sources
SLOSH Storm Surge and MOM Tsunami Inundation Comparison

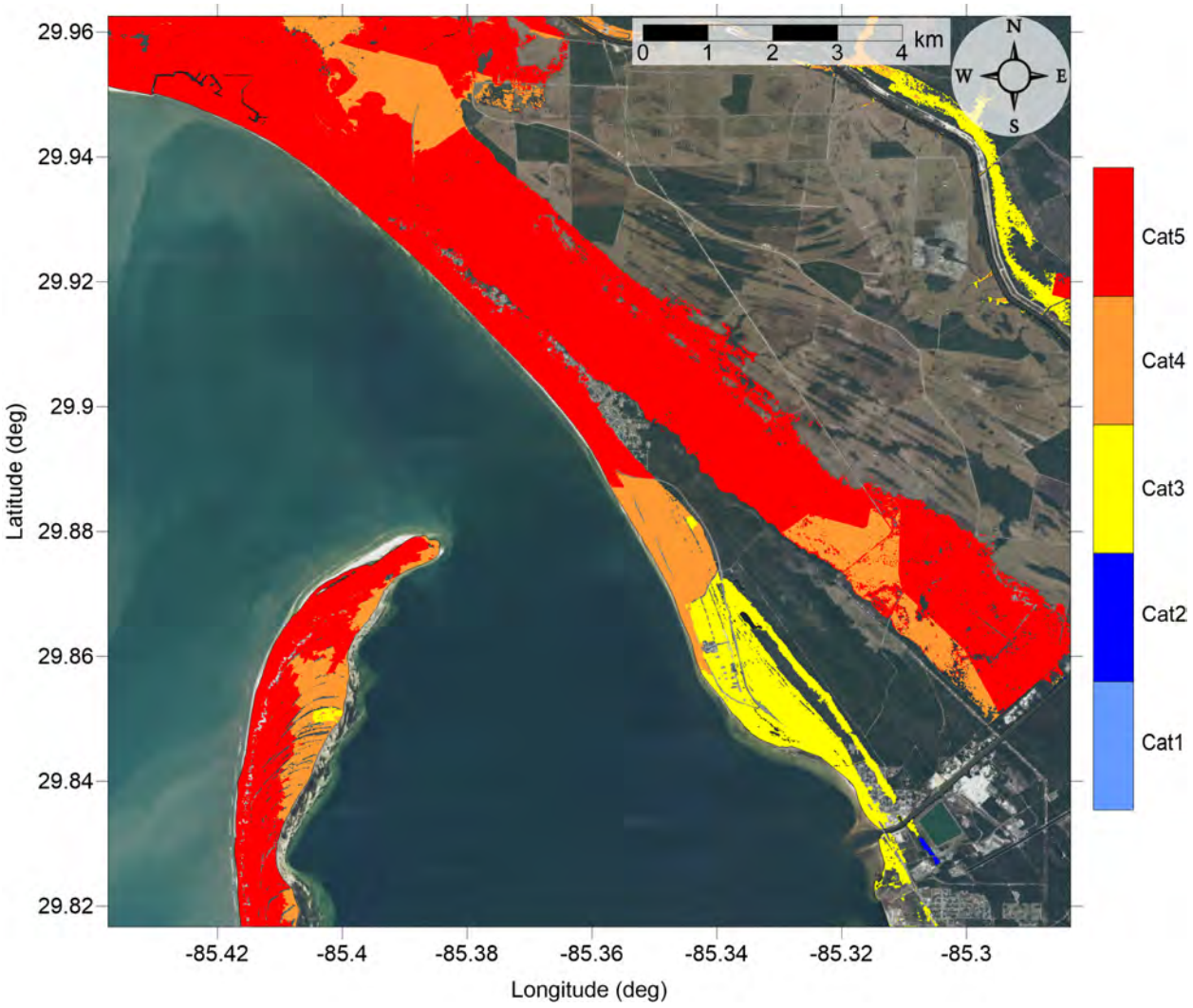

Figure 86: Hurricane category which produces inundation at high tide that best matches the MOM tsunami inundation shown in Figure **??** for Mexico Beach, FL. The contours drawn and labeled are at -5 m, -10 m, and -15 m levels.

Mexico Beach, FL
All Sources
SLOSH Storm Surge and MOM Tsunami Inundation Comparison

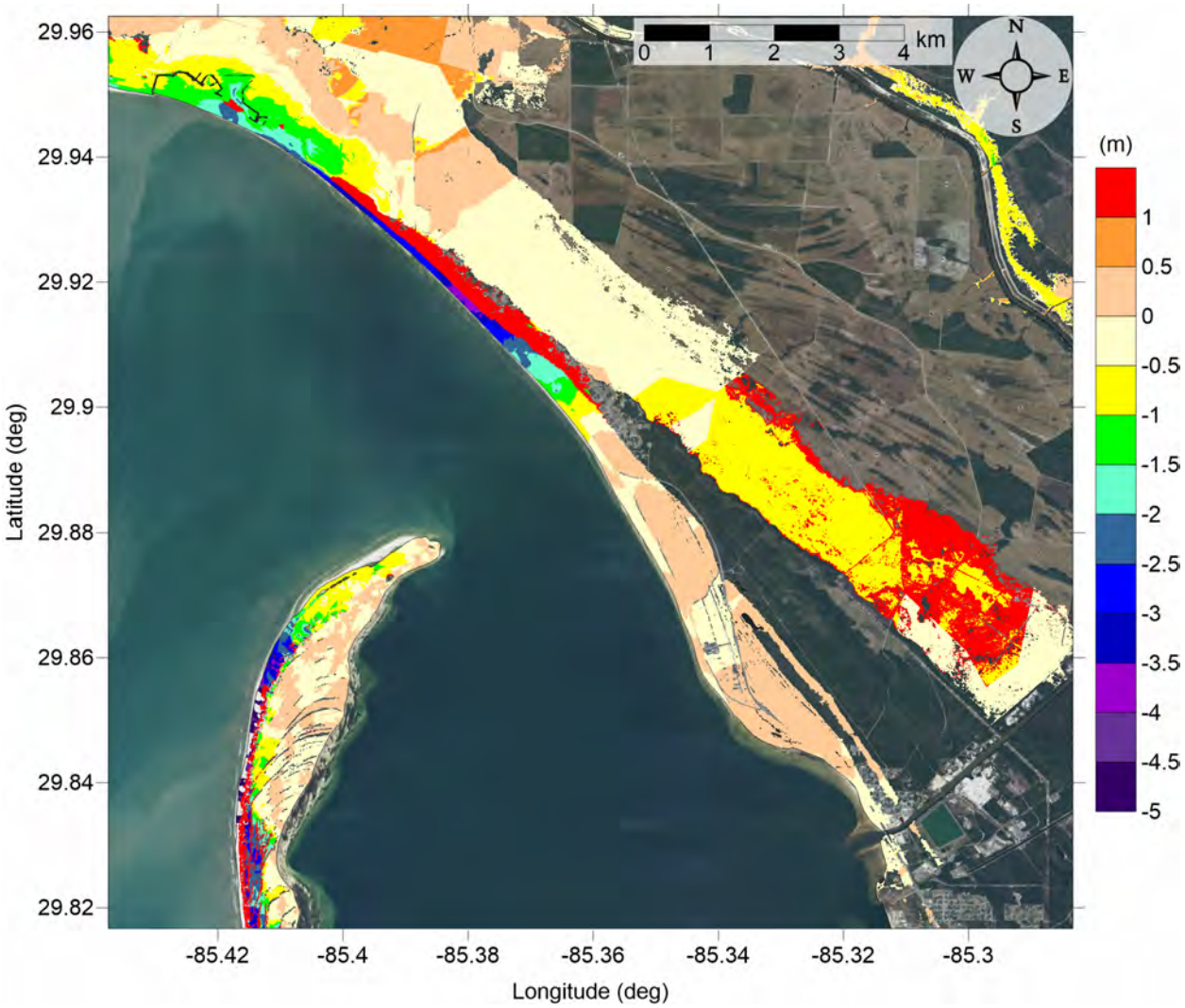

Figure 87: Actual difference $\Delta\zeta$ (in meters) between SLOSH MOM storm surge inundation and MOM tsunami inundation for the best-match hurricane category shown in Figure **??** for Mexico Beach, FL. Note that negative values indicate where tsunami inundation is higher than hurricane inundation, and pale colors indicate relatively good agreement between tsunami and storm surge inundation, i.e. $|\Delta\zeta| \leq 0.5$ m. The contours drawn and labeled are at -5 m, -10 m, and -15 m levels.

Mexico Beach, FL
All Sources
SLOSH Storm Surge and MOM Tsunami Inundation Comparison

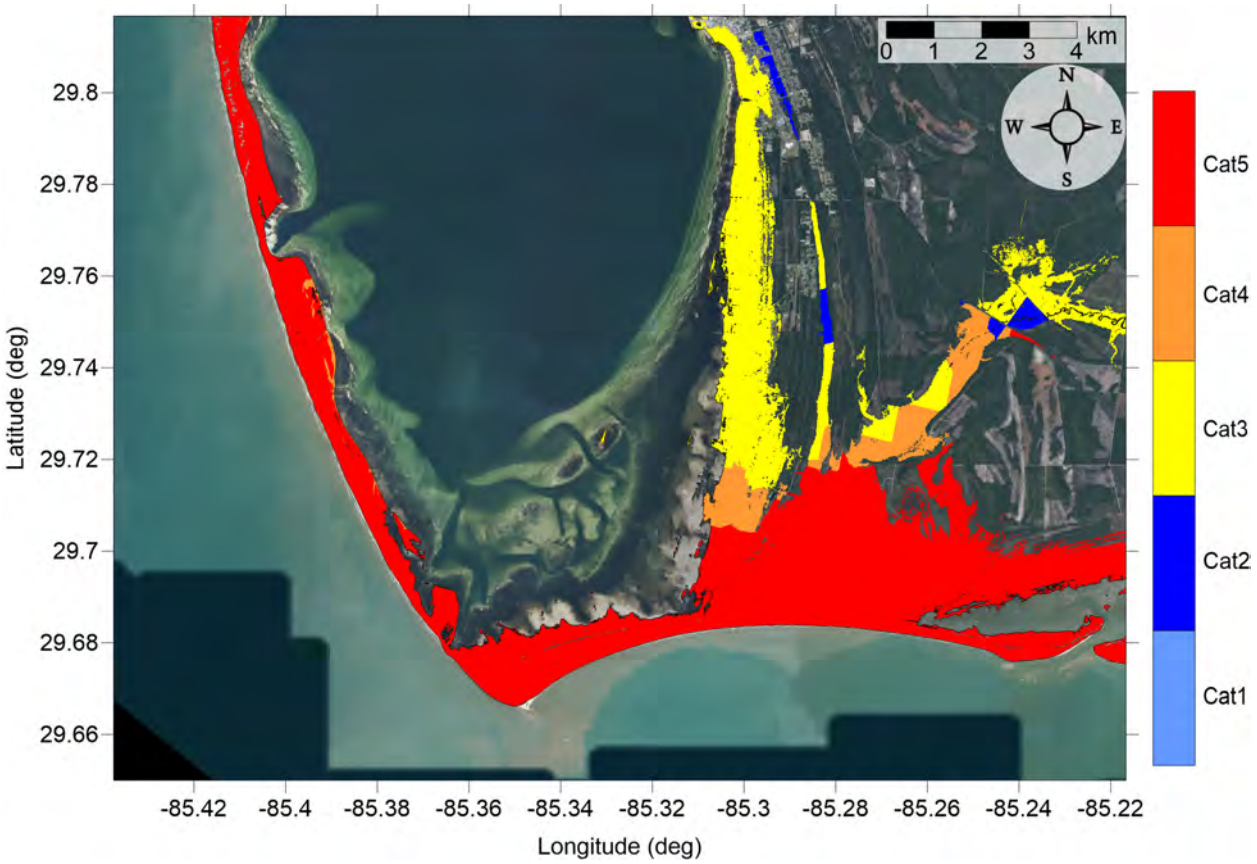

Figure 88: Hurricane category which produces inundation at high tide that best matches the MOM tsunami inundation shown in Figure **??** for Port St Joe, FL. The contours drawn and labeled are at -5 m, -10 m, and -15 m levels.

Mexico Beach, FL
All Sources
SLOSH Storm Surge and MOM Tsunami Inundation Comparison

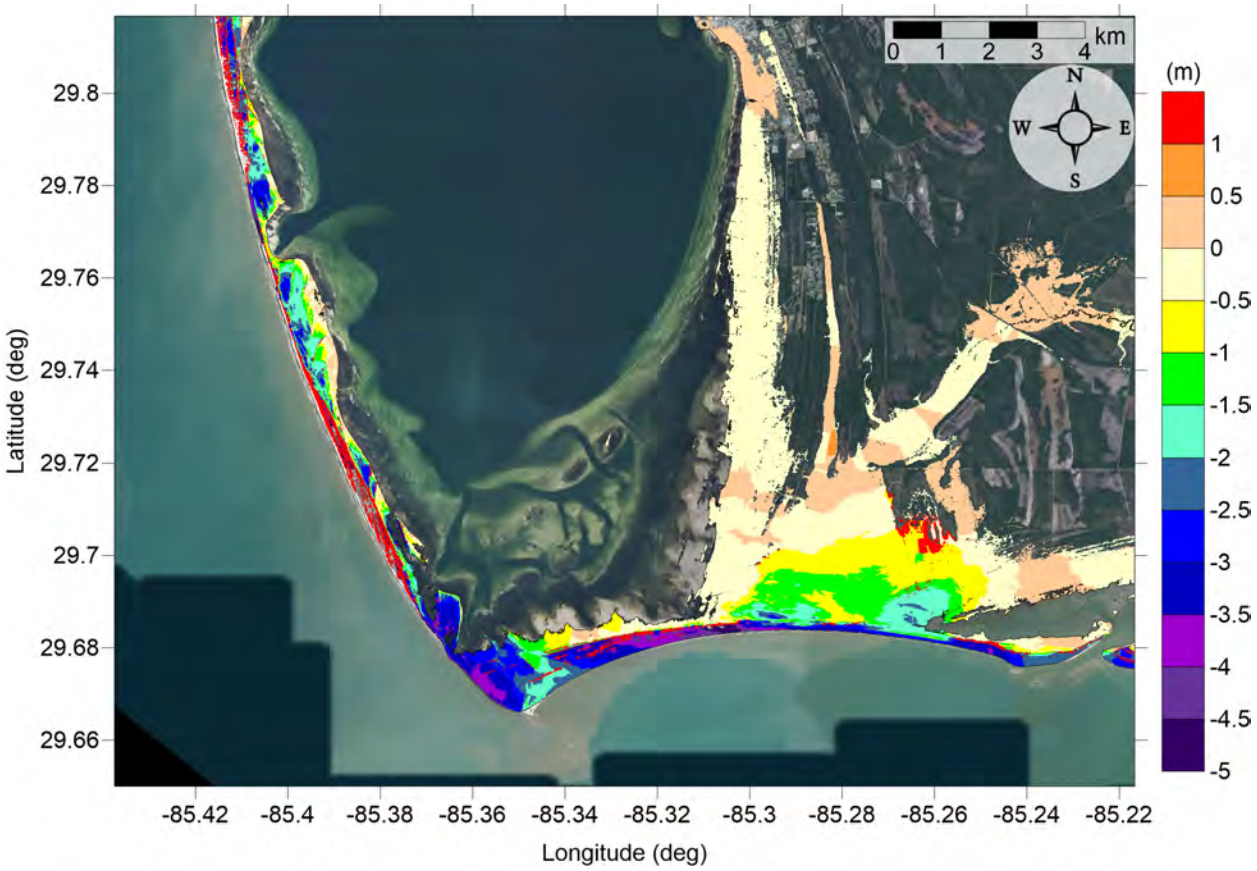

Figure 89: Actual difference $\Delta\zeta$ (in meters) between SLOSH MOM storm surge inundation and MOM tsunami inundation for the best-match hurricane category shown in Figure **??** for Port St Joe, FL. Note that negative values indicate where tsunami inundation is higher than hurricane inundation, and pale colors indicate relatively good agreement between tsunami and storm surge inundation, i.e. $|\Delta\zeta| \leq 0.5$ m. The contours drawn and labeled are at -5 m, -10 m, and -15 m levels.

6 Tsunami Maritime Products

Accurate estimates of tsunami wave amplitude do not necessarily equate to the prediction of localized damaging currents in a basin or harbor [Lynett et al., 2012]. Furthermore, damage potential in ports is strongly related to the current speed. Therefore, tsunami hazard mitigation products need to be advanced to predict damage potential in basins or harbors. Past tsunamis have shown that the maritime community requires additional information and guidance about tsunami hazards and post-tsunami recovery [Wilson et al., 2012, 2013]. To accomplish mapping and modeling activities to meet NTHMP's planning/response purposes for the maritime community and port emergency management and other customer requirements, it is necessary to continue the process to include maritime products in our current inundation map development. These maritime products will help identify impact specifically on ship channels, bay inlets, harbors, marinas, and oil infrastructures (e.g., designated lightering and oil tanker waiting zones).

In this study, Orange Beach, AL and Mexico Beach, FL are added to the maritime portfolio, where tsunami hazard maritime products such as tsunami current magnitude, vorticity, safe/hazard zones are generated.

Lynett et al. [2014] complied a general relationship between tsunami current speed and harbor damage based on observational data, in which the current speed is divided into four ranges of damaging potential, 0 - 3 knots means unharmful currents, 3 - 6 knots corresponds to minor-to-moderate damage, 6 - 9 knots moderate-to-major damage, and over 9 knots extreme damage. Since the extent of damage is very location-dependent, to make the text concise, we associate 0 - 3 knots to unharmful currents, 3 - 6 knots to minor damage, 6 - 9 knots to moderate damage, and finally over 9 knots to major damage. The four levels are denoted with white, blue, yellow and red colors, respectively, for all the velocity contour plots within our velocity maritime products.

Using this damage-to-speed relationship, we have plotted the maximum of maximum depth-averaged velocity for each computational subdomain of the two new communities. Fig. 90 shows the minimum offshore safe depth (approximately 200 m or 100 fathoms), and the maximum of maximum velocity magnitude contour plot across the entire Gulf of Mexico (15 arcsecond resolution) for all landslide scenarios (Eastbreaks, PSL-A, PSL-B1, PSL-B2, Mississippi Canyon, PSL-C, West Florida, Yucatán #3 and Yucatán #5). Potential damaging currents ($>$ 3 knots, blue, yellow and red areas) tend to be present in most of the area shallower than the minimum offshore safe depth. However, damaging currents could reach areas deeper than 200 m close to most of the landslide generation regions. Major damaging currents ($>$ 9 knots, red) can be expected in most of the landslide generation regions, in the continental shelf adjacent to Mississippi Canyon, offshore northwest Florida, and Yucatán shelf. Moderate ($>$ 6 knots and $<$ 9 knots, yellow) damaging current areas are scattered over the continental shelf, but mostly close to areas with major damage currents.

All locations
All Sources
Maximum of Maximum Velocity Magnitude

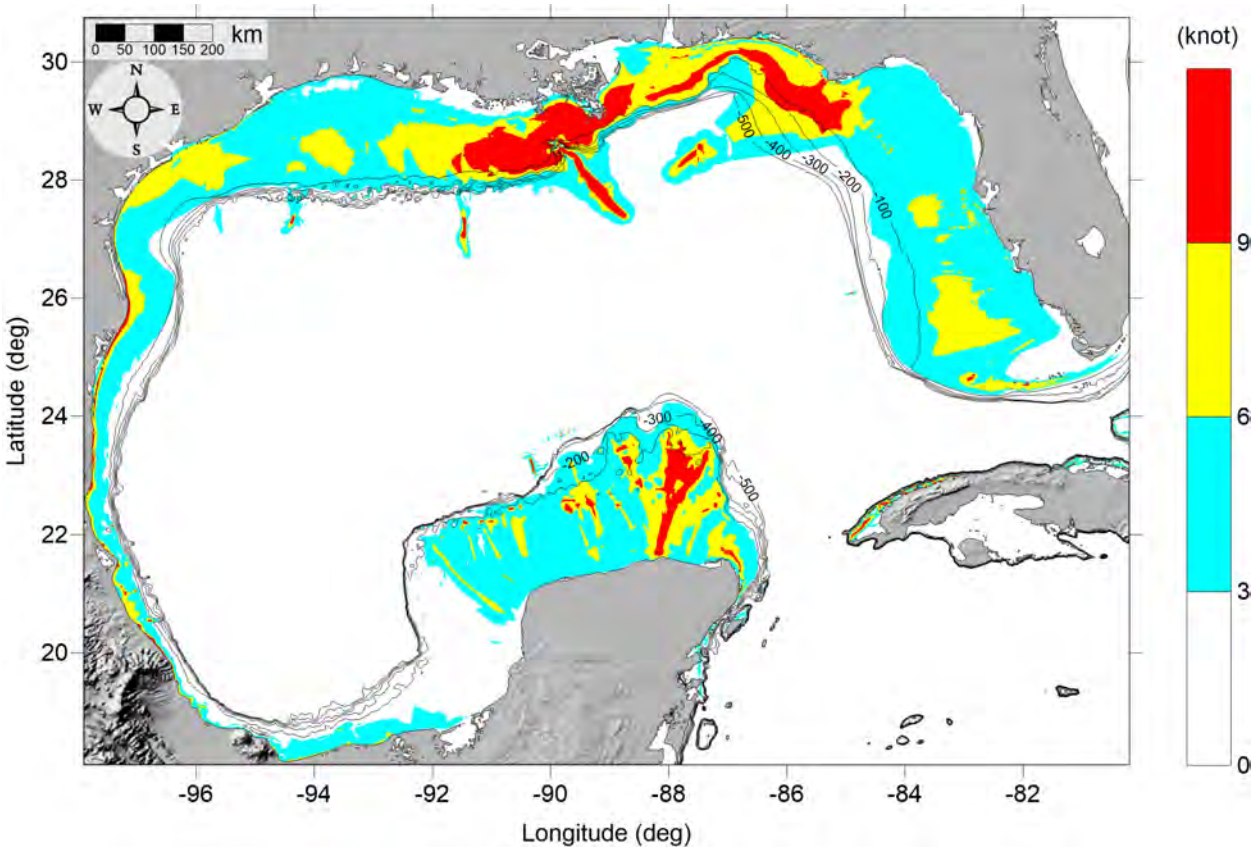

Figure 90: Maximum of maximum velocity magnitude contour in GOM for all landslide scenarios and all locations.

The MOM velocity magnitude (damaging potential) contour maps and the MOM vorticity magnitude contour maps for the finer computational subdomains of Orange Beach, AL and Mexico Beach, FL are presented from Fig. 91 to Fig. 104.

Fig. 93 and Fig. 94 shows the MOM velocity magnitude contour plot result for the Orange Beach area. Most of offshore region is expected to have moderate damaging currents, with major damaging currents occurring along the coastline, inlets, and the immediate bay side of the barrier island. There is generally no moderate damaging currents farther behind the barrier islands, however, the exception is the Little Lagoon where it is filled with moderate and major damaging currents (over 6 knots). In Mexico Beach, FL mapping region (Mexico Beach and Port St Joe), the situation is a bit different from Orange Beach, AL. In general, the worst case (MOM) tsunami currents are more severe; major damaging current is more prevalous across the GOM and around St Joseph Pennisula (Fig. 92). Behind the pennisula, St Joseph Bay sees much calmer tsunami current velocities (< 6 knots) except for the small region adjacent to the pennisula. The exposed Mexico Beach and Saint Joe Beach should expect major damaging currents along the beach.

For both Orange Beach, AL and Mexico Beach, FL, vorticity distribution displays similar patterns to their velocity distribution, where high vorticity appears around the barrier island, and are more intense near the bay entrances.

6.1 Orange Beach, AL

Orange Beach, FL
All Sources
Maximum of Maximum Velocity Magnitude

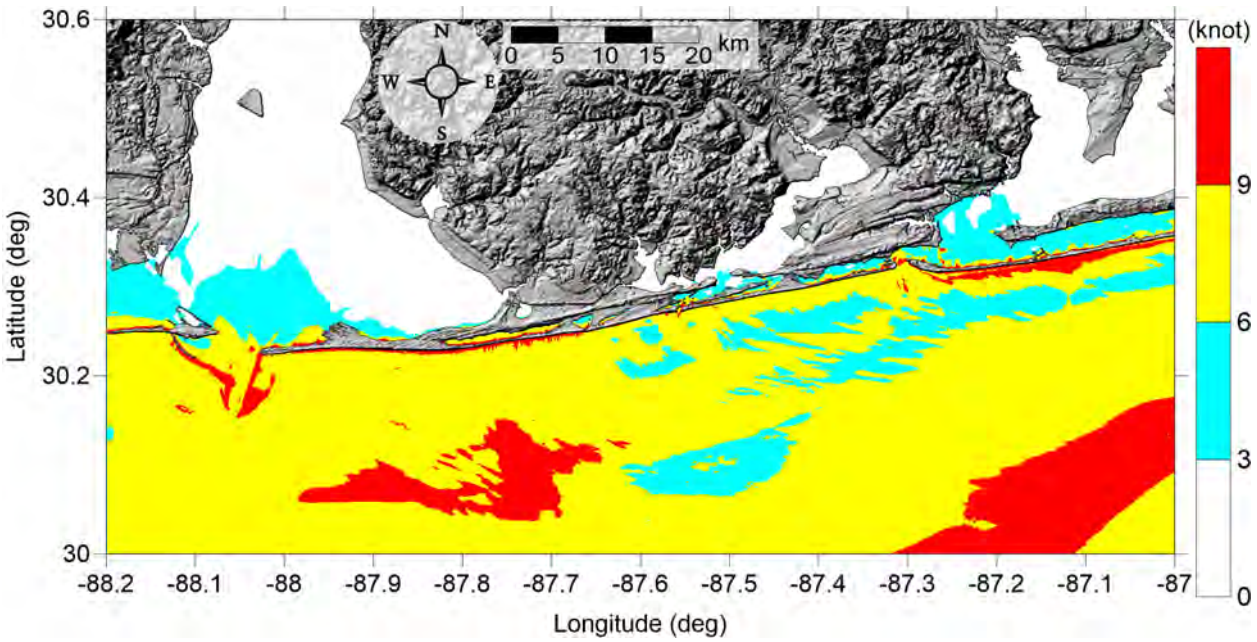

Figure 91: Maximum of maximum velocity magnitude contour in Orange Beach, FL (Grid 2 - 3 arcsecond) for all landslide scenarios.

Orange Beach, FL
All Sources
Maximum of Maximum Velocity Magnitude

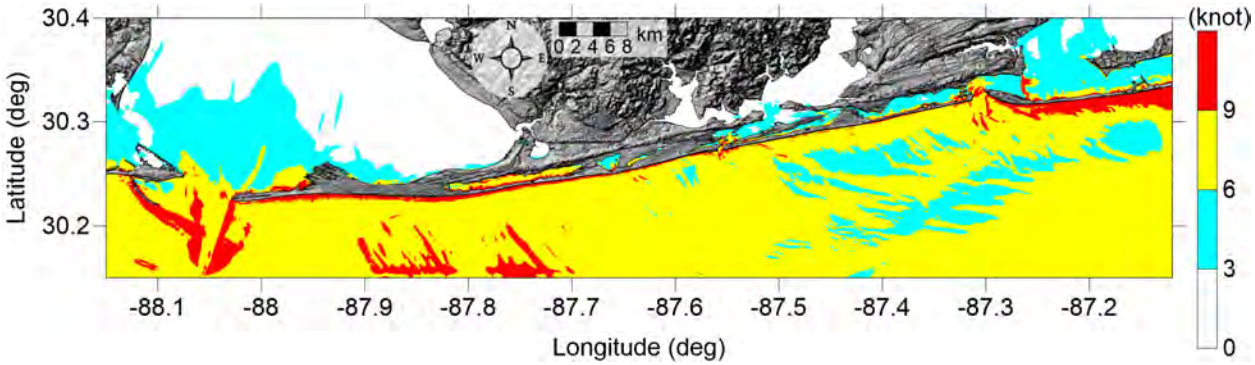

Figure 92: Maximum of maximum velocity magnitude contour in Orange Beach, FL (Grid 3 - 1 arcsecond) for all landslide scenarios.

Orange Beach, FL
All Sources
Maximum of Maximum Velocity Magnitude

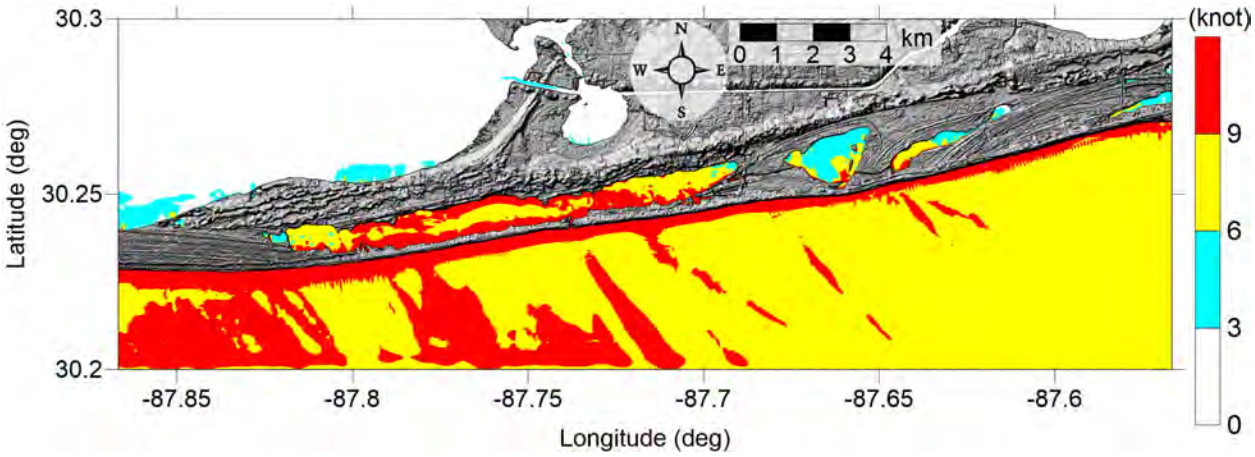

Figure 93: Maximum of maximum velocity magnitude contour in Gulf Shores, AL (Grid 4 - 1/3 arcsecond) for all landslide scenarios.

Orange Beach, FL
All Sources
Maximum of Maximum Velocity Magnitude

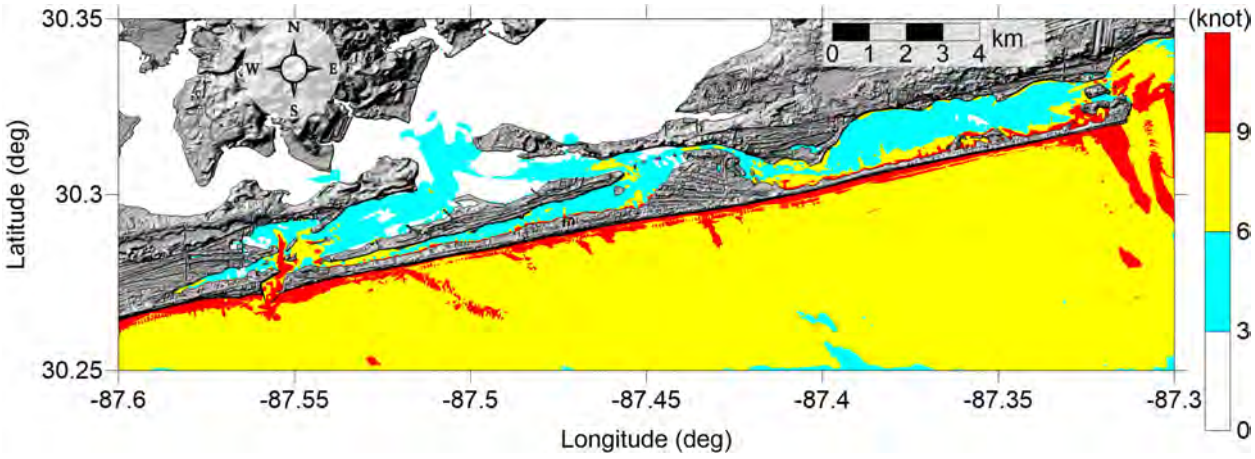

Figure 94: Maximum of maximum velocity magnitude contour in Orange Beach, FL (Grid 5 - 1/3 arcsecond) for all landslide scenarios.

Orange Beach, FL
All Sources
Maximum of Maximum Vorticity Magnitude

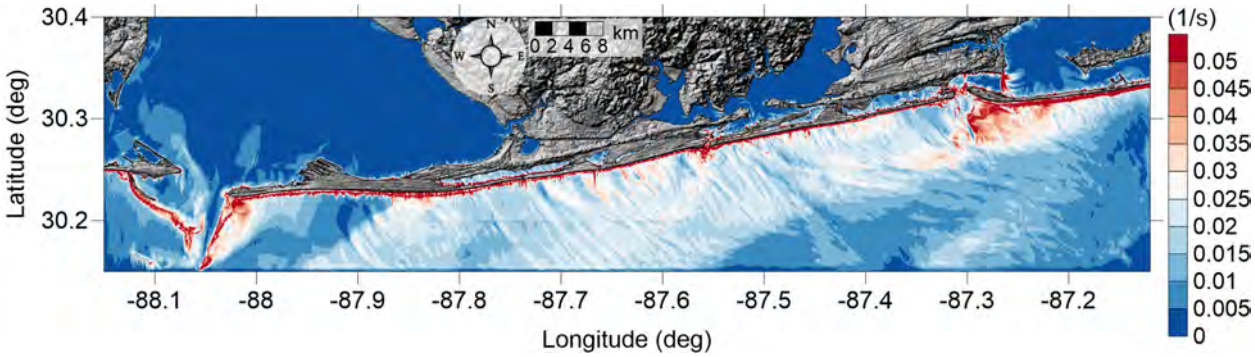

Figure 95: Maximum of maximum vorticity magnitude contour in Orange Beach, FL Grid 3 (1 arcsecond) for all landslide scenarios.

Orange Beach, FL
All Sources
Maximum of Maximum Vorticity Magnitude

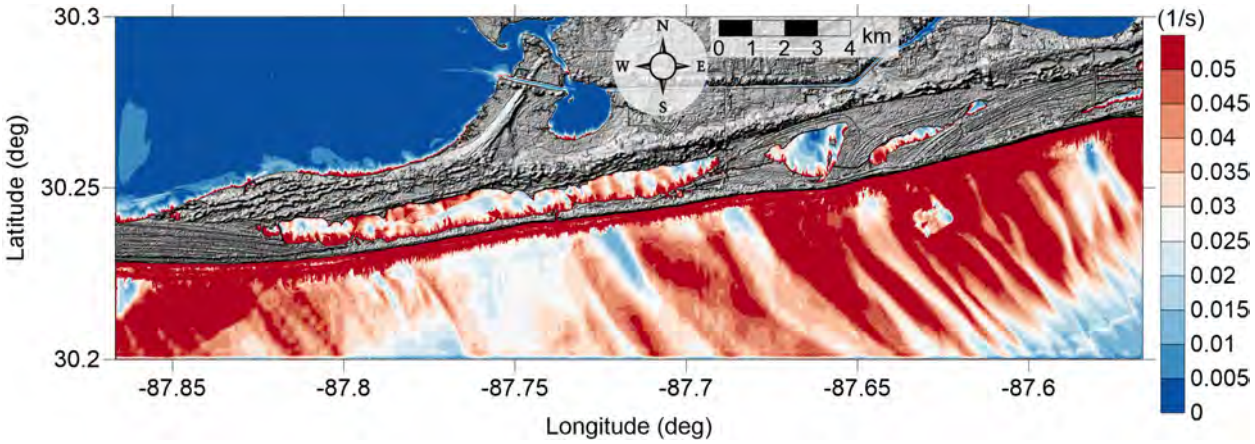

Figure 96: Maximum of maximum vorticity magnitude contour in Gulf Shores, AL Grid 4 (1/3 arcsecond) for all landslide scenarios.

Orange Beach, FL
All Sources
Maximum of Maximum Vorticity Magnitude

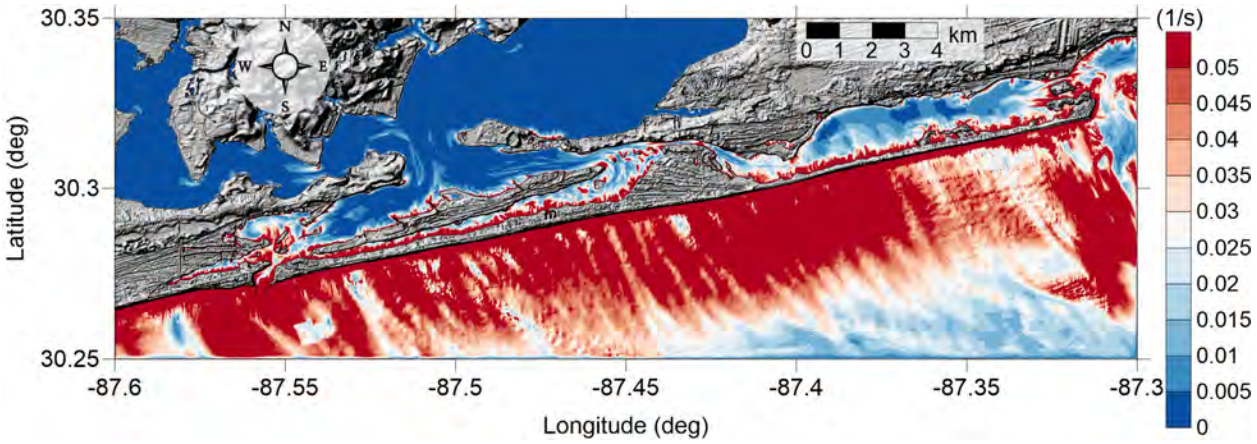

Figure 97: Maximum of maximum vorticity magnitude contour in Orange Beach, FL Grid 5 (1/3 arcsecond) for all landslide scenarios.

6.2 Mexico Beach, FL

Mexico Beach, FL
All Sources
Maximum of Maximum Velocity Magnitude

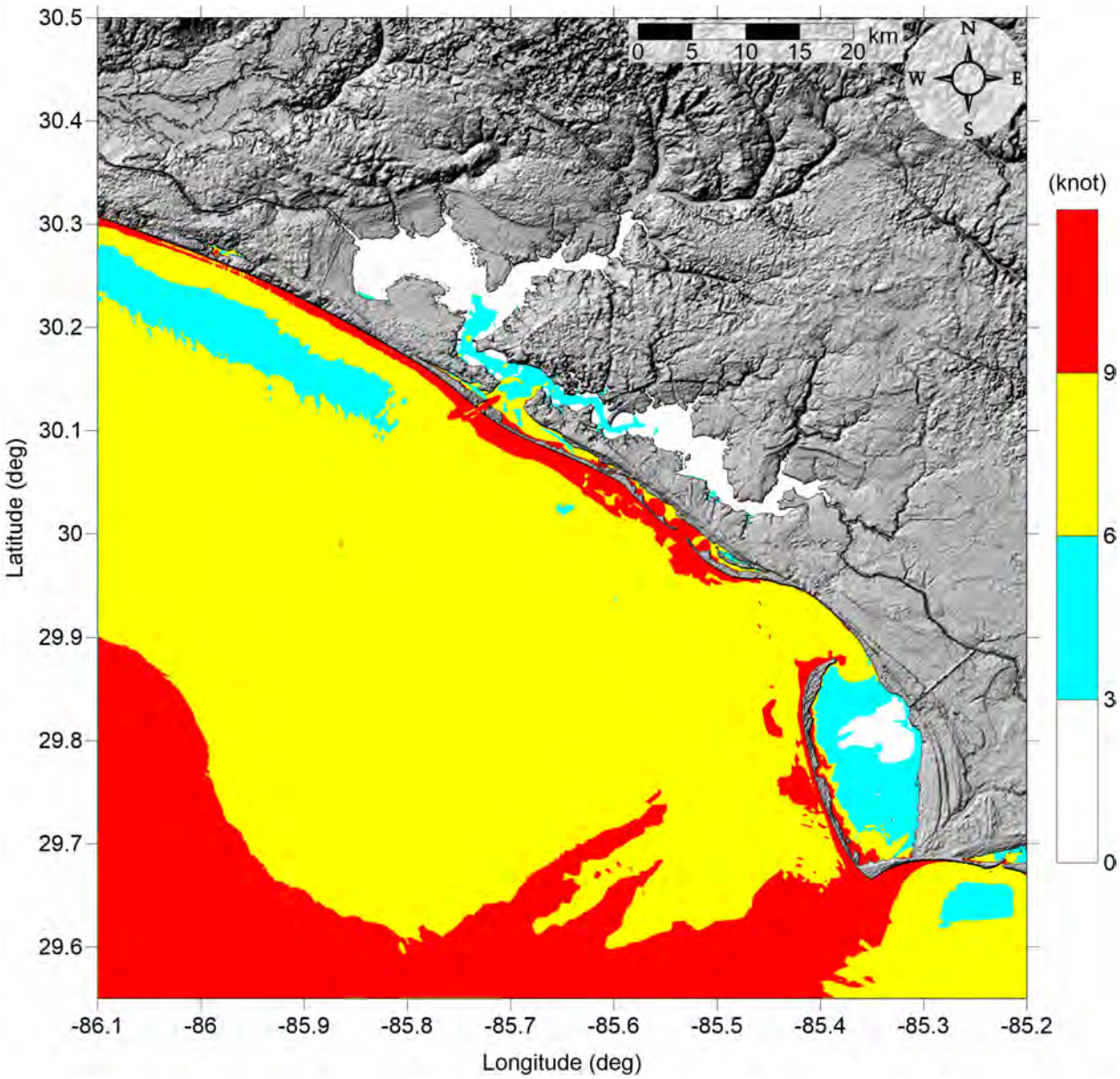

Figure 98: Maximum of maximum velocity magnitude contour in Mexico Beach, FL (Grid 2 - 3 arcsecond) for all landslide scenarios.

Mexico Beach, FL
All Sources
Maximum of Maximum Velocity Magnitude

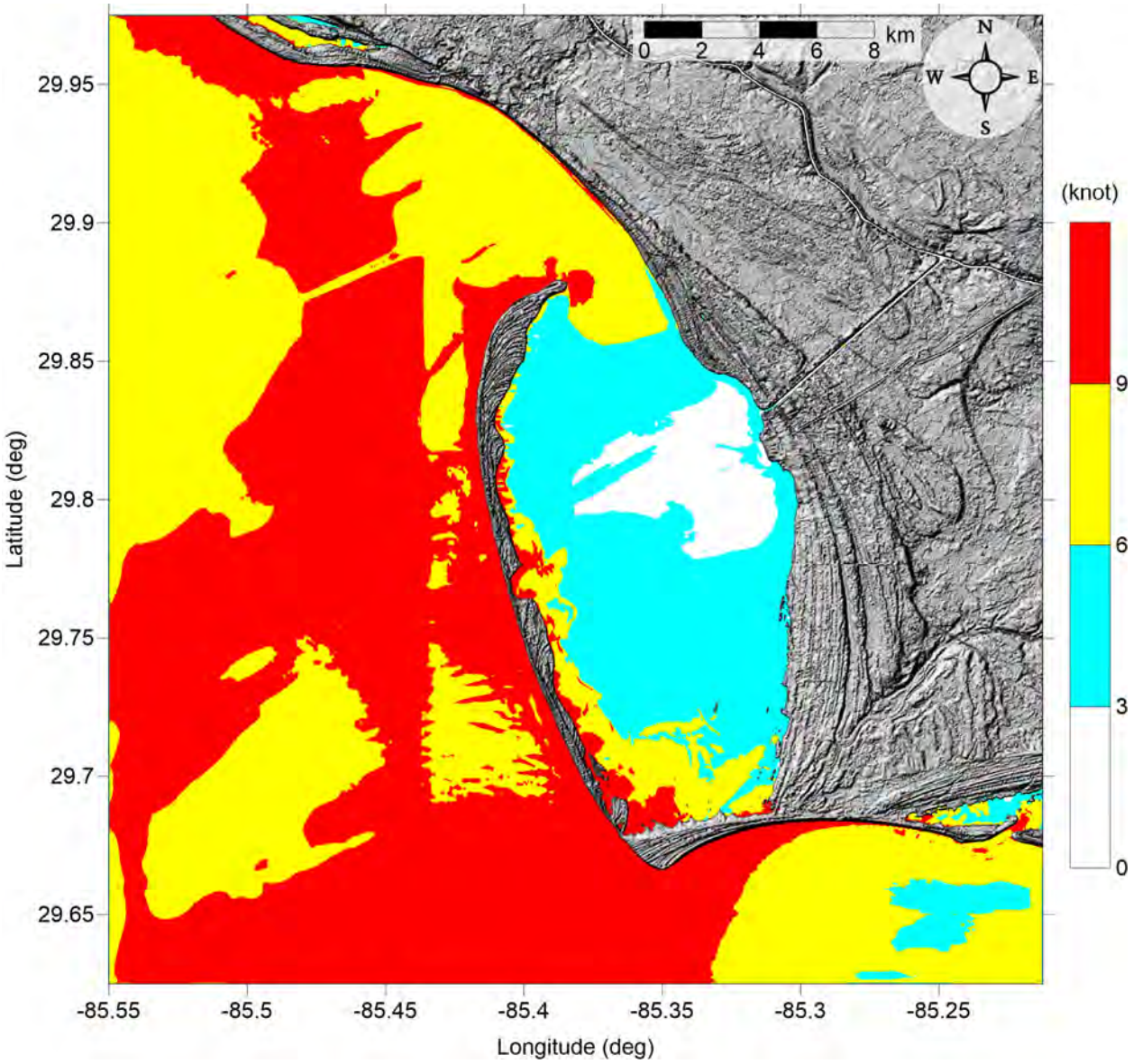

Figure 99: Maximum of maximum velocity magnitude contour in Mexico Beach, FL (Grid 3 - 1 arcsecond) for all landslide scenarios.

Mexico Beach, FL
All Sources
Maximum of Maximum Velocity Magnitude

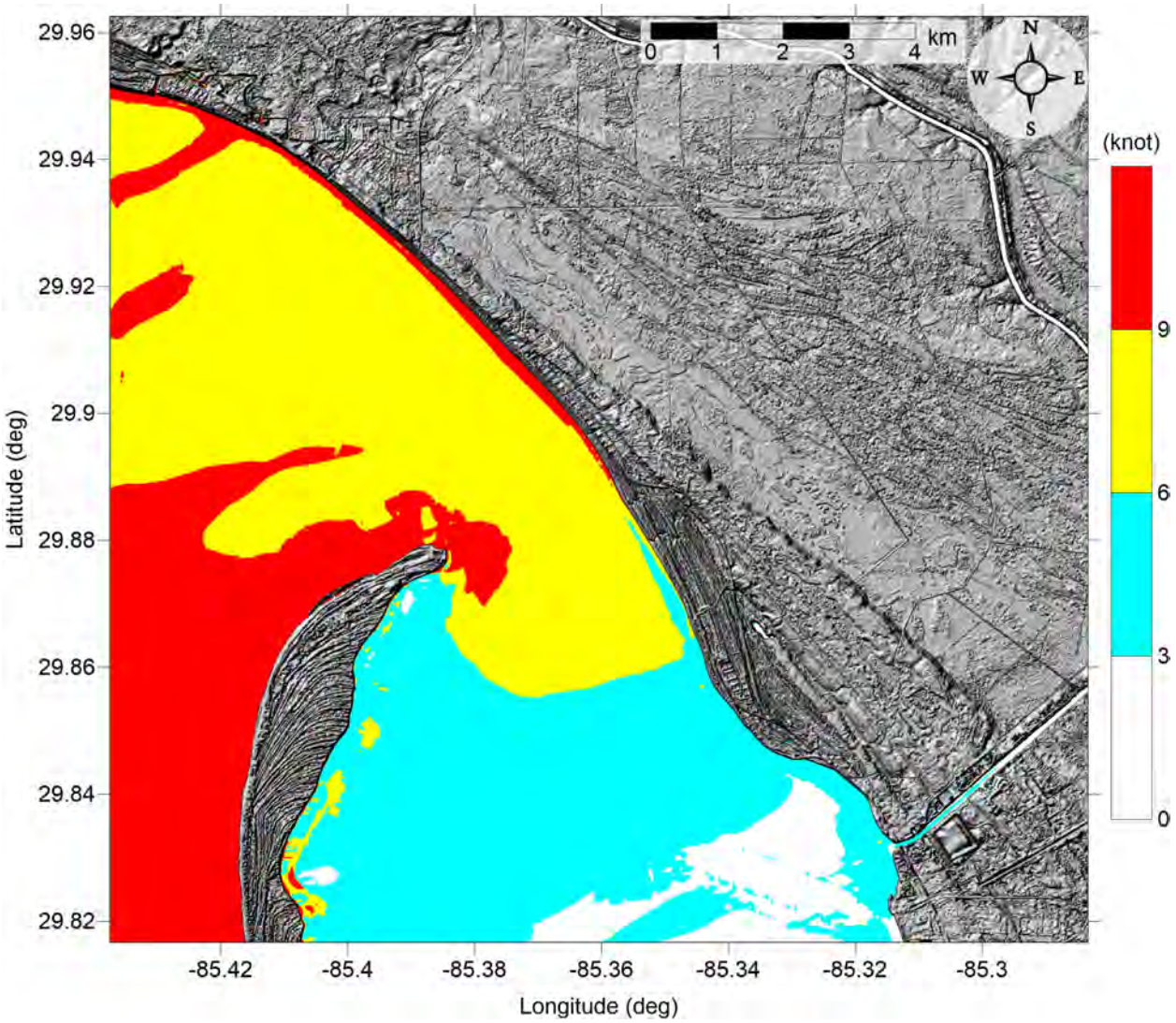

Figure 100: Maximum of maximum velocity magnitude contour in Mexico Beach, FL (Grid 4 - 1/3 arcsecond) for all landslide scenarios.

Mexico Beach, FL
All Sources
Maximum of Maximum Velocity Magnitude

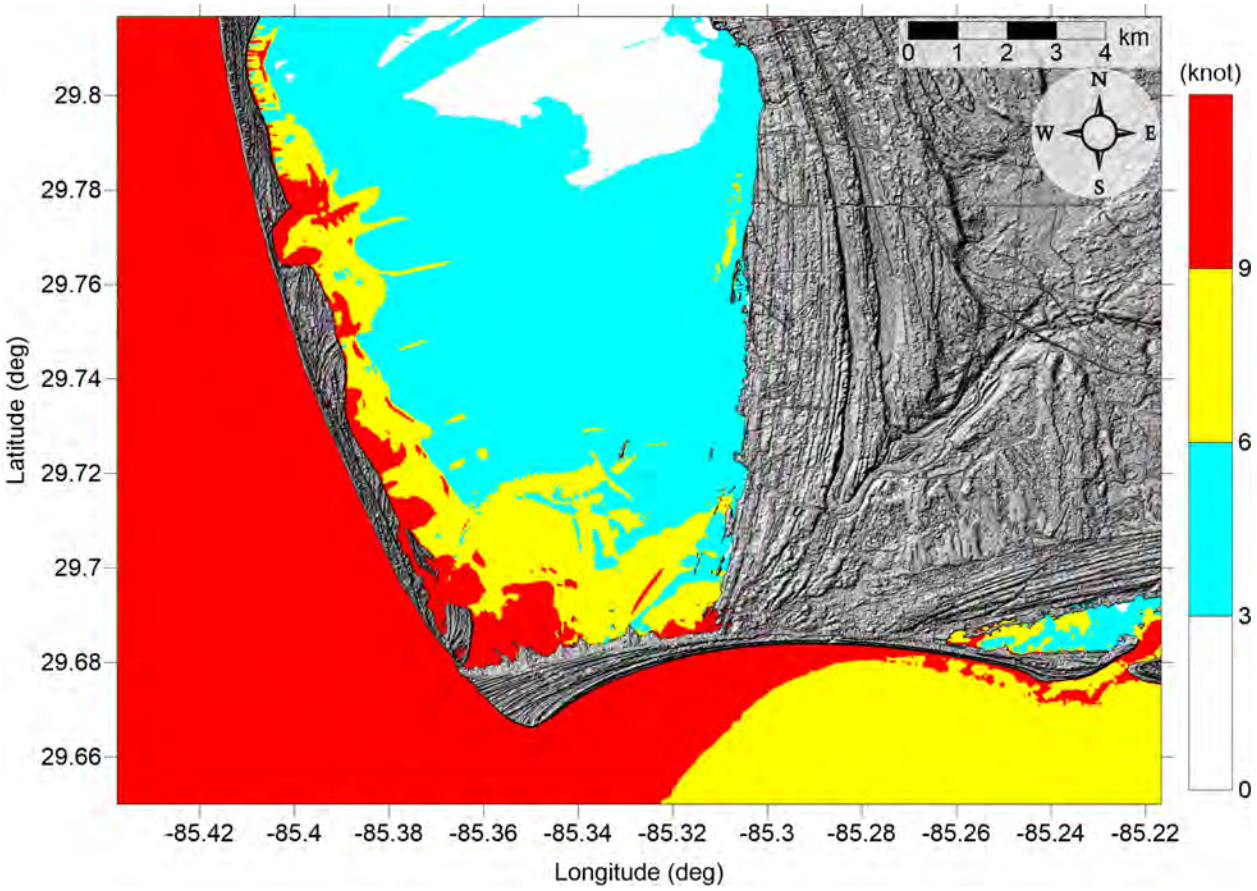

Figure 101: Maximum of maximum velocity magnitude contour in Port St. Joe, FL (Grid 5 - 1/3 arcsecond) for all landslide scenarios.

Mexico Beach, FL
All Sources
Maximum of Maximum Vorticity Magnitude

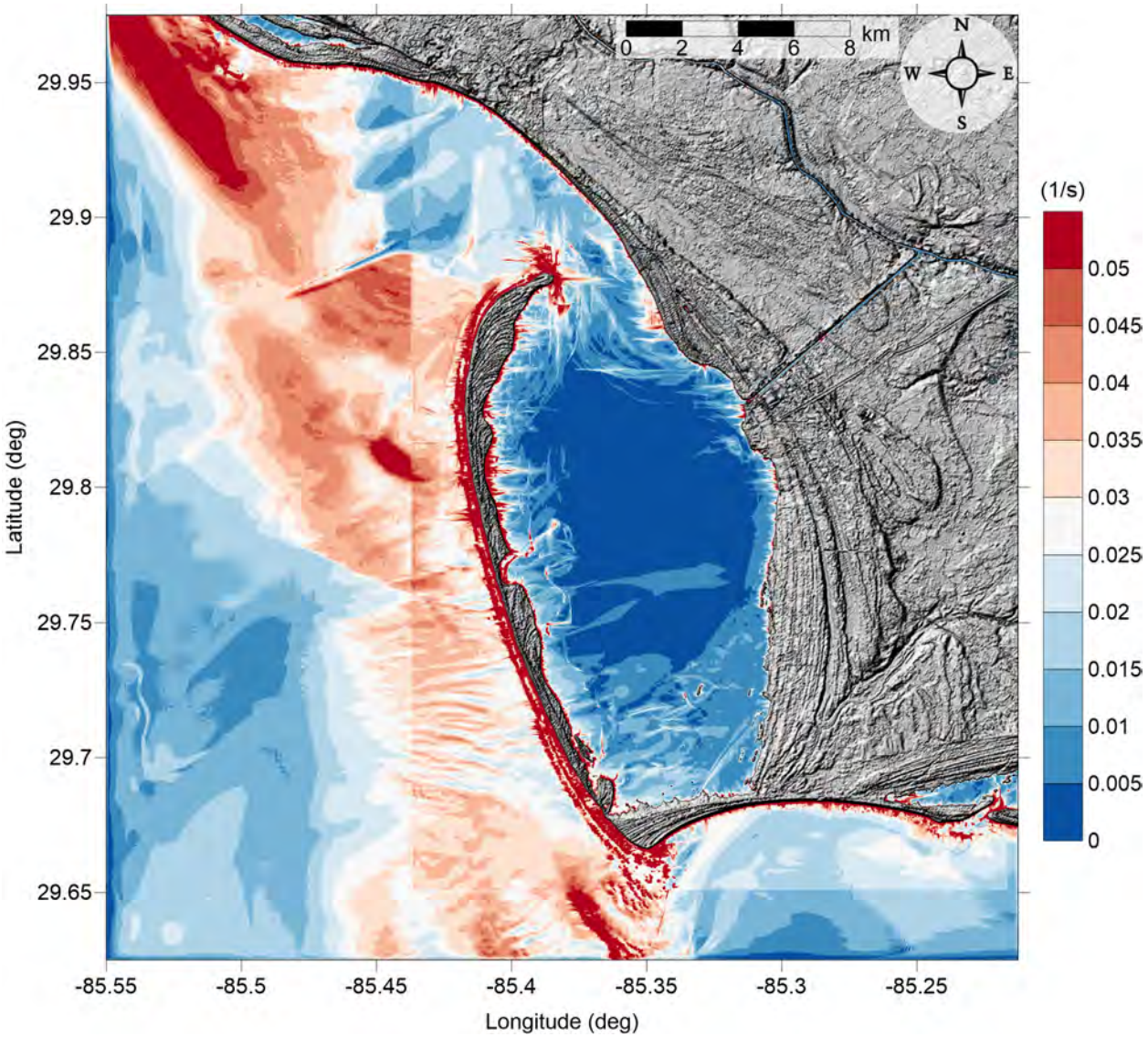

Figure 102: Maximum of maximum vorticity magnitude contour in Mexico Beach, FL Grid 3 (1 arcsecond) for all landslide scenarios.

Mexico Beach, FL
All Sources
Maximum of Maximum Vorticity Magnitude

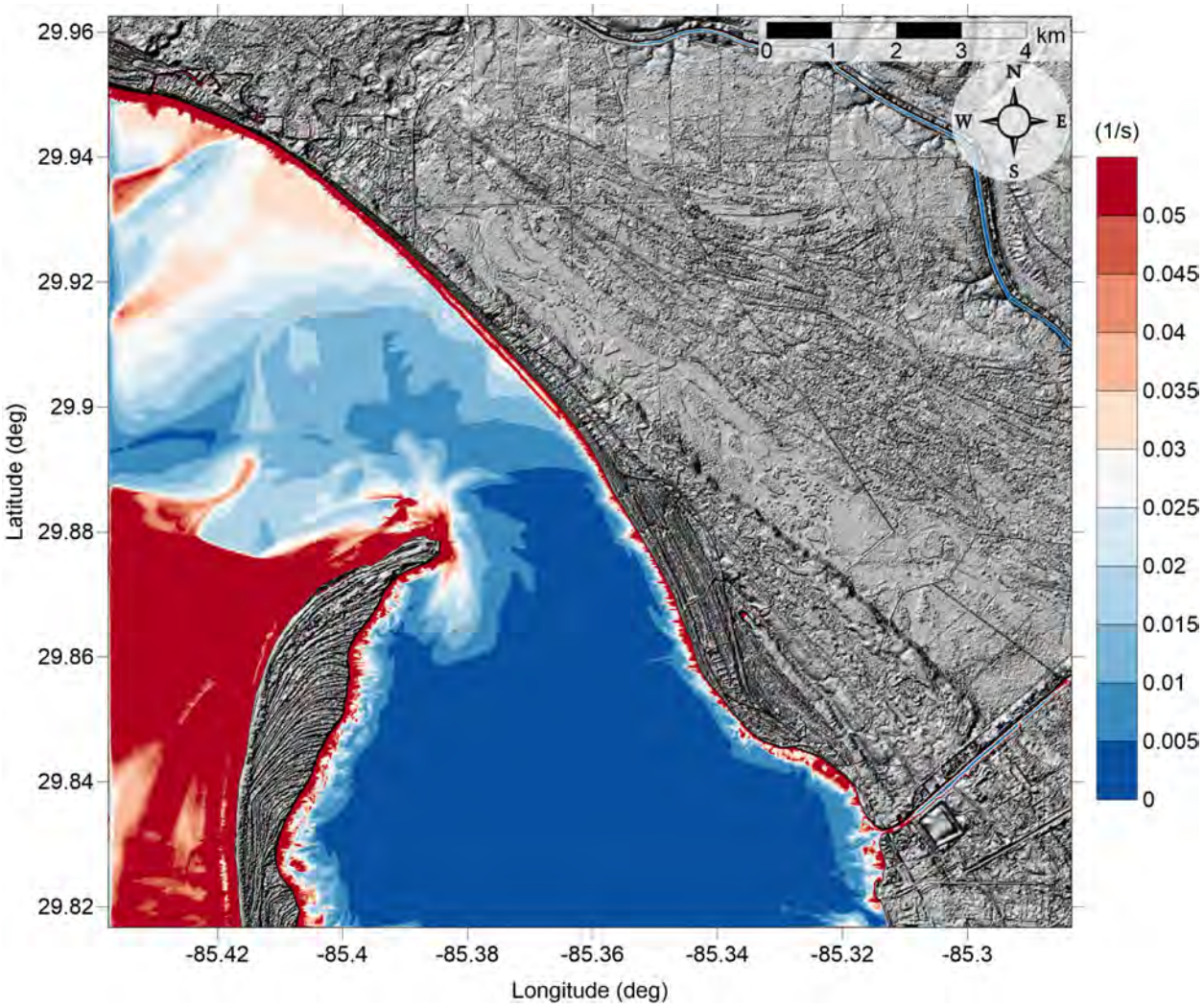

Figure 103: Maximum of maximum vorticity magnitude contour in Mexico Beach, FL Grid 4 (1/3 arcsecond) for all landslide scenarios.

Mexico Beach, FL
All Sources
Maximum of Maximum Vorticity Magnitude

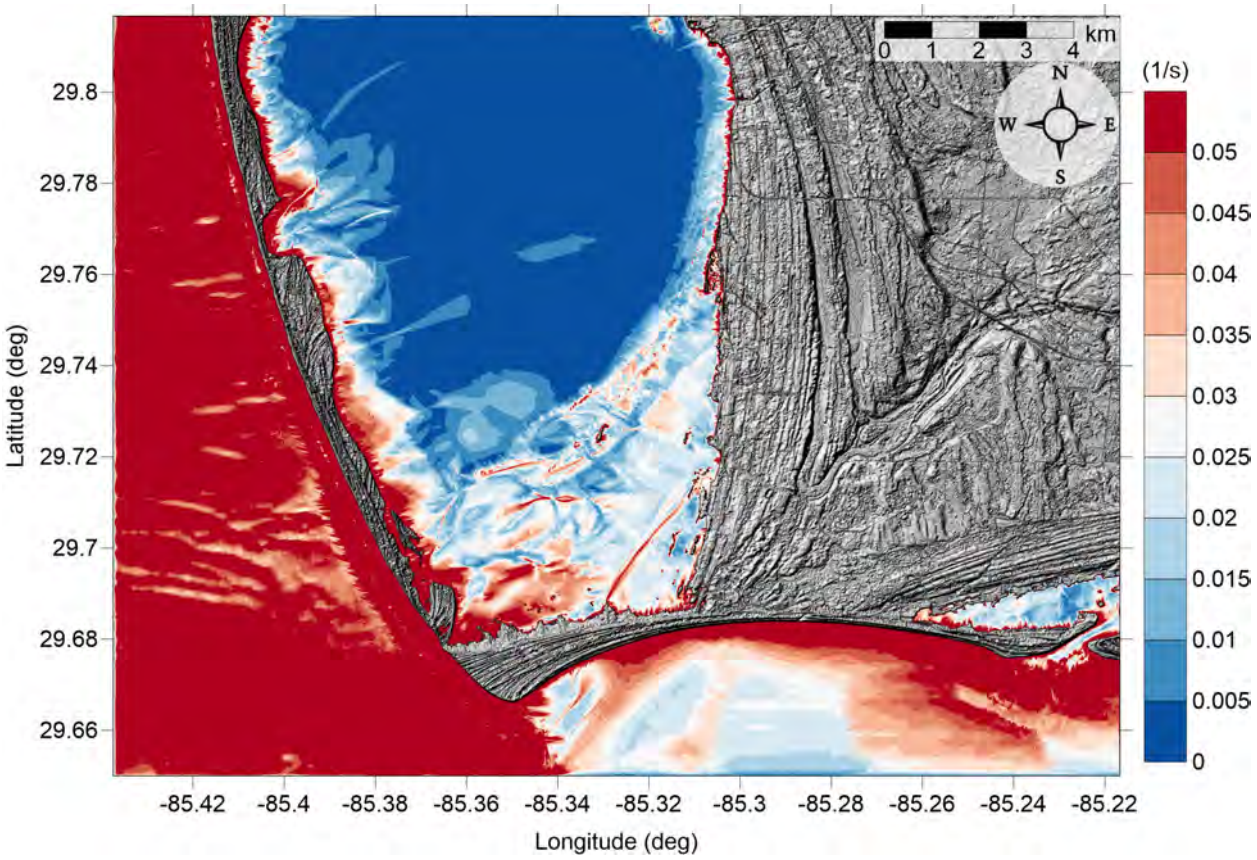

Figure 104: Maximum of maximum vorticity magnitude contour in Port St. Joe, FL Grid 5 (1/3 arcsecond) for all landslide scenarios.

7 Meteosunami Hazard Analysis in Northwestern and Northeastern GOM

Although relatively rare, meteotsunamis are capable of causing coastal infrastructure damage and casualties. Analyses of water level and meteorological data in the U.S. show that meteotsunamis occur more frequently than expected, and therefore, it is important to include meteotsunami assessment in coastal hazard mitigation efforts.

In previous studies, we conducted numerical experiments to investigate the generation and propagation of meteotsunami waves and assessed hazards on a broad scale in the northwestern Gulf of Mexico (GOM) [Horrillo et al., 2021], as well as northeastern GOM [Cheng et al., 2021, Horrillo et al., 2020]. The numerical experiments used a simple 2D depth-averaged hydrostatic shallow water model forced by an idealized atmospheric pressure disturbance on a set of trajectories and directions covering the whole) GOM shelf. The disturbance parameters are based on a 2010 event that generated strong meteotsunami along the Florida GOM coast.

In those previous numerical experiments, for each subregion (northeastern or northwestern GOM), we conducted 1260 runs (i.e., 12 incident wave directions $\times$ 15 trajectories $\times$ 7 velocities). Using a numerical model based on CPU and parallelized by OpenMP, we were able to finish each 30h run on a 1 arcminute grid in around 5 to 6 minutes, thereby finishing the whole 1260 runs within one week. However, we couldn't use the more accurate 15 arcsecond resolution grid due to each run taking several hours. In this project, we converted our CPU meteotsunami code to CUDA, and with the help of a newly built multi-GPU workstation which has three Nvidia RTX 3090 GPUs that is capable of running our meteotsunami Fortran code in CUDA 50 – 100 times faster than the CPU version, depending on the grid, we expanded the previous parameter study to 17280 runs (i.e., 36 incident wave directions $\times$ 30 trajectories $\times$ 16 velocities) for each subregion. The result is a significantly improved resolution of different incident wave direction, forward speed and trajectory position, and their effect on maximum gauge water elevation across the whole GOM.

7.1 Introduction

Meteotsunamis are long waves having meteorological origins such as atmospheric gravity waves, frontal passages, squalls, and storms, which typically exhibit large pressure and/or wind-stress gradient [Monserrat et al., 2006a]. Similar to ordinary tsunamis, i.e. those generated by earthquakes or landslides, meteotsunamis have periods from a few minutes to 2-3 hours. Meteotsunamis cannot be distinguished from ordinary tsunamis in terms of coastal transformation and amplification within bays and harbors [Rabinovich and Monserrat, 1996], however, they differ in that meteotsunami wave generation requires resonant coupling between the atmospheric disturbance and the shelf, otherwise sea level fluctuations would be on the order of a few centimeters solely due to the inverse barometric effects. The resonance mechanisms have been thoroughly studied, including the Proudman resonance [Proudman, 1929], Greenspan resonance [Greenspan, 1956], and shelf resonance [Monserrat et al., 2006a]. Proudman resonance occurs when the pressure disturbance forward speed matches the lo-

cal shallow water wave celerity, ideally traveling over a long distance, which is analogous to tsunamis generated by landslides [Monserrat et al., 2006a]. In addition to the resonant coupling between the air disturbance and shelf, the generated meteotsunami could be further enhanced by shoaling effects and local harbor resonance.

Meteotsunami events have been reported to occur in oceans around the globe. The most prominent places include Mediterranean Sea, for example the Adriatic Sea and Balearic Sea; Nagasaki Bay, Japan and Longkou, China; in North America, the Great Lakes and the Atlantic coasts [Monserrat et al., 2006a, Vilibić et al., 2014b, Pattiaratchi and Wijeratne, 2015]. Although meteotsunamis cannot reach the level of destruction of seismic tsunamis [Pattiaratchi and Wijeratne, 2015], their damaging potential should not be ignored. Regarding the GOM, there have been several documented meteotsunami events in recent decades with wave height close to or over 1 m [Rabinovich, 2020]. On March 25, 1995, eye witnesses at Tampa Bay, Florida reported a solitary wave up to 3 m high moving southeastward followed by a line of clouds 15 min later that was generated by a large-amplitude atmospheric gravity wave [Paxton and Sobien, 1998]. On March 28, 2014, Panama City saw a sea level rise of 1.3 m. The meteotsunami wave was reported across the northwestern GOM from New Canal, Louisiana to Naples, Florida, which was caused by a squall-line initially traveling eastward along the coastline and thus moving in-phase with the wave [Olabarrieta et al., 2017]. A sharp drop in barometric pressure accompanying a south-moving frontal system over the Naples shelf resulted in a maximum wave height of 0.92 m on January 11, 2012, the largest meteotsunami on the southwestern coast of Florida between 2007 and 2015 [Paxton, 2016]. A 1.5 m high meteotsunami damaged coastal infrastructure near Naples, Captiva and Sanibel Islands in southwestern Florida on December 20, 2018, which was associated with a cold front bringing sudden temperature and pressure changes [Rabinovich, 2020].

In addition to these notable events, meteotsunamis occur much more frequently than expected. Olabarrieta et al. [2017] analyzed water level, atmospheric pressure, wind speed/direction and radar reflectivity data of three open water NOAA gauges from 1996 to 2016, and discovered that there are around 20 meteotsunami events on average in the above three locations. This result should not come as a surprise as the GOM is a region where tropical cyclones and winter storms occur frequently. However, only 1 – 3 of the 20 events at each location exceeds 0.5 m. In addition, Shi et al. [2020] showed that meteotsunamis are frequently triggered by Tropical Cyclone Rainbands via a study of Atlantic hurricanes landfalling in the GOM over a 20 year span. Similar studies on the Great Lake show that there is an annual water level of 0.83 m and 10-year return water level of 1.3 m, which demonstrates that meteotsunamis as severe as the 1954 Chicago event occur more frequently than is normally thought [Bechle et al., 2016]. Along the U.S. east coast, a total of 548 meteotsunamis were recorded from 1996 to 2017 with wave height of 30 cases exceeding 0.6 m [Dusek et al., 2019].

Since these studies of past events in the U.S. all utilize NOAA tide gauges which are mostly not positioned in open oceans, they may not always capture a meteotsunami event. Moreover, these gauges may not have recorded the maximum wave [Dusek et al., 2019] because of their sparsity. Numerical modeling is often employed to bridge the gap when there is not enough data, in order to gain a better understanding of the generation, propagation, and inundation processes during meteotsunami events, which can help recreate historical events, predict potential vulnerable locations, and ultimately contribute to hazard mitigation.

There has been a plethora of numerical meteotsunami studies near the Mediterranean Sea, for example: In order to mitigate meteotsunami hazards, Šepić and Vilibić [2011] created a meteotsunami warning system by constructing a warning matrix based on previous events, theoretical estimations and numerical modelling. To investigate the generation, amplification and propagation properties of meteotsunamis in the Balearic Sea, Ličer et al. [2017] applied nested ocean modelling system (ROMS) forced by synthetic atmospheric gravity waves, and quantified the contribution of Mallorca shelves and Menorca Channel to meteotsunami intensity, and analyzed subcritical and supercritical propagation conditions. Kim and Omira [2021] identified meteotsunami hazard hot spots along the coast of Portugal using a series of idealized numerical simulations with comparison to observed data.

In the U.S., there has been more modeling development in the Great Lakes since this region has relatively high meteotsunami occurrence. Anderson et al. [2015] showed the importance of wave reflection, focusing, and edge wave formation in enclosed basin via numerical reconstruction of the May 27, 2012 Lake Erie event. Later, Linares et al. [2016] conducted numerical experiments with different disturbance speeds and directions on northern Lake Michigan using a 3D Reynolds-averaged Navier-Stokes model, and found out that wind and pressure have similar contribution to meteotsunami hazard. For the U.S east coast, the destructive 2008 Boothbay event sparked interests from the research community [Vilibić et al., 2014b]. Whitmore and Knight [2014] and Vilibić et al. [2014a] both simulated the Boothbay meteotsunami for the purpose of the development of a meteotsunami warning system. Similar effort on numerical development was carried out in the GOM. Shi et al. [2019] employed the Coupled Ocean-Atmosphere-Waves-Sediment Transport (COAWST) modeling system and showed that tropical cyclone induced meteotsunami waves are more influenced by wind stress, and in contrast, during winter storms atmospheric pressure fluctuations dominate wave generation, especially at depth deeper than 40 m.

In Horrillo et al. [2020] and Cheng et al. [2021], we studied the generation and propagation/amplification patterns of meteotsunami waves in northeastern GOM and identified coastal communities vulnerable to meteotsunami inundation through a suite of idealized numerical experiments using parameters based on a real event. In Horrillo et al. [2021], the same study was extented to the northwestern GOM (Texas and Louisiana coasts). Section 7.2 introduces our meteotsunami numerical scheme, grid and gauge setup. Section 7.3 derives air pressure disturbance parameters from a historical meteotsunami event in the GOM using an idealized exponential decay function, and examines the generation and propagation of the resultant waves. Section 7.5 describes the CUDA adaptation of the meteotsunami model, our newly-built GPU workstation and its performance. Section 7.6 presents a parameter study, in northeastern and northwestern GOM subregion, respectively, where we use 36 the incident wave directions (0°, 10°, 20°, ..., and 350°) of the disturbance, 30 trajectories and 16 speeds (from 10 m/s to 40 m/s), thus there are a total of 17280 ($36 \times 30 \times 16$) cases for each subregion.

7.2 Numerical model description

The numerical model utilized in this study is a 2D hydrostatic model in spherical coordinates built on the nonlinear shallow water equations. The governing equations, staggered grid

setup, and numerical solution scheme are based on Kowalik et al. [2005]. In order to simulate meteotsunamis driven by atmospheric pressure disturbances, the momentum equations are modified to include spatially-dependent surface air pressure in addition to the hydrostatic pressure. Wind stress and astronomical tide contributions are not included in the equations.

The governing equations are derived from the incompressible Navier-Stokes equation and the incompressibility condition of the continuity equation in a spherical coordinates system in which λ is the longitude, ϕ is the latitude, and z denotes the normal distance from the still water level (SWL). The momentum equations along λ and ϕ directions are:

$$\begin{aligned}\frac{\partial U}{\partial t}+\frac{U}{R\cos\phi}\frac{\partial U}{\partial \lambda}+\frac{V}{R}\frac{\partial U}{\partial \phi}-\left(2\Omega+\frac{U}{R\cos\phi}\right)V\sin\phi \;&=\\ -\frac{g}{R\cos\phi}\frac{\partial \zeta}{\partial \lambda}-\frac{1}{\rho R\cos\phi}\frac{\partial p}{\partial \lambda}-n^2\frac{g}{D^{1/3}}\frac{U\sqrt{U^2+V^2}}{D}&\end{aligned} \tag{2}$$

$$\begin{aligned}\frac{\partial V}{\partial t}+\frac{U}{R\cos\phi}\frac{\partial V}{\partial \lambda}+\frac{V}{R}\frac{\partial V}{\partial \phi}+\left(2\Omega+\frac{U}{R\cos\phi}\right)U\sin\phi \;&=\\ -\frac{g}{R}\frac{\partial \zeta}{\partial \phi}-\frac{1}{\rho R}\frac{\partial p}{\partial \phi}-n^2\frac{g}{D^{1/3}}\frac{V\sqrt{U^2+V^2}}{D},&\end{aligned} \tag{3}$$

and the continuity equation is:

$$\frac{\partial \zeta}{\partial t}+\frac{1}{R\cos\phi}\frac{\partial (UD)}{\partial \lambda}+\frac{1}{R\cos\phi}\frac{\partial (VD\cos\phi)}{\partial \phi}=0, \tag{4}$$

where U and V are depth-averaged velocity components in the λ and ϕ directions respectively. The variable t is the time, ζ is the free surface elevation from the SWL, R is the earth's radius, Ω is the earth's angular velocity, ρ is the water density, g is the gravitational acceleration and n is the Manning's coefficient for the sea-bottom friction (0.025 $\mathrm{sm}^{1/3}$). The total depth is defined as $D=\zeta+h_b$, where h_b is the water depth. p is the atmospheric disturbance pressure.

To investigate meteotsunami effects on a global scale, and identify local as well as distant meteotsunami source areas affecting the northwestern area of the GOM, a model domain that encompasses the entire GOM (18.1 to 30.75 N, 97.9 to 80.2 W) is used. The bathymetry data were created with the NOAA Etopo1 dataset [Amante and Eakins, 2009] and referenced to the mean high water. Longitudinal and latitudinal grid spacing are both one arc-minute which achieves reasonable simulation time and resolves the meteotsunami wavelength well. A coastal wall is set at a water depth of 0.3 m to avoid runup on the wide cells on land. Outflow conditions are applied to all the boundaries of the model domain. 98 wave gauges (interpolation from the nearest four grid points) are set up at approximately 5 m deep open water locations along the coastline of northern GOM for hazard assessment, which record water level and air pressure every 20 seconds.

7.3 Air pressure definition

In Feburary 2010, one of the most intense meteotsunami was recorded in Clearwater Beach, Florida. The $\sim$ 1 m wave height long wave was triggered by a dry season storm, which is common during winter in GOM where low pressure systems usually move eastward and squall lines develop ahead of cold fronts [Olabarrieta et al., 2017]. This squall line came off the Florida coast near Panama City and moved toward southeast along the isobath of the southwestern Florida shelf. A numerical representation of this event is shown in Figure 105a.

Based on radar reflectivity data from NOAA (see Figure 11 in reference Olabarrieta et al. [2017]), we constructed an idealized surface air pressure function where the amplitude of the crest A_c and trough A_t decay exponentially along both the length and width of the squall, see Figure 105a and Equation 5,

$$P(x,y) = \begin{cases} A_c \cdot x \cdot exp\left(-(y)^2 - \left(\frac{x}{L_c}\right)^2\right), & x < 0 \\ A_t \cdot x \cdot exp\left(-(y)^2 - \left(\frac{x}{L_t}\right)^2\right), & x > 0 \end{cases}, \tag{5}$$

where (x, y) are the longitude and latitude excursions along length L, and L_c and L_t are the wavelength of the pressure crest and trough, respectively. The translation of the pressure disturbance is here simplified to a linear trajectory (single direction). Additionally, the pressure function is bent backwards (opposite of moving direction) to more realistically represent the geometry seen in the event, and is smoothed where crest and trough meet with quadratic stretching.

A customized ramping function (Equation 6) is applied to the beginning and ending of the atmospheric pressure forcing to avoid an abrupt entry or exit of the pressure disturbance. We found that 8 minutes (480 seconds) of ramping time was enough for a smooth transition. The inverse tangent function in Equation 6 is employed because of its asymptotic nature toward $x \to \pm\infty$.

$$\begin{aligned} f_{ramp} &= \frac{1}{2}\left(1 + \frac{tan^{-1}(12\frac{t'}{480} - 6)}{tan^{-1}(6)}\right) \\ t' &= \begin{cases} t, & 0 < t < 480 \\ t_{end} - t, & t_{end} - 480 < t < t_{end} \end{cases}, \end{aligned} \tag{6}$$

where t is in seconds, and t_{end} is the end time for air pressure presence.

7.4 Meteotsunami model parameters

The Etopo1 bathymetry is interpolated to a grid resolution of 15 arc-seconds to better resolve the generated waves.

The pressure disturbance profile parameters are estimated from NOAA Clearwater Beach, FL station (ID: 8726724) from 12 am Feb 12 to 12 am Feb 14 2010 with low frequency (period>6 h) pressure components filtered out (Figure 105c). We set crest amplitude A_c to be 5 mbar and trough amplitude A_t 1 mbar, and determined the lengths of crest L_c

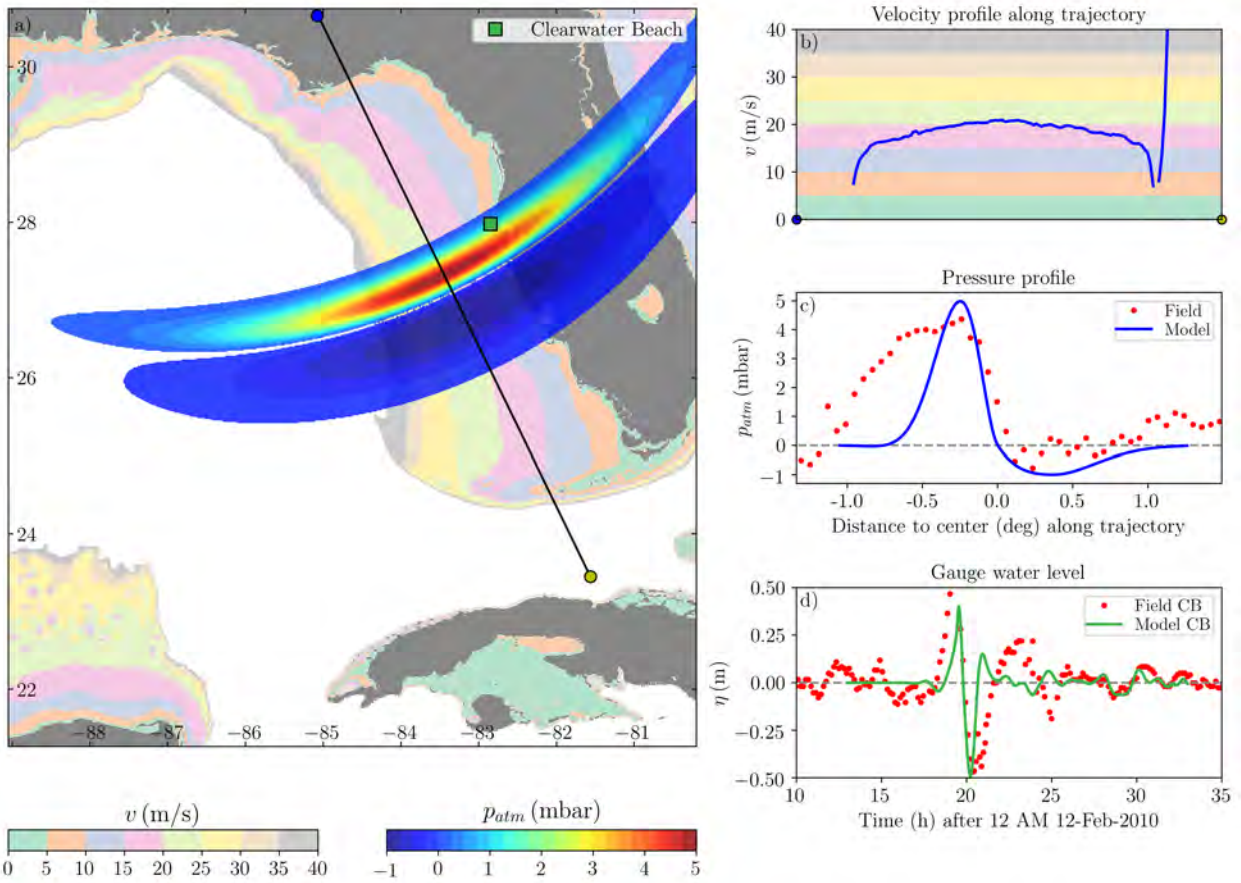

Figure 105: Model setup and Clearwater Beach gauge water level comparison for the Feb 12 2010 northern GOM meteotsunami. a) Meteotsunami atmospheric pressure contour plot and trajectory. Black solid straight line shows the trajectory on which pressure disturbance moves from the blue dot toward the yellow. Pressure contour is plotted with a lower cut-off at 0.05 mbar for both crest and trough, underneath which lies the contour of the continental shelf bathymetry expressed in terms of shallow water wave celerity $C = \sqrt{gh}$ from 0 – 40 m/s, where h is depth of ocean floor. b) Speed (shallow water wave celerity) profile along the trajectory. In this case, it follows the 20 m/s contour line. c) Air pressure profile along the trajectory, where the leading trough amplitude is 1 mbar and the crest amplitude 5 mbar. Pressure anomaly (de-tided) measurement data is from NOAA Clearwater Beach, FL station (ID: 8726724). d) De-tided water level records at NOAA Clearwater Beach (CB) gauge (dots) and model results starting at 10 am Feb 12 2010 UTC.

(0.7 deg) and trough L_t (1.05 deg) through trial-and-error until the simulated wave height reached close to 1 m. Other parameters are estimated from NEXRAD reflectivity data (Figure 105a): Arc length R is 5 deg with 8 deg radius, and start and end coordinates of the pressure disturbance trajectory are (blue dot: 30.747 N, -85.107 W) and (yellow dot: 23.448 N, -81.562 W). Pressure disturbance forward speed is estimated to be 20 m/s and it takes $\sim$ 13.5 hours to complete the trajectory (cf. on methodology Sheremet et al. [2016]).

Total run time is set to 20 hours to ensure that water level fluctuations at all locations have settled down.

The formation and propagation of meteotsunami waves are demonstrated in Sec. 4 (Fig. 2) from Cheng et al. [2021], and the influence of trajectory location and forward speed on wave elevation at the coastline are demonstrated in Sec. 5 (Fig. 3) from Cheng et al. [2021].

7.5 CUDA model and performance description

In this project, we converted our CPU meteotsunami code to CUDA, and with the help of a newly built multi-GPU workstation which has three Nvidia RTX 3090 GPUs that is capable of running our meteotsunami Fortran code in CUDA 50 100 times faster than the CPU version, depending on the grid. With this CUDA code, we were able to expand the previous parameter study to 17280 runs (i.e., 36 incident wave directions × 30 trajectories × 16 velocities) on a much finer 15 arcsecond grid.

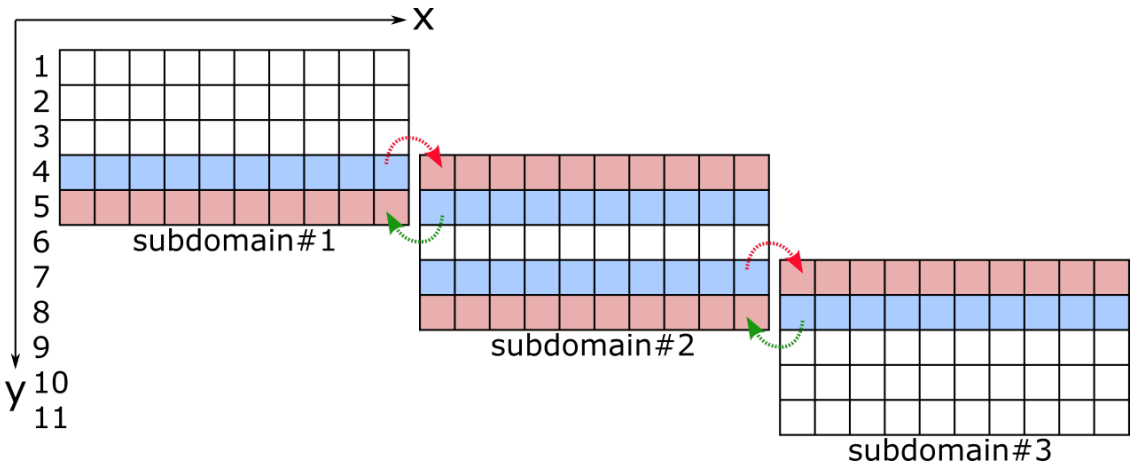

Figure 106: Domain decomposition along the y-axis. Ghost cells are red rows, and blue rows are their corresponding cells in adjacent domains, from where values are passed during each time interval (dashed arrows).

CUDA model workflow

CUDA was created by Nvidia to utilize its Graphics Processing Units (GPU) for general purpose computing. Numerical models that are converted from conventional CPU code to CUDA usually gain substantial performance, especially ones that uses large grid sizes, due to the massive parallel capability of GPUs. For the purpose of using finer grid resolution and conducting more detailed parameter study, we built a GPU workstation, which has three Nvidia RTX 3090 GPUs (henceforce referred to as RTX3090). RTX3090 was the best consumer-level Nvidia GPU available in 2021, which is on a new Ampere architecture, has 10496 CUDA cores and 24GB 384bit GDDR6X memory. The original workstation purchased from Puget Systems had two air-cooled RTX3090s. Two is the maximum number of RTX3090 possible on the original motherboard due to its large cooling fan blocking additional PCI-E

access. In order to accomodate a third GPU, we upgraded the system to watercooling, which kept the system below 75 °C even runing the most demanding program for a long period of time.

We chose CUDA Fortran that comes with NVIDIA HPC SDK for an easier migration of the existing Fortran code. To take full advantage of the three RTX3090s, we also applied domain decomposition to our meteotsunami code. The computational domain is devided along the y-axis such that adjacent subdomains have two cells overlapping with each other, which allows one row of ghost cell for each subdomain. Fig. 106 illustrates that, given a domain of size 11 (y) by 10 (x), during each time interval, the ghost row(s) of each subdomain updates its values from (dashed arrows) their adjacent subdomain's corresponding internal row(s).

A general CUDA workflow is presented in Fig. 107. Left of the time arrow are the four steps of a typical domain decomposition technique used in CUDA for forward numerical models. Step a): For each device/GPU (Ndev: number of devices is 3 in this case), perform numerical calculations in CUDA kernel functions. New sea level (zn) and x & y velocities (un & vn) are updated based on old sea level (zo) and x & y velocities (uo & vo); Step b): Update the old variables (zo, uo, vo) with new ones (zn, un, vn) using $cudaMemcpyAsync$ function; Step c): See red arrows in Fig. 106. For each device/subdomain on the left of halo/boundary, copy its 2^{nd} last row of (zo, uo, vo) to its adjacent subdomain's 1^{st} row (ghost cell) using $cudaMemcpyAsync$ function, and finally, Step d): See green arrows in Fig. 106. For each device/subdomain on the right of halo/boundary, copy its 2^{nd} row of (zo, uo, vo) to its adjacent subdomain's last row (ghost cell) using $cudaMemcpy$ function. Note that step a), b) and c) all use asynchronous functions $model\_kernel$ and $cudaMemcpyAsync$, which means that CPU does not wait for the CUDA functions to finish and simply proceeds to the next task. This queues up all the CUDA functions in steps a) b) c) for each subdomain in their corresponding GPU/device, ensuring that all devices run in parallel. The last step d) uses $cudaMemcpy$ which is synchronous, therefore CPU waits for all the CUDA operations to finish before moving to the next time step.

Using the CPU-OpenMP code on a 12th generation Intel i9-12900k CPU (using 8 threads, which proved to be the fastest) and the new CUDA code on three RTX3090s, we ran the Florida test case for 10 hours to compare their performance. Each model's run time for different grid sizes is recorded in Table 4.

Table 4: Performance comparison of 3 RTX3090s using CUDA Fortran versus Intel i9-12900K using Intel Fortran for 10 hour meteotsunami model run without plotting.

Grid resolution (NY×NX)	CUDA (3 RTX3090s)	CPU (i9-12900K)
1 arcminute (1063×760)	0m7s	1m4s
15 arcseconds (4249×3037)	1m5s	47m53s
10 arcseconds (6473×4555)	2m34s	2h48m10s
5 arcseconds (12745×9109)	24m56s	23h22m54s

For the 1 arcminute grid (1063×760), CUDA took 7 seconds, more than 9 times faster than CPU's 1 minute 4 seconds. For the 15 arcseconds grid (4249×3037), CUDA took 1

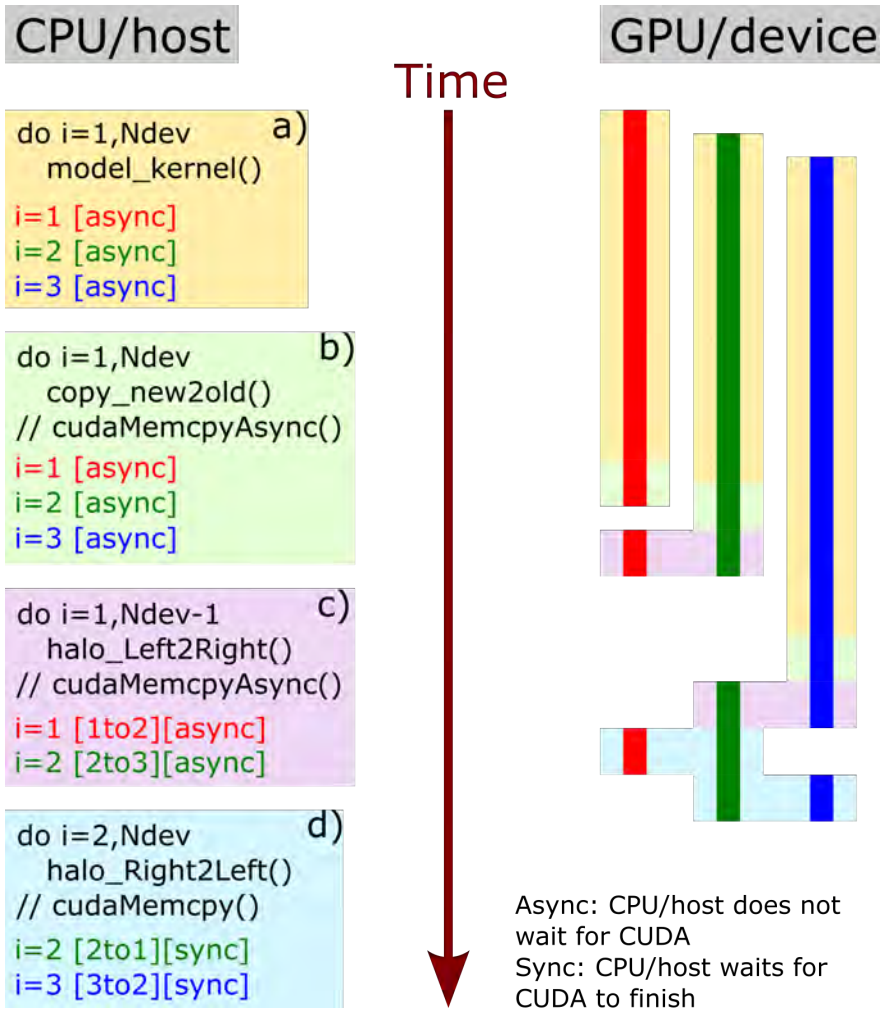

Figure 107: Implementation flowchart of meteotsunami model domain decomposition in CUDA. Left of the time arrow are the four steps of a typical domain decomposition technique used in CUDA for forward numerical models. Step a): For each device/GPU (Ndev: number of devices is 3 in this case), perform numerical calculations in CUDA kernel functions. New sea level (zn) and x & y velocities (un & vn) are updated based on old sea level (zo) and x & y velocities (uo & vo); Step b): Update the old variables (zo, uo, vo) with new ones (zn, un, vn); Step c): See red arrows in Fig. 106. For each device/subdomain on the left of halo/boundary, copy its 2^{nd} last row of (zo, uo, vo) to its adjacent subdomain's 1^{st} row (ghost cell), and finally Step d): See green arrows in Fig. 106. For each device/subdomain on the right of halo/boundary, copy its 2^{nd} row of (zo, uo, vo) to its adjacent subdomain's last row (ghost cell). Right of the time arrow illustrates a possible scenario where the 3 GPUs have different speeds or are assigned different subdomain sizes (thus taking different time in model kernel execution). Colors denote the four steps (a,b,c,d).

minute 5 seconds, more than 44 times faster than CPU's 47 minutes 53 seconds. For the 10 arcseconds grid (6473×4555), CUDA took 2 minutes 34 seconds, more than 112 times faster

than CPU's 2 hours 48 minutes 10 seconds. For the 5 arcseconds grid (12745×9109), CUDA took 24 minutes 56 seconds, more than 56 times faster than CPU's 23 hours 22 minutes 54 seconds. Except for the 1 arcminute grid, all other grids achieved around $50-100$ times speed up using CUDA. The reason could be that the initialization phase of the CUDA program, including reading bathymetry & parameter files and other data preparation, is taking some time on the order of a few seconds, which should be taken out the 7 seconds total run time.

7.6 Northeastern & northwestern GOM meteotsunami risk assessment

In previous two projects [Horrillo et al., 2020, 2021] , we conducted numerical experiments to investigate the generation and propagation of meteotsunami waves and assessed hazards on a broad scale in the northeastern & northwestern GOM, respectively. In those previous numerical experiments, for each subregion (northeastern or northwestern GOM), we conducted 1260 runs (i.e., 12 incident wave directions × 15 trajectories × 7 velocities). Each case ran for 30 hours on a 1 arcminute grid. With the new meteotsunami CUDA Fortran code running 44 times faster than the CPU code on the more accurate 15 arcsecond resolution grid, we greatly expanded the parameter space in this project.

Northeastern GOM meteotsunami risk assessment

In order to study the influence of different incident directions and assess meteotsunami hazard under all possible scenarios, the parameter space covers the entire northwestern GOM with 36 incident directions that are illustrated in Figure 108a. The 36 directions are 0°, 10°, 20°, ..., and 350°, where 0° means the pressure originates from south and 90° means from west, etc., in a clockwise order. Under each incident direction scenario the same 30 trajectories and 16 speeds, thus there are a total of 17280 ($36 \times 30 \times 16$) cases.The total run time for this parameter study is about 20 days.

Starting at gauge #8, data of all 17280 cases at every 5th gauge is compiled into a rose diagram, which plots the maximum water level of the 480 (30×16) cases under each incident direction. Take gauge #13 for instance, there is less than 0.15 m wave resulting from pressure disturbance coming from north, whereas it can reach over 0.4 m from the east and the rest lie in the middle at around 0.3 m. Similarly for gauge #58, since it is situated at the southeast corner of the shelf, there is no room for meteotsunami wave to develop from pressure disturbance coming from south or east (the second quadrant). The coastal region from Hernando to Charlotte County, FL, i.e. from gauge #43 to #53, seem to suffer from high meteotsunami waves from all directions except from the land. This high risk zone should not come as a surprise because of the protruding morphology of its coastline, and long straight continental shelf isobath starting from the Florida panhandle (around gauge #8 to # 28) favorable for wave resonance. Furthermore, this zone also faces higher waves (> 0.3 m) propagating perpendicularly to the coastline, comparing to the Florida panhandle area (< 0.3 m), likely due to the wider continental shelf allowing more air-water energy transfer. In contrast, the coastal area around Taylor, Dixie and Levy counties, FL, i.e., around gauge

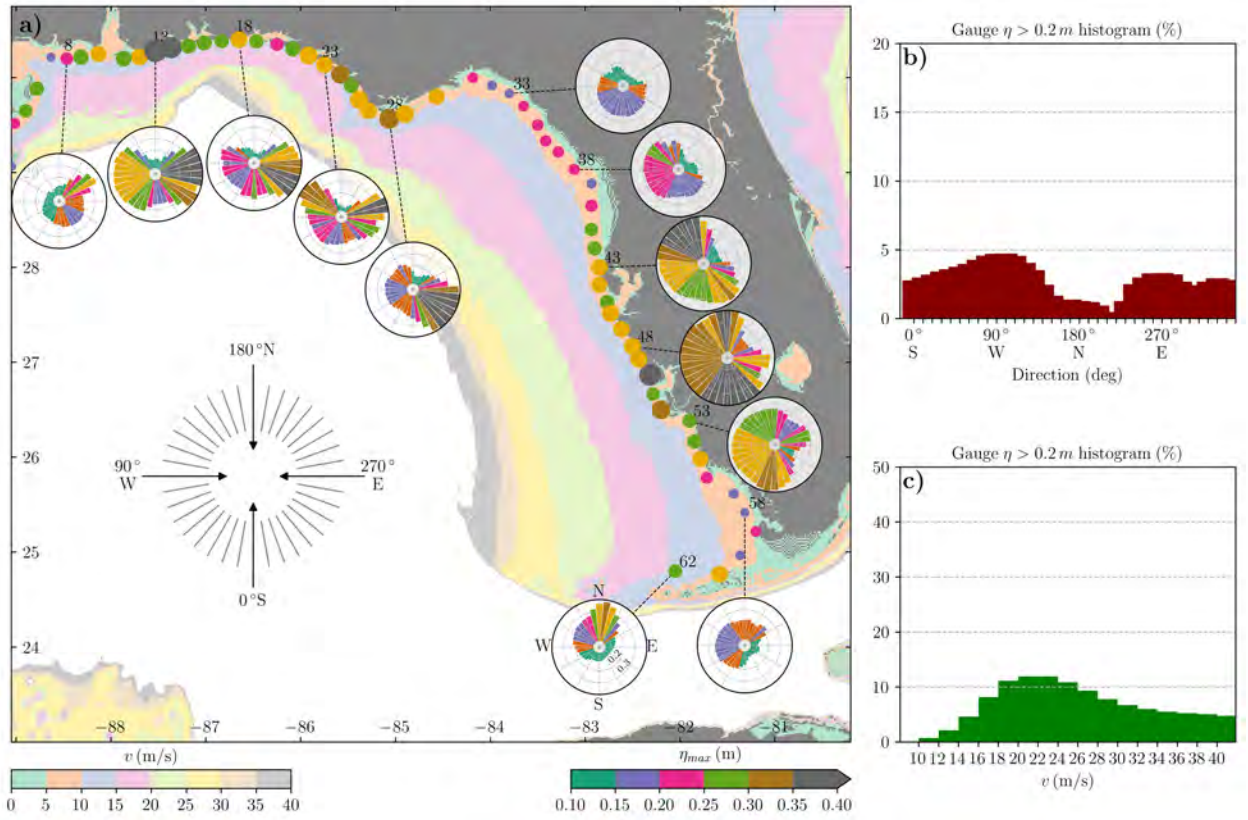

Figure 108: a) Rose diagram of select northeastern GOM gauges each showing the maximum water level (η_{max}) recorded for each direction from a parameter study of 17280 cases (36 incident directions, each with 30 trajectories and 16 pressure disturbance forward speeds). Rose diagram radial scale (η_{max} from 0.1 m to 0.4 m) and directions (NWSE) are marked in gauge #62, which are the same for all the gauges. Maximum water level recorded from all events at each gauge are shown with circles in corresponding size and color (same color scale as the rose diagram). Contour plot of the continental shelf bathymetry is expressed in terms of shallow water wave celerity $C = \sqrt{gh}$ from 0 – 40 m/s, where h is depth of ocean floor. Incident direction is illustrated with arrows where 0° means the pressure disturbance originates from south and 90° means from west, etc., in a clockwise order. b) Incident direction distribution of cases whose recorded water level exceeds 0.2 m (each gauge counts separately). c) Pressure disturbance forward speed distribution of cases whose recorded water level exceeds 0.2 m (each gauge counts separately).

#33 to #38, having concave coastlines, is generally shielded from meteotsunamis, expecting less than 0.3 m waves.

The maximum water level data from all cases (each gauge counts separately) is further compiled into histograms in search for directions and velocities with higher meteotsunami risk in the northeastern GOM. Fig. 108 b) shows the distribution in incident direction where gauge water level exceeds 0.2 m and it indicates that the most favorable direction for higher water level are 0° - 120° (south to west, 3rd quadrant), and also around 270° (east), with

each direction bin (1/36) accounting for more than 3%. According to the rose diagrams in Fig. 108 a), pressure disturbances coming from the south to west (0° - 120°) direction result in higher water level near south Florida region, while the east (270°) direction to the panhandle region. Similarly, Fig. 108 c) shows the distribution in forward speed where gauge water level exceeds 0.2 m. The result shows that 18 m/s – 26 m/s are the forward speeds with the most potential, together accounting for more than 40% of the cases.

Northwestern GOM meteotsunami risk assessment

Similar to northeastern GOM, the parameter space covers the entire northwestern GOM with 36 incident directions that are illustrated in Figure 109a. The 36 directions are 0°, 10°, 20°, ..., and 350°, where 0° means the pressure originates from south and 90° means from west, etc., in a clockwise order. Under each incident direction scenario the same 30 trajectories and 16 speeds, thus there are a total of 17280 ($36 \times 30 \times 16$) cases.

Starting at gauge #2, data of all 17280 cases at every 3rd gauge are compiled into a rose diagram, which plots the maximum water level of the 480 (30×16) cases under each incident direction. Besides, maximum water level recorded from all events at each gauge are also shown at their sites with circles in corresponding size and color. Take gauge #14 for instance, there is less than ∼0.2 m wave resulting from pressure disturbance coming from north and west, whereas it can reach over 0.4 m from the east (including northeast and southeast) and the rest lie in the middle at around 0.3 m. Similarly for gauge #29, the only high waves are brought by meteotsunamis traveling from the northwest, because of the continental shelf tapering toward Louisiana. Under the assumptions made in this study, that is, all meteotsunamis travel in a straight line and there are equal chances of different incident directions, overall the Texas coasts would expect higher meteotsunami water elevation than Louisiana. Within the Texas coastline, the convex sections generally face high meteotsunami waves from more directions than the concave sections. For example, Cameron County (near gauge #1–2) and Matagorda and Brazoria counties (near gauge #12–14) have convex coastlines and those in between are more protected, which is consistent to the findings in Florida GOM coast.

The maximum water level data from all cases (each gauge counts separately) is further compiled into histograms in search for directions and speeds with higher meteotsunami risk in the northwestern GOM. Figure 109b shows the distribution in incident direction where water level exceeds 0.2 m and it indicates that the most favorable direction for higher water level are 0° – 60° (south – southwest, third quadrant), and also around 220° – 350° (northeast – southeast), with each direction accounting for more than 3%. Similarly, Figure 109c shows the distribution in forward speed where water level exceeds 0.2 m. The result shows that 18 m/s – 28 m/s are the forward speeds with the most potential, together accounting for more than 40% of the cases. The most common speed is similar to Florida GOM coast because the 15 – 30 m/s bathymetry wave celerity bands account for a large portion of the continental shelf.

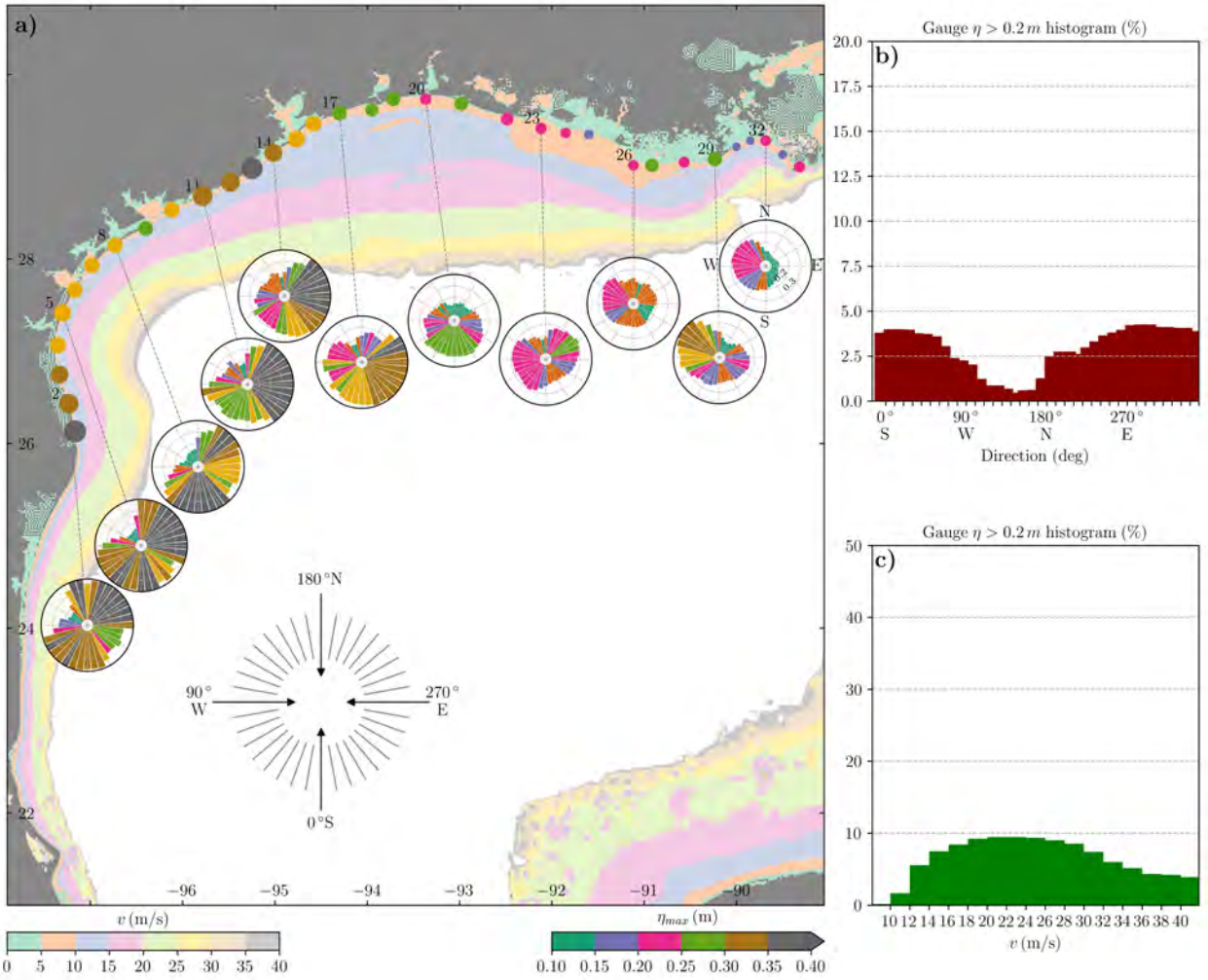

Figure 109: a) Rose diagram of select northwestern GOM gauges each showing the maximum water level (η_{max}) recorded for each direction from a parameter study of 17280 cases (36 incident directions, each with 30 trajectories and 16 pressure disturbance forward speeds). Rose diagram radial scale (η_{max} from 0.1 m to 0.4 m) and directions (NWSE) are marked in gauge #32, which are the same for all the gauges. Maximum water level recorded from all events at each gauge are shown with circles in corresponding size and color (same color scale as the rose diagram). Contour plot of the continental shelf bathymetry is expressed in terms of shallow water wave celerity $C = \sqrt{gh}$ from 0 – 40 m/s, where h is depth of ocean floor. Incident direction is illustrated with arrows where 0° means the pressure disturbance originates from south and 90° means from west, etc., in a clockwise order. b) Incident direction distribution of cases whose recorded water level exceeds 0.2 m (each gauge counts separately). c) Pressure disturbance forward speed distribution of cases whose recorded water level exceeds 0.2 m (each gauge counts separately).

8 Meteotsunamis Characterization in northern GOM using Meteotsunami Rose Charts

8.1 Introduction

In the FY 2020 NOAA project report [**?**], a novel approach to the characterization of Meteotsunami (MT) hazard in Clearwater, FL, was introduced using visualization rose charts describing sealevel increase of hypothetical approaching atmospheric disturbances (AD) due to a cold front or rain band. A total of 1260 (12 directions x 15 trajectories x 7 velocities) cases were simulated by using a fast depth integrated MT model. This report discusses an extension of this effort where, 17,280 (36 directions *times* 30 trajectories *times* 16 velocities) numerical experiments were conducted for both, northeastern & northwestern Gulf of Mexico(GOM) using the MT model discussed in detail in [**?**], making it a total of 34,560 runs. The previous MT rose charts were modified to a finer resolution (adding more directions and including other variables or parameters, example: forward speed of the AD, etc.), at 98 numerical gauges or locations along the GOM coastline. However, the sealevel increase of most of the MT cases represented in the MT hazard rose chart is small. In order to better represent the MTs posed with extreme hazards, a new visualization hazard rose chart was developed, named the severe meteotsunami rose chart. This visualization chart facilitates identification of severe case scenarios. Severe MT rose charts were then used to characterize the MT hazard for the 98 locations along the GOM; eight of these locations are shown in this report and are discussed in greater detail in the following sections.

8.2 Higher resolution data generation

This report analyzes 34,560 numerical hazard scenarios of Meteotsunami generation along the US GOM coastline. The MT model used has been described previously in FY 2020 report, [Horrillo et al., 2021]. AT each region, a total of 30 paths were simulated for 36 directions of propagation (angles in steps of 10°) and 16 forward speeds of propagation($V_{f_{AD}}$). The path of the atmospheric disturbance (AD) and $V_{f_{AD}}$ are varied, as shown in Table 5. The range of $V_{f_{AD}}$ was chosen based on Monserrat et al. [2006b]. Northward moving AD is taken as 0°, and angles are measured clockwise. For each direction, a set of parallel paths are simulated, with a spacing of 0.5 deg (approx. 55 km at the equator). Fig. 110 shows a couple of sets of these cases on the northern-east of the GOM or western Florida. The configuration of the AD along one of the paths is also shown in the figure. In this study, we take a long path that ends beyond the shelf or on land. AD paths are expected to give complete coverage of the forcing and its effects in the region or community of interest. Notice, that colorbar indicates water depth in terms of wave celerity to facilitate identification of regions with Proudman resonance according to the given forward speed of the AD.

Angles	0°	10°	20°	30°	40°	50°	60°	70°
	80°	90°	100°	110°	120°	130°	140°	150°
	160°	170°	180°	190°	200°	210°	220°	230°
	240°	250°	260°	270°	280°	290°	300°	310°
	320°	330°	340°	350°				
Distances (deg)	0.00	0.26	0.52	0.78	1.03	1.29	1.55	1.81
	2.07	2.33	2.59	2.84	3.10	3.36	3.62	3.88
	4.14	4.40	4.66	4.91	5.17	5.43	5.69	5.95
	6.21	6.47	6.72	6.98	7.24	7.50		
$V_{f_{AD}}$ (m/s)	10	12	14	16	18	20	22	24
	26	28	30	32	34	36	38	40

Table 5: Variable parameters of AD used in MT study for western Florida coast

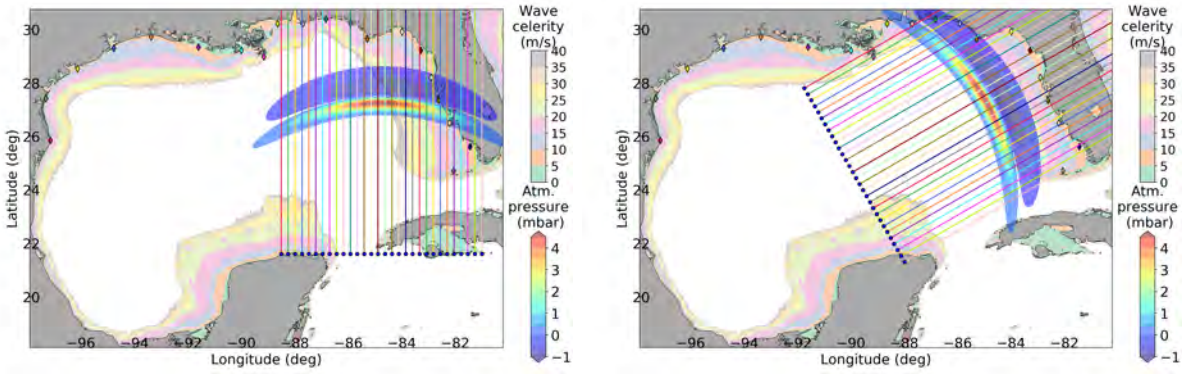

Figure 110: Various paths of AD used in MT study for western Florida coast 0° (left) and 60° (right).

8.3 Study of Clearwater Beach, FL meteotsunami hazard using higher resolution rose chart

The data generated by the numerical experiments conducted in section 8.2 was used to generate a set of higher resolution MT rose charts for Clearwater Beach, FL. A sample case is shown in Figure 111. The counter-clockwise case with $V_{f_{AD}} = 20m/s, \phi_{AD} = 150°and d_{AD} = 1.5deg$ has been shown along with the AD path for better understanding. Here, maximum MT amplitude $\eta_{max\_MT} = 0.38m$ and the MT rose chart tells us that an η_{max_MT} of 0.35 to 0.40m is to be expected for the given case scenario. Also, it can be seen from the figure that the (η_{max_MT}) occurs in the range of AD direction (ϕ_{AD}) between 100° and 160° Counter-clockwise relative to Clearwater Beach, FL, for $V_{f_{AD}} = 20$ m/s. A total of 32 MT rose charts (16 clockwise and 16 counter-clockwise with $V_{f_{AD}}$ varying from 10 to 40m/s) are generated to characterize MT hazard for Clearwater Beach, FL. MT rose charts have also been generated for another 101 locations (for a total of 3264 MT rose charts for the entire US Gulf coast). Analyzing the MT rose charts for Clearwater Beach shows that there are 13 of them that show scenarios that have MT greater than 0.3 m. Figures111, 112, and 113 show these cases. Carefully study of these charts shows that ADs coming in a direction between 100° and 160° with forward speeds between 14 m/s and 26 m/s are capable of producing significant MTs at Clearwater Beach, FL. ADs coming at ϕ_{AD} 310° and 340° with forward speeds between 18 m/s and 24 m/s also can produce substantial MTs.

8.4 Severe meteotsunami rose charts

8.5 Introduction

As seen in section 8.3, several MT rose charts are required to represent the scenarios of particular interest to emergency managers. In order to simplify this further, a new method of characterization was developed that focuses on the MT generation scenarios with MT bigger than 0.3m. A Severe Meteotsunami rose chart for Clearwater Beach, FL, is shown in Fig. 114. It is read similarly to the former MT rose charts. The bars indicating the MT's $\eta_{max_{MT}}$ are replaced by a series of color-coded blocks representing the $V_{f_{AD}}$s, which generate MT greater than 0.3m. The $V_{f_{AD}}$s can be read using the adjacent color bar. The series of blocks enable us to represent the most severe MT events with their respective $V_{f_{AD}}$s. Severe MT rose charts are to be read in combination with their corresponding MT rose charts. Example, after referring to Figure 114 due to the assessment of an approaching cold or rain front with $V_{f_{AD}} = 20m/s$ we determine that it could be a severe MT. To obtain the expected MT amplitude, we consult the MT rose chart that represents this scenario labeled in Figure 111 to find the expected MT amplitude close to 0.4 m.

Severe MT rose charts were generated for 98 locations around the US Gulf coast. Sections 8.6 to 8.13 show the Severe MT rose charts for 8 of these locations. These locations have been identified in the map shown in Figure 115. After analyzing the 8 locations, a study was done to identify the most severe cases to expect MT for each place. These results are presented in Table 6.

All the locations analyzed show susceptibility to severe MTs when ADs move along

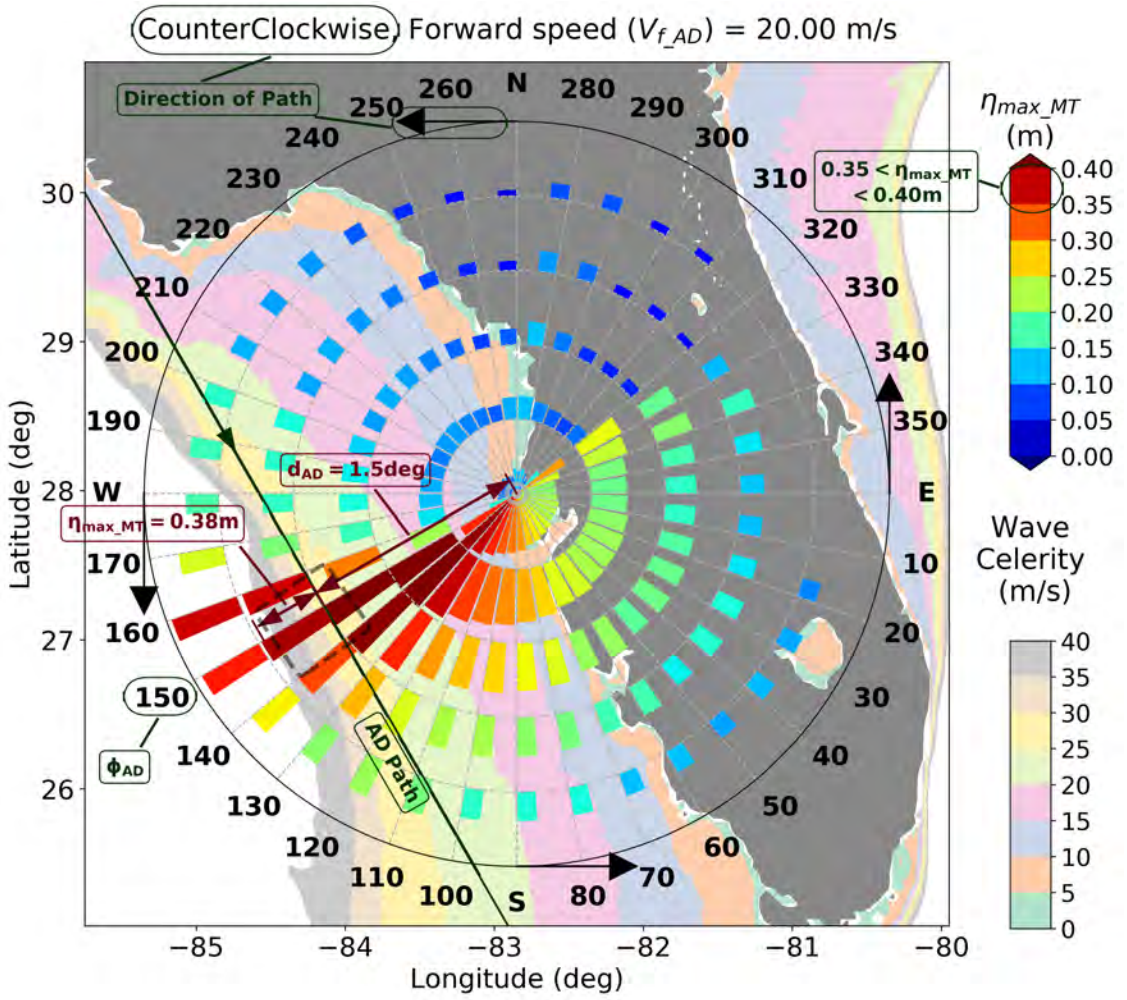

Figure 111: MT rose chart explained for η_{max_MT} at a field site near Clearwater Beach (82.85 W 27.98 N), water depth = 3.5 m from MHW represented by the bar's height for an AD(p_{AD} = 6 mbar) from direction $\phi_{AD} = 150°$ moving counterclockwise relative to the field site, with $d_{AD} = 1.5$ deg and $V_{fAD} = 20$ m/s

Location	$\mathbf{V_{f_{AD}}}$ m/s	$\boldsymbol{\phi_{AD}}^{\circ}$
Naples, FL	16-32	10-100
	16-20	240-260
	20-24	160-180
Clearwater Beach, FL	14-26	70-180
	16-24	310-340
Panama City, FL	18-40	240-290
	18-30	100-130
	36-38	100-130
Pensecola Beach, FL	20-34	250-260
Gulf Shores, AL	18	250-270
	24-40	250-270
Galveston, TX	10-28	0,230-350
Mustang Island, TX	14-26	210-250
	22-26	290
	14-20	320-350,0-10
	22-40	30-70
South Padre Island, TX	18-26	340-350,0-50
	14-30	200-280
	20-30	170-180

Table 6: Case scenarios for locations along the GOM with the possibility of MT greater than 0.3m

Location	$\mathbf{V_{f_{AD}}}$ m/s	$\boldsymbol{\phi_{AD}}^{\circ}$	$\eta_{\mathbf{max_{MT}}}$ m
Naples, FL	20	250	0.381
Clearwater, FL	16	160	0.427
Panama City, FL	28	260	0.434
Pensecola Beach, FL	24	250	0.377
Gulf Shores, AL	40	260	0.429
Galveston, TX	14	240	0.403
Mustang Island, TX	14	220	0.403
South Padre Island, TX	16	230	0.475

Table 7: Most Extreme MT scenario for locations along GOM

(parallel) to the coastline over the continental shelves. ADs moving up or down along the coastline can create higher MTs. In general, the wide and gently sloping shelves of GOM aid the production of MTs. Further, ADs with forward speeds in the range of 16 to 28 m/s are the ones that create most of the severe MT hazard scenarios.

Based on the cases identified using the severe MT rose charts, a closer look was taken at the MT amplitudes generated by those cases using the corresponding original MT rose charts. The most extreme of the severe MT events in each of the 8 locations have been shown in table 7. In the northwestern GOM, slower-moving ADs with speeds near 14 m/s are responsible for the most extreme MTs (up to 0.48 m MT in South Padre, TX). In the eastern GOM coast along FL, where the shelves are broader, slightly faster moving ADs between 16 and 24 m/s create large MTs (maximum 0.43 m at Clearwater Beach, FL). Faster moving ADs ranging from 24 to 40 m/s create the largest MTs for the northwestern region of the GOM, where the continental shelves get narrower (up to 0.43 m MT in Panama City, FL). These results further exemplify the close relationship between the MT amplitude at a location and the bathymetry in nearby continental shelves.

8.6 Naples, FL

8.7 Clearwater Beach, FL

8.8 Panama City, FL

8.9 Pensecola Beach, FL

8.10 Gulf Shores, AL

8.11 Galveston, TX

8.12 Mustang Island, TX

8.13 South Padre Island, TX

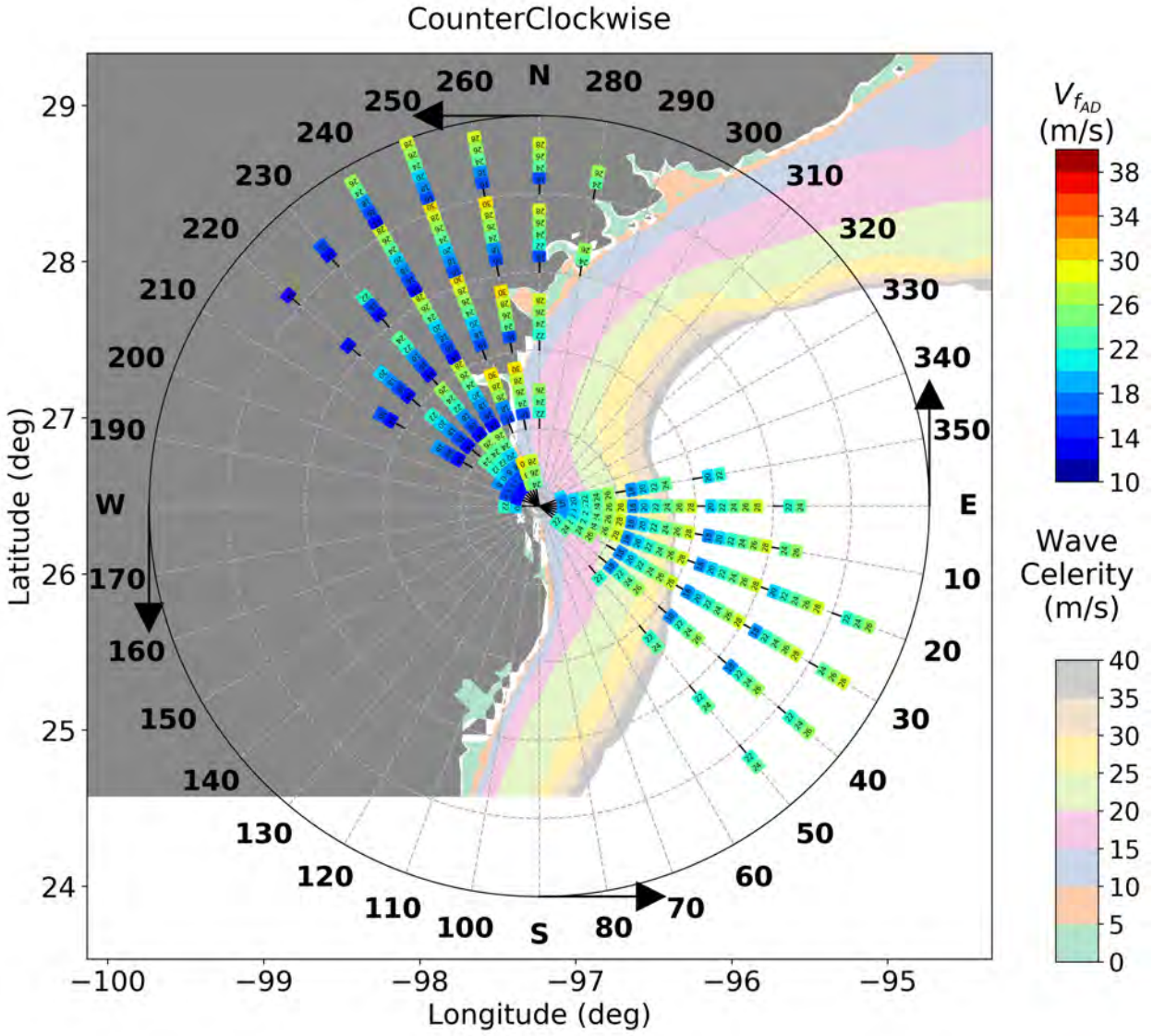

Figure 131: Severe MT rose chart for MT events with η_{max_MT} greater than 0.3 m at a field site near South Padre, TX(97.23 W 26.43 N), Water depth = 7.5 m from MHW for an AD($p_{AD} = 6$ mbar) moving counterclockwise relative to the field site, with $V_{f_{AD}}$s representing color-coded blocks

8.14 Summary

This study further developed the previous meteotsunami (MT) characterization effort in the Gulf of Mexico (GOM). A larger number of runs (34,560) has been incorporated in the MT characterization analysis for the entire GOM. Previous MT rose charts were modified to a finer resolution (adding more directions and forward speed of the Atmospheric disturbance

(AD)) at 98 numerical gauges or locations along the GOM coastline. New visualization tools have been included, namely, severe MT rose chart. This new visualization tool facilitates the identification of severe case scenarios along the 98 studied locations. Eight of these locations are shown in this report and MT hazards are presented in greater detail. Table 6 summarizes the direction and forward speed of the AD that generates more than 0.3 m MT.

All the locations analyzed show susceptibility to severe MTs when ADs move along (parallel) to the coastline over the continental shelves. ADs moving up or down along the coastline can create higher MTs. In general, the wide and gently sloping shelves of GOM aid the production of MTs. Further, ADs with forward speeds in the range of 16 to 28 m/s are the ones that create most of the severe MT hazard scenarios.

Based on the cases identified using the severe MT rose charts, a closer look was taken at the MT amplitudes generated by those cases using the corresponding original MT rose charts. In the northwestern GOM, slower-moving ADs with speeds near 14 m/s are responsible for the most extreme MTs (up to 0.48 m MT in South Padre, TX). In the eastern GOM coast along FL, where the shelves are broader, slightly faster moving ADs between 16 and 24 m/s create large MTs (maximum 0.43 m at Clearwater Beach, FL). Faster moving ADs ranging from 24 to 40 m/s create the largest MTs for the northwestern region of the GOM, where the continental shelves get narrower (up to 0.43 m MT in Panama City, FL). These results further exemplify the close relationship between the MT amplitude at a location and the bathymetry in nearby continental shelves.

9 Application of ANN in meteotsunami water elevation prediction

9.1 Introduction

In the previous study [Horrillo et al., 2021], in order to provide a broader and faster way to predict the hazards on a broad scale in the northeastern Gulf of Mexico (GOM), an optimal Backpropagation (BP) artificial neural network (ANN) was trained using the large combination of pressure disturbance forward speed and trajectory information simulated using the numerical method. The method was based on the numerical results generated from Section 7.6 in Horrillo et al. [2020], where a total of 1260 (12 directions x 15 trajectories x 7 velocities) cases were simulated using MT model. An additional 4320 (18 directions x 15 trajectories x 16 velocities) cases within the same input parameter ranges were also included, therefore there are a total of 5580 cases. Regression analysis of the output of ANN was performed, and the results are consistent with numerical simulation with a correlation coefficient greater than 96%. The formula of the ANN was then presented, providing a reliable predicting method for water level caused by meteotsunamis.

However, the previous study only considered the trajectories and forward speed as parameters, whereas all the other parameters are assumed to be constant in order to simplify the problem.

After conducting the sensitivity study for each parameters, it can be noticed that some parameters' effect on the MT might be more of a linear relation, which can be simplified as a

factor. While the effects of other parameters, such as storm surge, are harder to be simplified. Therefore, this continuous study takes into account three more parameters (Storm surge(S), Yaw angle(Y), and Pressure Slope(PS)) besides the trajectories and pressure disturbance forward speed.

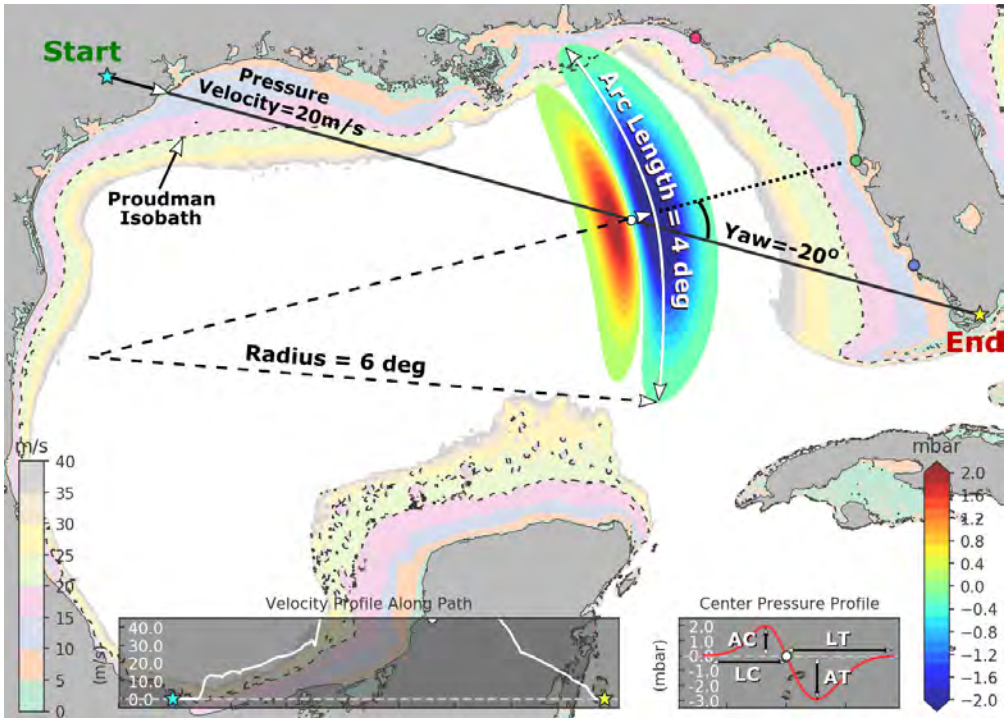

Figure 132: Meteotsunami pressure disturbance parameter definition.

Since three more parameters are included, it is more difficult to generate a comprehensive data set to train the neural network. Therefore, each parameter is limited within a relatively smaller range compared to the previous study in order to test the capability of the ANN in analyzing this problem. In total, 2325 cases are simulated using the MT model mentioned above to be used to train and test the ANN.

9.2 Artificial Neural Network (ANN) structures

The 8-30-20-1 BP neural network architecture (Fig. 133) is used in this study. The eight input layer neurons perform the function of distributing, scaling (if it is necessary), and transfer the eight inputs to the processing elements of the next layer. The second and third layers are the processing or hidden layer, and the neurons process the inputs and send their results to the next layer. Finally, the output-layer neuron represent the maximum wave elevation in the clearwater. The Marquardt–Levenberg algorithm (MLA) was used to optimize the ANN, and the stochastic gradient descend method was used for the learning procedure.

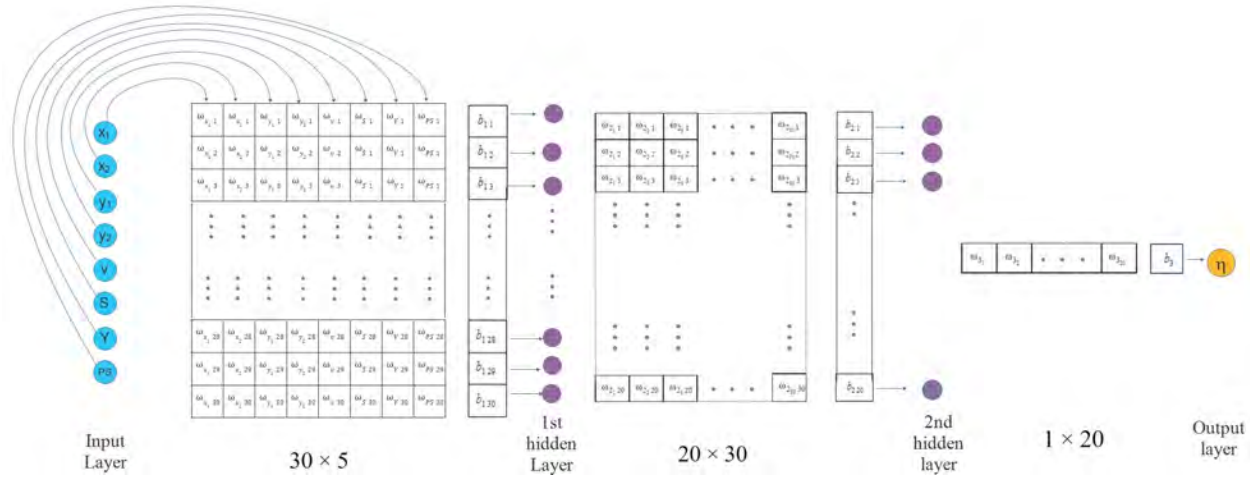

Figure 133: Neural network architecture.

In the present study, all nine variables (eight inputs and one output) are normalized within a range of [-1,1], and the original range of each input and output parameter before normalizing is tabulated in Table 8. The definition of all the parameters is shown in Fig. 132. Storm surge(S), Yaw angle(Y), and Pressure slope(PS) are the three new parameters. Pressure Slope (PS) is defined as distance between the crest and trough of the pressure disturbance profile (Fig. 132). Moreover, to avoid over-fitting, the early stopping approach presented by Prechelt [1998] is applied by classifying the inputs-outputs of our numerical simulated data in three random groups. 70% of the numerically simulated data are used to train the ANN, 15% are used to validate the trained ANN to avoid over-fitting, and the other 15% are used to test the forecasting quality of the ANN.

Table 8: Input and output ranges for ANNs

	Variables	**Range**	**Units**
Input	Longitude of the start point (x1)	-77 to -92	Degree
	Longitude of the end point (x2)	-77 to -92	Degree
	Latitude of the start point (y1)	20 to 35	Degree
	Latitude of the end point (y2)	20 to 35	Degree
	Foward speed, (V)	10 to 40	m/s
	Yaw angle (Y)	-15 to 15	degree
	Storm surge (S)	10 to 40	meter
	Pressure slope (PS)	0 to 0.4	degree
Output	Maximum MT wave elevation(H)	0 to 0.35	meter

Mean squared errors (MSE) and correlation coefficient R are two factors selected to evaluate the quality of the predicted results of the ANN as shown in Equations (7) and (8). N is the number of evidence data and T_i is the reference data (target values). In addition, O_i represents the predicted values using the trained Neural Networks. $\bar{O}$ and $\bar{T}$ are the average values of the reference data and outputs of the Neural Network, respectively. Notably, smaller

MSE and proximity of R to 1 imply a more accurate prediction, referring to a better quality of the Neural Networks.

$$\text{MSE} = \frac{\sum_{i=1}^{N} (O_i - y_{\text{desired}})^2}{N} \tag{7}$$

$$R = 1 - \frac{\sum_{i=1}^{N} (O_i - y_{\text{desired}})}{\sum_{i=1}^{N} (O_i - \bar{y}_{\text{desired}})} \tag{8}$$

The quality of the training process is evaluated using linear regression analysis, which is performed for the training sample set, and validation sample set, separately, the results at Clearwater Beach, FL are shown in Fig. 134, with MSE less than 0.0031 and R bigger than 98% for both sample sets, showing a decent training quality.

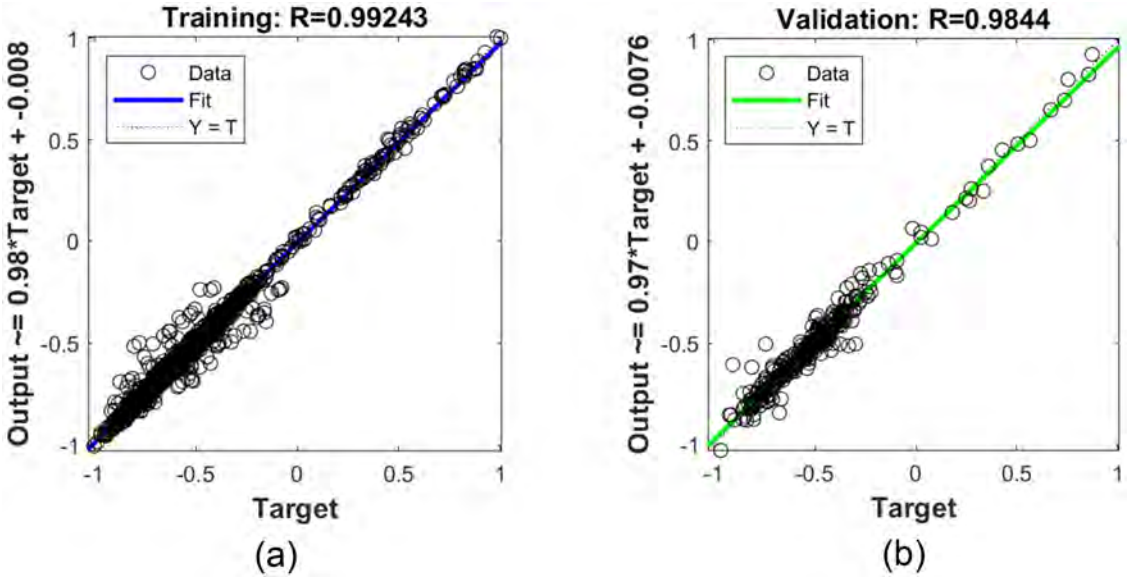

Figure 134: Regression Analysis of the Neural network's output using (**a**) training sample set (**b**) validation sample set at Clearwater Beach, FL

Similarly, the other 350 numerical simulated data are used to test the trained ANN. The correlation analysis was performed using the same method, with a $R = 96.37\%$. As shown in the prediction error of the ANN (Fig. 135 where cases with maximum water elevation less than 0.1 m are removed), it can be concluded that the optimized ANN is able to accurately predict the maximum water elevation under different trajectories, velocity, storm surge, yaw angle and pressure slope conditions.

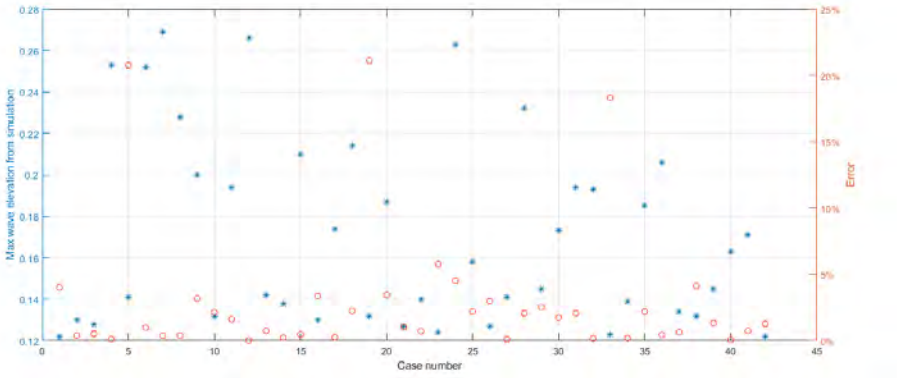

Figure 135: Error of the ANN compared to the simulation results at Clearwater Beach, FL. Cases with maximum water elevation less than 0.1 m are removed.

As can be concluded by looking at Fig. 135, the differences for all 350 cases are less than 0.04m, and less than 0.02m for the most of the cases. All the large error spikes occur in those cases where maximum water elevations at the gauges are very small (less than 0.1 m). Which is much smaller compared to the actual simulation results. So, we can conclude that the ANN can be used to substitute the traditional simulation method if the forecast time is limited and still provide a reasonably good prediction.

9.3 Equations of the ANN

The linear transfer function is used between the second hidden layer and output layer as shown in Equation (9), where ω_{3i} and b_3 are the interconnection weights and bias between the second hidden layer and output layer, respectively. Index i represents the ith nodes in the second hidden layer and each Z_{2i} can be calculated using Equation (10).

$$H = \sum_{i=1}^{20} \omega_{3i} \cdot Z_{2i} + b_3, 1 < i < 20 \tag{9}$$

$$\begin{aligned} &Z_{2i} = tansig(\textstyle\sum_{j=1}^{30} \omega_{2ij} \cdot Z_{1ij} + b_{2i}), \\ &1 < i < 20,\ 1 < j < 30 \end{aligned} \tag{10}$$

Where j represents the jth nodes in the first hidden layer, the $tansig$ function is defined in Equation (11). Each Z_{1ij} can be calculated using Equation (12).

$$tansig(A) = \frac{2}{1 + e^{-2A}} - 1 \tag{11}$$

$$\begin{aligned} &Z_{1j} = tansig(\omega_{x_1 j} \cdot x_1 + \omega_{x_2 j} \cdot x_2 \\ &+\omega_{y_1 j} \cdot y_1 + \omega_{y_2 j} \cdot y_2 + \omega_{vj} \cdot v + \omega_{Yj} \cdot Y + \omega_{Sj} \cdot S + \omega_{PSj} \cdot PS + b_{1j}), 1 < j < 30 \end{aligned} \tag{12}$$

Weight(ω) and bias(b) in Eq. (9) – (12) in hidden and output layers of ANN are achieved from the trained Artificial Neural Networks.

9.4 Results and discussion

In order to investigate effects of storm surge, yaw angle and pressure slope at different pressure disturbance forward speed, the trained BP neural network is used to generate a more comprehensive data set on a single trajectory (from (-85.5764,23.4924) to (-79.4524,28.8149)), while all the other parameters are kept as variables. For instance, as shown in Fig. 136, x-axis is the storm surge, y-axis is the yaw angle, and z-axis is the max water elevation.

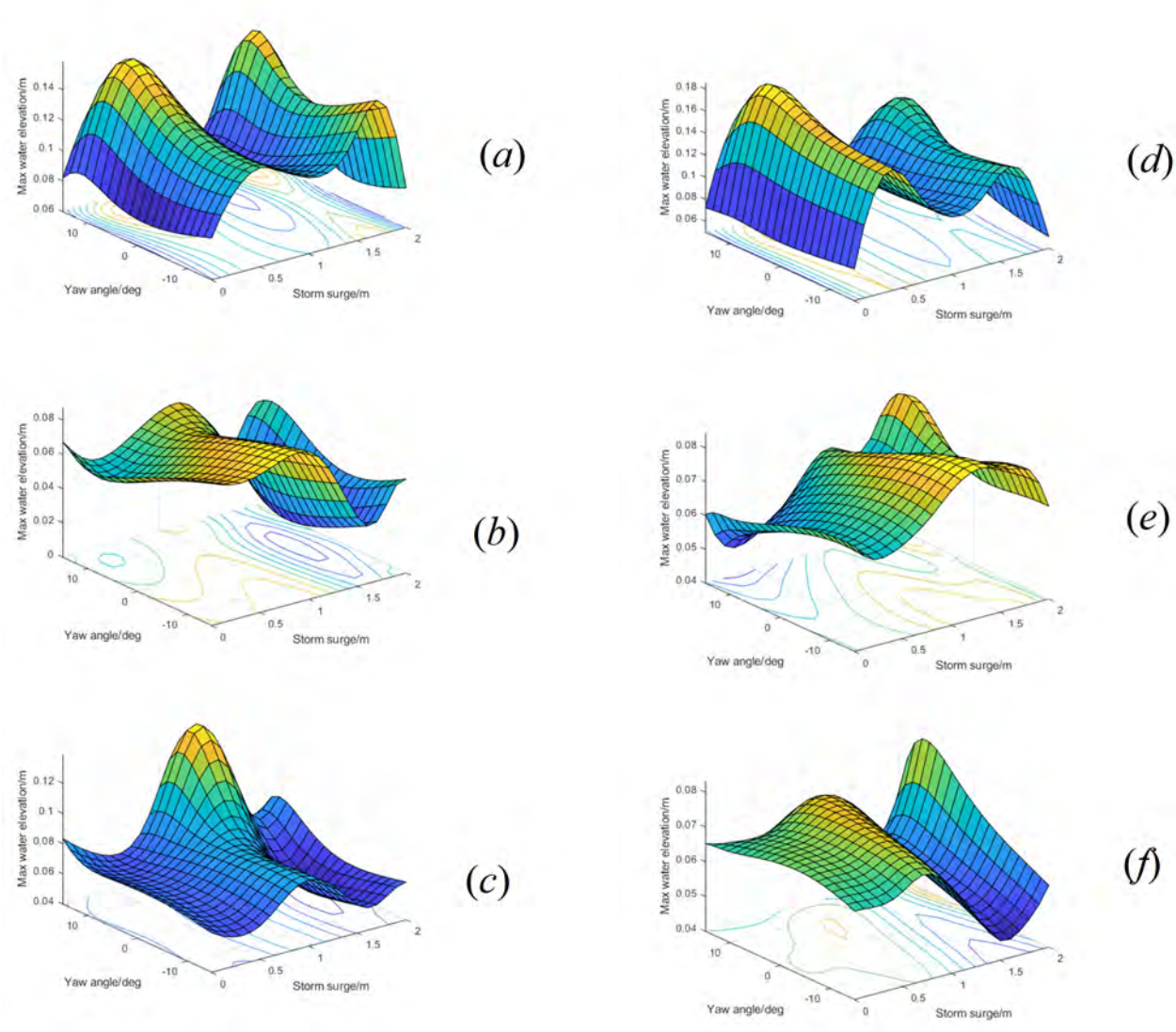

Figure 136: Max water elevation at different storm surge and yaw angle at Clearwater Beach, FL, when (**a**) v=20m/s and PS = 0, (**b**) v=20m/s and PS=0.2, (**c**) v=20m/s and PS=0.4, (**d**) v=30m/s and PS=0, (**e**) v=20m/s and PS=0.2, (**f**) v=20m/s and PS=0.4

By comparing Fig. 136 (**a**), (**b**), (**c**), where the forward speed are fixed at 20m/s, the figures have totally different patterns at different PS levels. In addition, comparing the same

pressure slope but different forward speeds (20 m/s vs 30 m/s) in Fig. 136 (**a**) and (**d**), which might have a similar pattern (the maximum wave elevation does not change much when yaw angle changes, and two similar peaks are observed when storm surge is around 0.5 m and 1.5 m), it shows that when PS is around 0, the yaw angle might not be a major factor for the MT effect. However, this is not true for other PS level because it can be seen that Fig. 136 (**b**), (**c**) have totally different pattern from Fig. 136 (**e**), (**f**). Especially Fig. 136 (**c**), when yaw angle is around 15° and storm surge is around one meter, significant MT will be observed, which does not happen at v=30 m/s (Fig. 136 (**f**)). In other words, unlike other parameters like pressure wave height and wave length, which effect might be more linear for most of the cases, storm surge, yaw angle, and pressure slope have significant contribution to the occurrence of MTs, and does not have a fixed pattern. In this situation, ANN seems to be a essential method to substitute the traditional numerical simulation to forecast the MT hazard.

9.5 Conclusions and future work

To provide a broader and faster way to predict the hazards on a broad scale, an optimal BP artificial neural network (ANN) was trained using data from a large number of MT simulations in the northeastern GOM.

By varying incident direction, prescribed trajectory location, forward speed of the pressure disturbance, storm surge, yaw angle, and pressure slope, in total, 2325 runs were performed in order to generate a database of meteotsunami effects to train an ANN. The whole data set is divided into three sample sets, which are training data(70%), validation data(15%) and test data(15%). The inputs and output of the sample set were first normalized to a range of [-1, 1], respectively. An 8-30-20-1 BP ANN is built and trained and optimized the using the training sample set and the validation sample set is applied in order to avoid over-fitting at Clearwater Beach, FL.

Additionally, regression analysis of the output of ANN is performed using the training and validation sample set, resulting a correlation (R) bigger than 98%. Besides, the test sample set is used to test the performance of the trained ANN, and the results are compared with the numerical simulation, showing a correlation (R) bigger than 96%, and all the forecasting error are less than 0.04m and most of the errors are less than 0.02m. Furthermore, the formula of the ANN is presented, providing a reliable and timely predicting method comparing to the traditional numerical simulation method which could take longer to forecast the maximum wave elevation caused by the MT.

The trained BP neural network is then used to generate a more comprehensive data set in order to investigate the effect of three new parameters. Even thought some regular pattern can be found for some situation, it is difficult to come up with an easy pattern for most of the cases, which makes it even more important to use ANN to forecast MT.

In the current study, due to the limitation of the computational resource, the range of all the parameters are limited in a small range. Even thought the capability of ANN on forecasting in this range is validated, more cases need to be simulated in order to forecast all the possible cases.

In the future, more data needs to be generated within different areas in the Gulf of Mexico

in order to get a more comprehensive tool for us to forecast and mitigate the hazard caused by MTs.

10 Conclusions

This project focused on the implementation of recent developments in the tsunami science recommended by the National Tsunami Hazard Mitigation Program - Modeling Mapping Subcommittee - Strategic Plan (NTHMP-MMS-SP) into our current Gulf of Mexico (GOM) tsunami mitigation products. Three main developments for tsunami mitigation have been created under this project for two new communities in the GOM (Orange Beach, AL and Mexico Beach, FL) that will provide guidance to state emergency managers for tsunami hazard mitigation and warning purposes. The first task is the development of tsunami inundation maps for the two selected communities with nine landslide sources. The second is the comparison between existing SLOSH hurricane flooding data and our tsunami inundation result for the two new communities in order to facilitate temporal-low-order estimate for tsunami hazard areas (community) where inundation studies have not yet been assigned/executed or where little bathymetric and elevation data exists. The third is to produce maritime products (maximum of maximum (MOM) velocity and velocity magnitude maritime maps) for both communities to help identify impact specifically on ship channels, bay inlets, harbors, marinas, and other infrastructures. An additional task is a study where we conducted numerical experiments to investigate the generation and propagation of meteotsunami waves and assessed hazards on a broad scale in the whole Gulf of Mexico (GOM). In this project, we expanded the previous parameter study from 1260 runs on 1 arcminute grid to 17280 runs on a more accurate 15 arcsecond grid, thanks to the huge performance increase brought by converting our meteotsunami code to CUDA using a newly built triple GPU workstation. Also in this study we attempt an MT characterization for Clearwater,FL along the west coast of Florida to get maximum MT wave amplitude (η_{max_MT}) expected for a given pressure disturbance condition using MT Rose Plots. This characterization can be used to generate Emergency Response Playbooks (ERP) for various places that can be used by emergency planners and interested parties to add the MT component to the storm surge. Last, to provide a broader and faster way to predict the hazards on a broad scale in the northeastern Gulf of Mexico, an optimal artificial neural network (ANN) was trained using the large combination of pressure propagating speed and path generated from the numerical simulations.

Tsunami wave propagation and inundation in Orange Beach, AL and Mexico Beach, FL was modeled to obtain maximum inundation and extent, momentum flux, current velocity and vorticity maps considering the entire suite of nine landslide sources. In Gulf Shores, AL, under the worst case scenario, tsunami waves would inundate all of the barrier islands south of the Fort Morgan Road (west of Alabama's Coastal Connection or State Highway 135) and south of the Gulf Oak Ridge Trail and the Rattlesnake Ridge Trail. The highest inundation ($>$ 4 m) occurs immediate ocean front and around the Little Lagoon, and the other potentially at-risk area would expect less than 3 meters of inundation. The area around the Oyster Bay is also inundated, albeit this area is not populated and the inundation is mostly under 1.5 m. In Orange Beach, AL (also including Ono Island, AL and Perdido Key, FL), under the worst case scenario, tsunami would inundate all of the barrier islands. Overall water depth exhibits decreasing trend from oceanfront toward the bay, with maximum over 4 m. The MOM tsunami inundation at Orange Beach and western section of Perdido Key,

FL are generally higher than eastern Perdido Key, as > 4 m also could occur north of the Perdido Beach Blvd. On Ono Island, AL, > 4 m inundation only occurs at the south ocean front, while 2 - 3 m inundation occurs around the intersection between River Rd and Ono Blvd. On mainland Florida, the areas south of the Gulf Beach Hwy and S Blue Angel Pkwy can be flooded. Tsunami inundation area higher than 4 m is larger south of S Blue Angel Pkwy than south of Gulf Beach Hwy due to its proximity to the inlet (between Fort Pickens and Fort McRee).

In Mexico Beach and Port St Joe mapping area, the St Joseph Pennisula/barrier island could be completely inundated under the worst case scenario. The pennisula provides ample protection for Port St Joe, but not so much for the exposed Mexico Beach. While inundation depth at the St Joseph Pennisula ranges from 2 to over 4 m from the GOM side to the bay, the residential areas mostly fall under > 4 m zone since they are closer to the GOM. Similarly on the south barrier island of Port St Joe, high inundation can be expected south of the line connecting Cape San Blas Rd, Florida County Rd 30A, and Indian Pass Rd, where the residential areas are located. On the mainland, Mexico Beach's worst case scenario (MOM) inundation is much higher than Port St Joe due to its lack of protection from St Joseph Pennisula. Southeast of Highway 98 in Mexico Beach, inundation is larger than 3 - 4 m. Northeast of Highway 98, high (> 3 - 4 m) inundation occurs mostly around the water channels/marinas, while it decreases from 3 to 1 m outwards from the channels. Moving south toward Port St Joe, inundation is mostly contained southeast of Highway 98, however, high (> 3 - 4 m) water depth starts to occurs south of the line formed by Lightkeepers Dr, See Pines Ln, Cristins Curve Rd, Ocean Ridge Ln, and Alabama Ave. Pass the north tip of St Josepth Pennisula, maximum inundation in Port St Joe adjacent to St Joseph Bay falls below 3 m. South of Gulf County Canal, the worst case scenario (MOM) inundation in Port St Joe occurs mostly south of Marine Dr (First St) and west of Woodward Ave based (on)Fig. 79). For both communities, MOM tsunami inundation is produced solely by the Mississippi Canyon failure. This geological failure is the largest in both, area and volume of material removed, and therefore produces the highest amplitude wave of all simulated sources.

While high-resolution tsunami inundation studies have been completed for these 20 communities and are planned for additional locations, vulnerability assessments are still essential for coastal locations where inundation studies have not yet been performed or planned, or where there is a lack of high-resolution bathymetric and/or elevation data. Therefore, we aim to extend the results of the completed mapping studies in order to provide estimates of tsunami inundation zones for hazard mitigation efforts in unmapped locations. We anticipate that communities which lack detailed tsunami inundation maps, but which have modeled hurricane storm surge information, would be able to use the results presented here to estimate their potential tsunami hazard level based on their regional topographical/bathymetric features. We stress, however, that such results should be used only in a broad, regional sense given the differences seen among and within communities based on local details of bathymetry, topography, and geographical location within the GOM basin. There is no guarantee that comparison results will be identical in areas with similar topography, and comparisons should only be made after understanding the limitations and simplifications of the methodology presented here. Comparisons of MOM tsunami inundation results with the

SLOSH MOM high tide storm surge inundation indicate that while the details of referencing tsunami inundation to hurricane storm surge is dependent on local topographic effects, general regional trends can be identified.

In Gulf Shores, AL, the hurricane category that best matches tsunami inundation closely follows the MOM tsunami inundation trend, where Category 5 appears near the beach and around the Little Lagoon. Going away from Category 5 are Category 4 and 3 for the barrier island and Category 2 and 1 appear around the Oyster Bay. The difference between hurricane flooding and tsunami inundation is mostly within ± 1 m. In Orange Beach, AL, the hurricane category that best matches tsunami inundation closely follows the MOM tsunami inundation trend. On Perdido Key, Category 3 to 5 appears from the beach to the bay, and similar to the higher inundation at western Perdido Key, there are predominantly Category 4 and 5. On mainland Florida, Category 3 and 4 appear in the areas south of the Gulf Beach Hwy and Category 4 and 5 south of S Blue Angel Pkwy. The difference between hurricane flooding and tsunami inundation is mostly within ± 1 m. For Mexico Beach and Port St Joe, the matching hurricane category distribution closely reflects that of tsunami inundation. Category 5 is dominant on St Joseph Pennisula and on the south barrier island. On Mexico Beach, similarly, there are mostly Category 5. Following south along Highway 98 (where there are residents), hurricane category reduces from 5 to 4, and eventually to 3 when entering St Joseph Bay. South of Gulf County Canal, Category 3 becomes dominant until it reaches south of W Rutherford St where it is close to the south barrier island. The difference between hurricane flooding and tsunami inundation $\Delta\zeta$ is generally within $\pm$ 0.5 m, except for Mexico Beach and GOM side of the St Joseph Pennisula and most of the Port St Joe barrier island. This difference means storm surge inundation depth is shallower than tsunami inundation.

We produced the MOM velocity and vorticity magnitude maps for all the landslide scenarios, for Orange Beach, AL and Mexico Beach, FL, based on a simplified current velocity damage scale where we associate 0 - 3 knots to unharmful currents, 3 - 6 knots to minor damage, 6 - 9 knots to moderate damage, and over 9 knots to major damage. The four damage levels are denoted with white, blue, yellow and red colors, respectively.

From the MOM velocity magnitude results in the entire Gulf of Mexico, it can be observed that, potential damaging currents ($>$ 3 knots, blue, yellow and red areas) tend to be present in most of the area shallower than the minimum offshore safe depth (approximately 200 m or 100 fathoms). However, damaging currents could reach areas deeper than 200 m close to most of the landslide generation regions. Major damaging currents ($>$ 9 knots, red) can be expected in most of the landslide generation regions, in the continental shelf adjacent to Mississippi Canyon, offshore northwest Florida, and Yucatán shelf. Moderate ($>$ 6 knots and $<$ 9 knots, yellow) damaging current areas are scattered over the continental shelf, but mostly close to areas with major damage currents. For Orange Beach, AL, most of offshore region is expected to have moderate damaging currents, with major damaging currents occurring along the coastline, inlets, and the immediate bay side of the barrier island. There is generally no moderate damaging currents farther behind the barrier islands, however, the exception is the Little Lagoon where it is filled with moderate and major damaging currents (over 6 knots). In Mexico Beach, FL mapping region (Mexico Beach and Port St Joe), the situation is a bit different from Orange Beach, AL. In general, the worst case (MOM)

tsunami currents are more severe; major damaging current is more prevalous across the GOM and around St Joseph Pennisula. Behind the pennisula, St Joseph Bay sees much calmer tsunami current velocities (< 6 knots) except for the small region adjacent to the pennisula. The exposed Mexico Beach and Saint Joe Beach should expect major damaging currents along the beach. For both Orange Beach, AL and Mexico Beach, FL, vorticity distribution displays similar patterns to their velocity distribution, where high vorticity appears around the barrier island, and are more intense near the bay entrances. Tsunami hazard maritime products such as tsunami current magnitude, vorticity, safe/hazard zones would be central for future developments of maritime hazard maps, maritime emergency response and as well as infrastructure planning.

Although relatively rare, meteotsunamis are capable of causing coastal infrastructure damage and casualties. Analyses of water level and meteorological data in the U.S. show that meteotsunamis occur more frequently than expected, and therefore, it is important to include meteotsunami assessment in coastal hazard mitigation efforts. In those previous numerical experiments, for each subregion (northeastern or northwestern GOM), we conducted 1260 runs (i.e., 12 incident wave directions $\times$ 15 trajectories $\times$ 7 velocities). Using a numerical model based on CPU and parallelized by OpenMP, we were able to finish each 30h run on a 1 arcminute grid in around 5 to 6 minutes, thereby finishing the whole 1260 runs within one week. However, we couldn't use the more accurate 15 arcsecond resolution grid due to each run taking more than 5 hours. In this project, we converted our CPU meteotsunami code to CUDA, and with the help of a newly built multi-GPU workstation which has three Nvidia RTX 3090 GPUs and is capable of running our meteotsunami Fortran code in CUDA 50 – 100 times faster than it CPU versoin, depending on the grid, we expanded the previous parameter study to 17280 runs (i.e., 36 incident wave directions $\times$ 30 trajectories $\times$ 16 velocities). The result is a significantly improved resolution of different incident wave direction, forward speed and trajectory position, and their effect on maximum gauge water elevation across the whole GOM.

Parameter study result in northeastern GOM indicates that the most favorable direction for higher water level are 0° - 120° (south to west, 3rd quadrant), and also around 270° (east), with each direction bin accounting for more than 3%, where gauge water level exceeds 0.2 m. Pressure disturbances coming from the south to west (0° - 90°) direction result in higher water level near south Florida region, while the east (270°) direction to the panhandle region. Similarly, the forward speed distribution result shows that 18m/s – 26 m/s are the forward speeds with the most potential, together accounting for more than 40% of the cases. In northwestern GOM, results show that Louisiana coasts are less likely to be hit with a high meteotsunami wave than Texas, and that the convex sections of Texas coastline are more susceptible to meteotsunami waves coming from various directions. Statistical analysis indicates that pressure disturbances coming from south – east direction result in higher water level in this region. The forward speed distribution shows that 18 m/s – 28 m/s have the most potential.

This study further developed the previous meteotsunami (MT) characterization effort in the Gulf of Mexico (GOM). A larger number of runs (34,560) has been incorporated in the MT characterization analysis for the entire GOM. Previous MT rose charts were modified to a finer resolution (adding more directions and forward speed of the Atmospheric disturbance

(AD)) at 98 numerical gauges or locations along the GOM coastline. New visualization tools have been included, namely, severe MT rose chart. This new visualization tool facilitates the identification of severe case scenarios along the 98 studied locations. Eight of these locations are shown in this report and MT hazards are presented in greater detail. All the locations analyzed show susceptibility to severe MTs when ADs move along (parallel) to the coastline over the continental shelves. ADs moving up or down along the coastline can create higher MTs. In general, the wide and gently sloping shelves of GOM aid the production of MTs. Further, ADs with forward speeds in the range of 16 to 28 m/s are the ones that create most of the severe MT hazard scenarios. Based on the cases identified using the severe MT rose charts, a closer look was taken at the MT amplitudes generated by those cases using the corresponding original MT rose charts. In the northwestern GOM, slower-moving ADs with speeds near 14 m/s are responsible for the most extreme MTs (up to 0.48 m MT in South Padre, TX). In the eastern GOM coast along FL, where the shelves are broader, slightly faster moving ADs between 16 and 24 m/s create large MTs (maximum 0.43 m at Clearwater Beach, FL). Faster moving ADs ranging from 24 to 40 m/s create the largest MTs for the northwestern region of the GOM, where the continental shelves get narrower (up to 0.43 m MT in Panama City, FL). These results further exemplify the close relationship between the MT amplitude at a location and the bathymetry in nearby continental shelves.

Last, to provide a broader and faster way to predict the hazards on a broad scale, an optimal artificial neural network (ANN) was trained using data from a large number of MT simulations in the northeastern GOM. Regression analysis of the output of ANN was performed at Clearwater Beach, FL, and the results are consistent with numerical simulation with a correlation coefficient greater than 98%. An additional three parameters were investigated (yaw angle, storm surge, and pressure slope), unlike other more predictive parameters like pressure wave amplitudes, their effects on maximum meteotsunami water elevation at the gauges are highly nonlinear.

Although the recurrence of destructive tsunami events have been verified to be quite low in the GOM, our work has confirmed that submarine landslide events with similar characteristics to those used here, have indeed the potential to cause severe damage to GOM coastal communities. GOM is a region where tropical cyclones and winter storms occur frequently. From 1996 to 2016, there are around 20 meteotsunami events on average in Florida. Our results indicate meteotsunami water level could reach as high as 0.5 m in some locations and has the potential to cause damage. Therefore, this work is intended to provide guidance to local emergency managers to help managing urban growth, evacuation planning, and public education with the final objective to mitigate potential landslide tsunami and meteotsunami hazards in the GOM.

Acknowledgments

This work was supported by the National Oceanic and Atmospheric Administration (NOAA) under awards NA21NWS4670012, "Development of two tsunami inundation maps and continuation of the meteotsunami characterization for the GOM". The authors wish to thank all NTHMP modeling and Mapping Subcommittee members and GOM's emergency manager

representatives for their helpful insights. *****Special thanks go to Brad Baker for their helpful insight and support. Also thank Kelly Carignan and Kelly Stroker for providing the DEMs. High resolution inundation maps are available from `http://www.tamug.edu/tsunami/NTHMP/NTHMP.html` or by contacting corresponding author upon request.

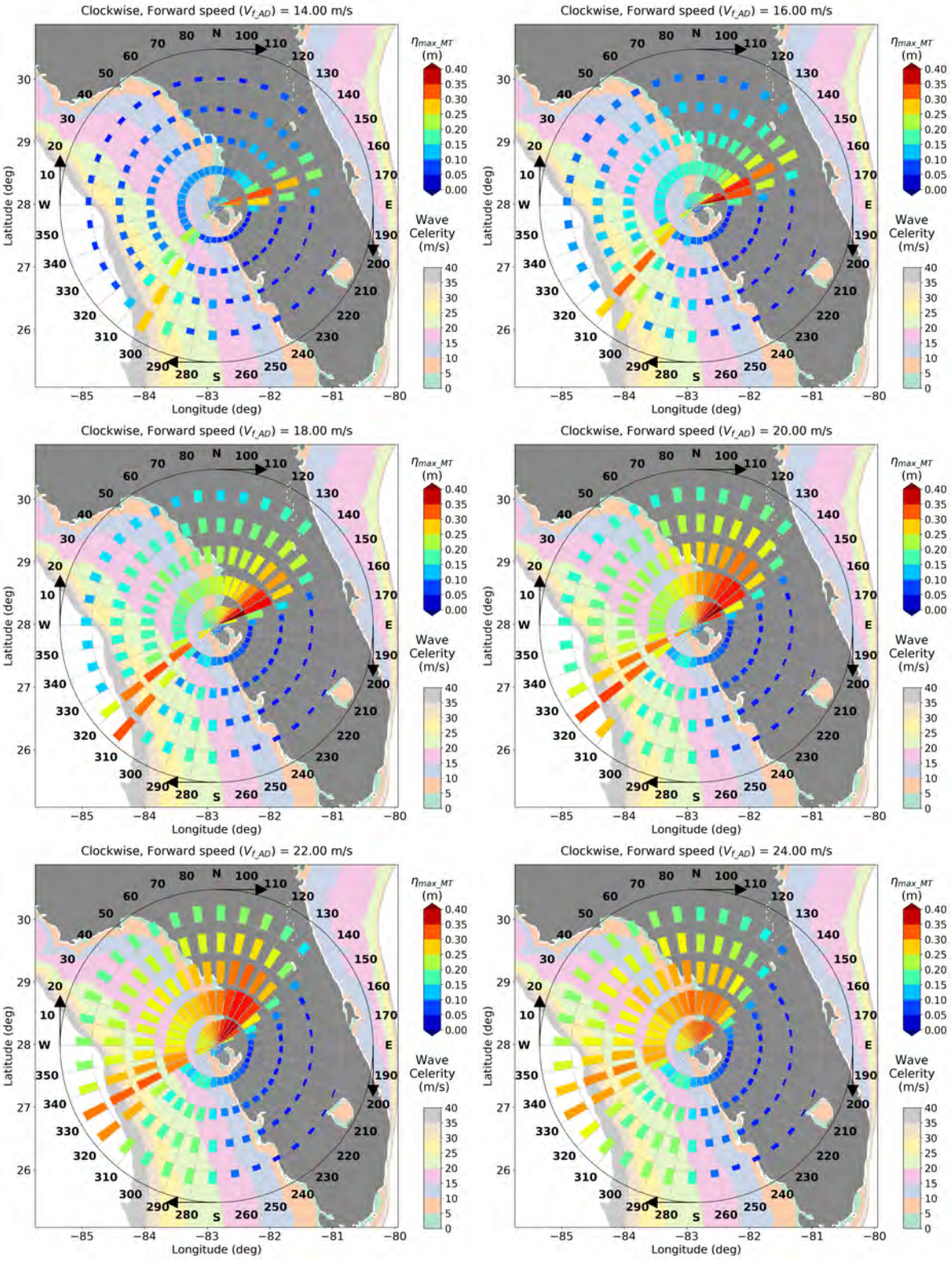

Figure 112: MT rose charts for η_{max_MT} at a field site near Clearwater Beach (82.85 W 27.98 N), water depth = 3.5 m from MHW represented by bar's height for an AD(p_{AD} = 6 mbar) moving clockwise relative to the field site, with $V_{f_{AD}}$ = 14,16,18,20,22,24 m/s

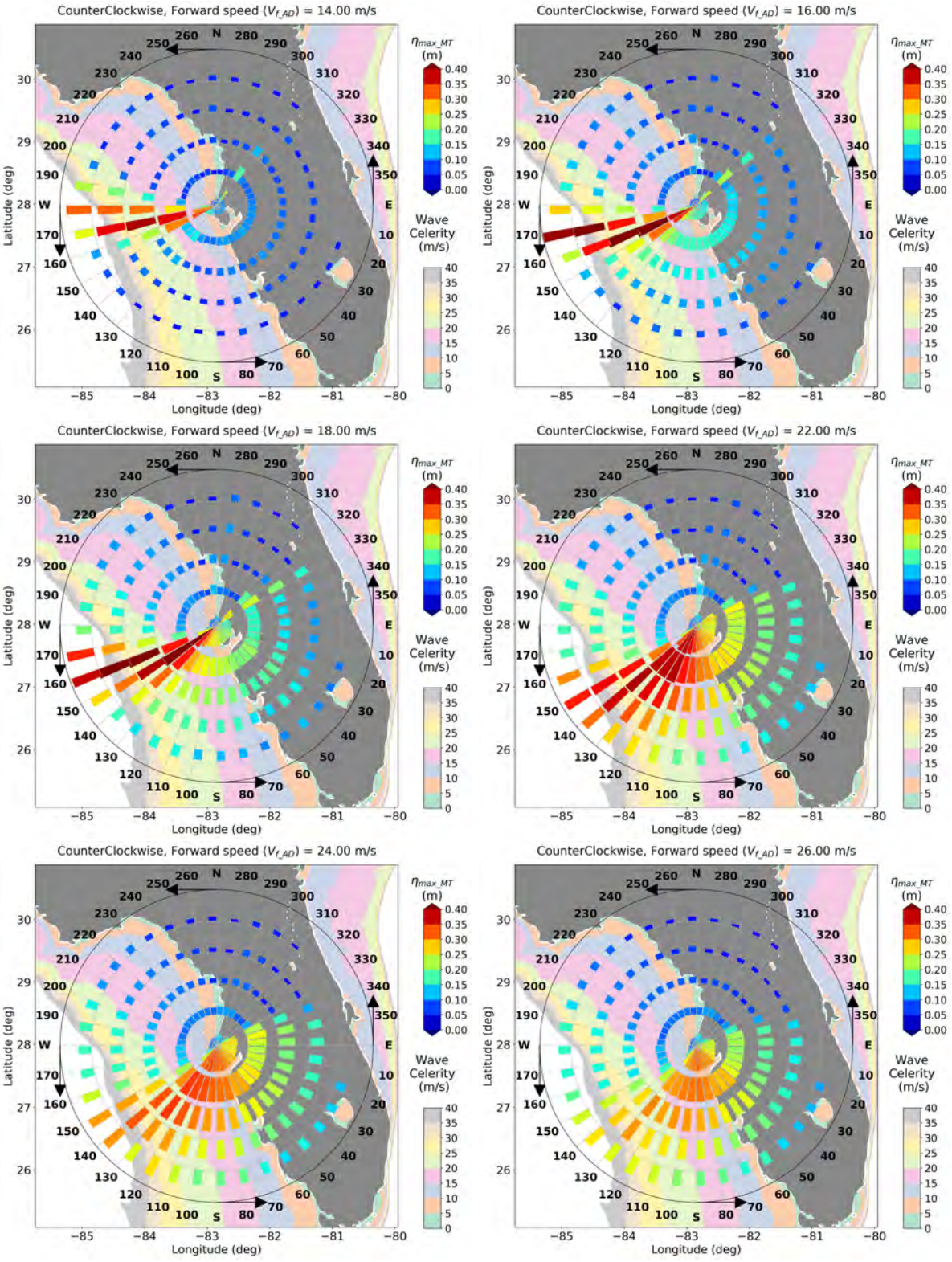

Figure 113: MT rose charts for η_{max_MT} at a field site near Clearwater Beach (82.85 W 27.98 N), water depth = 3.5 m from MHW represented by the bar's height for an AD(p_{AD} = 6 mbar) moving counterclockwise relative to the field site, with $V_{f_{AD}}$ = 14,16,18,22,24,26 m/s

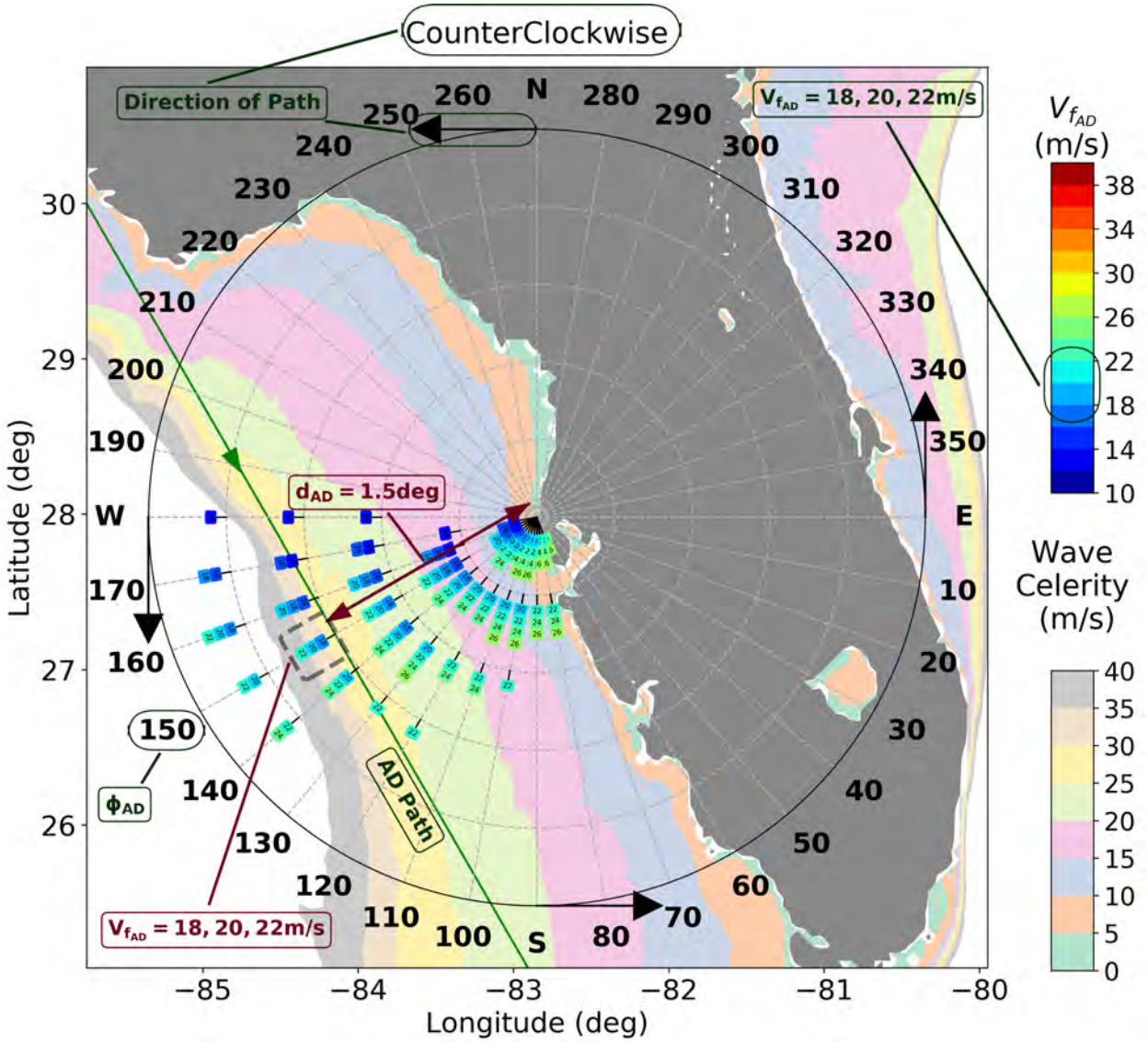

Figure 114: Severe MT rose chart for MT events with η_{max_MT} greater than 0.3 m at a field site near Clearwater Beach, FL (82.85 W 27.98 N), water depth = 3.5 m from MHW for an AD(p_{AD} = 6 mbar) from direction $\phi_{AD} = 150°$ moving counterclockwise relative to the field site, with $d_{AD} = 1.5$ deg with $V_{f_{AD}} = 18$, 20, 22 m/s color-coded blocks

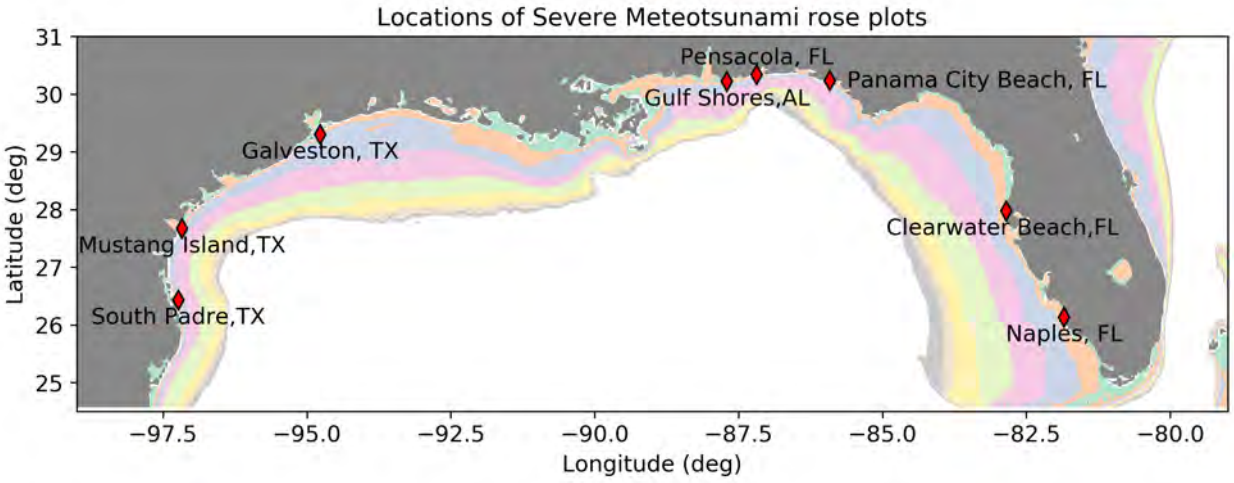

Figure 115: Locations along the GOM for severe MT rose charts

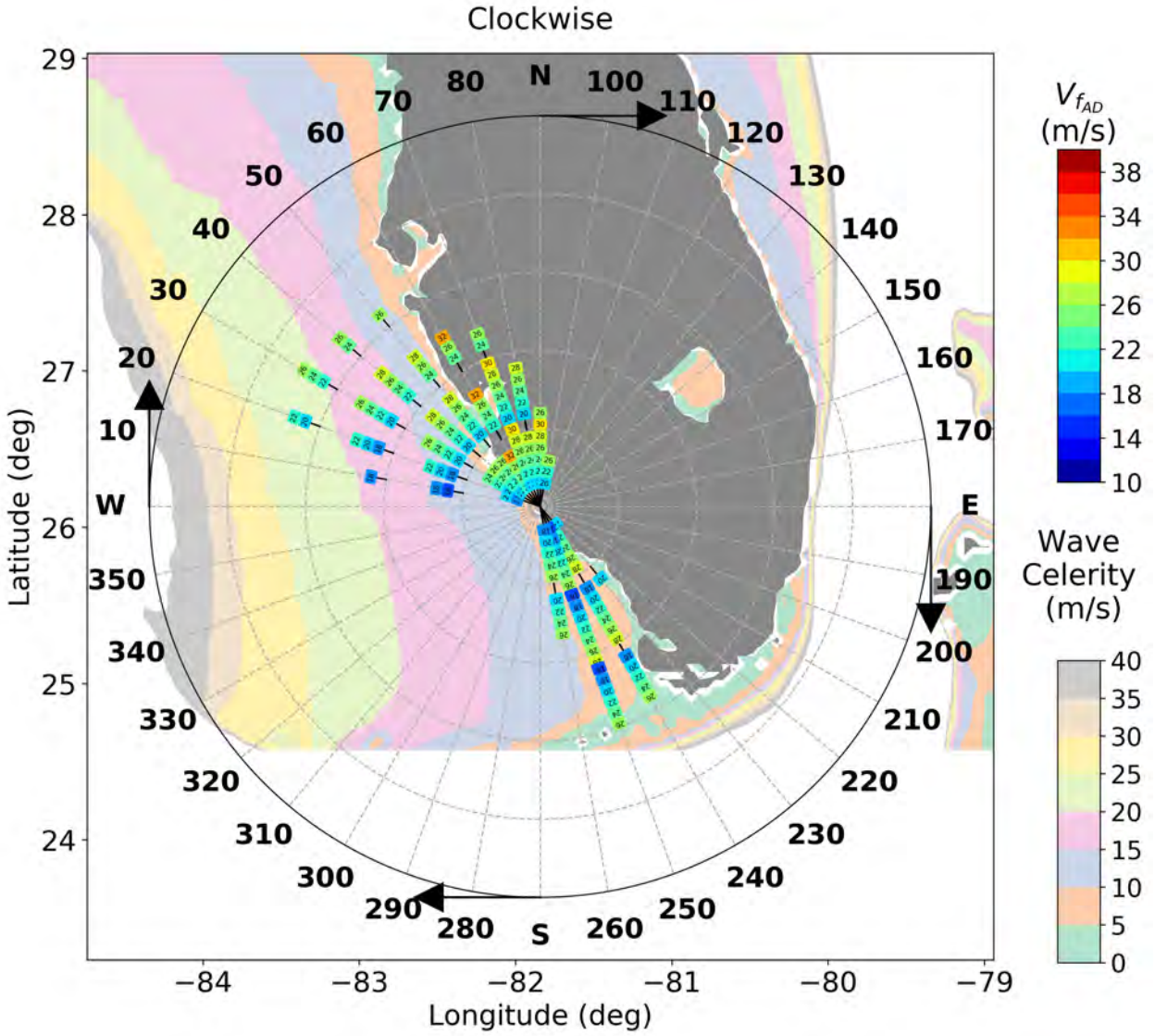

Figure 116: Severe MT rose chart for MT events with η_{max_MT} greater than 0.3 m at a field site near Naples, FL(81.84 W 26.13 N), Water depth = 7.8 m from MHW for an AD($p_{AD} = 6$ mbar) moving clockwise relative to the field site, with $V_{f_{AD}}$s representing color-coded blocks

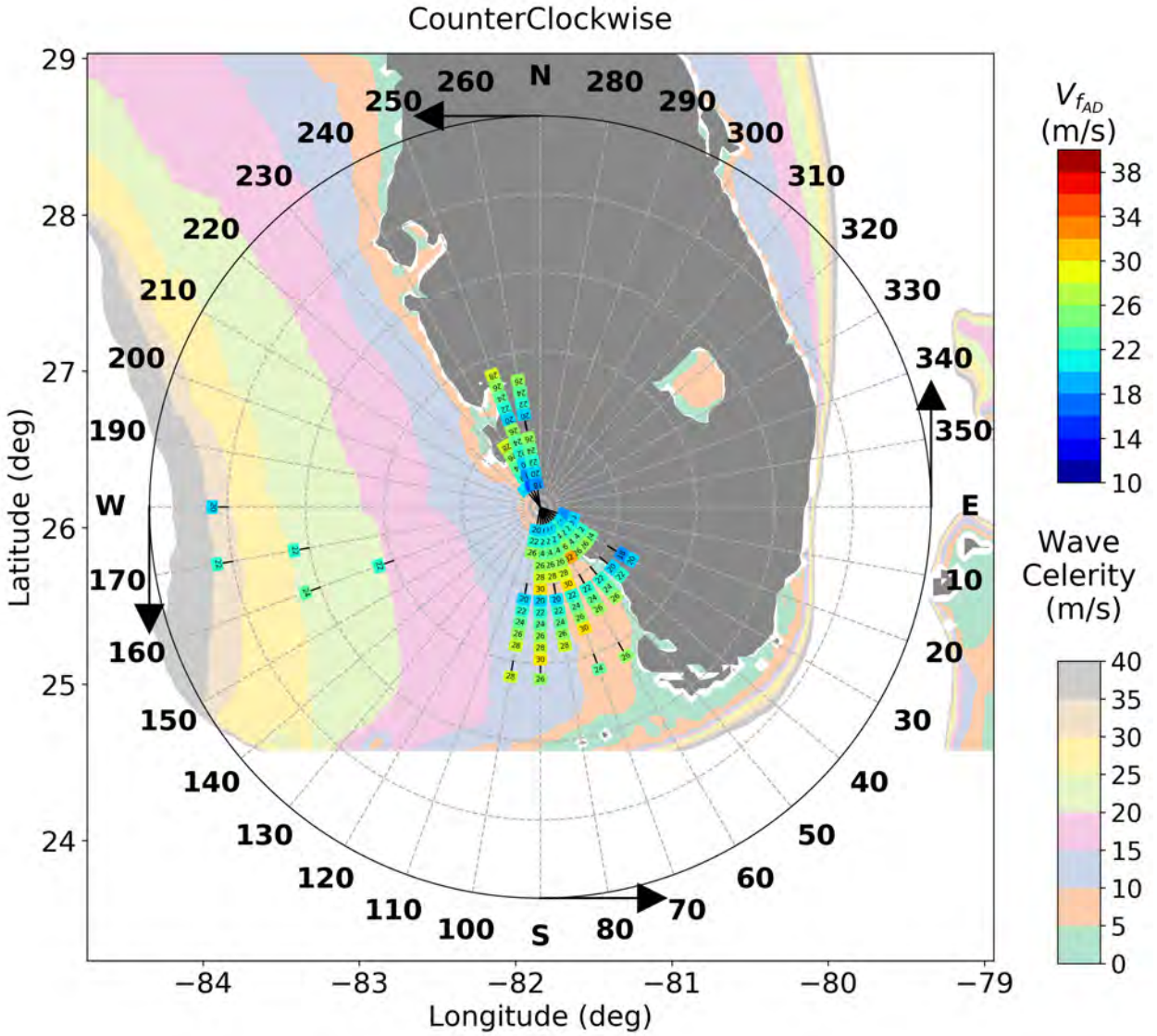

Figure 117: Severe MT rose chart for MT events with η_{max_MT} greater than 0.3 m at a field site near Naples, FL(81.84 W 26.13 N), Water depth = 7.8 m from MHW for an AD($p_{AD} = 6$ mbar) moving counterclockwise relative to the field site, with $V_{f_{AD}}$s representing color-coded blocks

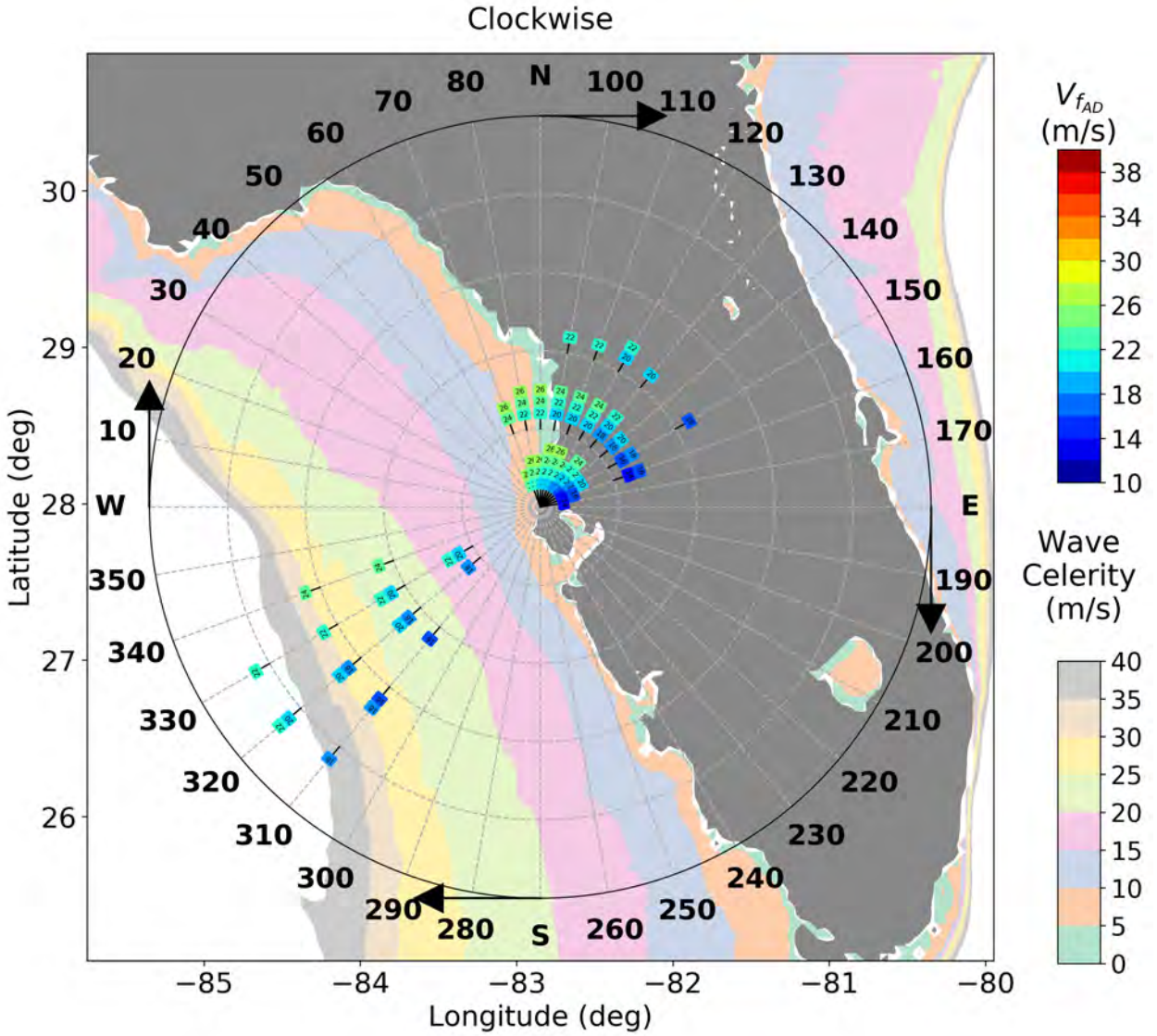

Figure 118: Severe MT rose chart for MT events with η_{max_MT} greater than 0.3 m at a field site near Clearwater Beach, FL (82.85 W 27.98 N), Water depth = 3.5 m from MHW for an AD(p_{AD} = 6 mbar) moving clockwise relative to the field site, with $V_{f_{AD}}$s representing color-coded blocks

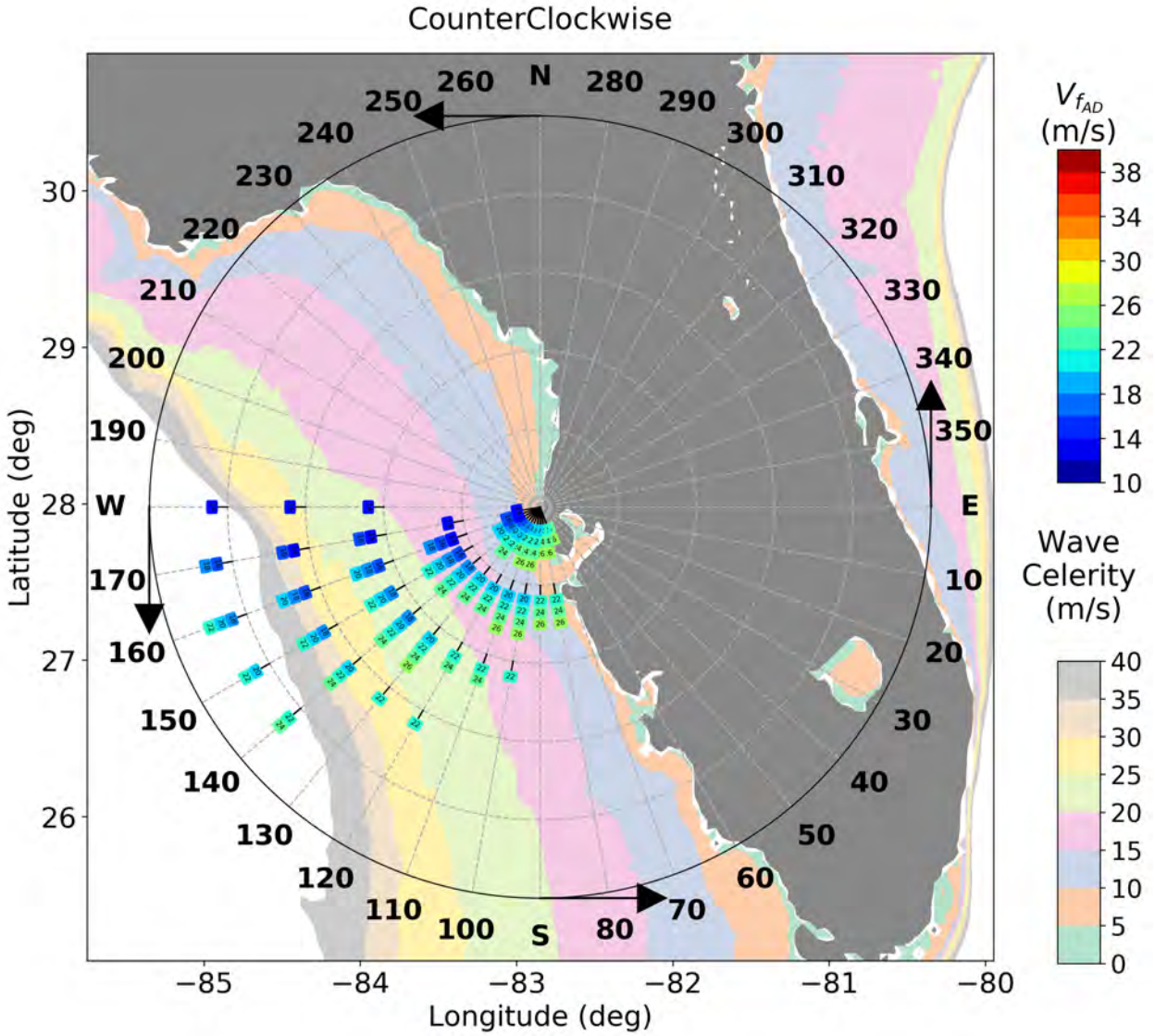

Figure 119: Severe MT rose chart for MT events with η_{max_MT} greater than 0.3 m at a field site near Clearwater Beach, FL (82.85 W 27.98 N), Water depth = 3.5 m from MHW for an AD(p_{AD} = 6 mbar) moving counterclockwise relative to the field site, with $V_{f_{AD}}$s representing color-coded blocks

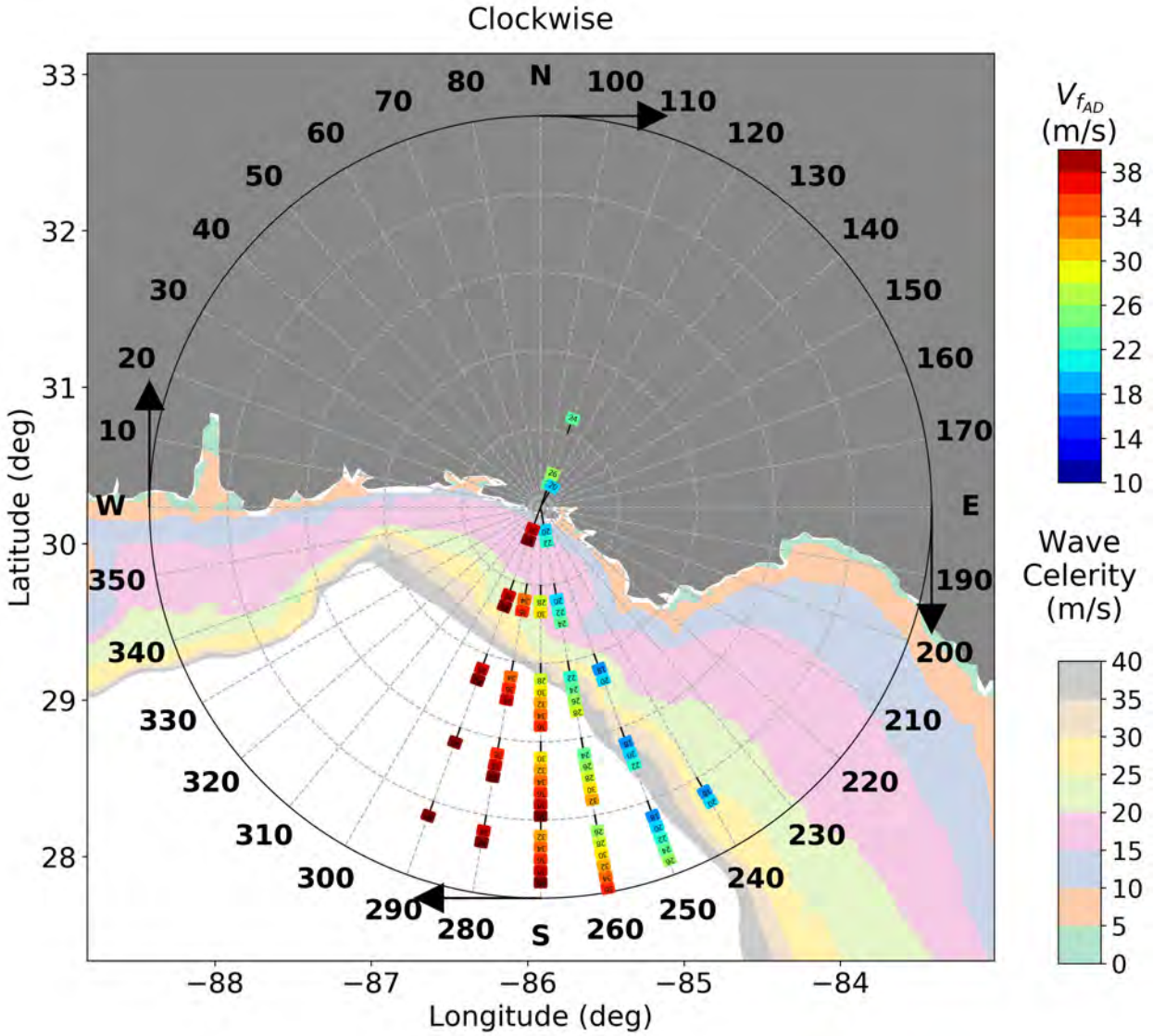

Figure 120: Severe MT rose chart for MT events with η_{max_MT} greater than 0.3 m at a field site near Panama City Beach, FL(85.92 W 30.23 N), Water depth = 9.9 m from MHW for an AD(p_{AD} = 6 mbar) moving clockwise relative to the field site, with $V_{f_{AD}}$s representing color-coded blocks

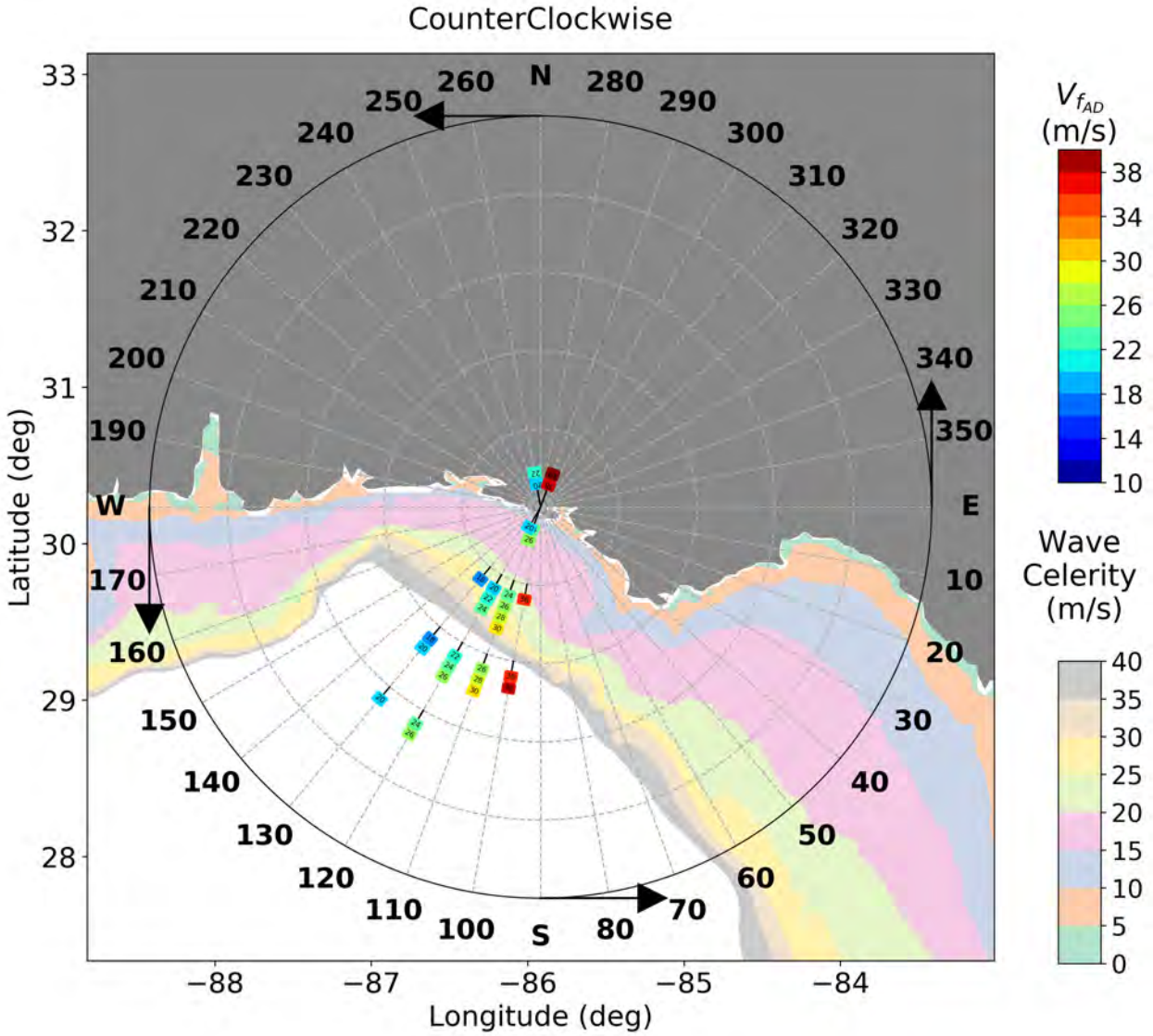

Figure 121: Severe MT rose chart for MT events with η_{max_MT} greater than 0.3 m at a field site near Panama City Beach, FL(85.92 W 30.23 N), Water depth = 9.9 m from MHW for an AD(p_{AD} = 6 mbar) moving counterclockwise relative to the field site, with $V_{f_{AD}}$s representing color-coded blocks

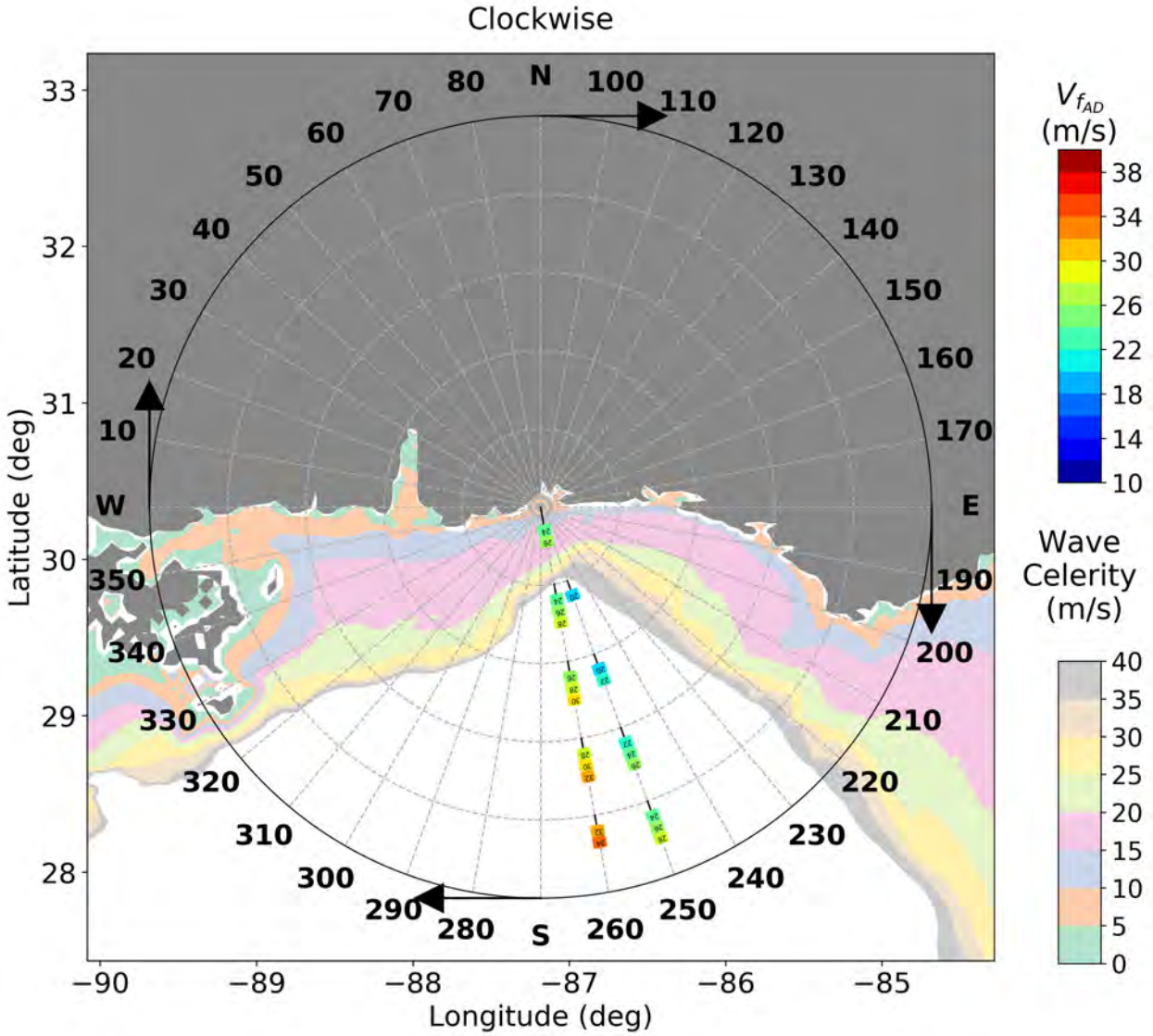

Figure 122: Severe MT rose chart for MT events with η_{max_MT} greater than 0.3 m at a field site near Pensacola, FL(87.18 W 30.33 N), Water depth = 5.5 m from MHW for an AD(p_{AD} = 6 mbar) moving clockwise relative to the field site, with $V_{f_{AD}}$s representing color-coded blocks

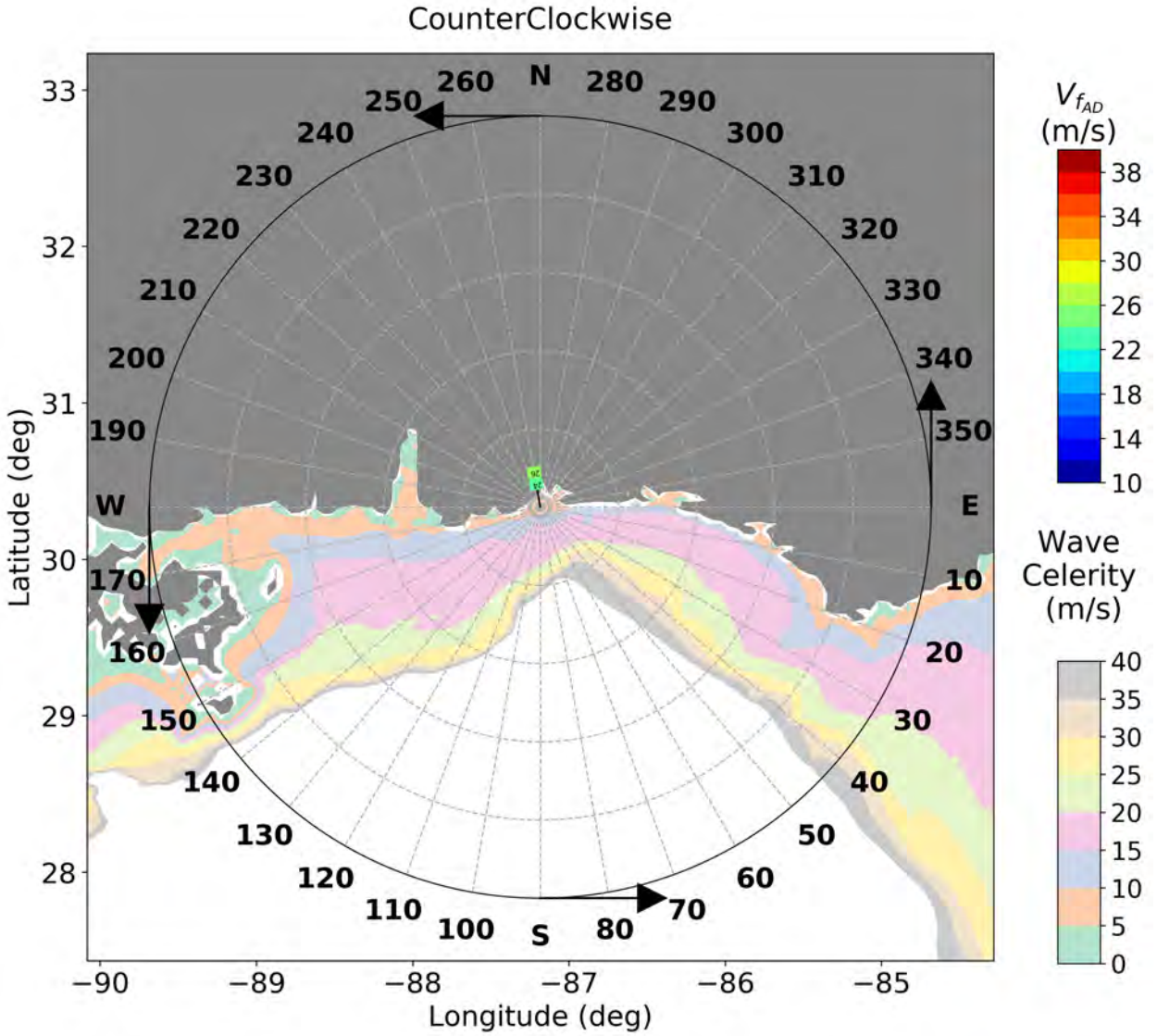

Figure 123: Severe MT rose chart for MT events with η_{max_MT} greater than 0.3 m at a field site near Pensacola, FL(87.18 W 30.33 N), Water depth = 5.5 m from MHW for an AD($p_{AD} = 6$ mbar) moving counterclockwise relative to the field site, with $V_{f_{AD}}$s representing color-coded blocks

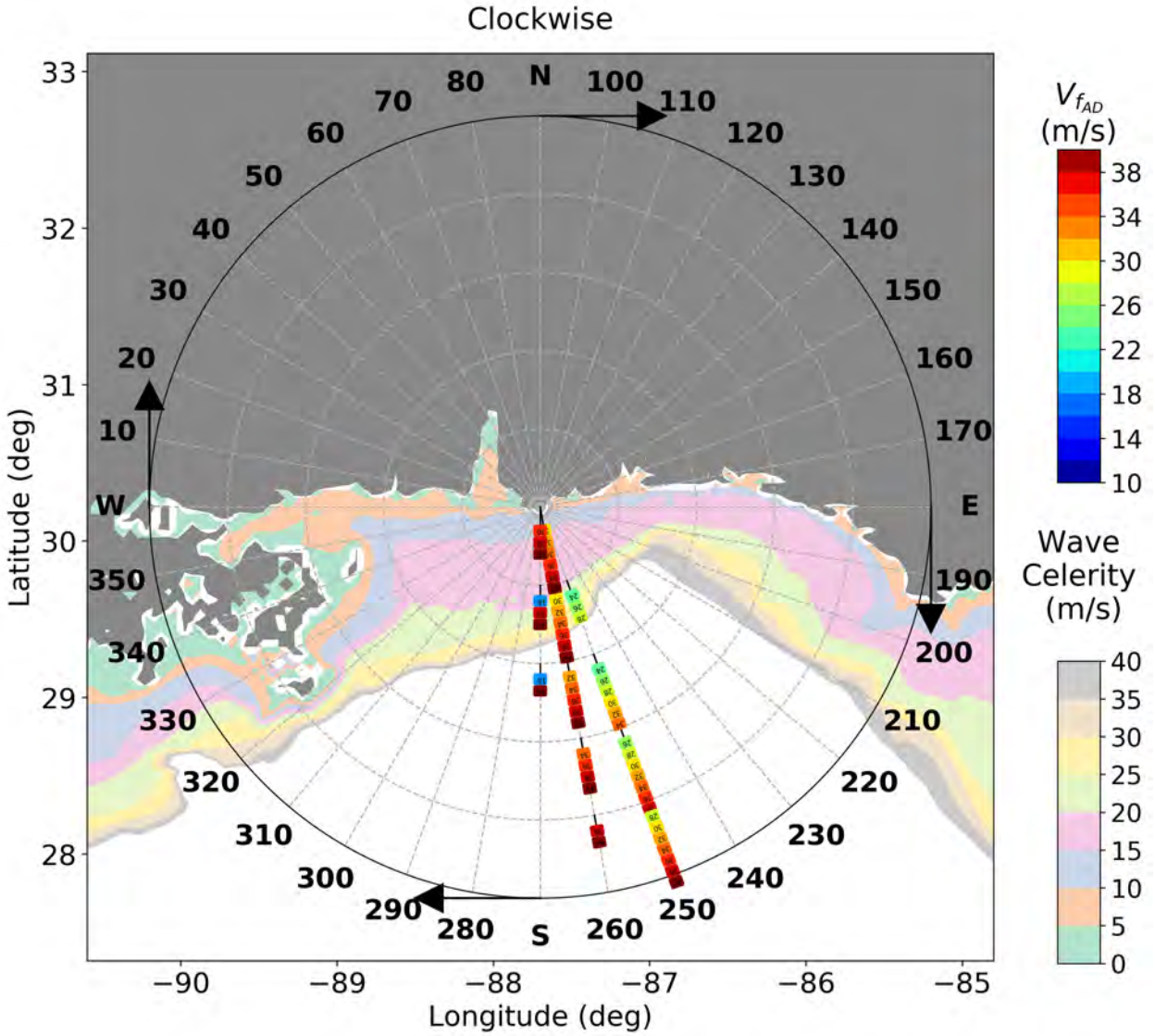

Figure 124: Severe MT rose chart for MT events with η_{max_MT} greater than 0.3 m at a field site near Gulf Shores, AL(87.70 W 30.22 N), Water depth = 10.8 m from MHW for an AD(p_{AD} = 6 mbar) moving clockwise relative to the field site, with $V_{f_{AD}}$s representing color-coded blocks

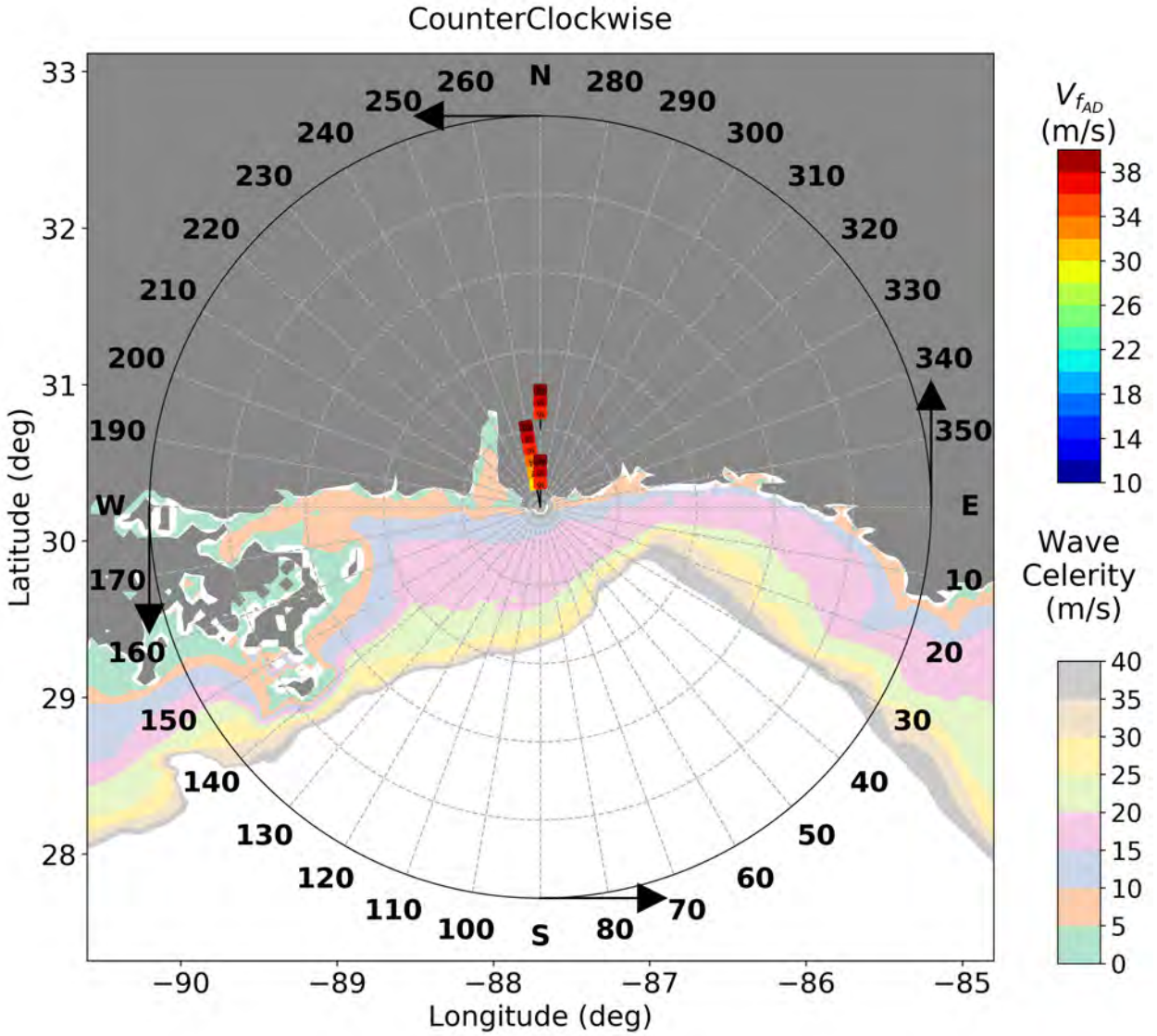

Figure 125: Severe MT rose chart for MT events with η_{max_MT} greater than 0.3 m at a field site near Gulf Shores, AL(87.70 W 30.22 N), Water depth = 10.8 m from MHW for an AD($p_{AD} = 6$ mbar) moving counterclockwise relative to the field site, with $V_{f_{AD}}$s representing color-coded blocks

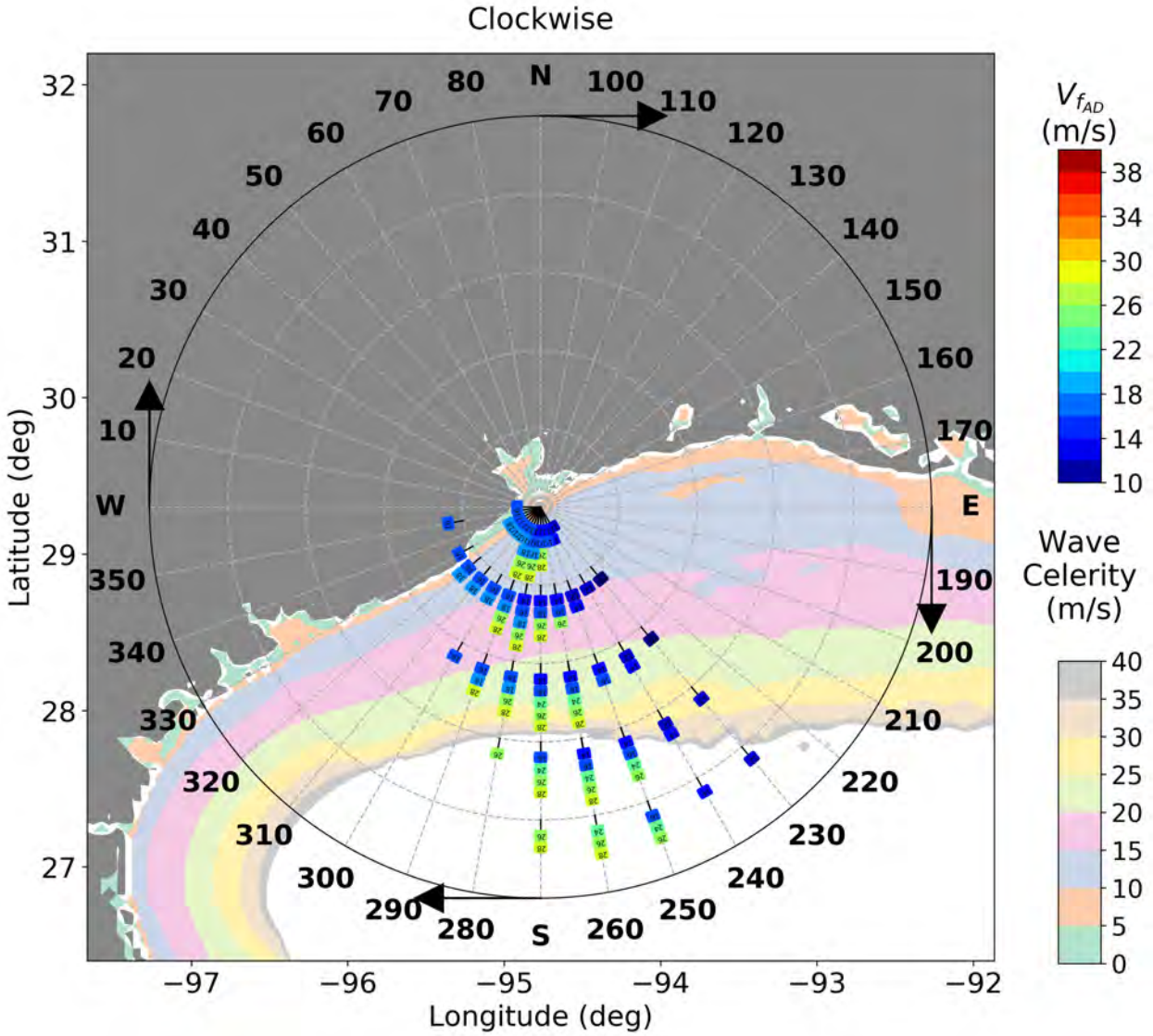

Figure 126: Severe MT rose chart for MT events with η_{max_MT} greater than 0.3 m at a field site near Galveston, TX(94.77 W 29.30 N), Water depth = 8.2 m from MHW for an AD(p_{AD} = 6 mbar) moving clockwise relative to the field site, with $V_{f_{AD}}$s representing color-coded blocks

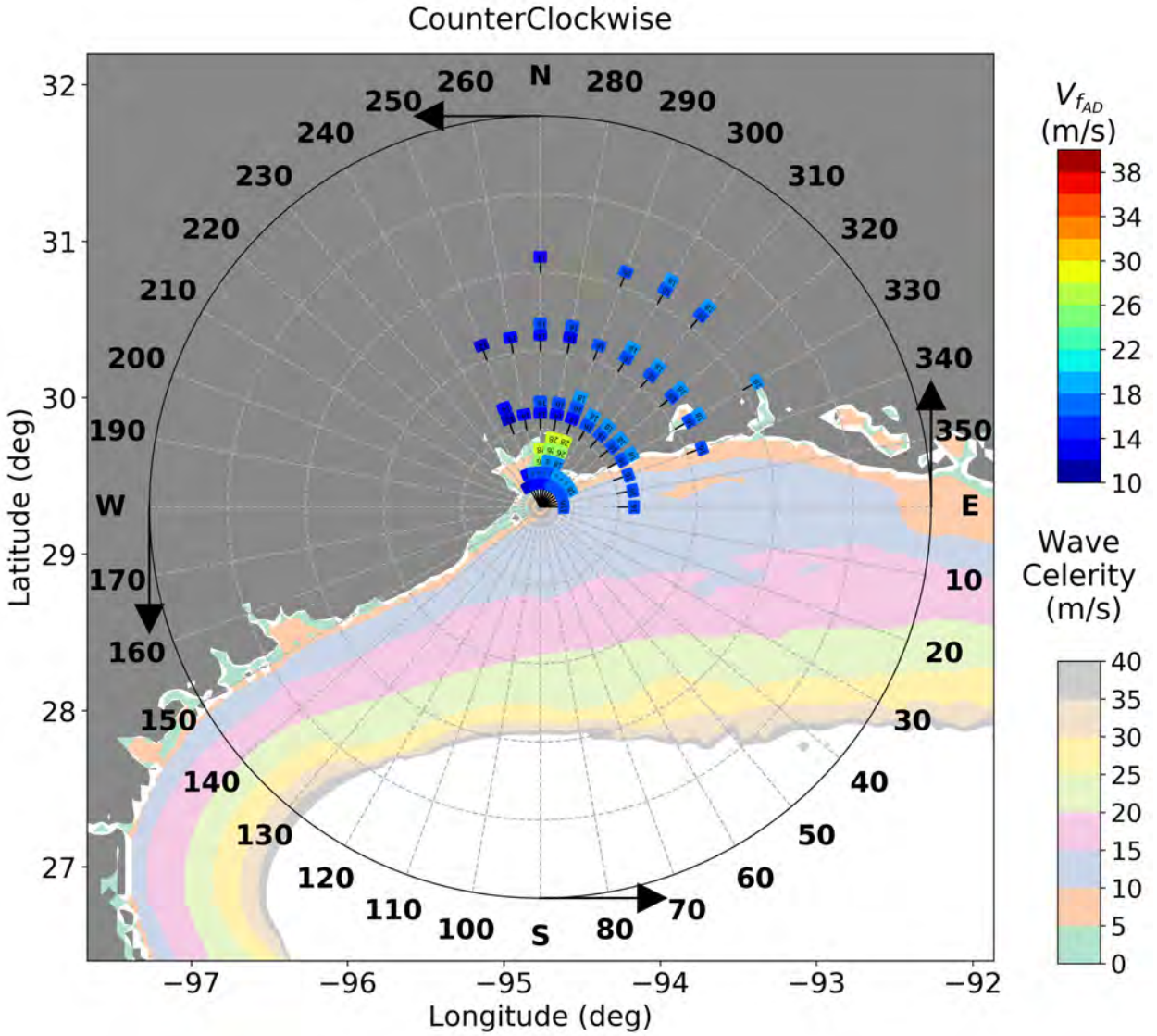

Figure 127: Severe MT rose chart for MT events with η_{max_MT} greater than 0.3 m at a field site near Galveston, TX(94.77 W 29.30 N), Water depth = 8.2 m from MHW for an AD($p_{AD} = 6$ mbar) moving counterclockwise relative to the field site, with $V_{f_{AD}}$s representing color-coded blocks

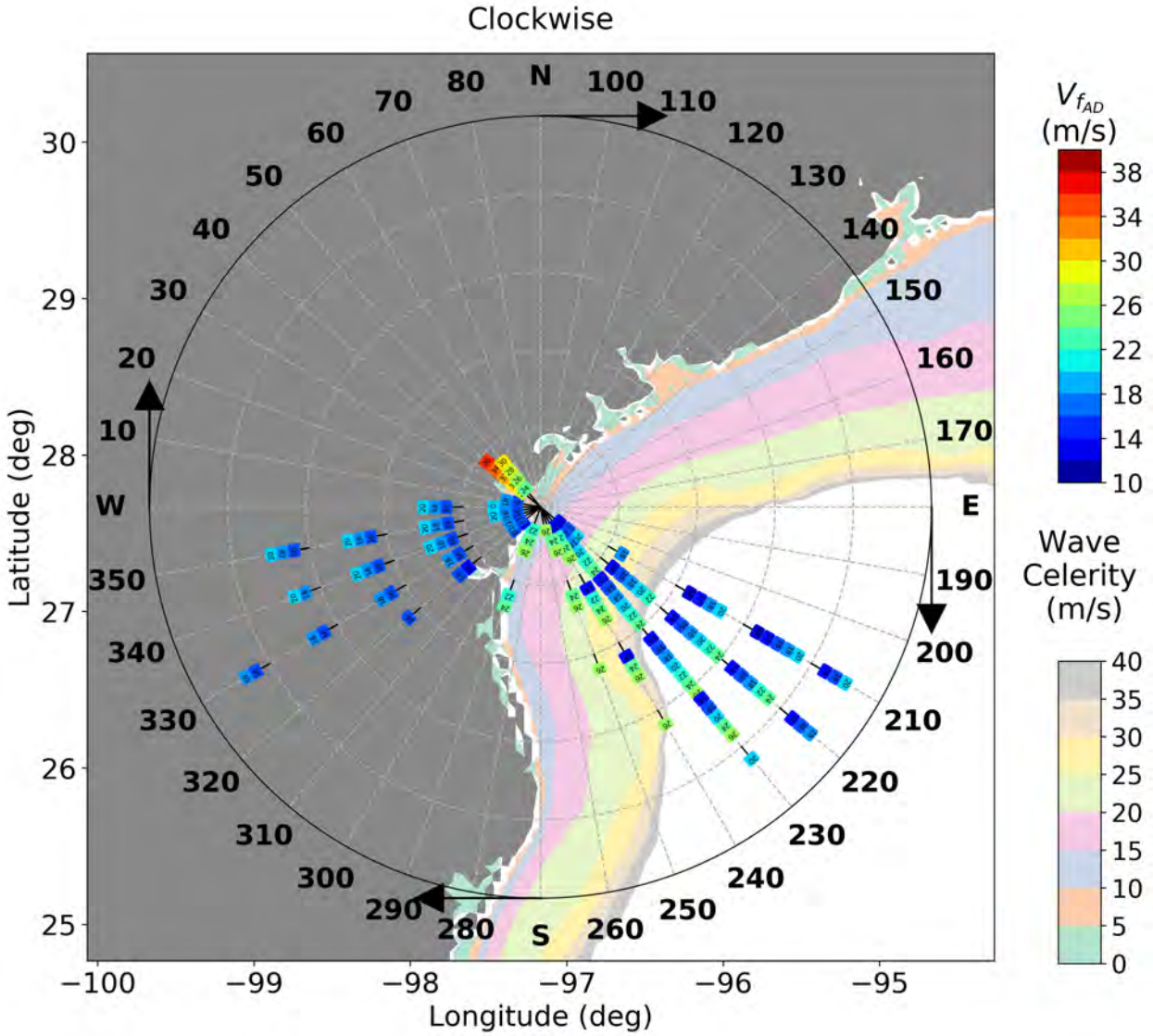

Figure 128: Severe MT rose chart for MT events with η_{max_MT} greater than 0.3 m at a field site near Mustang Island, TX(97.17 W 27.67 N), Water depth = 13.1 m from MHW for an AD(p_{AD} = 6 mbar) moving clockwise relative to the field site, with $V_{f_{AD}}$s representing color-coded blocks

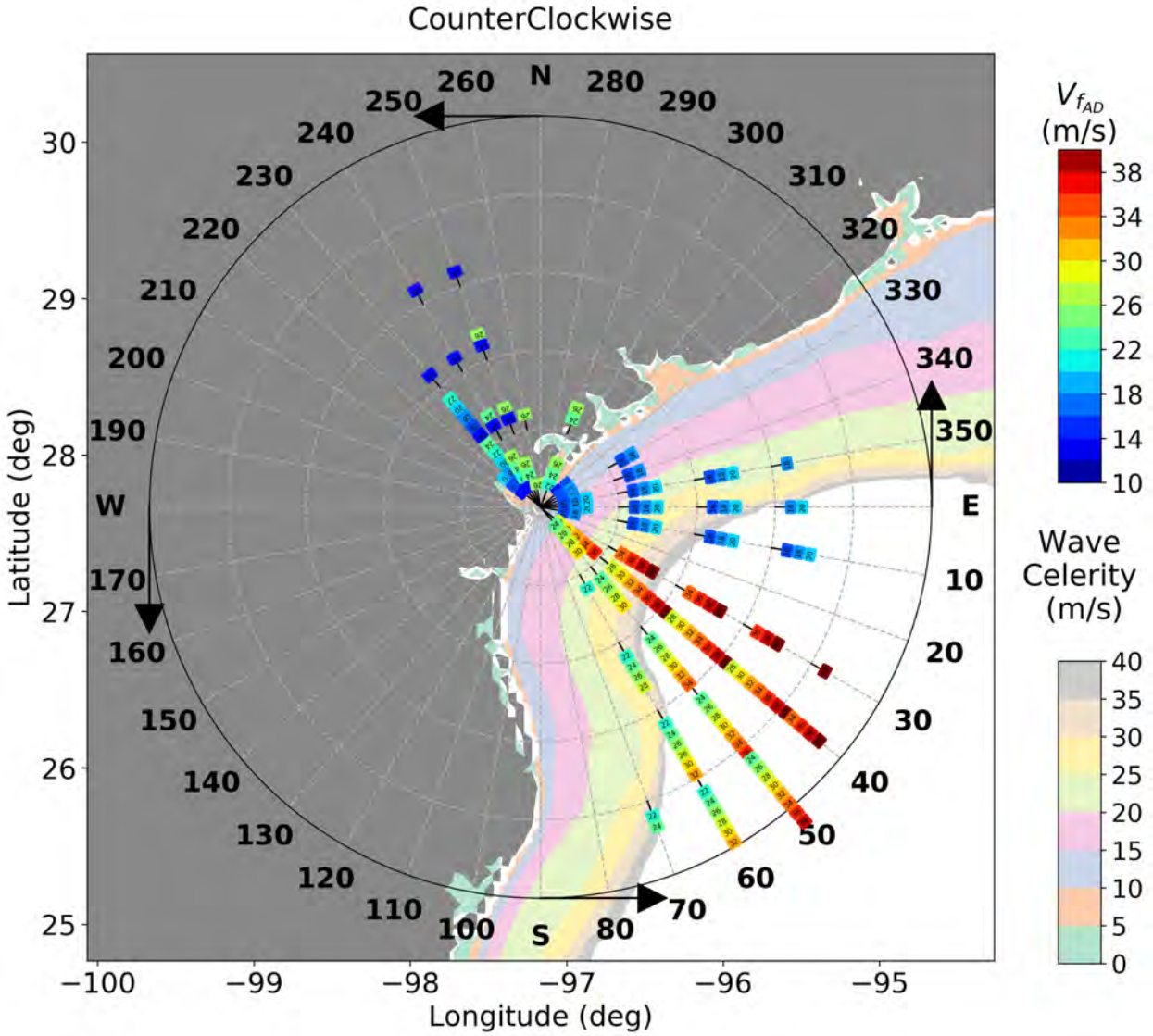

Figure 129: Severe MT rose chart for MT events with η_{max_MT} greater than 0.3 m at a field site near Mustang Island TX(97.17 W 27.67 N), Water depth = 13.1 m from MHW for an AD($p_{AD} = 6$ mbar) moving counterclockwise relative to the field site, with $V_{f_{AD}}$s representing color-coded blocks

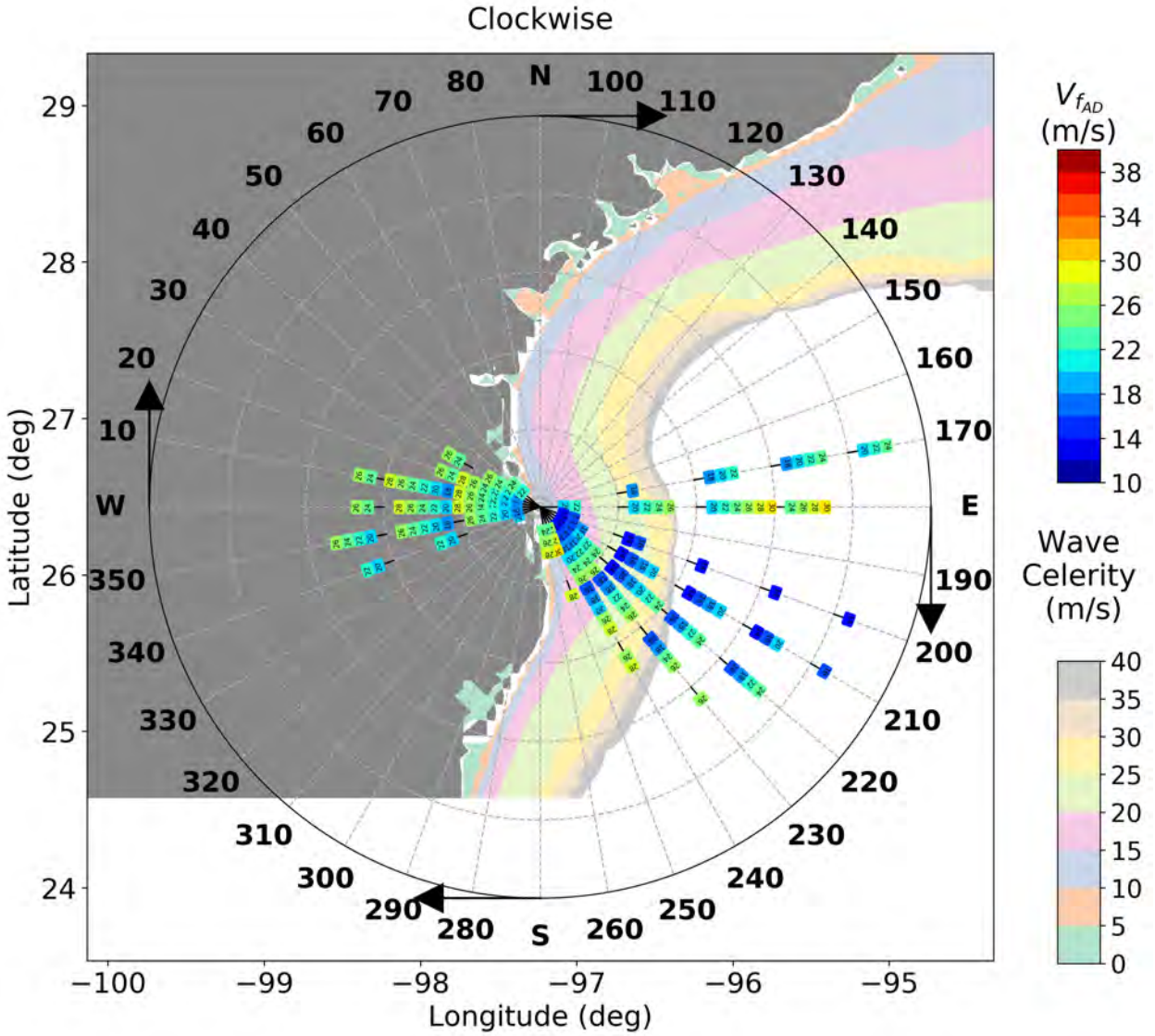

Figure 130: Severe MT rose chart for MT events with η_{max_MT} greater than 0.3 m at a field site near South Padre, TX(97.23 W 26.43 N), Water depth = 7.5 m from MHW for an AD(p_{AD} = 6 mbar) moving clockwise relative to the field site, with $V_{f_{AD}}$s representing color-coded blocks

References

C. Amante and B. Eakins. ETOPO1 1 arc-minute global relief model: Procedures, data sources and analysis. *NOAA Technical Memorandum NESDIS NGDC-24. National Geophysical Data Center, NOAA*, 2009. doi: 10.7289/V5C8276M. [accessed 01-March-2019].

E. J. Anderson, A. J. Bechle, C. H. Wu, D. J. Schwab, G. E. Mann, and K. A. Lombardy. Reconstruction of a meteotsunami in Lake Erie on 27 may 2012: Roles of atmospheric conditions on hydrodynamic response in enclosed basins. *Journal of Geophysical Research: Oceans*, 120(12):8020–8038, 2015.

D. Basco and C. Klentzman. On the classification of coastal storms using principles of momentum conservation. In *Proc. 31st Int. Conf. on Coastal Eng.* ASCE, 2006.

A. J. Bechle, C. H. Wu, D. A. Kristovich, E. J. Anderson, D. J. Schwab, and A. B. Rabinovich. Meteotsunamis in the Laurentian Great Lakes. *Scientific reports*, 6:37832, 2016.

J. D. Chaytor, E. L. Geist, C. K. Paull, D. W. Caress, R. Gwiazda, J. U. Fucugauchi, and M. R. Vieyra. Source characterization and tsunami modeling of submarine landslides along the yucatán shelf/campeche escarpment, southern gulf of mexico. *Pure and Applied Geophysics*, 173(12):4101–4116, Dec 2016. ISSN 1420-9136. doi: 10.1007/s00024-016-1363-3. URL `https://doi.org/10.1007/s00024-016-1363-3`.

W. Cheng, J. Horrillo, and R. Sunny. Numerical analysis of meteotsunamis in the northeastern gulf of mexico. *Natural Hazards*, Sep 2021. ISSN 1573-0840. doi: 10.1007/s11069-021-05009-9.

B. Dugan and J. Stigall. Origin of overpressure and slope failure in the Ursa region, northern Gulf of Mexico. In D. C. Mosher, R. C. Shipp, L. Moscardelli, J. D. Chaytor, C. D. P. Baxter, H. J. Lee, and R. Urgeles, editors, *Submarine Mass Movements and Their Consequences*, pages 167–178. Springer Netherlands, 2010.

P. K. Dunbar and C. S. Weaver. *U.S. States and Territories National Tsunami Hazard Assessment: Historical Record and Sources for Waves*. U.S. Department of Commerce, National Oceanic and Atmospheric Administration, National Geophysical Data Center Tech. Rep.No. 3, 2008.

G. Dusek, C. DiVeglio, L. Licate, L. Heilman, K. Kirk, C. Paternostro, and A. Miller. A meteotsunami climatology along the US East Coast. *Bulletin of the American Meteorological Society*, 100(7):1329–1345, 2019.

E. L. Geist, J. D. Chaytor, T. Parsons, and U. ten Brink. Estimation of submarine mass failure probability from a sequence of deposits with age dates. *Geosphere*, 9(2):287–298, 2013.

H. P. Greenspan. The generation of edge waves by moving pressure distributions. *Journal of Fluid Mechanics*, 1(6):574–592, 1956.

S. T. Grilli, O.-D. S. Taylor, C. D. P. Baxter, and S. Maretzki. A probabilistic approach for determining submarine landslide tsunami hazard along the upper east coast of the United States. *Mar. Geol.*, 264:74–97, 2009.

C. B. Harbitz, F. Løvholt, and H. Bungum. Submarine landslide tsunamis: How extreme and how likely? *Nat. Hazards*, 72(3):1341–1374, 2014.

C. W. Hirt and B. D. Nichols. Volume of fluid method for the dynamics of free boundaries. *J. Comput. Phys.*, 39:201–225, 1981.

J. Horrillo. *Numerical Method for Tsunami calculations using Full Navier-Stokes equations and the Volume of Fluid method*. PhD thesis, University of Alaska Fairbanks, 2006.

J. Horrillo, A. Wood, C. Williams, A. Parambath, and G. Kim. Construction of tsunami inundation maps in the Gulf of Mexico. Technical report, Award Number: NA09NWS4670006 to the National Tsunami Hazard Mitigation Program (NTHMP), National Weather Service Program Office, NOAA, 2011. avail. from http://www.tamug.edu/tsunami/NTHMP.html.

J. Horrillo, A. Wood, G.-B. Kim, and A. Parambath. A simplified 3-D Navier-Stokes numerical model for landslide-tsunami: Application to the Gulf of Mexico. *J. Geophys. Res.-Oceans*, 118:6934–6950, 2013. doi:10.1002/2012JC008689.

J. Horrillo, A. Pampell-Manis, C. Sparagowski, L. Parambath, and Y. Shigihara. Construction of five tsunami inundation maps for the Gulf of Mexico. Technical report, Award Number: NA12NWS4670014 and NA13NWS4670018 to the National Tsunami Hazard Mitigation Program (NTHMP), National Weather Service Program Office, NOAA, 2015. avail. from http://www.tamug.edu/tsunami/NTHMP.html.

J. Horrillo, W. Cheng, A. Pampell-Manis, and J. Figlus. Implementing nthmp-mms strategic plan in tsunami hazard mitigation products for the Gulf of Mexico. Technical report, Award Number: NA14NWS4670049 to the National Tsunami Hazard Mitigation Program (NTHMP), National Weather Service Program Office, NOAA, 2016. avail. from http://www.tamug.edu/tsunami/NTHMP.html.

J. Horrillo, W. Cheng, and J. Figlus. Development of four additional tsunami inundation maps with revision of Port Aransas, TX and updating existing ones with maritime products. Technical report, Award Number: NA15NWS4670031 and NA16NWS4670039 to the National Tsunami Hazard Mitigation Program (NTHMP), National Weather Service Program Office, NOAA, 2017. avail. from http://www.tamug.edu/tsunami/NTHMP.html.

J. Horrillo, W. Cheng, and J. Figlus. Development of two tsunami inundation maps in the GOM and inclusion of the USGS' Yucatan landslide tsunami sources. Technical report, Award Number: NA17NWS4670015 to the National Tsunami Hazard Mitigation Program (NTHMP), National Weather Service Program Office, NOAA, 2018. avail. from http://www.tamug.edu/tsunami/NTHMP.html.

J. J. Horrillo, W. Cheng, R. Sunny, A. Jose, and Y. Shang. Development of two tsunami inundation maps and continuation of the meteotsunami characterization for the gom. Technical report, Award Number: NA19NWS4670015 to the National Tsunami Hazard Mitigation Program (NTHMP), National Weather Service Program Office, NOAA, 2020. avail. from http://www.tamug.edu/tsunami/NTHMP.html.

J. J. Horrillo, W. Cheng, A. Jose, and Y. Shang. Development of two tsunami inundation maps and continuation of the meteotsunami characterization for the gom. Technical report, Award Number: NA20NWS4670066 to the National Tsunami Hazard Mitigation Program (NTHMP), National Weather Service Program Office, NOAA, 2021. avail. from http://www.tamug.edu/tsunami/NTHMP.html.

J. L. Irish and D. T. Resio. A hydrodynamics-based surge scale for hurricanes. *Ocean Eng.*, 37:69–81, 2010.

L. Kantha. Time to replace the Saffir-Simpson hurricane scale? *Eos, Transactions American Geophysical Union*, 87(1):3–6, 2006.

J. Kim and R. Omira. The 6–7 july 2010 meteotsunami along the coast of portugal: insights from data analysis and numerical modelling. *Natural Hazards*, 106(2):1397–1419, Mar 2021. ISSN 1573-0840. doi: 10.1007/s11069-020-04335-8.

W. Knight. Model predictions of Gulf and Southern Atlantic Coast tsunami impacts from a distribution of sources. *Sci. of Tsunami Hazards*, 24:304–312, 2006.

Z. Kowalik, W. Knight, T. Logan, and P. Whitmore. Numerical modeling of the global tsunami: Indonesian tsunami of 26 December 2004. *Science of Tsunami Hazards*, 23(1): 40–56, 2005.

Á. Linares, A. J. Bechle, and C. H. Wu. Characterization and assessment of the meteotsunami hazard in northern Lake Michigan. *Journal of Geophysical Research: Oceans*, 121(9):7141–7158, 2016.

M. Ličer, B. Mourre, C. Troupin, A. Krietemeyer, A. Jansá, and J. Tintoré. Numerical study of Balearic meteotsunami generation and propagation under synthetic gravity wave forcing. *Ocean Modelling*, 111:38 – 45, 2017. ISSN 1463-5003. doi: https://doi.org/10.1016/j.ocemod.2017.02.001.

A. M. López-Venegas, J. Horrillo, A. Pampell-Manis, V. Huérfano, and A. Mercado. Advanced tsunami numerical simulations and energy considerations by use of 3D - 2D coupled models: The October 11, 1918, Mona Passage tsunami. *Pure Appl. Geophys.*, 172(6):1679–1698, 2015.

P. J. Lynett, J. C. Borrero, R. Weiss, S. Son, D. Greer, and W. Renteria. Observations and modeling of tsunami-induced currents in ports and harbors. *Earth and Planetary Science Letters*, 327:68–74, 2012.

P. J. Lynett, J. Borrero, S. Son, R. Wilson, and K. Miller. Assessment of the tsunami-induced current hazard. *Geophysical Research Letters*, 41(6):2048–2055, 2014.

S. Maretzki, S. Grilli, and C. D. P. Baxter. Probabilistic SMF tsunami hazard assessment for the upper east coast of the United States. In V. Lykousis, D. Sakellariou, and J. Locat, editors, *Submarine Mass Movements and Their Consequences*, pages 377–385. Springer Netherlands, 2007.

D. Masson, C. Habitz, R. Wynn, G. Pederson, and F. Lovholt. Submarine landslides: Processes, triggers and hazard protection. *Philos. Trans. R. Soc. A*, 364:2009–2039, 2006.

S. Monserrat, I. Vilibić, and A. B. Rabinovich. Meteotsunamis: atmospherically induced destructive ocean waves in the tsunami frequency band. *Natural Hazards and Earth System Science*, 6(6):1035–1051, Dec. 2006a.

S. Monserrat, I. Vilibić, and A. B. Rabinovich. Meteotsunamis: atmospherically induced destructive ocean waves in the tsunami frequency band. *Natural hazards and earth system sciences*, 6(6):1035–1051, 2006b.

M. Olabarrieta, A. Valle-Levinson, C. J. Martinez, C. Pattiaratchi, and L. Shi. Meteotsunamis in the northeastern Gulf of Mexico and their possible link to El Niño Southern Oscillation. *Natural hazards*, 88(3):1325–1346, 2017.

A. Pampell-Manis, J. Horrillo, Y. Shigihara, and L. Parambath. Probabilistic assessment of landslide tsunami hazard for the northern Gulf of Mexico. *J. Geophys. Res.-Oceans*, 2016. doi:10.1002/2015JC011261.

C. B. Pattiaratchi and E. Wijeratne. Are meteotsunamis an underrated hazard? *Philosophical Transactions of the Royal Society A: Mathematical, Physical and Engineering Sciences*, 373(2053):20140377, 2015.

C. K. Paull, D. W. Caress, R. Gwiazda, J. Urrutia-Fucugauchi, M. Rebolledo-Vieyra, E. Lundsten, K. Anderson, and E. J. Sumner. Cretaceous–paleogene boundary exposed: Campeche escarpment, gulf of mexico. *Marine Geology*, 357:392–400, 2014.

C. H. Paxton and D. A. Sobien. Resonant interaction between an atmospheric gravity wave and shallow water wave along Florida's west coast. *Bulletin of the American Meteorological Society*, 79(12):2727–2732, 1998.

L. D. Paxton. Development of a forecast process for meteotsunami events in the Gulf of Mexico. Master's thesis, University of South Florida, 2016.

L. Prechelt. Automatic early stopping using cross validation: quantifying the criteria. *Neural Networks*, 11(4):761–767, 1998.

J. Proudman. The effects on the sea of changes in atmospheric pressure. *Geophysical Supplements to the Monthly Notices of the Royal Astronomical Society*, 2(4):197–209, 1929.

A. Rabinovich and S. Monserrat. Meteorological tsunamis near the Balearic and Kuril Islands: Descriptive and statistical analysis. *Natural Hazards*, 13(1):55–90, 1996.

A. B. Rabinovich. Twenty-seven years of progress in the science of meteorological tsunamis following the 1992 daytona beach event. *Pure and Applied Geophysics*, 177(3):1193–1230, 2020.

A. B. Rabinovich, J. Šepić, and R. E. Thomson. The meteorological tsunami of 1 November 2010 in the southern Strait of Georgia: a case study. *Natural Hazards*, 106(2):1503–1544, Mar 2021. ISSN 1573-0840. doi: 10.1007/s11069-020-04203-5.

J. Šepić and I. Vilibić. The development and implementation of a real-time meteotsunami warning network for the Adriatic Sea. *Natural Hazards and Earth System Sciences*, 11(1): 83–91, 2011.

A. Sheremet, U. Gravois, and V. Shrira. Observations of meteotsunami on the Louisiana shelf: a lone soliton with a soliton pack. *Natural Hazards*, 84(2):471–492, Nov 2016. ISSN 1573-0840. doi: 10.1007/s11069-016-2446-2.

L. Shi, M. Olabarrieta, A. Valle-Levinson, and J. C. Warner. Relevance of wind stress and wave-dependent ocean surface roughness on the generation of winter meteotsunamis in the Northern Gulf of Mexico. *Ocean Modelling*, 140:101408, 2019.

L. Shi, M. Olabarrieta, D. S. Nolan, and J. C. Warner. Tropical cyclone rainbands can trigger meteotsunamis. *Nature communications*, 11(1):1–14, 2020.

U. S. ten Brink, H. J. Lee, E. L. Geist, and D. Twichell. Assessment of tsunami hazard to the U.S. East Coast using relationships between submarine landslides and earthquakes. *Mar. Geol.*, 264:65–73, 2009a.

U. S. ten Brink, D. Twichell, P. Lynett, E. Geist, J. Chaytor, H. Lee, B. Buczkowski, and C. Flores. Regional assessment of tsunami potential in the Gulf of Mexico. *U. S. Geol. Surv. Admin. Rep.*, 2009b.

I. Vilibić, K. Horvath, N. Strelec Mahović, S. Monserrat, M. Marcos, Á. Amores, and I. Fine. Atmospheric processes responsible for generation of the 2008 Boothbay meteotsunami. *Natural Hazards*, 74(1):25–53, Oct 2014a. ISSN 1573-0840. doi: 10.1007/s11069-013-0811-y.

I. Vilibić, S. Monserrat, and A. B. Rabinovich. Meteorological tsunamis on the US East Coast and in other regions of the World Ocean. *Natural Hazards*, 74(1):1–9, Oct 2014b. ISSN 1573-0840. doi: 10.1007/s11069-014-1350-x.

P. Whitmore and B. Knight. Meteotsunami forecasting: sensitivities demonstrated by the 2008 Boothbay, Maine, event. *Natural Hazards*, 74(1):11–23, Oct 2014. ISSN 1573-0840. doi: 10.1007/s11069-014-1056-0.

R. Wilson, C. Davenport, and B. Jaffe. Sediment scour and deposition within harbors in california (usa), caused by the march 11, 2011 tohoku-oki tsunami. *Sedimentary Geology*, 282:228–240, 2012.

R. I. Wilson, A. R. Admire, J. C. Borrero, L. A. Dengler, M. R. Legg, P. Lynett, T. P. McCrink, K. M. Miller, A. Ritchie, K. Sterling, et al. Observations and impacts from the 2010 chilean and 2011 japanese tsunamis in california (usa). *Pure and Applied Geophysics*, 170(6-8):1127–1147, 2013.

Y. Yamazaki, Z. Kowalik, and K. F. Cheung. Depth-integrated, non-hydrostatic model for wave breaking and run-up. *Int. J. Numer. Meth. Fl.*, 61:473–497, 2008.